

**Measurement of the Neutral
Current Reaction at high Q^2 in
the H1 Experiment at HERA II**

Dissertation

zur Erlangung des Doktorgrades
des Fachbereichs Physik
der Ludwig-Maximilians Universität

vorgelegt von

Stanislav Shushkevich

aus Korolev, Russland

München

2012

Gutachter der Dissertation: Prof. Dr. Christian Kiesling

Gutachter der Disputation: Prof. Dr. Jochen Schieck

Tag der mündlichen Prüfung: 15.02.2012

Abstract

This thesis presents inclusive $e^\pm p$ double and single differential cross section measurements for neutral current deep inelastic scattering of longitudinally polarized leptons on protons as a function of the negative four-momentum transfer squared Q^2 and the Bjorken variable x . The data were collected in the years 2003-2007 in the H1 experiment at HERA with positively and negatively longitudinally polarized lepton beams of 27 GeV and a proton beam of 920 GeV corresponding to the centre-of-mass energy of $\sqrt{s} = 319$ GeV. The integrated luminosity is about 330 pb^{-1} . An overview of the phenomenology of the deep inelastic scattering is given and the experimental apparatus is described. The NC cross section measurement procedure is presented and discussed in details. The measured cross sections are used to investigate electroweak effects at high Q^2 . The proton structure function $x\tilde{F}_3$, sensitive to the valence quarks in the proton, is measured. The polarization effects sensitive to the chiral structure of neutral currents are investigated. The Standard Model predictions are found to be in a good agreement with the measurement.

Kurzfassung

Diese Arbeit präsentiert doppelt- und einfachdifferenzielle inklusive $e \pm p$ Wirkungsquerschnittsmessungen für den neutralen Strom in tiefinelastischer Streuung von longitudinal polarisierten Leptonen auf Protonen als Funktion des negativen quadrierten Viererimpulsübertrags Q^2 und der Bjorkenvariable x . Die Daten wurden in den Jahren 2003-2007 mit dem H1 Experiment bei HERA mit positiven und negativen longitudinal polarisierten Leptonstrahlen von 27 GeV und einem Protonstrahl von 920 GeV aufgezeichnet. Das entspricht einer Schwerpunktsenergie von $\sqrt{s} = 319$ GeV. Die integrierte Luminosität ist etwa 330 pb^{-1} . Eine Übersicht der Phenomenologie der tiefinelastischen Streuung wird gegeben und die experimentelle Anordnung wird beschrieben. Die Methode der neutralen Wirkungsquerschnittsmessung wird vorgestellt und im Detail diskutiert. Der gemessenen Wirkungsquerschnitte werden verwendet um elektroschwache Effekte bei hohem Q^2 zu untersuchen. Die Protonstrukturfunktion $x\tilde{F}_3$, welche sensitiv auf die Valenzquarks des Protons ist, wurde gemessen. Der Polarisationseffekte, welche sensitiv auf die chirale Struktur des neutralen Stroms sind wurden untersucht. Die Standardmodellvorhersagen sind in guter Übereinstimmung mit der Messung.

Contents

1	Introduction	7
2	Theoretical Overview	11
2.1	Deep Inelastic Scattering (DIS)	11
2.1.1	Kinematics of DIS Process	11
2.1.2	Structure Functions in DIS	12
2.2	The Quark Parton Model (QPM)	14
2.3	Quantum Chromodynamics (QCD)	17
2.3.1	The QCD Running Coupling α_S	17
2.3.2	Factorization	18
2.3.3	Scaling Violation	19
2.3.4	Parton Distribution Functions in QCD	21
2.3.5	Longitudinal Structure Function in QCD	23
2.4	The Neutral Current Cross Section	24
2.5	The Charged Current Cross Section	26
2.6	Radiative Corrections	27
3	Electron-proton Collider HERA	31
3.1	HERA Accelerator	31
3.2	Polarization at HERA	33
3.3	Run Periods for HERA II	34
4	The H1 Experiment at HERA	37
4.1	Calorimetry	37
4.1.1	Liquid Argon Calorimeter (LAr)	39
4.1.2	“Spaghetti” Calorimeter (SpaCal)	41
4.2	Tracking	41
4.2.1	Central Tracking Detector (CTD)	42
4.2.2	Forward Tracking Detector (FTD)	43
4.3	Trigger System	44
4.3.1	The First Trigger Level (L1)	44
4.3.2	The Second/Third Trigger Level (L2/L3)	47
4.3.3	The Fourth/Fifth Trigger Level (L4/L5)	48
4.4	Time-of-Flight Counters	48
4.5	The Luminosity Measurement in the H1 Experiment	49
4.6	Data Storage Model and Software Environment	51

5	Reconstruction of the Kinematic Variables	53
5.1	The Reconstruction Methods	53
5.2	Comparison of Methods	56
6	Monte Carlo Simulation	61
6.1	Generation of the NC DIS Events	62
6.2	Generation of the Background Events	62
7	Data Analysis	65
7.1	General Strategy of the Analysis	65
7.2	Electron Identification	66
7.2.1	Identification of the Scattered Electron	66
7.2.2	Efficiency of the Scattered Electron Identification	68
7.3	Electron Energy Measurement	70
7.3.1	Electron Energy Calibration	70
7.3.2	Electron Energy Resolution	71
7.3.3	Check of the Calibration with the Compton Events	71
7.3.4	Electron Energy Scale Uncertainty	75
7.4	Electron Angles Measurement	75
7.4.1	Track Reconstruction	76
7.4.2	Vertex Reconstruction, DTRA and DTNV Tracks	78
7.4.3	Alignment of the LAr Calorimeter	78
7.4.4	The Polar Angle Measurement	80
7.5	Primary Interaction Vertex	80
7.5.1	The NC Optimal Vertex	82
7.5.2	Vertex and Track-Cluster Matching Efficiency	86
7.6	Hadronic Final State	91
7.6.1	Separation of the Electromagnetic and Hadronic Showers	91
7.6.2	The HADROOII Algorithm	92
7.6.3	Calibration of the Hadronic Energy	94
7.6.4	Hadronic Energy in SpaCal	96
7.6.5	The DTNV Sample	97
7.6.6	Noise Contribution to the HFS Measurement	99
7.7	Trigger Treatment	101
7.7.1	Triggering of Electron in LAr	103
7.7.2	Timing Conditions	104
7.7.3	Veto Conditions	105
7.7.4	Track Conditions	106
7.7.5	Trigger Level 2 Condition	106
7.7.6	Fiducial Volume Definition	107
7.7.7	Trigger Efficiency Uncertainty	107
7.8	Background Treatment	109
7.8.1	Charge Determination	109
7.8.2	Background Charge Asymmetry	110
7.8.3	Photoproduction Background Using Pythia MC	112
7.8.4	Rejection of Compton Events	113
7.8.5	Rejection of Non- ep Background	114

7.9	Vertex Reweighting in MC	117
7.10	QED Radiation Correction Uncertainty	118
7.11	Run Selection	118
8	NC Cross Section Measurement	121
8.1	Binning, Acceptance, Purity and Stability.	121
8.2	Cross Section Calculation	126
8.3	Meaning of the Measurement	128
8.4	Neutral Current Event Selection	130
8.5	Neutral Current Control Plots	132
8.6	Systematic Uncertainties	132
9	Results	137
9.1	Double Differential NC Cross Sections.	137
9.2	Single Differential NC Cross Sections.	140
9.3	The $x\tilde{F}_3$ Structure Function.	145
9.4	Polarization Asymmetry.	145
10	Summary and Outlook	153
A	Trigger Components Characteristics	155
B	Luminosity Correction	157
C	Cross Section Tables	159

Chapter 1

Introduction

The understanding of the structure of matter and interaction forces is the fundamental question of physics. Reducing the spatial scales at which the matter is examined from visible objects to single atoms, then to nucleons and further to constituents of those, we enter the field of knowledge called particle physics.

The main (and very powerful) instruments for such investigations are the scattering experiments. Particles of high momenta, and consequently short Compton wavelengths, in collisions “feel” the physical phenomena at a tiny scale; the bigger the initial energy the smaller the distance which can be probed. This idea was introduced in the classical Rutherford experiment [1] (also called Geiger-Marsden experiment) with (back-) scattering the α -particles generated by the natural radioactive decay of radium off a gold foil in which the small compact “central charge” inside the atom, known now as an atomic nucleon, was discovered. The key feature of the measurements was that the distribution of the scattered particles looked like as it was the scattering of light point-like objects on heavy point-like objects. This “point-likeness” property was checked down to scales of 10^{-12} cm.

With the time the accessible energies of the “probe” particles grew and in the 50’s the experiments accomplished by R. Hofstadter et. al. [2] on elastic scattering of electrons at the energies of 100-200 MeV on protons (hydrogen target) resulted in the discovery the of nucleon form-factors. Thus the nucleon appeared to have some sub-structure but the resolving power was not enough to go into details.

In the 70’s the inelastic scattering of electrons on protons (hydrogen target) at 10-20 GeV were accomplished in the SLAC experiments [3]. The term “inelastic” generally means that the proton “breaks up” in collision. The measurement showed the electrons were scattered off the point-like objects inside the proton, the so-called “partons”. With the progress in the theoretical investigations [4], [5] this led to the concept of hadrons to be consisted of point-like “quarks”.

The next qualitative step was done with the construction of the HERA electron-proton collider at DESY. The target is approximately 1 TeV proton beam probed with 30 GeV electrons allowing to substantially decrease the minimal spatial scale available for the investigation in the process of deep inelastic scattering (DIS). New details of the proton structure were observed, and although the constituent quarks have been seen before (the “valence” quarks), the dynamical processes of emission of electrically neutral “gluons” and the production of (“sea”) quarks out these gluons have been resolved. All these observations allowed to construct a consistent theory

of the strong interactions (QCD) [6], similar to the electromagnetic case.

Including the development of the electroweak theory, we have a self-consistent (probably, after some reasonable extension) theory of point-like elementary particles, known as Standard Model (SM) [7]. This theory operates with spin-1/2 objects (fermions: e, μ, ν_e, \dots participating electroweak interactions only and quarks participating also in the strong interactions) interacting via exchange of the spin-1 objects (gauge bosons: γ, Z, W for the electroweak interactions and gluons for the strong interactions). All particles gain mass via the Higgs mechanism interacting with the Higgs boson (spin-0 particle). For the time being this theory allows to calculate all the “hard” processes cross sections for the high energy physic experiments operating at the level of elementary particles.

The present work is devoted to the measurement of the electron-proton scattering cross section in H1 experiment at HERA. The process involves the electroweak and strong sectors of the SM. The data obtained at the HERA II running period (2003-2007) with polarized electron and positron beams at the ep center-of-mass energy $\sqrt{s} = 319$ GeV are used. The Neutral Current reaction $ep \rightarrow eX$ at large values of the negative squared momentum transferred from the electron to hadron $Q^2 \gtrsim 100$ GeV² is studied. The measurement is inclusive which means that final states with the scattered electron e and any other final state particles X are accepted.

The emphasis in this work is put on the precision of the measurement and possibility of further combination with the measurements on other data sets [8]. As a motivation, the following (inspiring) issues can be considered. First of all, the measurement of the Neutral Currents is an effective way to understand the strong interaction behavior in the low energy regime (and even without an assumption about the parton structure of the proton). Effects of parton dynamics in the limit of large coupling constant are uncalculable at the present time but very important for applications could be measured: the SM predictions are for the point-like particles, but in the real (LHC, Tevatron) experiments one has the hadronic beams being collided. To make the transfer from the level of compound particles to the level of primary, point-like particles, where the calculations can be done, the information from the DIS is used to extract the Parton Distribution Functions (PDFs) of the proton, for which the unique data are provided by the HERA collider. The PDF functions is an additional empirical input to SM for any calculation involving the hard interactions between protons.

The usefulness of most precise measurements which provides the best determination of the parton distributions can be demonstrated on a (nowadays) “hot topic” — the Higgs boson searches at the LHC. In [9] the influence of the uncertainty on the proton structure knowledge on the Higgs searches scenario is discussed. In the recent case [10] the conservative estimations of the uncertainty from the PDFs significantly decreases the confidence level for the Higgs exclusion limit in the region of the possible Higgs mass of [158, 175] GeV.

Electroweak effects like the polarization asymmetry can be measured and, with the inclusion of the Charged Current ($ep \rightarrow \nu X$) results, the investigation of the electroweak aspects [11] of the SM (with polarized beams) can be done: measurements of the couplings of the quarks to the Z boson and the left-handed nature of the weak interactions. The concept of point-like quarks can be examined [12] down to the scales of 10^{-18} m.

The thesis is organized as follows. The second chapter is devoted to the theoretical aspects of Deep Inelastic Scattering and related topics. The HERA ep collider and the H1 experiment are described in the third and fourth chapter respectively. Then, in Chapter 5, the reconstruction methods for the event kinematics are discussed and in Chapter 6 the Monte Carlo programs used in the analysis are described. Chapters 7, 8 and 9 are central to the whole work: the detailed description of the experimental methods and the results obtained are given here. The thesis is summarized in the last Chapter 10.

Chapter 2

Theoretical Overview

2.1 Deep Inelastic Scattering (DIS)

The term deep inelastic scattering (DIS) refers to the process in which a lepton, either charged or neutral, scatters off a nucleon with large four momentum transfer Q^2 such that the concept of the parton structure of a nucleon becomes essential.

The amplitude for such scattering process could be represented as a convolution of a lepton current, a propagator for the exchanged boson, and a hadronic current. According to the type of the exchanged boson the DIS processes are classified as:

- **Neutral Currents (NC)** $ep \rightarrow eX$, mediated by the exchange of a neutral boson γ or Z^0 . At moderate $Q^2 \ll M_Z^2$ the cross section is dominated by photon exchange, since Z^0 boson exchange is suppressed by the propagator of Z^0 . Here X denotes all possible hadronic final states, and M_Z is a mass of the Z boson.
- **Charged Currents (CC)** $ep \rightarrow \nu X$, mediated by the exchange of a charged boson W^\pm . At moderate $Q^2 \ll M_W^2$ the intensity of the CC process is much smaller than that for the NC, but becomes of the same order at high Q^2 , $Q^2 \gtrsim M_W^2$. M_W denotes mass of the W boson.

If one does not discriminate between the different hadronic final states X the process is called inclusive.

2.1.1 Kinematics of DIS Process

A deep inelastic scattering process is generally of the form

$$l(k) + h(p) \rightarrow l'(k') + X \quad (2.1)$$

where $l(k)$ represents a lepton of four-momentum k^μ , $h(p)$ a hadron of four-momentum p^μ and X an arbitrary hadronic final state. In case of HERA the hadron $h(p)$ is a proton. This process, illustrated in Fig. 2.1, is initiated by the exchange of a vector boson V .

In DIS, the momentum transfer between lepton and hadron q is space-like, i.e. $q^2 < 0$

$$\begin{aligned} q^\mu &= k^\mu - k'^\mu, \\ -q^2 &= Q^2 \end{aligned} \quad (2.2)$$

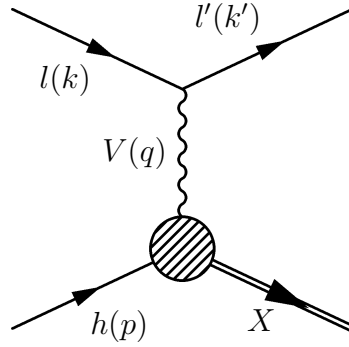


Figure 2.1: Deep inelastic scattering kinematics

The squared center-of-mass energy of the exchange boson – proton system, $W^2 = M_X^2$, is

$$W^2 = (p + q)^2 = m_p^2 + \frac{Q^2}{x}(1 - x). \quad (2.3)$$

and is the squared mass of the hadronic final state. Here x is the Bjorken scaling variable defined as

$$x = \frac{-q^2}{2p \cdot q} = \frac{Q^2}{2m_p \nu}, \quad (2.4)$$

where ν is the energy transferred from the lepton to the proton in the proton rest frame

$$\nu = \frac{p \cdot q}{m_p} = E_k - E_{k'}. \quad (2.5)$$

The inelasticity y measures the fraction of energy transferred from the lepton to the proton in the proton rest frame

$$y = \frac{p \cdot q}{p \cdot k} = \frac{E_k - E_{k'}}{E_k}. \quad (2.6)$$

The Mandelstam variable s is the square of the ep center-of-mass energy

$$s = (p + k)^2 \quad (2.7)$$

For a collider experiment, where the initial beam energies are fixed, s has a constant value.

The variables x, y and s are related to Q^2 by

$$Q^2 = sxy, \quad (2.8)$$

where the proton mass is neglected. Thus kinematically at fixed Q^2 small values of x correspond to the large values of y and vice versa.

2.1.2 Structure Functions in DIS

At lowest order in electroweak interactions, the cross section for the scattering of leptons off protons can be expressed as a sum of products of the leptonic and hadronic tensors

$$d\sigma = \frac{d^3k'}{8\pi s \left| \vec{k}' \right|} \sum_a p_a \cdot \mathfrak{L}_a^{\mu\nu}(k, q) \mathfrak{W}_{\mu\nu}^a(p, q), \quad (2.9)$$

where for the NC process a runs over γ for the pure photon exchange, Z for the pure Z^0 exchange, and γZ for the term appears from interference between the photon and Z^0 contributions in the squared matrix element. For the CC process there is only one term $a = W$ corresponds to the W^\pm exchange. Here the form $-g_{\alpha\beta}/(q^2 - m_V^2)$ for the vector boson V propagator is assumed (m_V is a mass of the boson), neglecting the gauge- and mass-dependent terms, proportional to $q_\alpha q_\beta$. Corrections to this approximation vanish for $V = \gamma$, and are suppressed by the ratio m_l/m_V for $V = Z, W^\pm$.

The factors p_a in (2.9) represent the corresponding propagators and couplings products

$$\begin{aligned} p_\gamma &= \frac{e^4}{Q^4}; & p_{\gamma Z} &= \frac{e^4}{Q^2(Q^2 + M_Z^2)}; & p_Z &= \frac{e^4}{(Q^2 + M_Z^2)^2}; \\ p_W &= \frac{e^4}{64 \sin^4 \Theta_W (Q^2 + M_W^2)^2}; \end{aligned} \quad (2.10)$$

with Θ_W is the Weinberg angle.

The leptonic tensor \mathfrak{L} can be evaluated explicitly in the electroweak theory with a conventional but arbitrary normalization. For the incoming leptons of charge $e = \pm 1$ and helicity $\lambda = \pm 1$ one takes [13]

$$\begin{aligned} \mathfrak{L}_\gamma^{\mu\nu} &= 2(k^\mu k'^\nu + k^\nu k'^\mu - k k' g^{\mu\nu} - i\lambda \epsilon^{\mu\nu\lambda\rho} k_\lambda k'_\rho), \\ \mathfrak{L}_{\gamma Z}^{\mu\nu} &= (v_e + e\lambda a_e) \mathfrak{L}_\gamma^{\mu\nu}, \\ \mathfrak{L}_Z^{\mu\nu} &= (v_e + e\lambda a_e)^2 \mathfrak{L}_\gamma^{\mu\nu}, \\ \mathfrak{L}_W^{\mu\nu} &= (1 + e\lambda)^2 \mathfrak{L}_\gamma^{\mu\nu}, \end{aligned} \quad (2.11)$$

where the vector coupling constant of electron to the Z boson is $v_e = -1/2 - 2e \sin^2 \Theta_W$, and the axial coupling constant is $a_e = -1/2$.

The hadronic tensor, being the result of strong interactions dynamics at low energies, parametrizes our ignorance of the hadronic current. But as soon as it could depend only on the two four-vectors, p^μ and q^μ , has to conserve the current at the hadronic vertex — $q_\mu \mathfrak{W}^{\mu\nu} = q_\nu \mathfrak{W}^{\mu\nu} = 0$ —, and because of the symmetry of the $\mathfrak{L}_{\mu\nu}$ tensor over the indices, the most general form of the hadronic tensor is

$$\begin{aligned} \mathfrak{W}_{\mu\nu}^a &= - \left(g_{\mu\nu} - \frac{q^\mu q^\nu}{q^2} \right) F_1^a(x, Q^2) \\ &+ \left(p_\mu - q_\mu \frac{pq}{q^2} \right) \left(p_\nu - q_\nu \frac{pq}{q^2} \right) \frac{1}{\nu m_p} F_2^a(x, Q^2) \\ &- i \epsilon_{\mu\nu\lambda\rho} p^\lambda q^\rho \frac{1}{\nu m_p} F_3^a(x, Q^2) \end{aligned} \quad (2.12)$$

The hadronic tensor is expanded in a sum of three independent dimensionless scalar functions $F_i^a(x, Q^2)$, $i = 1, 2, 3$ called the γ -, Z -, γZ - or W -structure functions (SF) of the proton. These three fully describe the process involves the proton in DIS. The dependence on just two arguments x and Q^2 is a consequence of the mentioned dependence on two four-vectors and the assumptions of the Lorentz-invariance and rotation-invariance of the interaction.

For the parity-conserving photon exchange only two structure functions are non-zero, and

$$F_3^\gamma(x, Q^2) = 0 \quad (2.13)$$

For the following it is convenient to define the structure function F_L

$$F_L^a = F_2^a - 2xF_1^a \quad (2.14)$$

For the Q^2 large enough to ignore mass terms (typically $Q^2 > 10 \text{ GeV}^2$), the virtual photon – proton cross section is given by

$$\sigma^\gamma = \frac{4\pi^2\alpha}{Q^2(1-x)} F_2^\gamma = \sigma_T^\gamma + \sigma_L^\gamma = \frac{4\pi^2\alpha}{Q^2(1-x)} (2xF_1^\gamma + F_L^\gamma) \quad (2.15)$$

where $\sigma_T^\gamma, \sigma_L^\gamma$ are the cross sections for transverse and longitudinal virtual photon scattering (real photons are transversely polarized only). Therefore F_L^γ measures the cross section of the longitudinally polarized photons scattering on the protons.

From (2.9), (2.11), (2.12), (2.14) after kinematical transformations the resulting double differential cross section in x and Q^2 plane

$$\frac{d^2\sigma^i(e^\pm p)}{dx dQ^2} = A^i \left[Y_+ \tilde{F}_2^i(x, Q^2) - y^2 \tilde{F}_L^i(x, Q^2) \mp Y_- x \tilde{F}_3^i(x, Q^2) \right] \quad (2.16)$$

where $Y_\pm = 1 \pm (1-y)^2$, and $i = \text{NC}, \text{CC}$ corresponds to neutral current ($ep \rightarrow ep$) or charged current ($ep \rightarrow \nu p$) process, respectively. A^i is a process dependent function

$$\begin{aligned} A^{\text{NC}} &= \frac{2\pi\alpha^2}{xQ^4} \\ A^{\text{CC}} &= \frac{G_F^2 M_W^4}{4\pi x (Q^2 + M_W^2)^2} \end{aligned} \quad (2.17)$$

where G_F is the Fermi coupling constant and α is the fine structure constant.

For the neutral currents the generalized structure functions, \tilde{F}_i^{NC} , are the sums with the appropriate coefficients, depend on lepton charge, helicity, and exchanged boson(s) type, of the structure functions $F_i^a, a = \gamma, Z, \gamma Z$ discussed above, and for the charged currents the $\tilde{F}_i^{\text{CC}} = F_i^W$.

Since the cross section at given s depends on the x and Q^2 only, the \tilde{F}_i^{NC} and \tilde{F}_i^{CC} structure functions can be found directly from scattering experiments with known energies of incoming particles in which only two independent variables like outgoing lepton's energy and scattering polar angle are measured.

2.2 The Quark Parton Model (QPM)

Within the Quark Parton Model hadrons, such as the proton, are supposed to be made up of massless point-like ‘‘partons’’. In the case of very large incoming momenta the momenta of this constituent partons can be safely assumed to be collinear to the momentum of the hadron. In this model, the cross section of deep inelastic ep scattering is expressed as the incoherent sum of elementary elastic electron-parton scattering processes. The partons are associated with either constituent or sea quarks.

The incoherence of these elastic processes, i.e. absence of the parton-parton interactions inside a hadron, is justified if the calculations are carried out in a limit of infinite Q^2 . In this case, the single electron-parton scattering process can be shown to take place on a much shorter time scale as the parton-parton interaction [4].

The probability to observe a structure quark of flavour i that carries the fraction x' of the total hadron's momentum p is given by initially unknown but certain for a given type of a hadron and independent on Q^2 distribution functions $q_i(x')$. These functions give the parton number, or density. The parton distribution functions (PDFs) are defined as the momentum distribution of the partons $x'q_i(x')$ also called the momentum density. This simple picture of scattering is presented in Fig. 2.2.

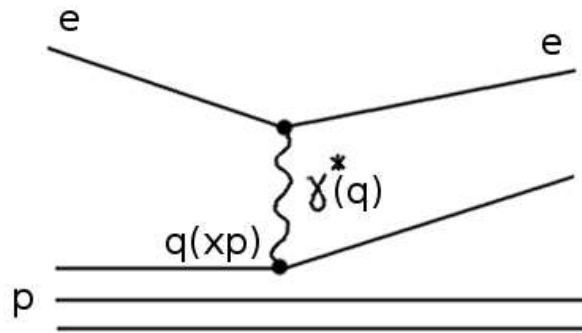


Figure 2.2: The QPM picture of the electron-proton scattering.

Since the partons are assumed to be massless before and after the interaction, for the single electron-parton scattering one could derive $(x'p + q)^2 = 0$, or

$$x' = \frac{Q^2}{2pq} = x \quad (2.18)$$

where the proton mass is neglected. Thus the momentum fraction x' in QPM is identified as the Bjorken scaling variable x introduced above.

The QPM model provides several valuable predictions for the ep scattering. It explains the (approximate) independence of the \tilde{F}_2 structure function on Q^2 at fixed x called scaling invariance or scaling. Scaling was predicted by J.Bjorken [4] and observed at a region of $x \approx 0.1 - 0.3$ in the late 1960ies at SLAC [3] where the high energy electrons ($7 < E_e < 17$ GeV) were scattered off nuclear targets. The results of these measurements are shown in Fig. 2.3. Within the QPM the explanation is straightforward: in the massless limit there is no other scale of dimension [GeV^2] in electron-parton scattering except the Q^2 , and the probability to find the certain parton inside a proton does not depend on Q^2 by the initial assumption, therefore the dimensionless \tilde{F}_2 function can not depend on Q^2 .

Let us now consider the ep NC cross section. For simplicity we restrict ourselves to the region of $Q^2 \ll M_Z^2$ where the contribution from the Z^0 boson is negligible,

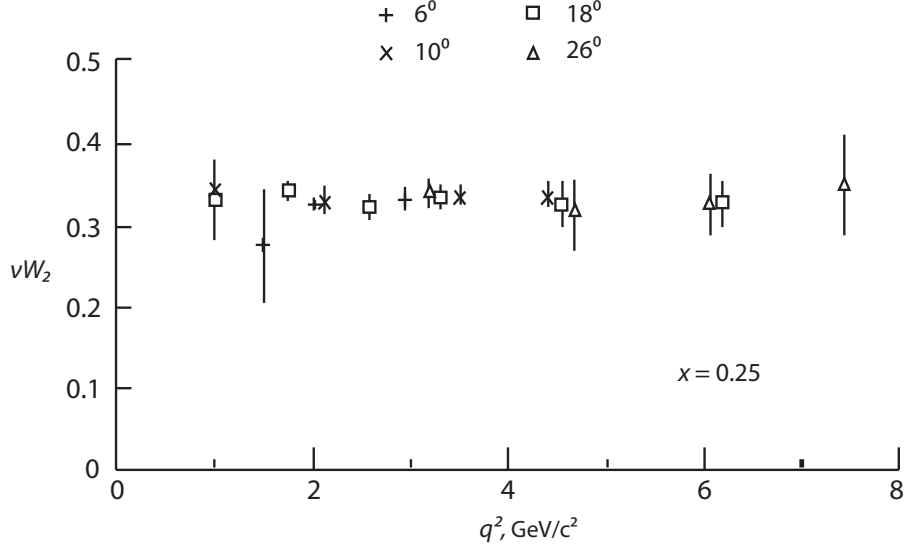


Figure 2.3: Observation of scaling: independence of the structure function $\nu W_2 = F_2$ of Q^2 at Bjorken variable $x = 0.25$.

and compare the QPM result with (2.16)

$$\begin{aligned}
 \text{QPM approach: } \quad \frac{d^2\sigma(e^\pm p)}{dx dQ^2} &= \frac{2\pi\alpha^2}{xQ^4} [(1 + (1 - y)^2) \cdot \sum_i e_i^2 x q_i(x) - y^2 \cdot 0] \\
 \text{SF approach: } \quad \frac{d^2\sigma(e^\pm p)}{dx dQ^2} &= \frac{2\pi\alpha^2}{xQ^4} [(1 + (1 - y)^2) \cdot \tilde{F}_2 - y^2 \cdot \tilde{F}_L]
 \end{aligned} \tag{2.19}$$

where e_i is the electric charge of the parton. The sum in (2.19) is the incoherent sum over the electron scatterings on the differently charged partons with the proton. In this calculation the partons are assumed to be spin-1/2 particles. This assures the absence of the second term in the QPM cross section.

Comparing the equations in (2.19) one obtains in the QPM

$$\begin{aligned}
 \tilde{F}_2 &= \sum_i e_i^2 x q_i(x) \\
 \tilde{F}_L &= 0
 \end{aligned} \tag{2.20}$$

This couples the \tilde{F}_2 structure function with the total content of the charged partons inside the proton.

Later both terms, \tilde{F}_2 and \tilde{F}_L , were measured in SLAC experiments separately. Within the experimental errors it was observed that $\tilde{F}_L = 0$, as it is predicted in (2.20). This confirms the spin-1/2 nature of the quarks assumed in QPM, and the equality $F_L^{\text{QPM}} = 0$ with the definition (2.14) gives

$$2xF_1^{\text{QPM}} = F_2^{\text{QPM}} \tag{2.21}$$

known as the Callan-Gross relation [14].

The total averaged momentum carried by the quarks was determined experimentally [15] and is given by

$$\int_0^1 \sum_i x q_i(x) dx \approx 0.54 \quad (2.22)$$

The result clearly suggested that about half of the proton momentum is carried by electrically neutral constituents nowadays known as gluons.

The latter and the observed [15] slight dependence of structure functions on Q^2 , called scaling violation, resulted in the development of the theory describing the interactions between the quarks and gluons called Quantum Chromodynamics.

2.3 Quantum Chromodynamics (QCD)

Quantum Chromodynamics (QCD) is the part of the Standard Model which describes the strong interactions. It is a quantum field theory which assumes quarks to be elementary spin-1/2 particles interacting via exchange of massless spin-1 gauge bosons, called gluons. The theory possesses $SU(3)$ symmetry, so the particles carry a new quantum number, called color.

The symmetry group of QCD¹ is non-Abelian² which leads to several non-trivial effects compared to Abelian theories like QED. In $SU(3)_C$ gluons themselves carry color charge, i.e. are self-interacting. There are eighth different gluon states in the theory; gluon and antigluon is the same particle.

Quarks do not exist free but are bound in colorless states (mesons — quark-antiquark pairs, and baryons — three-quark combinations) with spatial size of approximately 1 fm; this effect is known as confinement. Contrary, at small distances (which correspond to a big momentum transfer in ep scattering) quarks demonstrate asymptotic freedom — “free particles”-like behavior observed at SLAC experiments.

In the next subsections some aspects of QCD are discussed to give a feeling of the theoretical background and necessity of the inclusive measurements.

2.3.1 The QCD Running Coupling α_S

The Quark Parton Model, which made very successful predictions for the ep scattering, raises a fundamental question: how it could be that the forces between quarks are small at short distances (large Q^2) and are large at large distances (small Q^2).

The answer is in the non-Abelian character of the QCD theory. To renormalize the coupling constant [16] one has to sum over the diagrams shown³ in Fig. 2.4.

There are two types of contributions: one with coupling of fermion (quark) loops to the gluon and another one with self-interaction of bosons (gluons); the latter is absent in an Abelian theory. The gluon loops appear because gluons carry color charges. Both contributions diverge logarithmically with Q^2 , as for the case of electron-positron pairs contribution to the photon propagator in QED, but with coefficients of opposite sign. Writing the overall coefficient of $\ln(Q^2/\mu_0^2)$, where the μ_0^2

¹This group is called $SU(3)_C$.

²The theories with non-Abelian symmetry group known as non-Abelian theories.

³The sum does not include all possible corrections to the gluon propagator, but a class giving the largest correction known as “leading logs”.

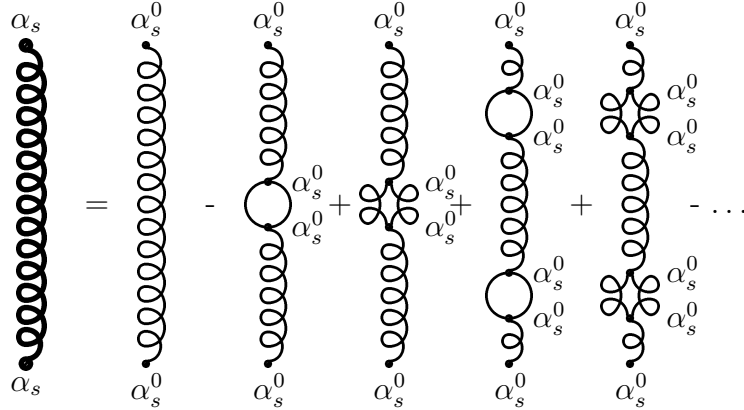


Figure 2.4: Loop corrections to the gluon coupling constant. The α_s^0 denotes a bare coupling constant, and α_s is the measured coupling.

is some reference scale at which we determine (measure) the coupling constant, one gets $\alpha(\mu_0^2)b_0$ with $b_0 = (33 - 2n_f)/12\pi$; n_f is a number of “active” quark flavours, i.e. those with masses smaller than the scale. In the Standard Model number of quark flavours is 6, the fermion loop contribute $-1/6\pi$ for each quark flavour and the gluon self-coupling loop give a positive contribution of $11/4\pi$.

With this leading order correction, one defines the strong running coupling $\alpha_s(Q^2)$, as

$$\alpha_s(Q^2) = \frac{\alpha_s(\mu_0^2)}{1 + \alpha_s(\mu_0^2)b_0 \ln\left(\frac{Q^2}{\mu_0^2}\right)}, \quad (2.23)$$

Because b_0 for QCD is positive, $\alpha_s(Q^2)$ decreases as Q^2 increases and formally $\alpha_s(Q^2) \rightarrow 0$ as $Q^2 \rightarrow \infty$. This remarkable result, known as asymptotic freedom is at the core of how QCD reconcile confined quarks in hadrons of the scale of femtometers (small Q^2) with almost free quarks in “hard processes” such as deep inelastic scattering at large Q^2 — this is justification of the incoherent sum in QPM (2.19).

2.3.2 Factorization

The basic idea how the QCD treats scattering of objects like protons, consisting of partons, is essentially the same as for the case of QPM: the total cross section is an incoherent sum of the hard parton-parton cross sections; but instead of unique process of absorption of γ^* by the charged partons (for the case of ep scattering) numerous processes involve gluon radiation from quark and quark-antiquark pair production from gluon are possible in QCD. Therefore one speaks about the QCD improved parton model. In Fig. 2.5a the case of QPM is shown in which the γ^* is absorbed directly by a quark in the proton carrying momentum xp ; Fig. 2.5b shows the generic QCD process in which the γ^* undergoes a more general hard scattering with a quark or gluon from the proton.

To be more precise, a parton with momentum $p_i = x'p$ interacts with the γ^* with 4-momentum q . Define $z = Q^2/2(p_i \cdot q) = x/x'$. The masses of all particles except the γ^* are taken to be zero⁴. The cross section $\hat{\sigma}$ for the parton-photon hard

⁴For the virtual photon we denote $m_{\gamma^*} = \sqrt{-q^2}$.

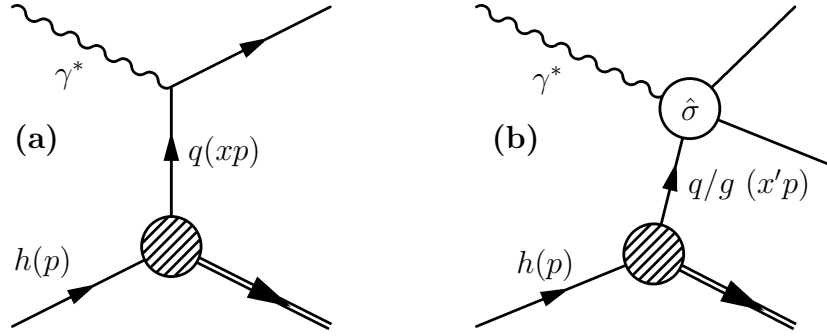


Figure 2.5: The basic idea of the QCD improved parton model for γ^*p interactions. (a). The QPM approach. (b). The QCD improved version.

interaction is calculable in pQCD and the overall γ^*p cross section is then given by a convolution of $\hat{\sigma}$'s with $f_i(x')$, the probability of finding a parton a_i of type i with momentum fraction x' in the proton

$$\sigma(x, Q^2) = \sum_i \int_0^1 dz \int_0^1 dx' \delta(x - zx') \hat{\sigma}_{\gamma^*a_i}(z, Q^2, \mu^2, \mu_f^2, \alpha_s(\mu^2)) f_i(x', \mu^2, \mu_f^2). \quad (2.24)$$

Here i denotes a sum over all partons: quarks, antiquarks and gluons.

The key feature of the parton model remains in the QCD approach, namely the cross section can be factorized into a probability density for finding a parton and the cross section of a hard scattering process.

In the field theory this is known as the theorem of factorization of long-distance from short-distance dependence for deeply inelastic scattering [17]. Compared to the parton model, two mass scales, μ^2 and μ_f^2 , are introduced. The former is the renormalization scale, which is necessary in any perturbative computation. The latter is specific to factorization calculations, and is called the factorization scale. Roughly speaking any propagator that is off-shell by μ_f^2 or more will contribute to the hard part $\hat{\sigma}$, and to the parton densities f_i otherwise.

The hard-scattering cross section is independent of long-distance effects, in particular of the identity of hadron h . The parton distributions contain all the infrared sensitivity of the original cross section and describe “long-distance” non-perturbative part of the interaction. It is specific to the hadron h , but universal, that is, it is independent of the particular hard scattering process.

2.3.3 Scaling Violation

The leading order part of the hard scattering cross section, $\hat{\sigma}$, is the QPM approximation. Let us consider an additional hard process beyond the QPM with gluon radiation from a quark line shown in Fig. 2.6.

This first order correction to the parton-level hard scattering cross section is very similar to the Compton process known in QED and the result is [18]

$$\hat{\sigma}_q = \int d\Omega \frac{2e_i^2 \alpha \alpha_s}{3 \hat{s}} \left[-\frac{\hat{t}}{\hat{s}} - \frac{\hat{s}}{\hat{t}} + \frac{2\hat{u}Q^2}{\hat{s}\hat{t}} \right], \quad (2.25)$$

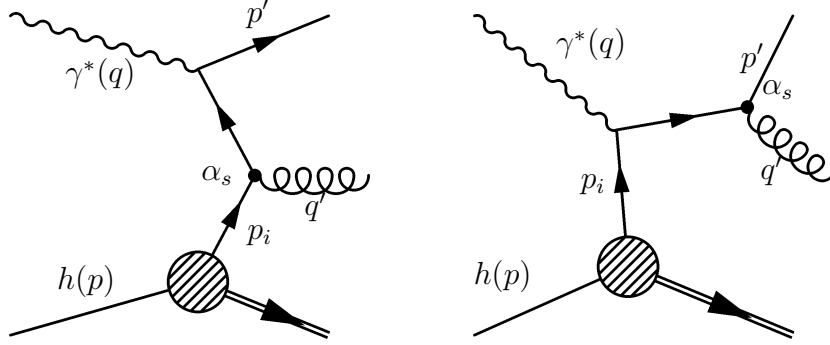


Figure 2.6: Diagrams for gluon radiation from a quark line.

where $\hat{s} = (p_i + q)^2$, $\hat{t} = (q - p')^2$, $\hat{u} = (q - q')^2$. This cross section has singularities correspond to the emission of soft and collinear gluons. Keeping only the dominant terms one can rewrite (2.25) using the gluon squared transverse momentum in the γ^* -parton centre of mass P_t^2

$$\hat{\sigma}_q \approx \hat{\sigma}_0 e_i^2 \frac{\alpha_s}{2\pi} \frac{4}{3} \left[\frac{1+z^2}{1-z} \right] \int_0^{P_t^{2,max}} \frac{dP_t^2}{P_t^2}, \quad (2.26)$$

where $\sigma_0 = 4\pi^2\alpha/s$. The integral is regulated at the lower limit by the introduction of a cut-off κ^{25} and it gives

$$\hat{\sigma}_q \approx \hat{\sigma}_0 e_i^2 \frac{\alpha_s}{2\pi} \left[P_{qq}^{(1)}(z) \ln \left(\frac{Q^2}{\kappa^2} \right) \right]. \quad (2.27)$$

Here the splitting function $P_{qq}^{(1)}(z)$ is introduced

$$P_{qq}^{(1)}(z) = \frac{4}{3} \left[\frac{1+z^2}{1-z} \right], \quad (2.28)$$

which corresponds to the probability distribution for quark to split into a quark carrying the fraction z and the gluon carrying fraction $(1-z)$ of the initial momentum of the quark. The correction for the gluon emission, $\hat{\sigma}_q(z)$, can now be added to the zeroth order QPM parton cross section (see (2.20)) to yield

$$F_2(x, Q^2) = x \sum_i e_i^2 \int_x^1 \frac{d\xi}{\xi} \left[\delta(1 - \frac{x}{\xi}) + \frac{\alpha_s}{2\pi} P_{qq}^{(1)} \left(\frac{x}{\xi} \right) \ln \left(\frac{Q^2}{\kappa^2} \right) \right] q_i(\xi) \quad (2.29)$$

To make the first order correction to F_2 complete one has to include the contribution from the process of quark pair production from the neutral partons within the proton, gluons, shown in Fig. 2.7.

The contribution from this correction is of the same form, namely

$$\Delta_g F_2(x, Q^2) \approx x \sum_i e_i^2 \int_x^1 \frac{d\xi}{\xi} \frac{\alpha_s}{2\pi} P_{qg}^{(1)} \left(\frac{x}{\xi} \right) \ln \left(\frac{Q^2}{\kappa^2} \right) g(\xi), \quad (2.30)$$

⁵This is so-called infrared cut-off as soon as it cuts the region of small p_t .

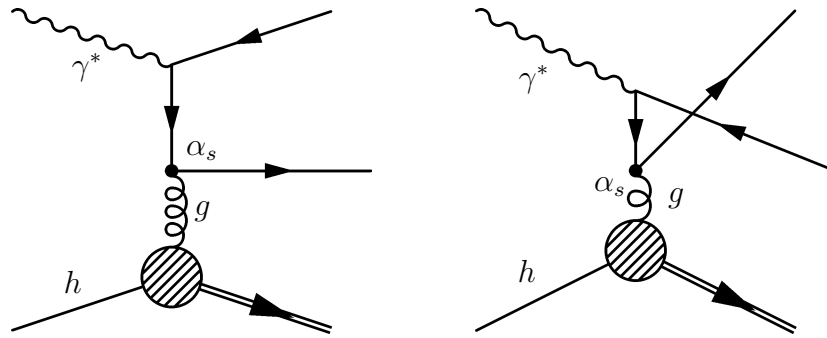


Figure 2.7: Diagrams for quark pair production from gluon in DIS.

where the splitting function $P_{qg}^{(1)}$ is

$$P_{qg}^{(1)}(z) = \frac{1}{2} [z^2 + (1-z)^2]. \quad (2.31)$$

From (2.29), (2.30) one clearly sees the key feature of the QCD predictions: the (logarithmic) dependence of the observables (like the structure function F_2) on the scale. This dependence of dimensional quantity on Q^2 is called “scaling violation”; it is preserved in higher orders, and become technically much more involved [18].

To demonstrate explicitly the scaling violation, the reduced cross section (see Section 2.4) for the e^+p scattering measured in fix target experiments (low Q^2) and in the H1 experiment (high Q^2) together with the theoretical predictions is shown in Fig. 2.8.

The scaling, observed in SLAC experiments, appear at a region of $x \approx 0.1 - 0.2$, where the interplay between different contributions leads to the numerical cancellation of the corrections.

To get a qualitative understanding of the PDFs behaviour and therefore the behaviour of the \tilde{F}_2 structure function (see (2.20)), let us assume that we get the $f(x, Q_0^2)$ distribution for a certain quark type at some certain scale Q_0^2 . If we now start to increase the scale, or the same increase the resolving capacity of our “electron microscope”, more details like the gluon emission from the structure quark could be resolved. But the gluon emission decreases “visible” fraction of energy of proton x , carried by the charged parton. Therefore with increase of the scale, the quarks observed at high x part of the $f(x)$ distribution will migrate to the part at low x . Measurements of the scaling violation with the inclusive cross sections is a straightforward test of the QCD.

2.3.4 Parton Distribution Functions in QCD

The calculation from the previous section formally leads to the physical quantities dependence on the arbitrary cut-off κ^2 which is not satisfactory. The solution is similar to renormalization: the $q_i(x)$ inherited from the QPM model (and $g(x)$ were introduced in the last section) and used so far must be considered as unmeasurable “bare” distributions. By introducing a new scale $\mu_f^2 \gg \kappa^2$, the soft non-perturbative physics is included in the renormalized parton density $f_i(x, \mu_f^2)$ which is now scale

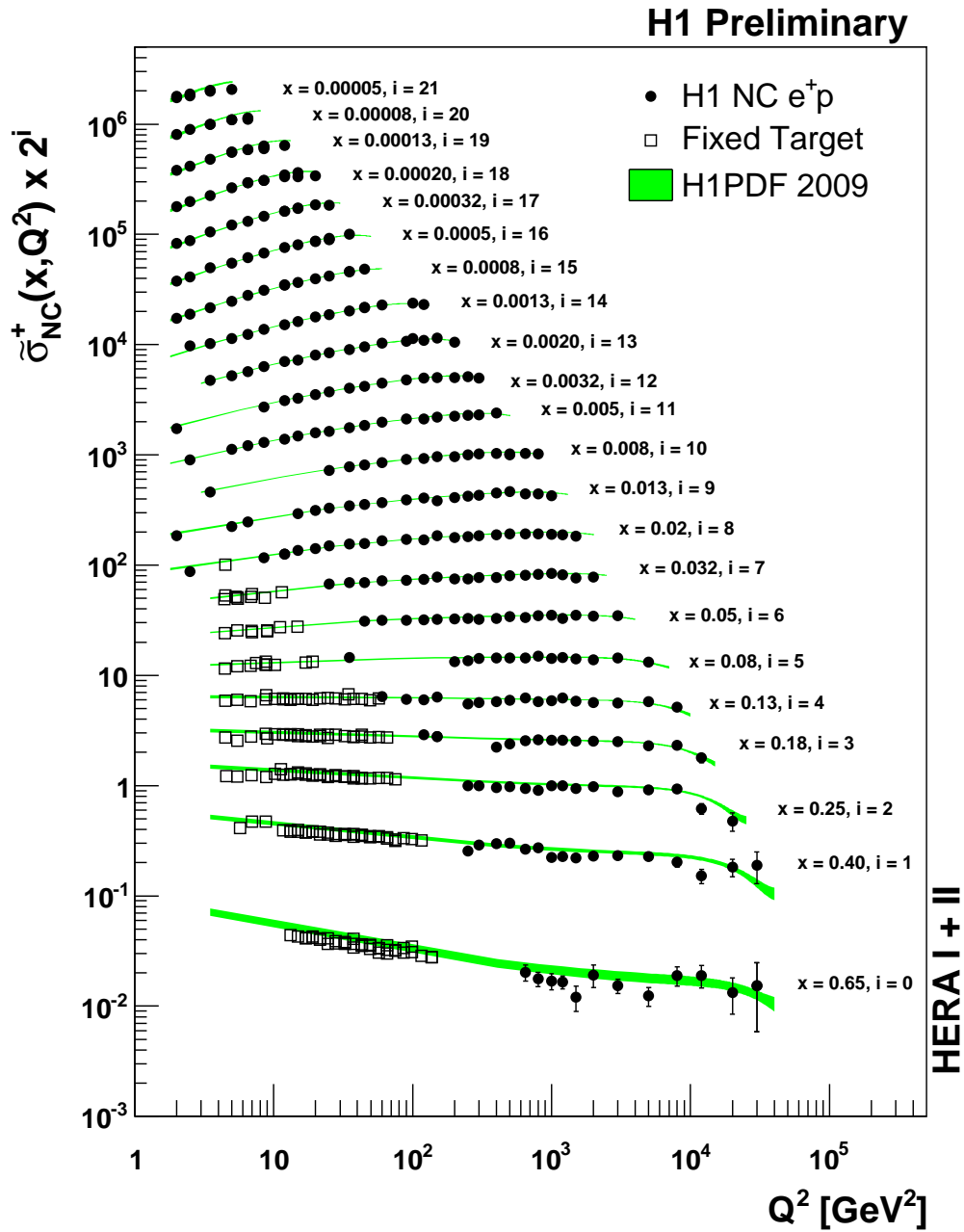


Figure 2.8: Measurement of the reduced cross section $\tilde{\sigma}(x, Q^2)$ as a function of Q^2 at fixed x by H1 and fixed target experiments. The results are compared with the Standard Model expectation determined from H1 PDF 2009 fit.

dependent. This is the (collinear) factorization scale and it is the scale at which the collinear singularity is absorbed into the parton density.

The exact definition of the parton density and the non-singular “hard” piece depends on the factorization scheme and is a matter of convention. The two most commonly used schemes are DIS and $\overline{\text{MC}}$ [13].

The evolution of the observable structure functions with the scale of interaction, Q^2 , induces the evolution of the parton distribution functions if one assigns⁶ $\mu_f^2 = Q^2$. It is described in terms of integro-differential equations

$$\frac{\partial}{\partial \ln Q^2} \begin{pmatrix} q_i(x, Q^2) \\ g(x, Q^2) \end{pmatrix} = \frac{\alpha_s(Q^2)}{2\pi} \sum_j \int_x^1 \frac{d\xi}{\xi} \begin{pmatrix} P_{q_i q_j}(x/\xi, \alpha_s(Q^2)) & P_{q_i g}(x/\xi, \alpha_s(Q^2)) \\ P_{g q_j}(x/\xi, \alpha_s(Q^2)) & P_{gg}(x/\xi, \alpha_s(Q^2)) \end{pmatrix} \begin{pmatrix} q_j(\xi, Q^2) \\ g(\xi, Q^2) \end{pmatrix}. \quad (2.32)$$

This equation is known as the Dokshitzer-Gribov-Lipatov-Altarelli-Parisi (DGLAP) evolution equation [19, 20]. The evolution kernels $P(x/\xi, \alpha_s)$ are called splitting functions and are calculated perturbatively for the factorization scheme in use; the leading order splitting functions (2.28, 2.31) given above correspond to the first terms of the expansions of splitting functions for the DIS scheme.

This approach allows to measure the parton distributions at some fixed scale and, because of the universality property, use them in any experiment involving protons, evolving the PDFs at given x to the scale Q^2 needed.

2.3.5 Longitudinal Structure Function in QCD

Because of conservation of helicity and angular momentum for the interacting quark and virtual γ^* , the absorption of a longitudinally polarized virtual photon in the QPM model is not possible, in agreement with the results above (see Eqns. (2.15), (2.19), (2.21)). However, in QCD many particle final states are possible like in Fig. 2.6, 2.7, and the helicity and angular momentum could be conserved simultaneously.

Thus, in higher orders a non-zero structure function \tilde{F}_L is allowed. The first non-vanishing contribution (which appears in the next-to-leading order approximation of the QCD improved parton model treated above) is given by [21]

$$F_L(x, Q^2) = \frac{\alpha_s(Q^2)}{2\pi} x^2 \int_x^1 \frac{d\xi}{\xi^3} \left[\frac{8}{3} \sum_{i \in \{q, \bar{q}\}} e_i^2 \xi q_i(\xi, Q^2) + 4 \left(\sum_{i \in \{q\}} e_i^2 \right) \xi g(\xi, Q^2) \left(1 - \frac{x}{\xi} \right) \right], \quad (2.33)$$

where the summations go over the “active”⁷ quark flavours.

⁶To define the DIS scheme one claims the validity of $F_2 = \sum_i e_i^2 x q_i(x, Q^2)$ in all orders, such that the Q^2 dependence is fully absorbed by the PDFs. For the same reason this scheme does not fix the gluon distribution.

⁷These are quarks with the masses above the scale Q^2 .

The second term corresponds to the gluon distribution inside the proton and enters the expression at the same order as the contribution from the quark distributions in the first term. This makes the longitudinal structure function sensitive to the gluon PDF $g(x, Q^2)$ yet in the first non-vanishing order, and allows to extract it [22]. Appearance of the non-zero F_L is a direct consequence of QCD.

2.4 The Neutral Current Cross Section

The lowest order (or “Born”) level cross section of the NC DIS reaction $e^\pm p \rightarrow e^\pm X$ can be written as [23, 24] (see (2.16))

$$\frac{d^2\sigma_{\text{NC}}^\pm}{dx dQ^2} = \frac{2\pi\alpha^2 Y_+}{xQ^4} \left(\tilde{F}_2 \mp \frac{Y_-}{Y_+} x\tilde{F}_3 - \frac{y^2}{Y_+} \tilde{F}_L \right) \equiv \frac{2\pi\alpha^2 Y_+}{xQ^4} \cdot \tilde{\sigma}_{\text{NC}}^\pm, \quad (2.34)$$

The “ \pm ” sign corresponds to the $e^\pm p$ scattering. Eq. (2.34) defines the reduced NC cross section $\tilde{\sigma}_{\text{NC}}^\pm$ which is a combination of the generalized proton structure functions \tilde{F}_2 , $x\tilde{F}_3$ and \tilde{F}_L

$$\tilde{\sigma}_{\text{NC}}^\pm(x, Q^2, s) = \tilde{F}_2(x, Q^2) \mp \frac{Y_-}{Y_+} x\tilde{F}_3(x, Q^2) - \frac{y^2}{Y_+} \tilde{F}_L(x, Q^2), \quad (2.35)$$

where y and Y_+ expressed via s with the relation $Q^2 = sxy$. In the reduced cross section $\tilde{\sigma}_{\text{NC}}^\pm$ the main “kinematic” dependence on Q^2 is removed, displaying mostly the “dynamics” of the ep scattering process. This makes the reduced cross section a convenient instrument for the proton structure investigation.

At HERA (see Section 3), with its longitudinally polarized lepton beams, separate measurements of all three structure functions and tests of the related electroweak effects are possible. The contribution from \tilde{F}_2 dominates over the whole range in x and Q^2 , carrying the information about a total quark content of the proton.

The main contribution to \tilde{F}_L is expected to come from gluons at small x ($x \lesssim 0.005$), where the gluon contribution to the proton structure dominates. The region of $x \gtrsim 0.0015$ is reachable at HERA at relatively low Q^2 , where the $x\tilde{F}_3$ function could be neglected. In the year 2007 at HERA measurements with different proton beam energies and consequently at different s values has been done. From (2.35) with two measurements at s_1 and s_2 one extracts the longitudinal structure function⁸

$$\tilde{F}_L(x, Q^2) = \frac{\tilde{\sigma}_{\text{NC}}(x, Q^2, s_1) - \tilde{\sigma}_{\text{NC}}(x, Q^2, s_2)}{\frac{y_1}{Y_{+,1}} - \frac{y_2}{Y_{+,2}}} \quad (2.36)$$

Measurements with positive and negative charged leptons (electron and positron beams) allow to treat the difference $(Y_+/Y_-)[\sigma_{\text{NC}}^- - \sigma_{\text{NC}}^+]$ which is the $x\tilde{F}_3$ structure function as can be seen from Eq. (2.35).

The generalized structure functions in case of polarized lepton beam in the reaction $e^\pm p \rightarrow e^\pm X$ may be presented [25] as a linear combination of the structure

⁸If the $x\tilde{F}_3$ term is omitted, then $\tilde{\sigma}_{\text{NC}}^+ = \tilde{\sigma}_{\text{NC}}^-$, (see (2.35)) and so one could treat just $\tilde{\sigma}_{\text{NC}}$.

functions with coefficients constructed from the EW couplings of the quarks to the neutral vector bosons

$$\begin{aligned} \tilde{F}_2^\pm = F_2 - (v_e \pm P_e a_e) \kappa \frac{Q^2}{Q^2 + M_Z^2} F_2^{\gamma Z} \\ + (v_e^2 + a_e^2 \pm P_e 2v_e a_e) \kappa^2 \left[\frac{Q^2}{Q^2 + M_Z^2} \right]^2 F_2^Z, \end{aligned} \quad (2.37)$$

$$\begin{aligned} x\tilde{F}_3^\pm = -(a_e \pm P_e v_e) \kappa \frac{Q^2}{Q^2 + M_Z^2} xF_3^{\gamma Z} \\ + (2a_e v_e \pm P_e [v_e^2 + a_e^2]) \kappa^2 \left[\frac{Q^2}{Q^2 + M_Z^2} \right]^2 xF_3^Z. \end{aligned} \quad (2.38)$$

Here $\kappa^{-1} = 4 \frac{M_W^2}{M_Z^2} (1 - \frac{M_W^2}{M_Z^2})$, and “ \pm ” signs correspond to positron and electron beams respectively. The longitudinal polarization is defined as

$$P_e = \frac{N_R - N_L}{N_R + N_L}, \quad (2.39)$$

where $N_R(N_L)$ is the number of right (left) handed leptons in the beam.

In the quark parton model, the hadronic structure functions are related to linear combinations of sums and differences of the quark and anti-quark momentum distributions $xq(x, Q^2)$ and $x\bar{q}(x, Q^2)$

$$[F_2, F_2^{\gamma Z}, F_2^Z] = x \sum_q [e_q^2, 2e_q v_q, v_q^2 + a_q^2] (q + \bar{q}), \quad (2.40)$$

$$[xF_3^{\gamma Z}, xF_3^Z] = 2x \sum_q [e_q a_q, v_q a_q] (q - \bar{q}) \quad (2.41)$$

where v_q and a_q are the vector and axial-vector couplings of the light quarks and e_q is the charge of the quark of flavor q .

Similarly, the longitudinal structure function \tilde{F}_L may be decomposed. However its contribution is important only at high y , is expected to be small and can be neglected at large x and Q^2 , where the Z boson exchange plays a role. Therefore from Eqns. (2.37), (2.38), (2.40), (2.41) coupling constants of the light quarks to the Z boson can be measured.

The differential cross section with respect to Q^2 is obtained by integration of Eq. (2.34) over the allowed kinematic phase space in x

$$\frac{d\sigma}{dQ^2}(Q^2) = \int_x dx \frac{d^2\sigma}{dx dQ^2} \quad (2.42)$$

The differential cross section with respect to x is defined in a similar way

$$\frac{d\sigma}{dx}(x) = \int_{Q^2} dQ^2 \frac{d^2\sigma}{dx dQ^2} \quad (2.43)$$

In the last two formulae the integration goes over the allowed kinematical region or (in this work) over the region defined in the analysis.

2.5 The Charged Current Cross Section

Similarly to the NC cross section, the weak Born level CC cross section for the collision of polarized leptons with unpolarized protons can be expressed as [24]

$$\begin{aligned} \frac{d^2\sigma_{\text{CC}}^{\pm}}{dx dQ^2} &= (1 - P_e) \frac{G_F^2}{4\pi x} \left[\frac{M_W^2}{M_W^2 + Q^2} \right]^2 \left(Y_+ \tilde{W}_2^{\pm} - Y_{\mp} x \tilde{W}_3^{\pm} - y^2 \tilde{W}_L^{\pm} \right) \\ &\equiv \frac{G_F^2}{2\pi x} \left[\frac{M_W^2}{Q^2 + M_W^2} \right]^2 \tilde{\sigma}_{\text{CC}}^{\pm}, \end{aligned} \quad (2.44)$$

where \tilde{W}_2^{\pm} , $x\tilde{W}_3^{\pm}$ and \tilde{W}_L^{\pm} are CC structure functions for $e^{\pm}p$ scattering, $\tilde{\sigma}_{\text{CC}}^{\pm}$ is the reduced cross section and the polarization P_e is defined as in (2.39). At moderate Q^2 the CC cross section is suppressed by the factor $1/(Q^2 + M_W^2)^2$, coming from the W^{\pm} propagator, compared to the NC process, where the main contribution comes from the γ^* exchange. For $Q^2 \gtrsim M_W^2 \approx M_Z^2$ the cross sections for NC and CC processes become compatible. In Fig. 2.9 the Q^2 dependence is shown for the neutral and charged current processes with the theoretical predictions from the Standard Model [26].

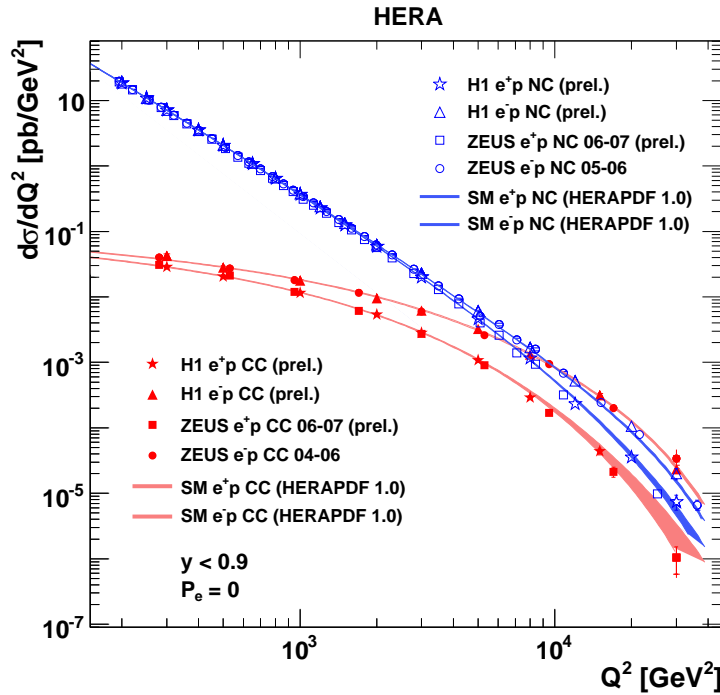


Figure 2.9: The Q^2 dependence of the unpolarized $e^{\pm}p$ NC and CC cross sections $d\sigma/dQ^2$ compared with the SM expectation from the HERAPDF1.0 fit [26].

In the QPM, where $W_L^{\pm} \equiv 0$, the reduced cross section for the $e^{\pm}p$ CC process may be expressed as the sum and difference of the quark and anti-quark momentum

distributions, $xq(x, Q^2)$ and $x\bar{q}(x, Q^2)$:

$$\tilde{\sigma}_{\text{CC}}^- = (xu + xc) + (1 - y)^2(x\bar{d} + x\bar{s}), \quad (2.45)$$

$$\tilde{\sigma}_{\text{CC}}^+ = (x\bar{u} + x\bar{c}) + (1 - y)^2(xd + xs). \quad (2.46)$$

As follows from (2.45), (2.46), the main contribution to the cross section for electron beam at high x is from the u quarks, and from the d quark for positron beam. Therefore measurements of the CC cross section with leptons of different signs allow to separate the PDFs for u and d valence quarks.

The charged current cross section of polarized leptons with unpolarized protons is predicted by the Standard Model to have a linear dependence on the lepton polarization P_e (see (2.44)). Because of the parity violation in the weak interactions, the W boson is coupled to “left-handed” particles (electrons) and “right-handed” antiparticles (positrons); thus the total CC cross section should be zero for pure “left-handed” positron and pure “right-handed” electron beams. The dependence of the total charged current cross section is shown in Fig. 2.10

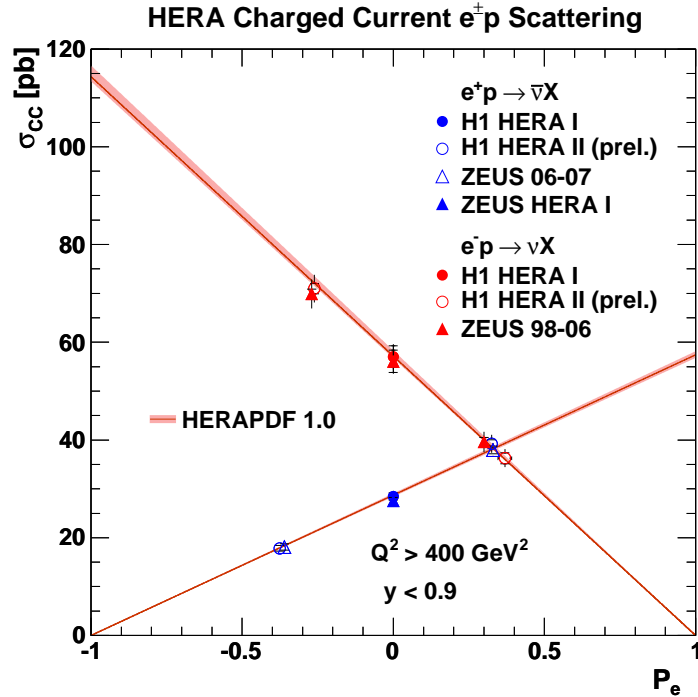


Figure 2.10: The dependence of the $e^\pm p$ CC cross section on the lepton beam polarization P_e in comparison with the SM prediction based on the HERAPDF1.0 parametrization [26].

2.6 Radiative Corrections

The cross sections from the last two sections present the leading-order (LO) calculations in QED (i.e. the Born cross sections). Increasing the precision of the DIS

measurements theoretical framework one has to go into higher order electroweak corrections.

The leading order correction comes from the QED process of emission of the additional photon from the electron or quark line in case of neutral currents, and in addition from the gauge boson in case of charged currents; examples of such processes are shown in Fig. 2.11.

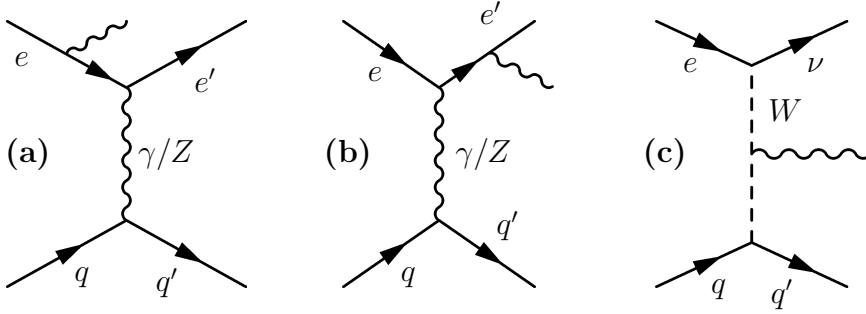


Figure 2.11: Feynman diagrams for radiation of additional photon in case of **(a)** NC ISR or Compton process, **(b)** NC FSR or Compton process and **(c)** emission from the gauge boson in CC.

Formally this correction to the inclusive DIS cross section diverges due to the emission of collinear and/or soft photons (and is called infrared divergence). As the Bloch-Nordsieck theorem states [27, 28], the divergence is canceled in all orders as soon as diagrams with loops are included into the scattering amplitude calculation. Nevertheless, after the regularization a non-negligible remainder from this first order correction is present in the cross section and reaches 10% in the analysis phase space shown in Fig. 2.12.

Numerically this correction for the case of neutral currents comes from three contributions. The first one is from the emission of a collinear (but not necessarily soft) photon from the incoming lepton and is called initial state radiation (ISR). The photon is emitted along the beam axis and escapes the experimental setup through the beam pipe. This process reduces the ep center-of-mass energy \sqrt{s} and thus changes the event kinematics. Next is the emission of a collinear photon from the outgoing lepton (final state radiation or FSR). To diminish the correction from this process, the scattered electron energy is measured in the calorimeter, such that in most cases the lepton and radiative photon go to the same calorimetric cell and the measured energy does not change. The third contribution corresponds to Compton scattering of the exchanged photon and appears as a radiative photon emitted at large angles relative to the lepton. These events contribute to the background for deep inelastic scattering.

Another type of the electroweak corrections comes from the fermionic contributions to the self energy of the exchange boson and purely weak corrections. These corrections are typically below 1% [29].

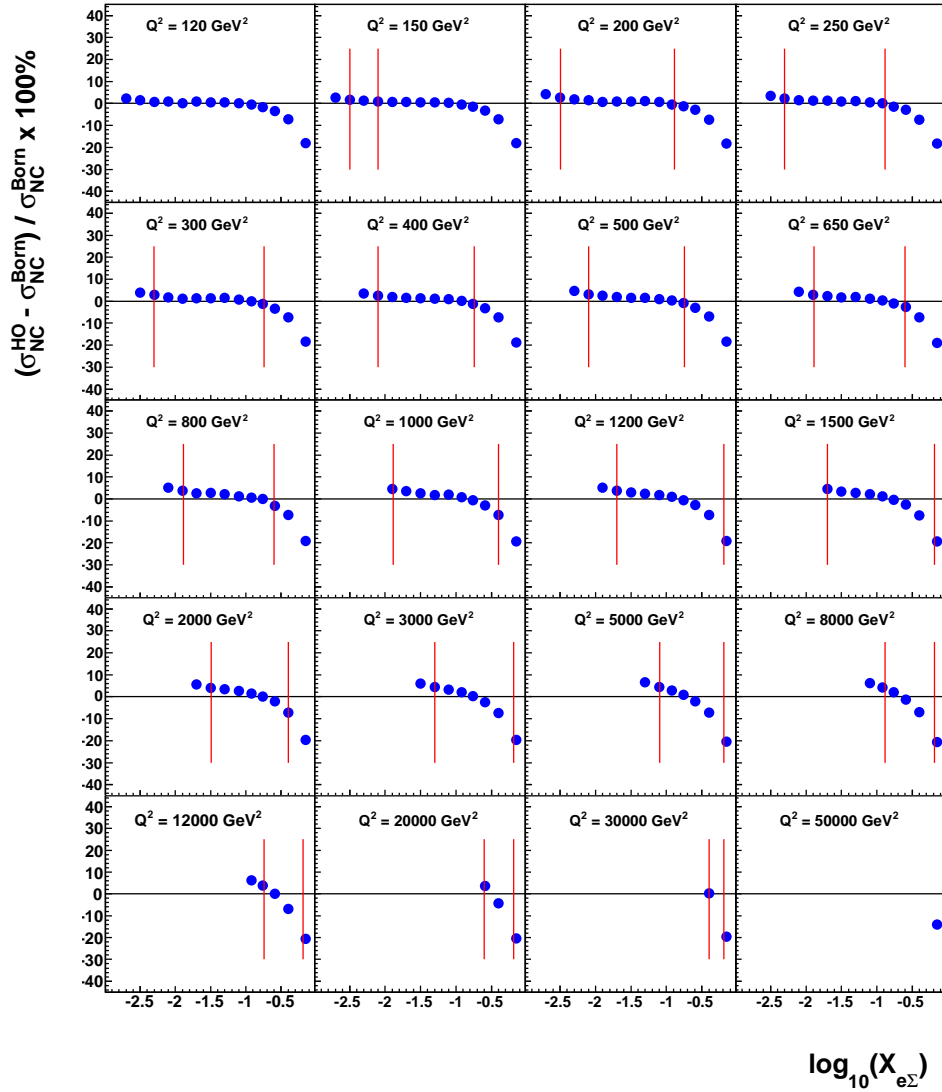


Figure 2.12: The effect of the higher order radiative corrections (HO) to the neutral current cross sections in $e\Sigma'$ variables obtained with the HECTOR 1.0 program [29]. Red delimiters refer to the ranges where HERA-II preliminary measurement has been done.

Chapter 3

Electron-proton Collider HERA

The HERA (Hadron Elektron Ring Anlage) collider is the only facility world-wide to provide electron-proton collisions at high energy. It is located at the DESY laboratory (Deutsches Elektron Synchrotron) at Hamburg, Germany, and operated from 1992 to 2007. The two multi-purpose detectors — H1 and ZEUS — collected in total about 0.5 fb^{-1} each at the center-of-mass energy $\sqrt{s} \approx 320 \text{ GeV}$ over this period.

Below a brief overview of the HERA collider is given. Emphasis is put on the details important for the analysis.

3.1 HERA Accelerator

The electron-proton accelerator HERA [30] is a double ring accelerator complex. The storage rings have been built in a common tunnel of about 6.3 km length situated 15 to 20 meters under ground and consists of four straight sections connected with four arcs. The general layout is shown in Fig. 3.1. The electron beam is guided with magnets operating at ambient temperature, while for the proton beam a superconducting magnetic system is used. The accelerator rings stored about 180 particle bunches each. The bunches contained 10^{11} particles and were separated with the 28.8 m distance, resulting in a 96 ns bunch crossing time which corresponds to a collision rate of 10.4 MHz. In addition to the colliding bunches, there were about 10 bunches without colliding partner for each beam (pilot bunches) used for estimation of the background due to interactions with the residual gas in the beam pipe, particularly for the luminosity measurement (see Section 4.5).

HERA was operating in two periods: HERA I from year 1992 until the end of 2000 and, after an upgrade of both HERA and the experiments, HERA II from 2003 till 2007. For the analysis in this thesis the data collected during the HERA II operation period is used. During the shutdown the beam focusing system was upgraded leading to an increase of the instantaneous luminosity and energy of the proton beam, in addition spin rotators were installed allowing for longitudinal polarization of the electron beam. The main parameters of the HERA collider are shown in Table 3.1.

The total collected luminosity L [$1/\text{cm}^2$] is related to the number of the observed events N in the reaction with a given cross section σ as

$$N = \sigma L. \tag{3.1}$$

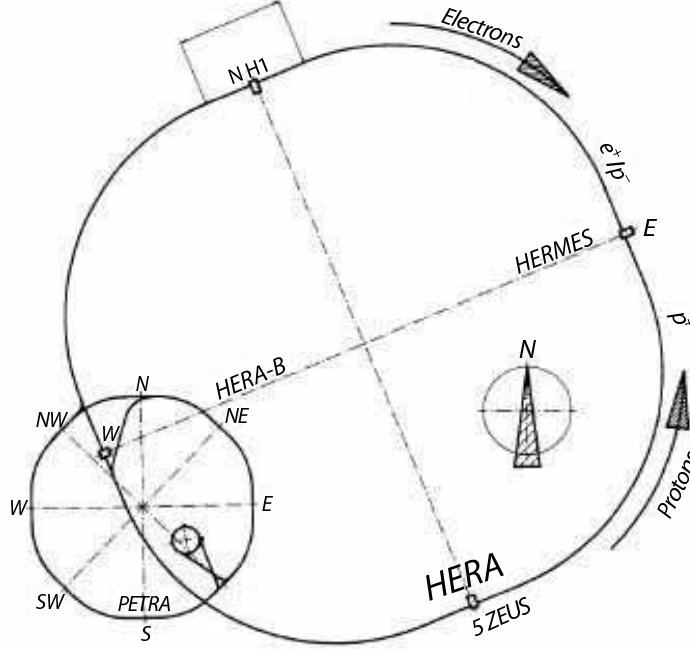


Figure 3.1: Schematic view of the HERA collider ring.

Parameter	HERA I		HERA II	
	e beam	p beam	e beam	p beam
Beam energy E [GeV]	27.5	820	27.5	920
Current I [mA]	45	100	58	140
Particles per bunch N ($\times 10^{10}$)	3.5	7.3	4.0	10.3
Number of bunches	189	180	189	180
Transversal beam sizes $\sigma_x \times \sigma_y$ [μm]	190 \times 50		112 \times 30	
Synchrotron radiation at IP [kW]	6.9		25	
Luminosity [$\text{cm}^{-2}\text{s}^{-1}$]	$1.4 \cdot 10^{31}$		$7 \cdot 10^{31}$	

Table 3.1: Main parameters of the HERA storage rings during the HERA I (1992-1998) and HERA II (2003-2007) operation periods [31].

The instantaneous luminosity \mathcal{L} [$1/(\text{cm}^2\text{s})$] for the machine is given by the relation [32]

$$\mathcal{L} = \frac{f N_e N_p}{4\pi\sigma_x\sigma_y}, \quad (3.2)$$

where f is the bunch crossing frequency, N_e (N_p) is the number of the electrons (protons) in the bunch, and σ_x (σ_y) is the transverse beam size in the x (y) direction at the interaction point (IP). The luminosity collected over HERA's running time is shown in Fig. 3.2. During the HERA I period about 100 pb^{-1} in positron runs and about 15 pb^{-1} for electrons runs were collected. For the HERA II period 180 pb^{-1} (for e^+p) and 150 pb^{-1} (for e^-p) of data acceptable for the analysis were collected.

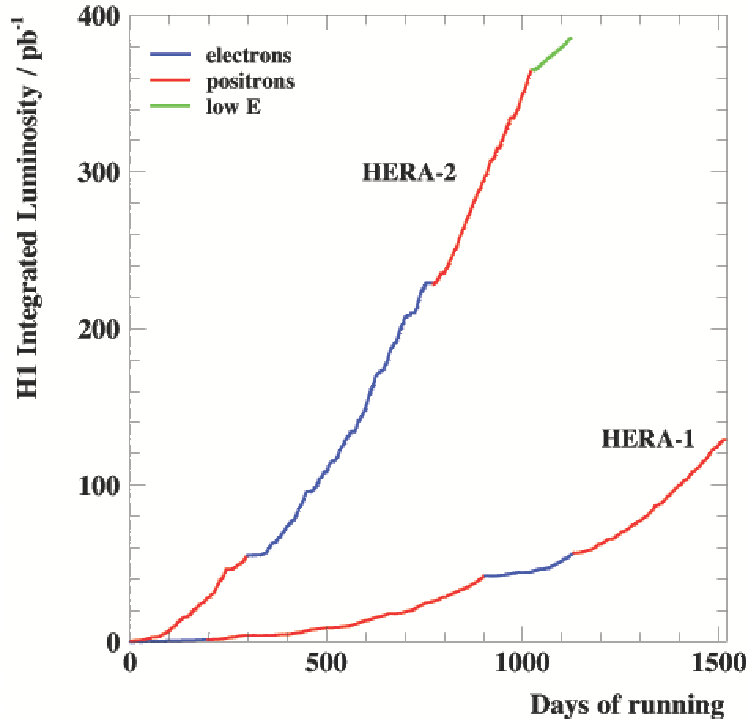


Figure 3.2: The integrated luminosity in the H1 experiment as a function of time for HERA I and HERA II periods.

The beam-beam collisions at zero crossing angle at a center-of-mass energy of $\sqrt{s} = 318$ GeV (301 GeV till year 1998) took place in two interaction regions: the Nord Hall where the H1 [33] detector is situated, and the South Hall with the ZEUS detector [34]. In the East and West Halls the fixed target experiments HERMES [35] and HERA-B [36] are situated correspondingly. The H1 and ZEUS detectors were the general propose experiments. The HERMES experiment investigated the proton spin structure with polarized electron beams on polarized gas targets. In HERA-B experiment the proton beam was used for the analysis of reactions with b quarks in final state.

3.2 Polarization at HERA

The relativistic electrons in the storage ring of the accelerator become transversely polarized. This happens because of the dipole field is transverse to the beam direction. In this field the electron has an energy difference for spin “up” and spin “down” states¹. Due to this difference the “up-down” flips of the electron’s spin due to synchrotron radiation are more probable than “down-up” flips (the Sokolov-Ternov effect [37]). This results in a time dependence of the polarization $P(t)$ of the

¹“Up” and “down” relative to the magnetic field direction.

initially unpolarized beam

$$P(t) = P_{\max}(1 - e^{-t/\tau}), \quad (3.3)$$

where P_{\max} is the theoretical limit for the polarization due to the Sokolov-Ternov effect and is about 0.93, τ is the build-up time and under HERA conditions it is about 40 minutes².

For any electroweak measurement investigating parity violation a longitudinal polarization is needed. At HERA II a set of spin rotators [38] were installed (before and after the interaction points). The influence of this additional optics with other depolarization effects result in a typical polarization achieved of about 40%, as shown in Fig. 3.3.

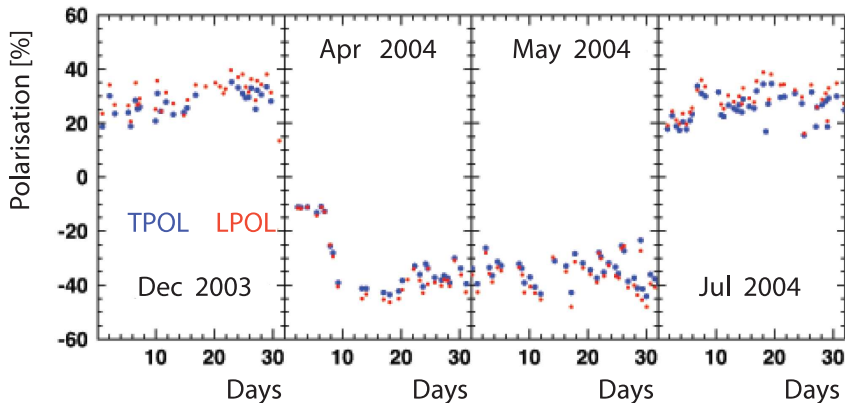


Figure 3.3: The average polarization achieved in the years 2003-2004 in positron runs.

For the polarization measurement two techniques were exploited. The Transverse Polarimeter (TPOL) [39], installed near the West Hall, measured the spatial vertical “up-down” asymmetry of the energy distribution of single back scattered Compton photons generated by an Ar laser. The Longitudinal Polarimeter (LPOL) [40], installed near the East Hall, measures the energy asymmetry of the backscattered photons delivered by a Nd:YAG laser. Since the spin rotators do not change the degree of the beam polarization, measurements with the TPOL and LPOL should be consistent in magnitude. This is indeed the case (see Fig. 3.3).

3.3 Run Periods for HERA II

For HERA II, the ep collisions with electrons and positrons of positive and negative polarities were provided. The run ranges, type of the lepton and polarity for each physical period (technical subperiods used for the tuning of the accelerator are omitted) with the calendar years they were taken and the names of the subperiods are shown in Table 3.2.

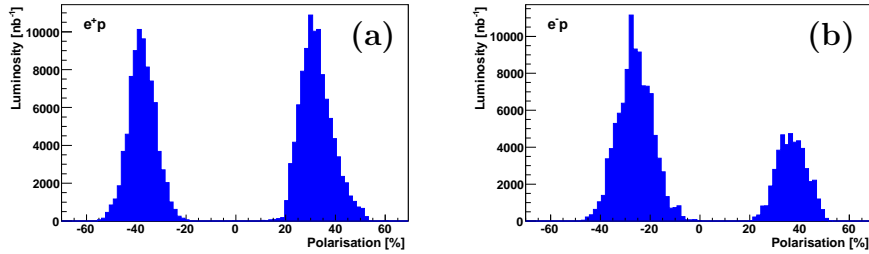
²For a storage ring of radius R and the electron energy E one derives $\tau \propto R^2/E^5$.

First Run	Last Run	Lepton sign	Polarity	Year	Name
362487	367256	e^+p	RH	2003	eEplus03RH1
367257	376562	e^+p	RH	2004	eEplus04RH1
376563	386696	e^+p	LH	2004	eEplus04LH1
386697	392213	e^+p	RH	2004	eEplus04RH2
399101	402991	e^-p	RH	2005	eEminus05RH1
402992	415619	e^-p	LH	2005	eEminus05LH1
415620	427812	e^-p	RH	2005	eEminus05RH2
427813	436893	e^-p	LH	2005	eEminus05LH2
444094	458792	e^-p	LH	2006	eEminus06LH1
458793	466997	e^-p	RH	2006	eEminus06RH1
468530	485713	e^+p	RH	2006	eEplus06RH1
485714	486072	e^+p	LH	2006	eEplus06LH1
486073	490161	e^+p	RH	2006	eEplus06RH2
490162	492499	e^+p	LH	2006	eEplus06LH2
492508	500611	e^+p	LH	2007	eEplus07LH1

Table 3.2: The run periods for the HERA II used for the analysis.

For the analysis, the run periods are grouped such that for each group the experimental conditions like polarity of the beam or trigger setup stayed the same. For different tasks of the analysis the criteria which determines the “similarity” of the subperiods could vary such that the subperiods are regrouped. In Table 3.3 these groups are named, and these names will be used in the following to designate the data set under consideration.

The luminosity weighed profiles of polarization for the positron and electron runs are shown in Fig. 3.4. The luminosity and mean polarizations for the periods used for the analysis are presented in Table 3.4.

Figure 3.4: The luminosity weighed polarization profiles for (a) e^+p and (b) e^-p data periods.

Period Name	Composition
Per0304RH	eEplus03RH1, eEplus04RH1, eEplus04RH2
Per0304LH	eEplus04LH1
Per0405RH	eEminus05RH1, eEminus05RH2
Per0405LH	eEminus05LH1, eEminus05LH2
Per06emRH	eEminus06RH1
Per06emLH	eEminus06LH1
Per0607RH	eEplus06RH1, eEplus06RH2
Per0607LH	eEplus06LH1, eEplus06LH2, eEplus07LH1
Per0304	Per0304RH, Per0304LH
Per0405	Per0405RH, Per0405LH
Per06em	Per06emRH, Per06emLH
Per0607	Per0607RH, Per0607RH
PerPosRH	Per0304RH, Per0607RH
PerPosLH	Per0304LH, Per0607LH
PerNegRH	Per0405RH, Per06emRH
PerNegLH	Per0405LH, Per06emLH
PerRH	Per0304RH, Per0405RH, Per06emRH, Per0607RH
PerLH	Per0304LH, Per0405LH, Per06emLH, Per0607LH
PerPos	Per0304, Per0607
PerNeg	Per0405, Per06em
PerTot	The full HERA II statistics: PerPos, PerNeg

Table 3.3: The naming convention for the data sets used in the analysis.

Period Name	Luminosity [pb^{-1}]	Polarization [%]
Per0304RH	26.28	33.6
Per0304LH	21.97	-40.3
Per0405RH	29.45	38.1
Per0405LH	67.47	-26.8
Per06emRH	16.54	34.8
Per06emLH	35.10	-24.6
Per0607RH	71.89	32.0
Per0607LH	59.54	-36.6

Table 3.4: The luminosity and mean polarizations for the data sets used in the analysis.

Chapter 4

The H1 Experiment at HERA

The H1 detector [33] situated at the North Hall (see Fig. 3.1) is a general purpose detector intended to study the ep interaction at HERA with an angular coverage of most of the solid angle around the interaction point (IP). It has the dimensions (length \times width \times height) of approximately $12 \times 10 \times 15$ m and weight of about 2800 tons. The adopted coordinate system is right-handed with the z axis direction along the proton beam and the x axis pointing to the center of the HERA ring. The origin of the reference frame is chosen at the nominal IP.

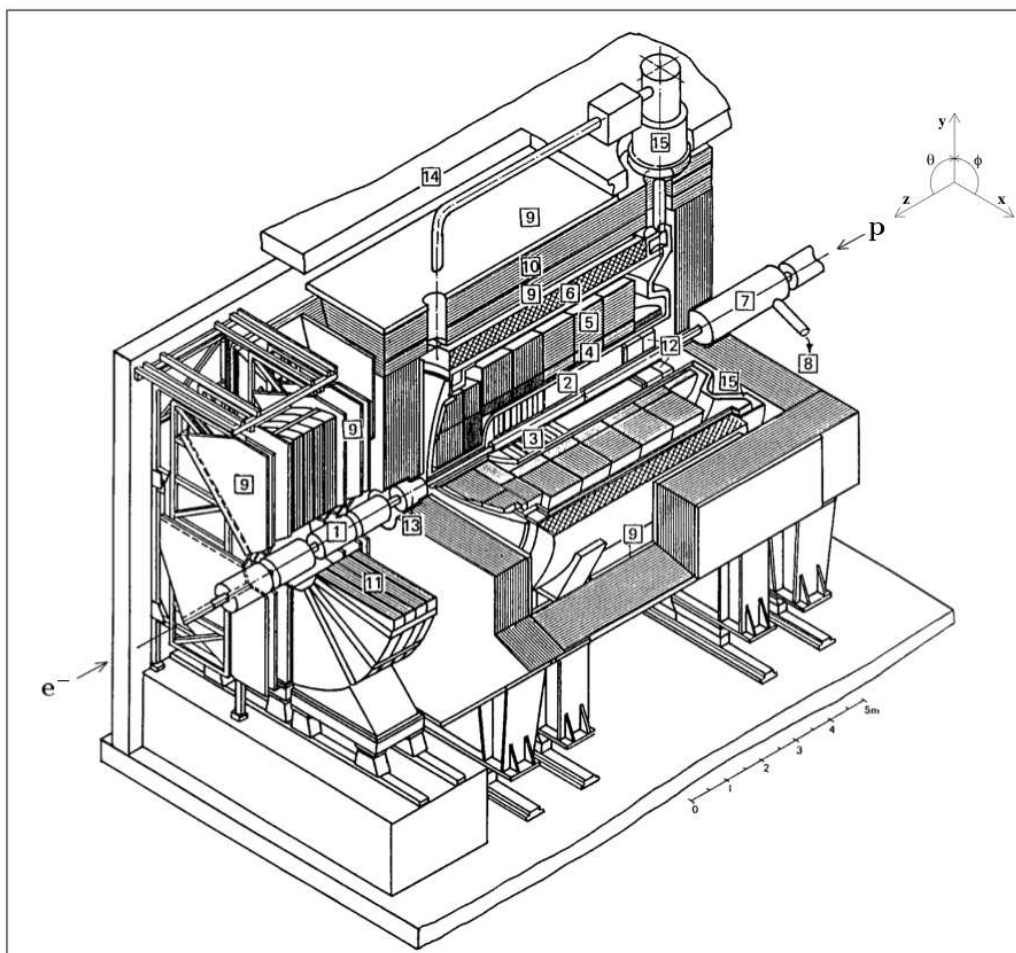
The general schematic view is shown in Fig. 4.1. The beam pipe [1] is surrounded by the central [2] and forward [3] tracking detectors. The Liquid-Argon (LAr) calorimeter, consisting of electromagnetic [4] and hadronic [5] sections, is situated in the central part around the tracking detectors. In turn the LAr calorimeter is surrounded by a superconducting 6 m diameter coil [6] in the cryostat vessel providing a magnetic field of 1.15 T. The entire detector is surrounded by an iron yoke [10] which returns the magnetic flux and provides the support for streamer tubes [9] for muon identification. The backward direction is covered with the SpaCal calorimeter [12]. The very forward angles are covered with the Plug calorimeter [13].

In order to extend the geometrical acceptance of the H1 detector the Very Forward Proton Spectrometer (VFPS) [41], the Forward Proton Spectrometer (FPS) [42], the Proton Remnant Tagger (PRT) [43] and the Forward Neutron Calorimeter (FNC) [44] were mounted downstream the proton beam. The Electron Tagger (ET or ETag6) is located at $z = -6$ m, and the Photon Detector (PD or PhTag) is at $z = -101.8$ m.

In the following a brief description of the components essential for the analysis is given.

4.1 Calorimetry

The calorimetric system measures the total energy of the outgoing particles. The detection principle for all the H1's calorimeters is the same: the device is made of alternating layers: passive absorber material and active sampling medium. In the dense material of the absorbers incoming particles start the electromagnetic and hadronic showers. The multiple particles of these showers enter the sampling sections, providing the excitation of the medium. This excitation is measured then



1	Beam pipe and beam magnets	9	Muon chambers
2	Central tracking device	10	Instrumented iron yoke
3	Forward tracking device	11	Forward muon toroid
4	Electromagnetic LAr calorimeter	12	Spaghetti Calorimeter (SpaCal)
5	Hadronic LAr calorimeter	13	PLUG calorimeter
6	Superconducting coil (1.15 T)	14	Concrete shielding
7	Compensating magnet	15	Liquid argon cryostat
8	Helium supply for 7		

Figure 4.1: General view of the H1 experimental setup.

by means of collection of free charges (in case of ionisation of the liquid argon in LAr calorimeter) or gathering of the light (in case of excitation in the plastic scintillators like in SpaCal calorimeter).

The calorimeter consists of cells — a minimal unit can provide the calorimetric information. The size of the cells defines a granularity of the calorimeter. The finer the granularity, the more precise measurement of the position of the incoming particle on the calorimetric surface (impact position) can be done¹. The compact energy deposit in neighboring cells from the incoming particle is called a cluster.

The shower development strongly depends on whether it has the electromagnetic or hadronic nature. In case of electromagnetic shower the processes contribute are the emission of the hard photon from the electron (bremsstrahlung), electron-positron pair production from the photon and Møller (electron-electron) scattering. For these processes the cross section depends on the transverse momentum P_t and atomic charge of the absorber material Z as $\propto Z^2/P_t^4$. This gives narrow short showers fully absorbed in the calorimeter. The longitudinal progress of the electromagnetic shower in a material of the calorimeter is characterized by the radiation length X_0 , the mean distance over which the energy of the shower decreases in e times, where $e \approx 2.7$ is the Euler's number.

For the hadronic shower the strong interaction is involved, such that high transverse momenta transfer is more probable and the interaction probability is proportional to the atomic number A . At the same time the bremsstrahlung process (with further development of the electromagnetic shower) for charged hadron of mass m_h is also theoretically possible but suppressed by the factor of $(m_h/m_e)^2$ [45]. For these reasons the hadronic showers go deeper into the calorimeter and have bigger spread in the transverse plane. The characteristic parameter of the hadronic shower is the interaction length λ . For lead which is often used as an absorber the $X_0 \approx 0.56$ cm and $\lambda \approx 17$ cm.

The H1 experiment contains asymmetrical LAr calorimeter which covers central and forward part (positive values of z) of the detector, SpaCal calorimeter for the backward part (mainly to detect scattered electrons), with the Plug calorimeter (for the very forward part $0.7^\circ < \Theta < 3.4^\circ$) and Tail Catcher, which are not used in the analysis. Below a short description of the LAr and SpaCal calorimeters is given.

4.1.1 Liquid Argon Calorimeter (LAr)

The Liquid Argon (LAr) calorimeter is the main H1 calorimeter used in the analysis for the triggering, identification, and measurement of the scattered electron and hadrons. It covers the polar angle range of $4^\circ < \Theta < 153^\circ$.

The general view of the detector is shown in Fig. 4.2. It is made of so-called wheels or barrels separated in radial direction is two parts (all except BBE part): inner electromagnetic (EM) and outer hadronic (HAD) stacks. In $r - \phi$ plane the wheels are segmented in 8 octants (the BBE had 16-fold polygonal structure). The naming convention for the wheels is the following: the Backward Barrel (BBE, at most negative values of z), the Central Barrels (CB1, CB2, CB3), the Forward Barrels (FB1, FB2), the Inner Forward (IF) and Outer Forward (OF) modules. The

¹Though if the granularity is much finer than a Molière radius [32], the further reduction of the cell sizes does not help anymore.

insensitive areas between the wheels and octants are called z -cracks and ϕ -cracks correspondingly.

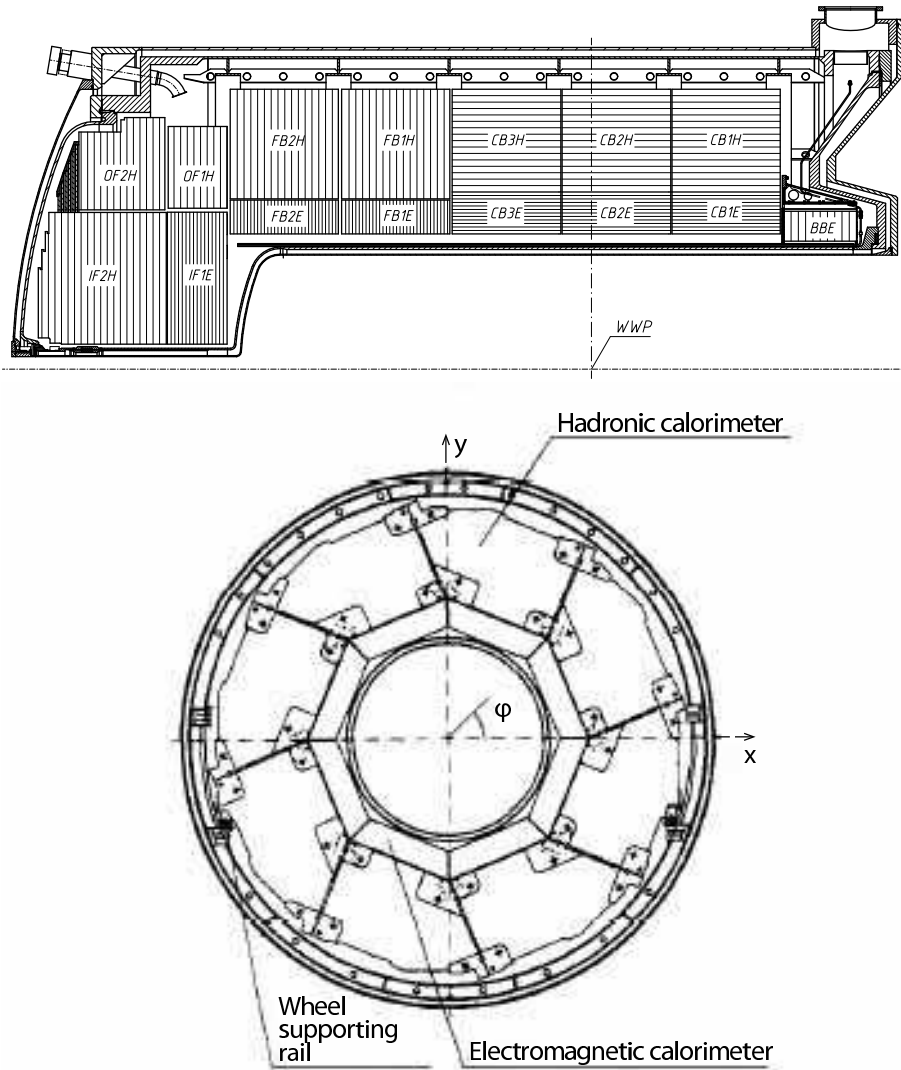


Figure 4.2: The (**top**) side and (**bottom**) frontal views of the Liquid Argon calorimeter.

The liquid argon technique was chosen for the good stability, homogeneous and fast response, possibility to provide a fine granularity. The calorimeter consisted of absorber plates in the liquid argon as a sampling medium. The EM section has 2.4 mm lead absorber plates and sampling gap of 2.35 mm in average, providing the absorption length from 22 to 30 X_0 . The HAD part consists of 19 mm stainless steel plates as an absorber with the sampling double gaps of 2.4 mm. The orientation of the absorber plates can be read from Fig. 4.2. The total deepness for the hadronic showers of the LAr calorimeter varies from 5 to 8 λ . The calorimeter is segmented into about 45000 read-out cells; the segmentation is more coarse in the backward part becomes more fine in the forward direction.

The calorimeter is non-compensating (see Section 7.6). The energy resolution has

been studied in test beam measurements [46, 47] and for the energy of the incident particle E [GeV] is $12\%/\sqrt{E}$ for electrons and $50\%/\sqrt{E}$ for charged pions.

Noise Suppression in LAr

The hadronic measurements in the LAr calorimeter can be affected by the noise contribution from the preamplifier electronics.

The typical value of electronic noise σ_{noise} of a single channel is 10-20 (20-30) MeV on electromagnetic energy scale in the electromagnetic (hadronic) part. After the on-line cut at the level of $2\sigma_{\text{noise}}$, the event energy gets from the positive noise about 48 GeV. For the off-line analysis only cells are kept with energy above $4\sigma_{\text{noise}}$ and all its directly neighboring cells (with the energies above $2\sigma_{\text{noise}}$ because of the on-line cut). After this first step of noise suppression the energy distribution of remaining noise in empty events peaks at 0.1 GeV and has a width of 0.5 GeV.

In a clustering procedure the formation of groups of cell which corresponds to the particle shower (clusters) occurs. Cluster with the significance $\sum_{\text{cells}} E_{\text{cell}}/\sigma_{\text{noise}} > 8$ are called “prominent”. Small clusters are suppressed if they are in the last layer of EMC or in HAC and far away (> 50 cm) from the center of gravity of any prominent cluster.

The further topological-wise noise suppression happens at the stage of the hadronic final state reconstruction (see Section 7.6.6).

4.1.2 “Spaghetti” Calorimeter (SpaCal)

The Spaghetti Calorimeter (SpaCal) [48] covers the polar angle range of $153^\circ < \Theta < 174^\circ$ and is used in the H1 experiment mainly for detection of the scattered electron. In the analysis it is used for measurement of the backward scattered hadrons and for trigger purposes.

The SpaCal is a non-compensating lead-fiber sampling calorimeter and consists of electromagnetic and hadronic sections. The electromagnetic section contains 1172 modules with an active volume of $40.5 \times 40.5 \times 250$ mm³ each. Each module made of lead sheets with grooves where the scintillator fibers lay². Light from the excited sampling material of the fibers is collected by the photomultipliers. The hadronic section consists of 128 cells of the same structure and bulk of $120 \times 120 \times 250$ mm³. Both electromagnetic and hadronic sections have thickness of one interaction length. The SpaCal calorimeter is characterized by low level of noise.

4.2 Tracking

The tracking system measures the charged particle trajectories which are called tracks. The general principle for each tracker device is the same: charged particles traversing the material of the detector (gas or semiconductor), ionize the medium, and free charges are collected and amplified. Each single measurement of the particle position is called hit. Through the hits the track is reconstructed; in the presence

²This “spaghetti” geometry gave the name to the device.

of the magnetic field the trajectory bends and this allows to extract the particle momentum from the curvature of the track (see Section 7.4.1).

The H1 tracking system is shown in Fig. 4.3. The basic overview of the angular coverage and spatial resolution of the tracking devices is given in Table 4.1.

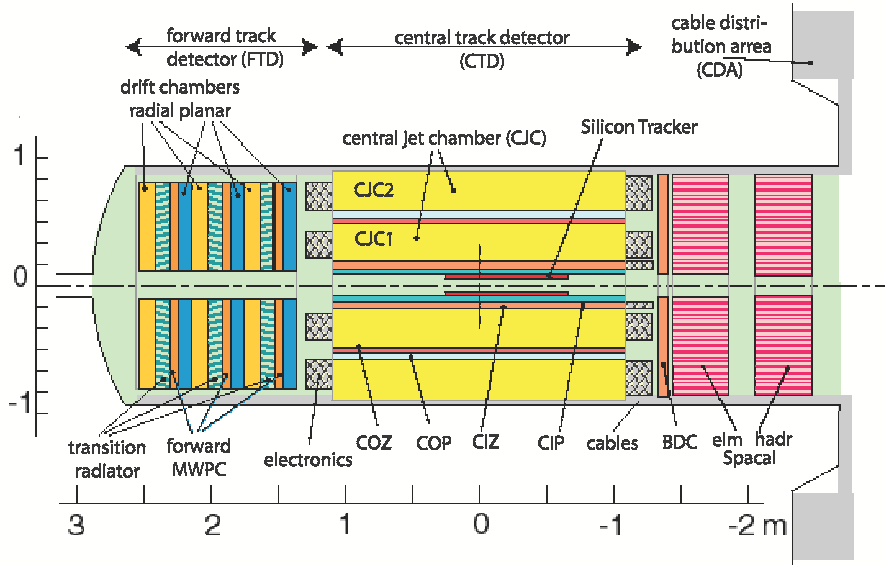


Figure 4.3: The side view of the H1 tracking system.

4.2.1 Central Tracking Detector (CTD)

The Central Tracking Detector (CTD) consisted of drift and proportional chambers and silicon detector.

Two coaxial cylindrical drift chambers, the Central Jet Chambers (CJC1 and CJC2) [33], comprise 30 and 60 drift cells each, with 24 and 32 sense (anode) wires per cell correspondingly. It has a good resolution in $r\phi$ plane and provide the precise measurement of the particle momentum. The wire planes are inclined with respect to the radial direction by about 30° (see Fig. 4.4), such that after ionisation free charges drift (in presence of the magnetic field of the H1 experiment) perpendicular to the wire planes, thus achieving a better track resolution. The z -coordinate of the hit is measured with the charge division technique [49] and the resolution achieved is about 2.2 cm.

The Central Outer z -Chamber (COZ) surrounds the CJC1 (see Fig. 4.4). It is a drift chamber with wires are strung perpendicular to the beam axis to allow a precise measurement of the z coordinate of the hit. The chamber contains 4 layers of sense wires. Another device located between the CJC1 and CJC2 is the Central Outer Proportional chamber (COP) which is a two layer multi-wire proportional chamber. It has a short response time and used for a fast vertex position determination.

Close to the beam pipe there is the Central Inner Proportional chamber (CIP) [50] which comprises five layers of multi-wire proportional chambers. Through backward

Detector	Angular coverage	Spatial resolution
Central Track Detector (CTD)		
Central Inner Proportional Chamber (CIP2k)	$15^\circ < \Theta < 165^\circ$	$\sigma_\phi = 5 \text{ mrad}$ $\sigma_z = 1.5 \text{ cm}$
Central Jet Chamber (CJC)		$\sigma_{r\phi} = 170 \mu\text{m}$
Central Outer Proportional Chamber (COP)		
Central Outer z-Chamber (COZ)		$\sigma_z = 350 \mu\text{m}$
Backward Drift Chamber (BDC)	$153^\circ < \Theta < 177^\circ$	$\sigma_r < 400 \mu\text{m}$
Central Silicon Tracker (CST)	$30^\circ < \Theta < 150^\circ$	$\sigma_{r\phi} = 14 \mu\text{m}$ $\sigma_z = 22 \mu\text{m}$
Forward Silicon Tracker (FST)	$8^\circ < \Theta < 16^\circ$	$\sigma_r = 16 \mu\text{m}$
Backward Silicon Tracker (BST)	$162^\circ < \Theta < 176^\circ$	$\sigma_r = 16 \mu\text{m}$
Forward Track Detector (FTD)		
Planar and radial drift chambers	$5^\circ < \Theta < 25^\circ$	$\sigma_{xy} = 1 \text{ mm}$

Table 4.1: The overview of the tracking detectors parameters composing the H1 tracking system.

propagation the z position of the interaction vertex could be determined within $2.3 \mu\text{s}$ with a resolution of approximately 16 cm . This information is used by the trigger to reject a background.

The Backward Drift Chamber (BDC) is situated in front of the SpaCal calorimeter and consists of six wire layers with three different orientations. It measures the particles going into the backward direction and allow to discriminate between charged and neutral particles.

The silicon track detector [51] consists of the Central Silicon Tracker (CST), the Forward Silicon Tracker (FST) and the Backward Silicon Tracker (BST) and is the detector closest to the beam pipe (see Fig. 4.4). The CST consists of two concentric cylindrical silicon layers with 12 and 20 modules of radii 5.75 cm and 9.75 cm , respectively. Both CST layers have 35.6 cm active length. The FST and BST extend the CST in forward and backward directions.

The momentum resolution for the track reconstructed with the CTD information after the alignment of the CTD's subdetectors [52] is $\sigma(P_t)/P_t = 1.5\% \oplus (0.17\% \cdot P_t/\text{GeV})$. It degrades at high particle momentum due to small curvature of the trajectory and at low momentum due to multiple scattering.

4.2.2 Forward Tracking Detector (FTD)

The Forward Track Detector (FTD) consisted of three modules which comprise five drift chambers each (four in case of the most forward module) with planar and radial wires stringed. The momentum resolution for the tracks reconstructed in FTD is $\sigma(P_t)/P_t^2 \approx 0.1 - 0.02 \text{ GeV}^{-1}$ depending on the length and polar angle of the track.

The tracks reconstructed with the FTD information only are called FTD tracks; if for the track reconstruction hits from both CTD and FTD were used it is called Combined track.

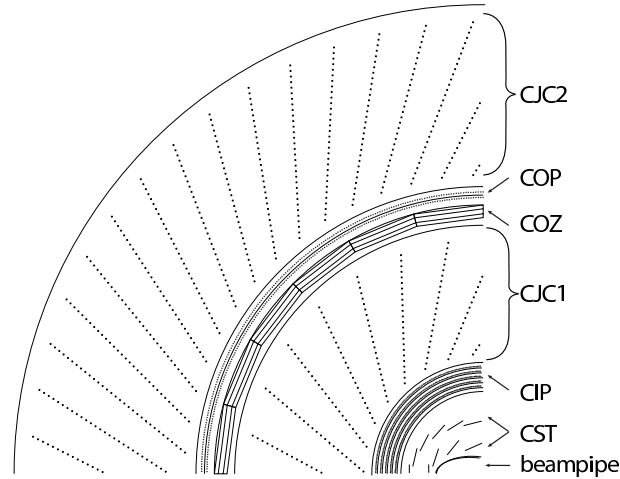


Figure 4.4: The central tracking detectors.

4.3 Trigger System

The bunch crossing (BC) frequency at HERA accelerator is approximately 10 MHz (96 ns — bunch crossing time), and each bunch collision produces some signal in the detector with synchrotron radiation and photoproduction, apart from the signals which come from beam halo, cosmic muons and electronics noise. The rate of the ep scattering at high Q^2 is about 10^4 times smaller. At the same time the manageable rate for the H1 data acquisition system is about 40 Hz.

Therefore it is essential to trigger on the collisions of interest. For this purpose, the H1 detector uses a pipelined multi-layered trigger system schematically shown in Fig. 4.5. The filtered data from one level are sent to the next level until manageable rate is reached. Levels L1, L2, L3 are hardware triggers, level L4/L5 are based on the online reconstruction of events.

4.3.1 The First Trigger Level (L1)

The first trigger level (L1) makes a decision within $2.3 \mu\text{s}$ on whether to accept or reject an event using the information provided by the different L1 trigger elements (TE) — signals sent by various subdetectors of the trigger system. The central trigger logic (CTL) combines these TE into 128 subtriggers. The response time (needed for charge collection, transportation of the signal from subdetector to CTL, etc.) for some subdetectors is relatively large, therefore the information first is sent into pipeline where it is kept for 24 BC (about $2 \mu\text{s}$). Then the TE are linked logically and the L1 decision is made. If any of the subtrigger conditions is fulfilled, the signal from the event is passed to the next trigger level. At the same time the pipeline is stopped and the dead-time of the detector starts.

The subtrigger could be prescaled. If the prescaling of the subtrigger is p , than only each p -th positive decision for this subtrigger can trigger the positive decision for the event. The prescaling is used for the subtriggers triggering relatively common

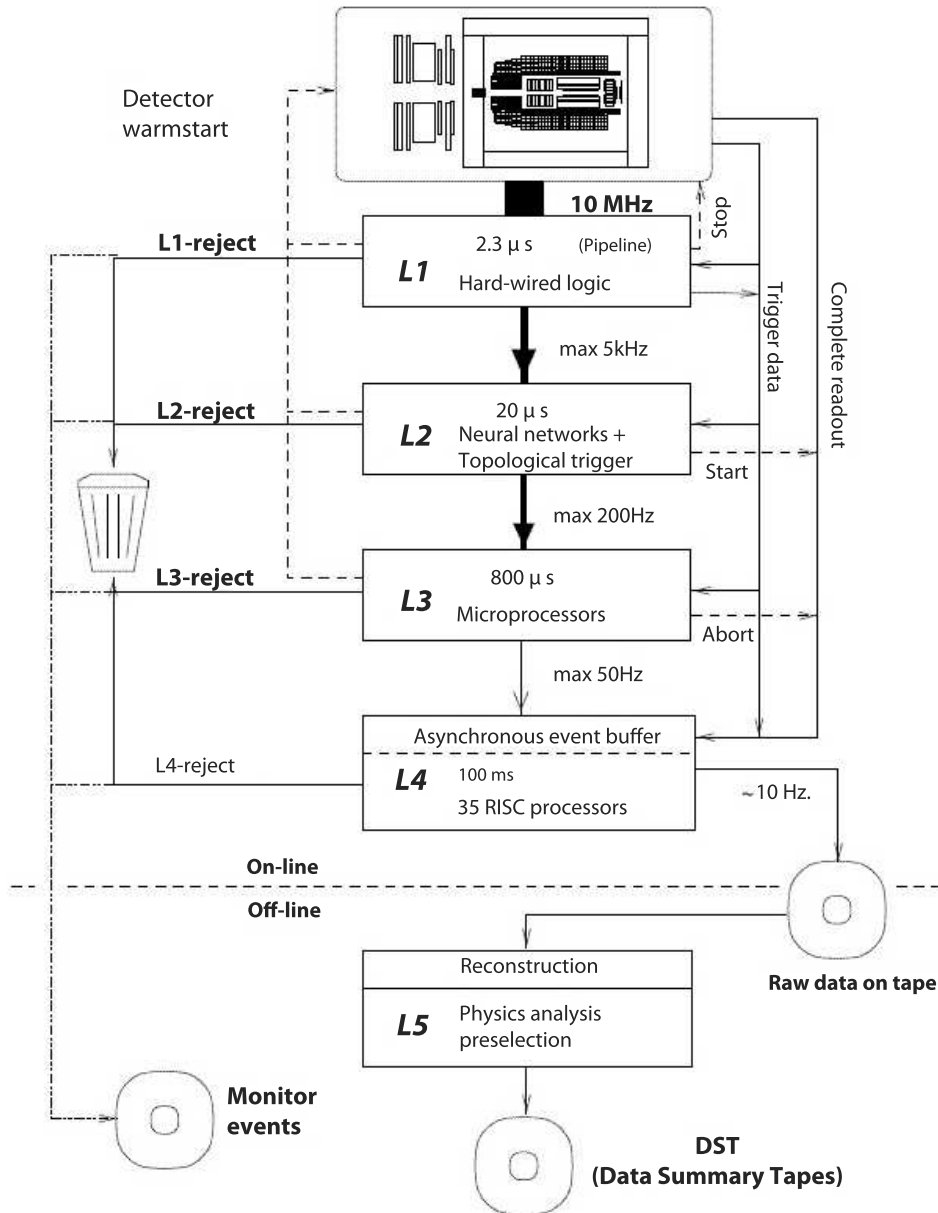


Figure 4.5: The H1 trigger system.

physics or used for performance of the detector to balance rate of such events with rare physics events. The L1 decision for the subtrigger X before the prescaling condition is applied is called raw and actual otherwise.

The L1 trigger elements essential for the analysis are the following

The LAr Calorimeter Trigger Elements

The LAr calorimeter provides signals to the CTL [53]. The analog signals provided from 45000 LAr cells added to “trigger cells” (TC) and further to “trigger towers” (TT) digitized using FADCs (flash analog to digital converter) and summed into 256 “big towers” (BT), having a projective geometry relatively to the nominal interaction point, see Fig. 4.6. Energy deposited in hadronic and electromagnetic parts of the calorimeter are counted separately. Several thresholds are introduced to suppress noise and backgrounds, there are so-called AGM-threshold for the sum of the analog signal, and the BT-threshold for the digital signals from BTs.

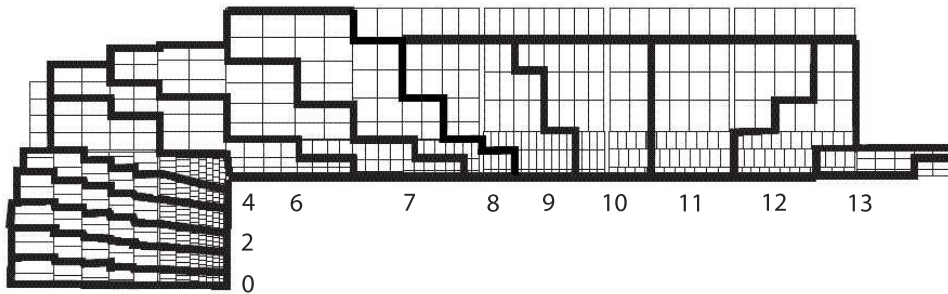


Figure 4.6: The projective Big Towers in LAr calorimeter. Each tower points toward the nominal interaction point.

The LAr TE used in the analysis are:

- **LAr_electron_1** and **LAr_electron_2**. The TEs are set if the electromagnetic energy deposited in the BTs exceeds a specific for this TE threshold (see Fig. 4.7) and the energy in the associated hadronic big tower is lower than a certain threshold value.
- **LAr_T0** (or “event T0”). The TE is set when the number of the BTs giving a T0 signal exceeds a certain value. For the actual setup one BT T0 is sufficient.

The Track Trigger Elements

The tracking chambers CJC, CIP, COP, COZ all provide the information for the CTL decision, details can be found in [50]. The trigger elements used in the analysis are

- **CIP_T0**. The TE set if there is at least one central track in coincidence with the interaction time.
- **CIP_mul** and **CIP_sig**. See below.
- **DCRPh_THig** and **FTT**.

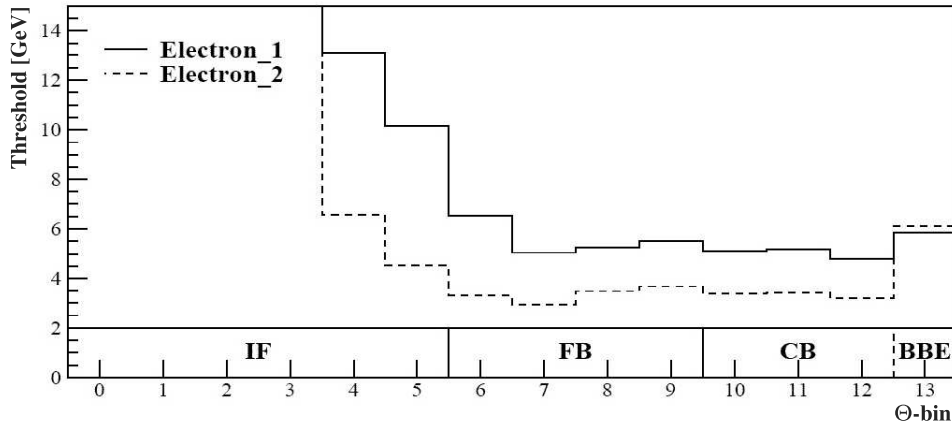


Figure 4.7: The thresholds for the **LAr_electron_1** and **LAr_electron_2** trigger elements as a function of Θ .

The Veto Conditions

Veto conditions are applied to most subtriggers in order to reject the backgrounds from beam halo and beam-gas interactions.

- **ToF_Veto.** The condition is used to reject the background events on the basis of the Time-of-Flight information. These trigger elements are based on the VETO_BG, BToF_BG, STof_BG, and FIT trigger elements of the ToF system described in Section 4.4.
- **CIP_Veto.** The CIP information is used to reject the background from the collimators close to the H1 interaction region. The requirement on the CIP: $(\text{CIP_mul} > 7) \ \&\& \ (\text{CIP_sig} == 0)$ efficiently rejects the background events with a high track multiplicity.

The SpaCal Calorimeter Subtriggers

The signal from the localized energy deposition in the electromagnetic section of the SpaCal calorimeter is also used as a trigger; in case of NC at high Q^2 it reacts on the hadrons which go to the backward direction. The SpaCal subtriggers involved are **s0** (threshold energy is $E^{\text{thr}} = 6$ GeV, minimal cluster radius is $r_{\text{sp}} = 12$ cm) and **s9** ($E^{\text{thr}} = 2.5$ GeV, $r_{\text{sp}} = 15$ cm). To keep a reasonable rate at low E^{thr} , **s9** contains an extra track condition.

4.3.2 The Second/Third Trigger Level (L2/L3)

The second level trigger exploits two trigger systems — the Neural Network Trigger (L2NN) [54] and the Topological Trigger (L2TT) [55] — and makes a decision within 20 μs . At this level the full information from all subdetectors is available, and there is enough time to inspect the correlations between them.

The results of the L2 trigger are given to the central trigger L2 decision logic (CTL2).

For the analysis the `L2TT_LAr_electron` TE is used. The condition is based on the approach in which the detector is represented with a matrix in $\Theta-\phi$ coordinates. This matrix is used to find a “distance to the background” and make a trigger decision. The detailed description of the level 2 trigger can be found at [56].

The third level trigger was not active until the end of 2005 year and was not used for this analysis.

4.3.3 The Fourth/Fifth Trigger Level (L4/L5)

The trigger levels L4/L5 performs the event full reconstruction from the complete readout of the event information [57]. It is the software asynchronous trigger. Event parameters (tracks, clusters, vertex) are reconstructed by the H1 software algorithms (H1REC, see below) on the dedicated PC farm.

The events are classified then with the so-called L4 filters. For the classes where statistics is enough only part of the data is stored and the rest gets “L4 trigger weights” applied to the data events. Events do not fit any interesting class are rejected.

The raw data for the events surviving all the trigger requirements are written to the production output tapes (POT, about 100 kb per event) and the reconstruction information is stored as the data summary tapes (DST, about 10 kb per event) at a rate of about 10 events per second.

4.4 Time-of-Flight Counters

To distinguish real ep interactions from beam induced background and suppress the latter, the event time of flight is used. Due to different path lengths particles produced near the nominal interaction point arrives the detector at a different time in compare with a particles produced from the (say, beam-gas) interactions far from the IP. To provide this measurement Time-of-Flight (ToF) system was designed out of several “fast”³ scintillator detectors [58] mentioned in Table 4.4. The arrangement of the ToF devices inside the H1 detector is shown in Fig. 4.8.

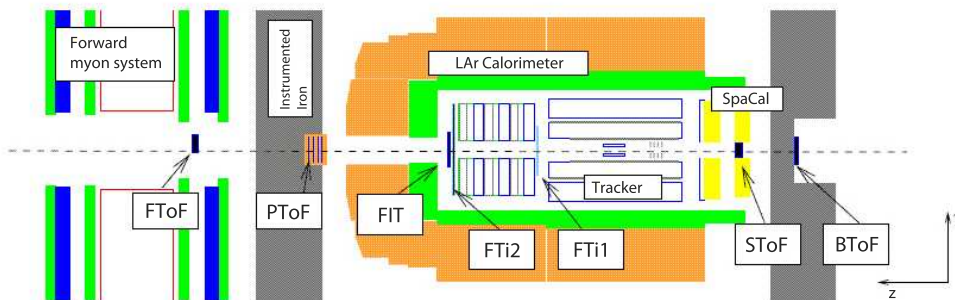


Figure 4.8: The Time-of-Flight system. Veto Wall is outside of the visible range to the right side.

³“Fast” means high time resolution property.

Part	z-position, m	Description
FToF	7.0	Forward ToF installed within the forward muon system
PToF	5.3	ToF installed behind the Plug calorimeter
FIT	2.7	Forward Interaction Timing system mounted behind the forward tracking
SToF	-2.4	ToF installed before the hadronic SpaCal calorimeter section
BToF	-3.3	Backward ToF mounted after SpaCal
Veto Wall	-(6.5—8.1)	Several small veto counters mounted close to the beam pipe

Table 4.2: Detectors of the ToF system.

4.5 The Luminosity Measurement in the H1 Experiment

In the H1 experiment the luminosity is measured using Bethe-Heitler events $ep \rightarrow ep\gamma$ [59]. The main source of background in the luminosity measurement is the interaction of the electrons with residual gas in the beam pipe $eA \rightarrow eA\gamma$ and is expected at 10% of the $ep \rightarrow ep\gamma$ process rate; it is subtracted using the pilot bunches. The instantaneous luminosity is calculated as [60]

$$L = \frac{R_{\text{Tot}} - (I_{\text{Tot}}/I_0)R_0}{\sigma_{\text{Vis}}}, \quad (4.1)$$

where R_{Tot} is the total rate of the photons detected in the luminosity monitor during the physical run, R_0 is the rate in the electron pilot bunches, I_{Tot} and I_0 are the corresponding electron beam currents and σ_{Vis} is the visible part of the $ep \rightarrow ep\gamma$ cross-section with acceptance and trigger efficiency included. The polar angles of the scattered electron and photon are of the order of $\Theta \approx O(m/E) \approx 17 \mu\text{rad}$.

Both electrons and photons are measured with the electron tagger (ET) and photon detector (PD) respectively (see Fig. 4.9). ET and PD are the hodoscopes of total absorption. The scattered electrons are deflected by a magnetic optics of the beam pipe and hit the ET at $z \approx -6$ m. The photons leave the proton beam pipe through a window at $z = -102.9$ m. A Pb filter ($2X_0$) followed by a water Cherenkov ($1X_0$) veto counter protects the PD from the high synchrotron radiation flux.

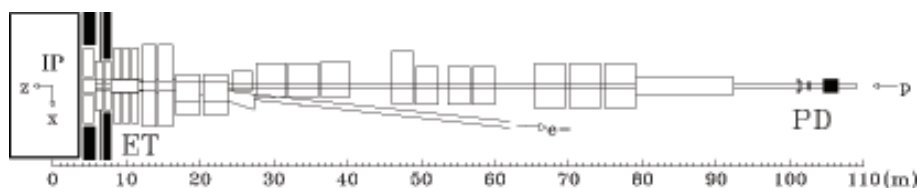


Figure 4.9: The luminosity monitor of the H1 experiment.

The main sources of the uncertainty on the luminosity measurement [60] come from the theoretical prediction of the σ_{BH} (0.5%), determination of the γ -energy scale (1%) and estimation of the geometrical acceptance, the latter is especially sensitive to the electron beam tilt. If all the components work well, the uncertainty on the luminosity measurement is about 2%.

Compton Luminosity Measurement Correction

Because of unidentified problems with the luminosity measurement for certain periods, the Compton analysis was done to cross check and correct the luminosity monitor measurement.

The independent measurement of the luminosity was done with the QED Compton events [61]. Cross section for this process is known theoretically to high precision and the event rate is large enough. The signature of the Compton event is the following generally: two⁴ energetic back to back electromagnetic clusters in SpaCal calorimeter with absence of the signal in the LAr calorimeter. Both clusters are required to be within the CIP acceptance ($40 < R_{clus} < 70$ cm) to allow precise vertex reconstruction. For the analysis special relative alignment of the tracker components and SpaCal calorimeter is done [61].

First Run	Last Run	Correction
356241	376562	0.98277
377533	386696	1.03835
387537	392213	0.97063
402992	414712	0.97399
415620	427474	1.00106
427813	436893	1.01643
444094	458154	1.02349
458841	466997	1.00089
468530	485679	1.01660
485715	485849	0.98691
486073	489866	1.05919
490135	500611	1.06993

Table 4.3: The correction factors from the Compton luminosity analysis.

The main sources of the common systematic uncertainty come from the theoretical predictions for the initial state radiation in Compton process (1.5%), estimation of the backgrounds (about 1.3%) and SpaCal calibration and alignment (0.5%); these result in the total systematic uncertainty on the luminosity measurement of 2%. The statistical uncertainty for the PerPosRH, PerPosLH, PerNegRH, PerNegLH periods for which the NC cross section measurement is provided is calculated from the Compton event's rate and is about 1.5%.

The correction factors applied to the luminosity monitor's measurement in different periods are shown in Table 4.3. Compton luminosity measurement is close

⁴Actually more clusters are allowed to take into account possible radiation of the hard photon from the electron. For these events further cluster merging is done.

to the luminosity monitor measurement for all periods except the second half of Per0607 period where the 6% difference is observed.

4.6 Data Storage Model and Software Environment

The H1 raw data (RAW) and the results of Monte Carlo simulation are reconstructed and stored on tape as a Production Output Tapes (POT). This low level data storage [62] is based on the memory management system Bank Object System (BOS) [63] (the BOS banks are the tables described by the data definition language (DDL)) and I/O package FPACK. The Data Summary Tapes (DST) is the reduced set of information and is kept on disk to allow the parallel access.

For the simulation of the detector the GEANT3 [64] based package H1SIM [65] is used. To accelerate the events processing the calorimetric response on the electromagnetic particles is parametrized and implemented in the H1FAST [66] routine. The hadronic showers undergo “full” GEANT simulation. Both data and Monte Carlo are reconstructed with the same reconstruction program H1REC [67]. All the data processing above is done with the FORTRAN based routines.

For the physics analysis the C++ based framework called H1OO [68] is developed. This is a ROOT [69] based system which provides tools for the analysis and keeps the data at three layers. The lowest layer, Object Data Store (ODS), is produced from DST or POT such that the content is 1-to-1 equivalent to the DST, but the information is stored in C++ objects. Two additional layers are micro-ODS (μ ODS) which contain calibrated and preselected analysis-ready information and H1 Analysis Tag (HAT) with the event-level information. Usually the ODS’s do not stored persistently and discarded after the creation of the μ ODS and HAT. μ ODS (≈ 2 kB/event) and HAT (≈ 0.4 kB/event) are much smaller than ODS, allowing faster selection of the events in the analysis. In addition the User Tree can be produced containing the information important for the given analysis⁵ but not included into the μ ODS/HAT.

The H1OO package provides the convenient framework for physics analysis. It contains the basic classes to steer the analysis and to run over the data and simulation events along with special tools for calibration, binning of the results etc. The *H1Calculator* package makes the automatic recalculation of the kinematical variables under the systematic shifts (see Section 8).

As an events viewer the ROOT based event viewer H1RED [70] is used.

⁵For the case of current analysis low-level trigger information has been stored this way.

Chapter 5

Reconstruction of the Kinematic Variables

5.1 The Reconstruction Methods

A precise reconstruction of kinematics from the final state is of vital importance for structure function measurements at HERA. As follows from Section 2, two inclusive kinematic variables are sufficient to describe the NC DIS process if the beam energies are known, e.g. the energy and the polar angle of the scattered electron or x and Q^2 . In the H1 experiment both the scattered electron and some characteristics of the hadronic final state can be measured. For the electron its energy E_e and scattering angle Θ_e are measured. The initial energy of the lepton beam we denote as E_e^0 .

Since some remnants of the incident proton escape through the beam pipe unobserved, the following hadronic final state (HFS) variables are chosen to be used in this analysis:

$$\Sigma = \sum_{i \in \{\text{HFS}\}} (E^i - P_z^i) \quad (5.1)$$

$$P_t^{\text{had}} = \sqrt{\left(\sum_{i \in \{\text{HFS}\}} P_x^i \right)^2 + \left(\sum_{i \in \{\text{HFS}\}} P_y^i \right)^2} \quad (5.2)$$

where E^i, \mathbf{P}^i are the energy and the 3-momentum of the i -th particle of the HFS, respectively; the summation goes over all the particles of the HFS. By construction, these variables are relatively insensitive to losses in the beam pipe in the positive z (forward) direction.

Other useful variables are $(E - P_z)$ and P_t , defined as

$$E - P_z = \sum_{i \in \{\text{All}\}} (E^i - P_z^i) = \Sigma + E_e (1 - \cos \Theta_e) \quad (5.3)$$

$$P_t = P_t^{\text{had}} + E_e \sin \Theta_e \quad (5.4)$$

For the ideal detector and without ISR photon emission (see Section 2.6) these variables should be the same before and after the ep interaction, therefore $(E - P_z) =$

$2E_e^0 \approx 55$ GeV and $P_t = 0$. For the real detector in the presence of resolution effects and losses due to detector acceptance they deviate from their “ideal” values.

The proton structure functions under measurement are functions of x and Q^2 variables (see Section 2.1.2). In principle they could be calculated from the measurement of two quantities. However, usage of more than just two quantities allows to over-constrain the final system and makes the reconstruction of the kinematics more precise; especially this is demanded for the measurements covering a wide range in the x - Q^2 plane when the precision of different measurements varies significantly. To make use of all the measurements available, the following reconstruction methods are used.

- **The Electron Method.** The event kinematics is determined solely from the scattered electron energy E_e and the angle Θ_e

$$Q_e^2 = 4E_e^0 E_e \cos^2 \frac{\Theta_e}{2}, \quad y_e = 1 - \frac{E_e^0}{E_e} \sin^2 \frac{\Theta_e}{2}, \quad x_e = \frac{Q_e^2}{s y_e} \quad (5.5)$$

This method takes advantage of the good single electron measurement in the H1 experiment. The disadvantage of the method is the relatively high sensitivity to the ISR process. The resolution of x_e degrades at low y since $\delta x_e/x_e \approx (1/y_e)\delta E_e/E_e^0$. However, the electron method is best for the Q^2 measurement, since

$$\frac{\delta Q_e^2}{Q_e^2} = \frac{\delta E_e}{E_e} \oplus \tan \frac{\Theta_e}{2} \delta \Theta_e \quad (5.6)$$

This method was used in the fixed-target experiments, e.g. R. Hofstadter [2], SLAC [3], etc.

- **The Hadron Method.** Here, the event kinematics reconstruction relies entirely on the hadronic system measurements. This method was introduced by Jacquet and Blondel [71] and is the only one available for the reconstruction of the Charged Currents kinematics.

The kinematical variables are determined as follows

$$y_h = \frac{\Sigma}{2E_e^0}, \quad Q_h^2 = \frac{(P_t^{\text{had}})^2}{1 - y_h}, \quad x_h = \frac{Q_h^2}{s y_h} \quad (5.7)$$

The method profits from the stability of Σ and P_t^{had} against the losses through the beam pipe in the forward direction. However, it is sensitive to the losses in the backward direction which occurs at the highest y , and to the calorimeter noise at small Σ values, i.e. at a region of small y . The resolution of the Q_h^2 variable is deteriorated by the $1/(1 - y)$ term at high y region. On the other hand, the method is rather insensitive to radiative corrections.

- **The Σ (Sigma) method.** This method, proposed in [72], exploits the information from the HFS and the scattered electron measurements simultaneously. The kinematical variables are defined with the relations

$$y_\Sigma = \frac{\Sigma}{E - P_z}, \quad Q_\Sigma^2 = \frac{E_e^2 \sin^2 \Theta_e}{1 - y_\Sigma}, \quad x_\Sigma = \frac{Q_\Sigma^2}{s y_\Sigma} \quad (5.8)$$

The determination of the kinematics is similar to the hadron method, but with two essential improvements: first, in NC the scattered lepton is used to measure the transversal momentum much more precise compared to P_t^{had} . Second, it accounts for the case of ISR: if ISR has occurred and the photon had an energy E_γ , then the initial energy of the interacting electron should be reduced to this amount and (see (5.3))

$$2E_e^0 \rightarrow 2(E_e^0 - E_\gamma) = E - P_z \quad (5.9)$$

Taking the latter into account one can reduce the sensitivity of y_Σ to the ISR process. But since x_Σ is calculated with the initial center of mass energy, the Σ -method retains some sensitivity to the initial state radiation. Finally this method provides a better resolution in x and y compared to the electron and hadron methods at low and medium y , and similar resolution in the high y region.

- **The $e\Sigma'$ (eSigma-prime) method.** Taking into account all the observations from the previous discussion, the $e\Sigma'$ -method is proposed for the reconstruction of the kinematics as a modification of the $e\Sigma$ -method [73].

The kinematical variables are defined as follows

$$Q_{e\Sigma'}^2 = Q_e^2, \quad x_{e\Sigma'} = \frac{x_\Sigma}{1 - y_e + y_h}, \quad y_{e\Sigma'} = \frac{Q_{e\Sigma'}^2}{s x_{e\Sigma'}} \quad (5.10)$$

On the one hand the resolution in Q^2 is as good as for the electron method. On the other hand, x and y are insensitive to the ISR process like in the Σ -method, but x is additionally corrected to the center of mass energy change for the case of initial state photon emission.

- **The Double Angle (DA) method.** To describe the kinematics reconstruction one defines the polar angle of the hadronic final state

$$\tan \frac{\gamma_h}{2} = \frac{\Sigma}{P_t^{\text{had}}} \quad (5.11)$$

In QPM, γ_h corresponds to the polar angle of the scattered quark.

The kinematical variables are then reconstructed with the relations [74]

$$\begin{aligned} Q_{\text{DA}}^2 &= \frac{4(E_e^0)^2(1 + \cos \Theta_e) \sin \gamma_h}{\sin \gamma_h + \sin \Theta_e - \sin(\Theta_e + \gamma_h)}, \\ y_{\text{DA}} &= \frac{(1 - \cos \gamma_h) \sin \Theta_e}{\sin \gamma_h + \sin \Theta_e - \sin(\Theta_e + \gamma_h)}, \\ x_{\text{DA}} &= \frac{Q_{\text{DA}}^2}{s y_{\text{DA}}}. \end{aligned} \quad (5.12)$$

This method assumes that in the interaction the scattered quark has formed a single massless jet. The latter condition allows the safe use of the method on the class of events with the special topology only (so called 1-jet events); the main difficulty is the estimation of the HFS angle γ_h .

As is seen from (5.12), only angle measurements are necessary. Since the double angle method reconstruction is almost independent from the calorimetric energy measurements, it can be used as a reference for the calibration of the LAr calorimeter (see Section 7 for details).

For latter let us provide here some useful formulae. The scattered electron energy, needed for the electromagnetic calibration, is given in the DA method by

$$E^{\text{DA}} = \frac{2E_e^0 \sin \gamma_h}{\sin \gamma_h + \sin \Theta_e - \sin(\Theta_e + \gamma_h)} \quad (5.13)$$

The transverse momentum in the event is used in the hadronic calibration, and is determined with the double angle method as

$$P_t^{\text{DA}} = \frac{2E_e^0}{\tan \frac{\gamma_h}{2} + \tan \frac{\Theta_e}{2}} \quad (5.14)$$

5.2 Comparison of Methods

A choice of the method to be used for reconstruction of an event kinematics is done on the basis of the resolution, and comparisons in the variables x and Q^2 are shown in Fig. 5.1, 5.2. The generated (true) value is compared with the reconstructed using the different methods discussed above. The relative RMS for the variable V shown on the y axis is calculated as RMS of the $(V_{\text{rec}} - V_{\text{gen}})/V_{\text{gen}}$ distribution within the “window” $[m - 2\sigma, m + 2\sigma]$, where the m and σ parameters are obtained in the Gaussian fit of the peak of the distribution.

For the reconstruction of Q^2 the $e\Sigma'$ method is chosen (or, the same, the electron method, see (5.10)) as it shows best resolution over the full kinematical range.

For x the best performance is achieved with two methods depending on y . Electron method at high y and $e\Sigma'$ method at moderate and low y region. In Section 8 the cross sections are measured with both methods, and a choice of the measurement for the final result in a certain point is done on the basis of the total uncertainties obtained in these measurements. For the points below a certain value of y_c one takes the $e\Sigma'$ measurement and for the points above the electron method. The separation between these two in the analysis is taken at $y_c = 0.19$.

Such an approach leads to a statistical correlation for the bins at the border between two methods: some events are reconstructed at moderate $y_{e\Sigma'}$ with the $e\Sigma'$ method and at high y_e with the electron method. To investigate this effect, the fraction of events reconstructed by both measurements is studied. In Fig. 5.3 the fraction of the events contributing twice is shown in bins of x and Q^2 . At the point where one converts from one method to another the correlation is maximal. Generally, over the phase space of the analysis it is under 30% and can be neglected in applications like PDF fits.

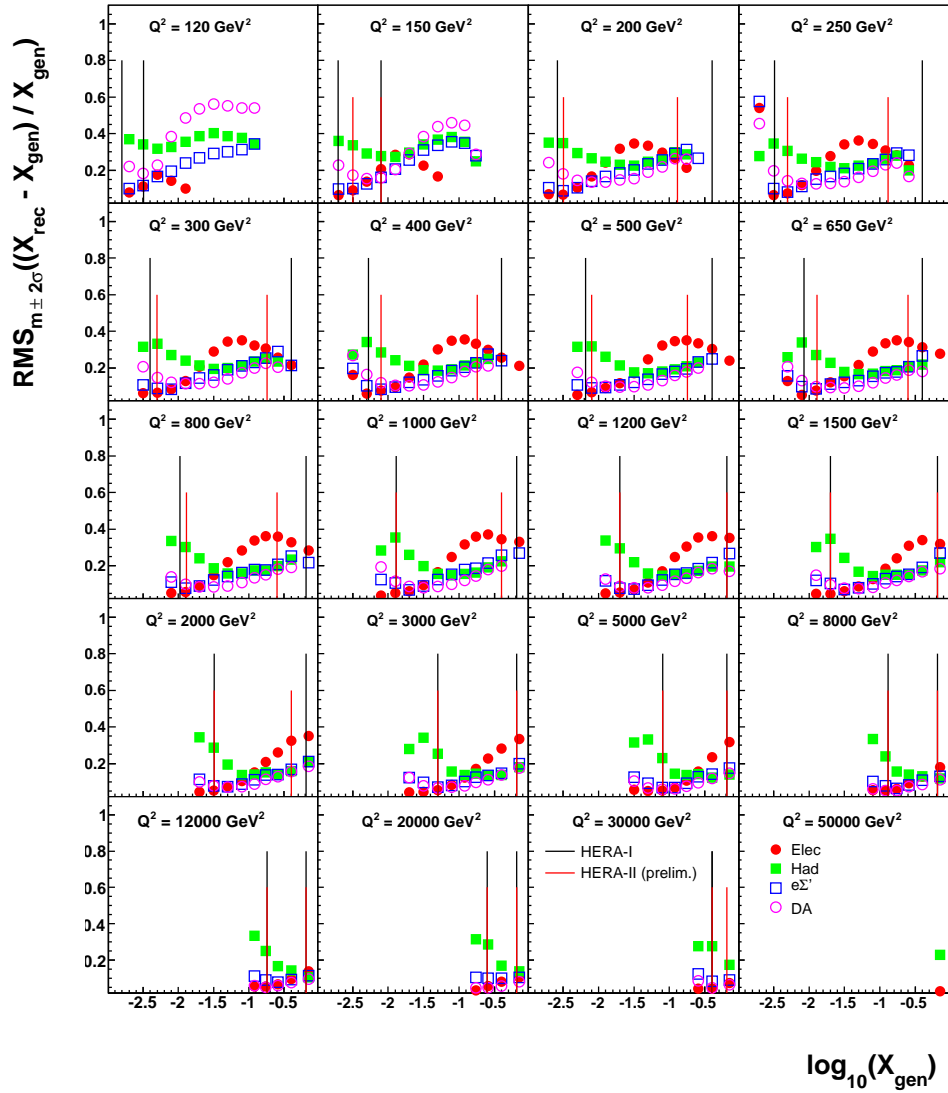


Figure 5.1: The resolution of the reconstructed variable x for different Q^2 bins for different reconstruction methods. x_{rec} (x_{gen}) refers to the reconstructed (generated) values of x . Black (red) symbols refer to the ranges where HERA-I (HERA-II preliminary) measurement has been done.

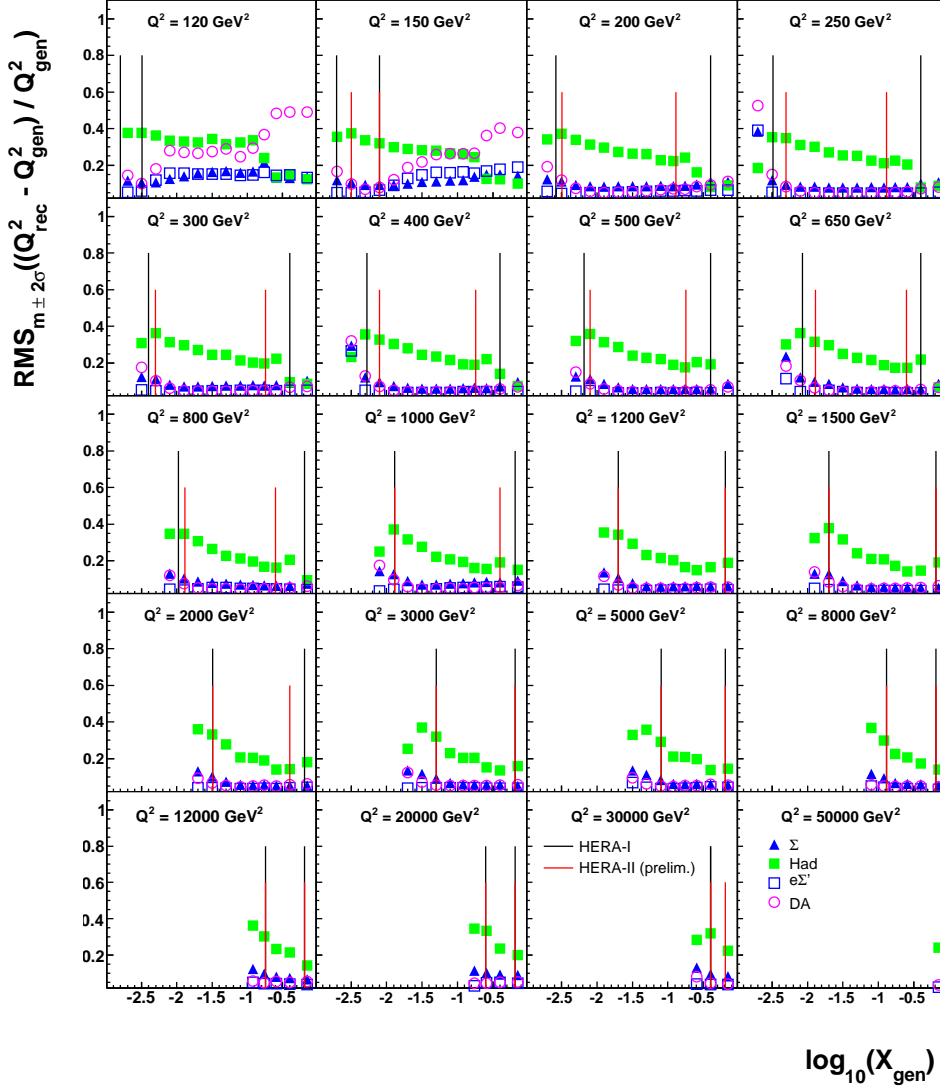


Figure 5.2: The resolution of the reconstructed variable Q^2 as a function of x for different Q^2 bins for different reconstruction methods. Q^2_{rec} (Q^2_{gen}) refers to the reconstructed (generated) values of Q^2 . Black (red) symbols refer to the ranges where HERA-I (HERA-II preliminary) measurement has been done.

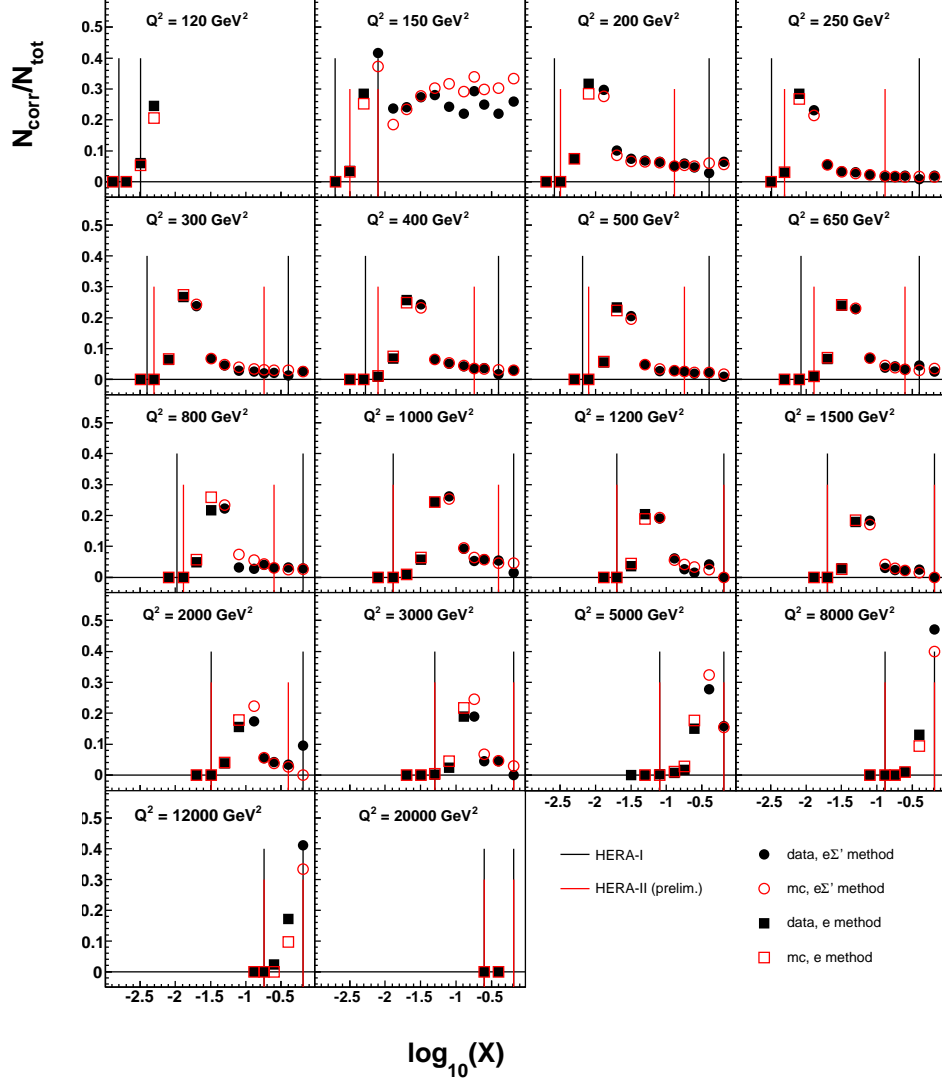


Figure 5.3: The statistical correlation between measurements with electron and $e\Sigma'$ methods as a function of x for different Q^2 bins. N_{tot} denotes the number of events registered in a given bin and used for the cross section calculation. N_{corr} denotes the number of events in a given bin which are used in the cross section measurement with both methods. The ratio of $N_{\text{corr}}/N_{\text{tot}}$ is the fraction of events in given bin which are also used for the cross section measurement in some other bins. Black (red) symbols refer to the ranges where HERA-I (HERA-II preliminary) measurement has been done.

Chapter 6

Monte Carlo Simulation

For the cross section measurement the corrections to the acceptance, resolution, trigger efficiency of the detector must be taken into account. For these purposes the stochastic technique known as Monte Carlo (MC) method is used, where the physical processes occurring in the detector are simulated as realistically as possible. This includes processes in the interaction point (the collision of the electron and proton with subsequent production of the final state particles) and the simulation of the interaction of the final state particles with the detector. This detector modelling includes “low-level” effects like particle showers in the material of the detector up to “high-level” effects like the peculiarities of the charge division in the wires of the tracking chamber. The detector simulation is done with the H1SIM [65] package (see Section 4.6). For each simulated physical process a unique MC generator, delivering 4-vectors of the final state particles, is used.

If the simulation closely follows the data, the rates of the simulated and data events passed the selection criteria are very similar, so the measured number of data events can be corrected with the MC to obtain the true number of data events in this region. When the discrepancy in the essential properties¹ of the simulation from the data due to some physical effect is observed, the simulation is corrected to this effect to make the generated events (“virtually”) undergo the same procedure as data events.

To assure good agreement between data and Monte Carlo, the simulation for each data period is done separately following time dependencies in the experimental setup. The data taking conditions including the distribution of the interaction vertex are simulated run-wise. To make the statistical uncertainty from the number of the MC events negligible, the simulated events sample is made several times the size of the data sample. A total of about 8 mio. of signal events and 6 mio. background events for each of the 8 data subperiods are simulated.

In the following the Monte Carlo generator programs used for the NC and backgrounds are described in more detail.

¹For example, for the measurement of the NC cross section the multiplicity of the particles in the hadronic final state is not very important. In contrast, the trigger efficiency is difficult to simulate, and so its determination is very important as soon as the efficiency is far from 100%; for this reason on the analysis level the trigger efficiency is measured in data and plugged into the MC.

6.1 Generation of the NC DIS Events

For the simulation of neutral current events the DJANGO 1.4 [75] (Django) generator is used. For the hard partonic interaction it exploits the ARIADNE 4.10 [76] routine, which combines $O(\alpha_s)$ matrix element with the parton showers in LHAPD ME+CDM model (color dipole model). The LUND string fragmentation as implemented in the JETSET 7.410 [77] simulation program is used to obtain the complete hadronic final state. For low-mass hadronic final state ($W < 5 \text{ GeV}^2$) SOPHIA [78] is used. The exact calculation of the QED radiative corrections with one additional photon emission from the lepton line with the inclusion of the electroweak corrections is done with the HERACLES 4.6 [79] module. Possible emission from the quark line (quarkonic radiation) is not taken into account. The inelastic part of the Compton scattering process (see Section 6.2) is simulated with the Django generator too.

Generation of the events is done with the CTEQ6L [80] PDF's with zero polarization with further reweighing during the analysis to HERAPDF1.0[81] and the polarization taken from the data. Both PDF's are obtained in NLO QCD fits to match with the Django generator. In order to obtain sufficient statistics at high Q^2 's the generation have been done in five steps: $Q^2 > 15 \text{ GeV}^2$ and $y > 0.3$, $Q^2 > 40, 60, 100, 1000, 10000 \text{ GeV}^2$.

6.2 Generation of the Background Events

The typical signature for a neutral current event is an isolated electromagnetic particle in the LAr calorimeter. Therefore, the background to NC are the events with an energetic electromagnetic shower in the final state, either from a real electron or a fake signal from a pion.

As backgrounds, photoproduction, lepton pairs production, W production, and Compton process are generated. In the following a short description of these contributions and used event generators are given.

Photoproduction

The main background contribution for the analysis is the photoproduction process, where the incident electron scatters at Q^2 close to zero and the proton interacts with a real photon. Interaction between a real photon and a proton can occur by two different mechanisms [82] (see Fig. 6.1). The photon may interact “directly” with a quark or gluon (interaction happens with a quark–antiquark pair from the gluon decay) from the proton (direct photoproduction, Fig. 6.1a) or it may resolve into its constituent quarks and gluons which then interact with the proton's partons (resolved photoproduction) as is shown in Fig. 6.1b. In the latter case the photon remnant is expected to be approximately collinear to the initial photon providing additional jets in the event.

In the photoproduction event the scattered electron comes out at zero scattering angle but with lowered energy and escapes through the beam pipe. Therefore particles (mainly pions) from the hadronic final state could mimic an electromagnetic candidate.

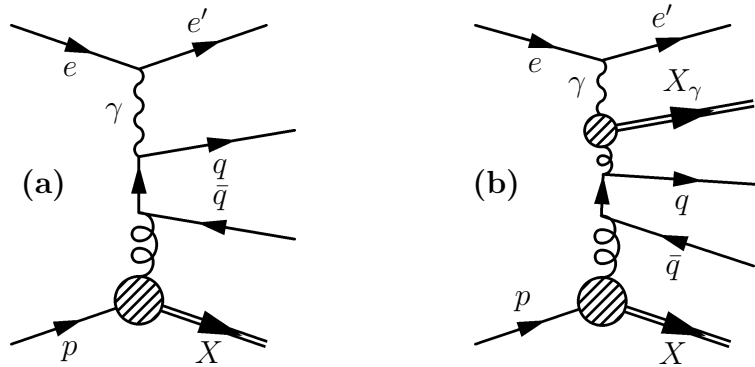


Figure 6.1: Examples of leading order (a) direct and (b) resolved hard photoproduction process diagrams.

The photoproduction (both direct and resolved processes) is simulated with the PYTHIA [77] event generator with leading order matrix element.

Lepton Pairs

Lepton (e, μ, τ) pair production provides electromagnetic candidates and could fake a neutral current event. At HERA conditions the main production mechanism involves photon-photon scattering, shown in Fig. 6.2.

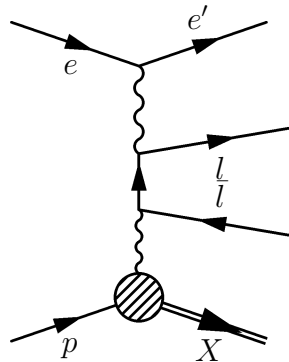


Figure 6.2: Example of the leading order diagram for lepton pair production.

The lepton pairs are simulated by the GRAPE [83] event generator. This program is based on the automatic amplitude calculation system GRACE [84], and includes all the electroweak diagrams at tree level except for proton- Z^0 couplings and lepton pair production through photon radiation from the proton. The generator is interfaced to PYTHIA to produce complete HFS.

W Production

A real W boson can be produced at HERA conditions and in case of leptonic decay (an example of such a process is shown in Fig. 6.3) the charged lepton can produce an isolated electromagnetic shower of high energy. The cross section for this process is relatively small.

This process is simulated with the LO Monte Carlo program EPVEC [85].

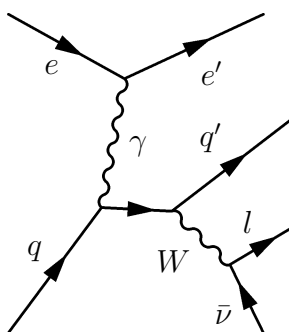


Figure 6.3: Example of leading order W production diagram.

QED Compton Scattering

In Compton scattering the photon from a scattered electron interacts mainly with the entire proton corresponding to very low Q^2 , and so this process is not included into the deep inelastic scattering cross section.

To simulate this contribution the WABGEN [86] generator has been used. It calculates the cross section from the two leading order diagrams shown in Fig. 6.4 in the Weizsäcker–Williams approximation for the photon emission from the scattered electron. Photon emission from the hadronic line, and the radiative corrections are neglected.

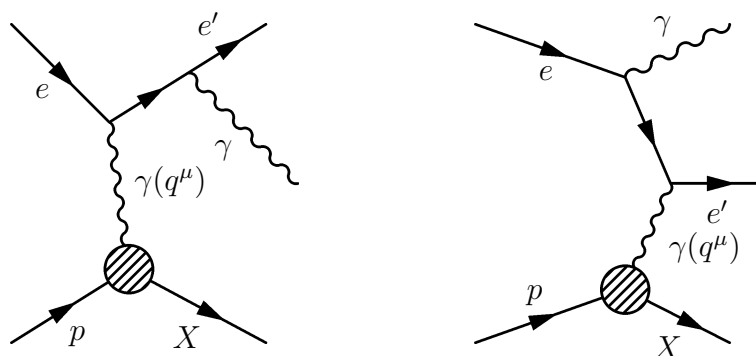


Figure 6.4: Leading order Compton scattering process diagrams.

In the limit of small Q^2 the dominant contribution comes from the elastic ($X = p$) process; at higher values of Q^2 the inelastic process starts to dominate. Resonance production (quasi-elastic process) also contributes to the process. Elastic and quasi-elastic parts of the Compton process cross section are taken for the analysis from the WABGEN generator.

Chapter 7

Data Analysis

7.1 General Strategy of the Analysis

The neutral current cross section in this analysis is measured in the kinematical region where the scattered electron is registered in the LAr calorimeter. This corresponds to an electron scattering angle¹ below $\Theta_e \approx 153^\circ$ and therefore to the relatively large values of $Q^2 \gtrsim 100 \text{ GeV}^2$. The electron candidate is recognized by a compact isolated energy deposition (cluster) in the LAr calorimeter and verified by tracker information such as an associated track in the CJC.

The phase space of the analysis is divided into two parts, at moderate y (either $y \leq 0.63$ or high Q^2), corresponding to the so-called Nominal analysis, and the region of high y ($y > 0.63$ and $Q^2 < 890 \text{ GeV}^2$) called HighY analysis. This division is motivated by the relation

$$y_e = 1 - \frac{E_e}{E_e^0} \sin^2 \frac{\Theta_e}{2},$$

where high y corresponds to low scattered electron energies. The region of low E_e suffers from severe background conditions, mostly photoproduction, demonstrated in Fig. 7.1 as a function of y and E_e . The explanation of such a behavior is related to the large number of low energy hadrons (mostly pions), which fake a scattered electron, which grows crucially with decreasing energy of the candidate.

In the Nominal part of the analysis [87, 88] we accept events with electron candidates which have a reconstructed vertex and an electron cluster in the LAr calorimeter. In this region of relatively high $E_e > 11 \text{ GeV}$ the trigger is almost 100% efficient. The cuts against background are loose. As long as the contamination by background events is small, the background can be simulated and then statistically subtracted despite the large uncertainty on the background Monte Carlo. The efficiency of the vertex reconstruction is an issue. It needs a careful treatment in the region of high x , where the events with low γ_h are present. Here the hadronic final state particles go forward along the beam pipe. Such particles can interact with the beam pipe producing many secondary tracks, which can cause reconstruction of a fake primary vertex far from the true position. For the proper treatment of such cases the *NC Optimal Vertex* has been developed. Also these forward particles

¹Note that the polar angle in H1 experiment is calculated relatively to the proton beam direction.

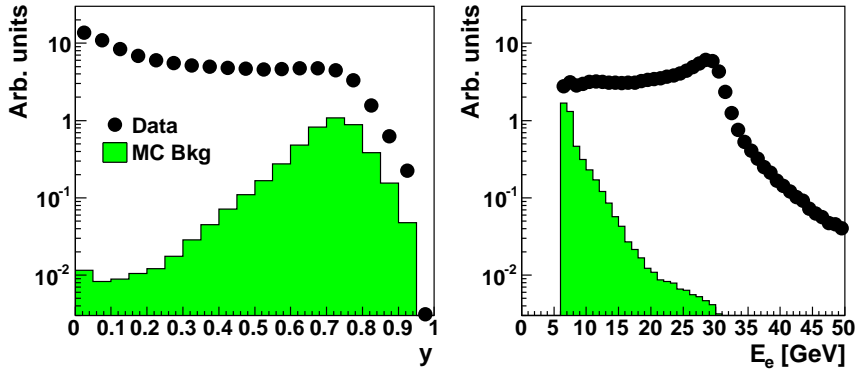


Figure 7.1: The data and background (mostly from the photoproduction) for the NC Nominal analysis selection.

can escape undetected which degrades the resolution of the reconstructed kinematic variables.

The HighY part of the analysis at low E_e is characterized by a high level of background contamination. The lowest electron candidate energy is limited by the electron trigger thresholds (see Section 4.3.1) in the LAr calorimeter. The correction on the threshold behavior of the trigger efficiency is essential here. Tight conditions on the scattered electron candidate are applied to suppress background. A well reconstructed track (DTRA track) and an electric charge coincident to the charge of the lepton beam (correct, “right” charge) are required. In this region one does not rely on the background simulation and estimates the background contribution using the “wrong” charge candidates, followed by a subtraction of the *wrong charge data*. The *charge asymmetry* between the background candidates of different signs is measured using e^+p and e^-p data.

In addition, common criteria for the events are applied in the analysis, like requirement on the position of the interaction along the z -axis, requirements against non- ep backgrounds and backgrounds with specific topologies (cosmics, Compton process), etc. (for details see Section 8).

7.2 Electron Identification

In the Neutral Current analysis at high Q^2 only events with an electron scattered into the LAr calorimeter are considered. The electron identification is based solely on calorimeter information and benefits from the fine granularity of the detector. Scattered electron candidates are identified as a compact isolated energy depositions corresponding to the shape of electromagnetic shower. The electron finding procedure used in this analysis exploits the QESCAT algorithm [89].

7.2.1 Identification of the Scattered Electron

For electron identification a cone around the axis from the interaction vertex to the barycentre of the cluster is considered, with the cone vertex being 1 m in front of

the barycentre and the opening angle of 7.5° as it is shown in Fig. 7.2. The cone contains the electromagnetic section and the first layer of the hadronic section of the LAr calorimeter. All calorimetric cells with a barycentre within this cone are associated with the initial cluster.

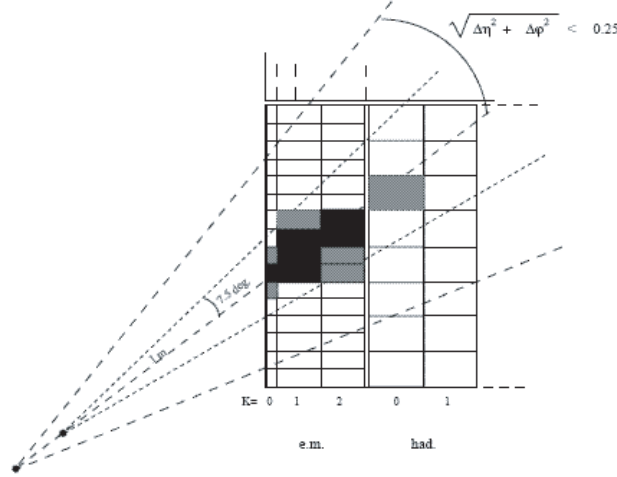


Figure 7.2: Schematic view of isolation cones used for the electron identification.

The electron candidates are identified with the QESCAT algorithm on the basis of several estimator variables, which quantify the shape and the size of the shower. These estimators are defined as follows:

- **EATOT and NCEL estimators.** The electron candidate cluster should contain a prominent energy deposition to separate it from the random noise and low energy hadrons. The EATOT estimator is true for an electron candidate with the cluster energy $E^{\text{Tot}} > 5$ GeV and the transverse momentum $P_t > 3$ GeV. The NCEL estimator is true if the cluster contains more than 3 calorimetric cells.
- **EAEM estimator.** The expected length of the electromagnetic shower from an electron candidate is relatively small compared to a hadronic shower. The variable $f_{\text{em}} = E^{\text{em}}/E^{\text{Tot}}$ is defined, where E^{em} is the energy deposited in the electromagnetic section of LAr calorimeter, and E^{Tot} is the total cluster energy. The estimator is true if $f_{\text{em}} > f_{\text{em}}^{\text{min}}(\theta)$ (for the $f_{\text{em}}^{\text{min}}(\theta)$ function see [89])
- **EATR estimator.** An expected transverse size of the electromagnetic shower should be relatively small. One defines the transverse size of the cluster $\sigma_R = \sqrt{\langle r^2 \rangle - \langle r \rangle^2}$ with the weighed averaged moments

$$\langle r^n \rangle = \omega^{-1} \sum_{\{\text{cells}\}} \omega_i r_i^n,$$

where r_i is a distance from the i -th energy deposit to the cone axis, $\omega_i = E_i/V_i$ and $\omega = \sum_{\text{cells}} \omega_i$, V_i and E_i are the volume and the energy of the i -th cell respectively. Taking the volumes into account allows to reduce an influence of the electronic noise. The moment $n = 2$ is used.

- **EAHN estimator.** The energy fraction in the hottest cells of the cluster is used as an estimator as well. One defines $f_{\text{HotN}} = E^{\text{HotN}}/E^{\text{em}}$, where E^{HotN} corresponds to energy absorbed in the group of N hottest cells of the cluster. N is equal to 4 for BBE, CB1, and CB2, 8 for CB3, FB1, and FB2, and 12 for the IF wheel. The estimator is true if $f_{\text{HotN}} > f_{\text{HotN}}^{\text{min}}(\theta)$ (for the $f_{\text{HotN}}^{\text{min}}(\theta)$ function see [89]). .
- **EAIF and EAHD estimators.** The following additional topological criteria for the scattering electron identification are used as well. In the Neutral Current event the scattered electron usually goes alone in its hemisphere, and the energy deposited by the electron in the cone around the electron should be the only energy deposited in this cone. To estimate the isolation of the electron candidate the isolation estimator is used $f_{\text{iso}} = E^{\text{Tot}}/E^{\text{iso}}$, where E^{iso} is the energy absorbed in the isolation cone around the axis from the interaction vertex to the barycentre of the cluster with the opening angle in the η (pseudorapidity)- ϕ (azimuthal angle) space of $R = \sqrt{\eta^2 + \phi^2} = 0.25$ (see Fig. 7.2). The electronic noise contribute to the energy detected in the calorimeter. Also the scattered electron could be accompanied by the final state radiation photon. So two criteria are applied
 - $f_{\text{iso}} > 0.98$ (EAIF estimator),
 - or $f_{\text{iso}} > 0.95$ and $E_{\text{had}}^{\text{iso}} < 300$ MeV, where $E_{\text{had}}^{\text{iso}}$ is the hadronic energy deposited in the isolation cone is the hadronic section but not in the electron cone (EAHD estimator).

With the QESCAT algorithm the chance for the hadron to be recognized as an electron is small [90]. Still, a candidate from the hadronic final state may fake the scattered electron. To reduce the number of such cases an isolation criteria is introduced. The candidate is marked as “isolated” if it has the highest P_t among all identified electromagnetic candidates² and the ratio of the calorimetric energy within the cone with the opening angle $R = 0.5$ in the $\eta - \phi$ space around the candidate to the candidate energy is less than 1.03. In the analysis the isolation criteria is used in addition to the QESCAT for the electron candidates with the energy above 8 GeV. For energy below 8 GeV electron candidate with the highest P_t is considered as a scattered electron.

7.2.2 Efficiency of the Scattered Electron Identification

As it was discussed above the electron identification is based on shower shape estimators to distinguish the scattered electron from the hadronic activity. To study an efficiency of this procedure, an independent track-based electron finder [91] is used.

The track-based electron finder is looking for isolated tracks within an isolation cone of radius $R_{\eta-\phi} = 0.5$ around the line from primary vertex to the cluster in the LAr calorimeter with a track transverse momentum $P_t > 1.2$ GeV. The main part of the calorimetric energy inside the cone is required to be compactly deposited in the electromagnetic part of the calorimeter. In addition a momentum-energy matching

²Therefore only one “isolated” electron candidate is chosen in the event.

between the track and the cluster is required. The track based electron finder has an efficiency of about 0.95. Therefore in this analysis it is used for the monitoring purposes only.

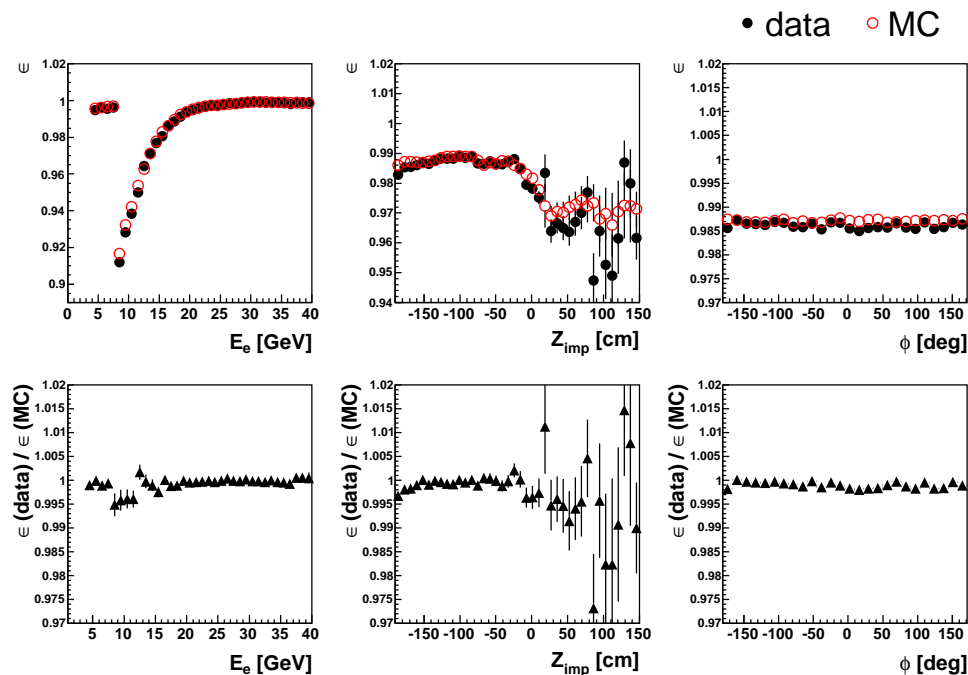


Figure 7.3: Efficiency of the electron finding as a function of E_e , Z_{imp} and ϕ for the whole HERA II statistics. For the $\varepsilon(Z_{\text{imp}})$ efficiency all the events with $Z_{\text{imp}} > 150$ cm are accumulated in the last bin.

The scattered electron identification efficiency determined using the track-based electron finder is shown in Fig. 7.3 for data and simulation as a function of the scattered electron energy E_e , impact position of the electron on the surface of the LAr calorimeter³ Z_{imp} and the polar angle ϕ_e . Generally the inefficiency is small everywhere except the region of small energies of the electron candidate, where the isolation criteria degrades the efficiency for $E_e > 8$ GeV. In the vicinity of the z - and ϕ -cracks of the LAr calorimeter the electron identification is also less efficient. In these regions the electron has to pass dead materials like supporting structures of the calorimeter. Furthermore in the ϕ -cracks and in the z -crack between the CB1 and CB2 wheels, the electron may enter the hadronic section of the LAr calorimeter escaping energy deposition in the electromagnetic part. This doesn't allow a recognition of the scattered electron as an electromagnetic candidate with the QESCAT algorithm. Therefore the CB1-CB2 z - and ϕ -cracks regions have been excluded for the cross section measurements.

In the remaining fiducial volume the electron identification efficiency for the data is described by the simulation within the statistical uncertainty. No time variations of the electron identification efficiency is observed. The statistics of the monitor sample is high for the region of $Z_{\text{imp}} < 0$ cm, where the tracks are reconstructed

³See Section 7.4.1.

with the CJC chamber information. To gather enough statistics at higher Z_{imp} all HERA II periods were added.

The systematic uncertainty on the electron identification is taken to be 0.2% for $Z_{\text{imp}} < 20$ cm for the Nominal part of the analysis and 0.5% for the HighY part of the analysis and 1% for $Z_{\text{imp}} > 20$ cm.

7.3 Electron Energy Measurement

For the NC measurement precise reconstruction of the scattered electron energy plays a crucial role. The reconstructed Q^2 variable is proportional to the electron energy, as well as $(E - P_z)$ at low and moderate y (see Section 5.1).

To calibrate the electron energy both in data and Monte Carlo, the double angle (DA) method of the reconstruction is used. As it was discussed, this method relies on the measured angles of the scattered electron and the hadronic final state as well as on the well known initial beam energies. Comparing the measured energy of the calorimetric cluster and the energy estimation from the DA method, one calibrates the calorimeter electromagnetic energy scale. The agreement between energy scales in data and simulation is shown in Fig. 7.4 as a function of the Z_{imp} variable.

The electromagnetic calibration is provided separately for data and MC for each data period.

7.3.1 Electron Energy Calibration

The electron energy calibration is performed using the NC event selection (see Section 8) with the following additional selection criteria which ensure a good performance of the DA method

- $E_e > 14$ GeV.
- $y_\Sigma < 0.3(0.5)$ for $Z_{\text{imp}} \leq 20$ cm ($20 < Z_{\text{imp}} < 100$ cm) and $\gamma_h > 10^\circ$.
- $44 < E - P_z < 66$ GeV.
- Exclude z and ϕ cracks in LAr calorimeter: $15 < Z_{\text{imp}} < 25$ cm, $|\phi_e - 45^\circ \cdot n| < 2^\circ$, $n = 0, \dots, 7$.

The mean values of the E_e/E^{DA} ratio are taken as the energy calibration factors. In order to reduce the influence of tails in the distributions, only events within the “calibration window” $0.85 < E_e/E^{\text{DA}} < 1.15$ are considered to get mean values.

During the calibration, the shape of the E_e/E^{DA} distributions could change which could lead to changes in the mean values of the distributions. For this reason the calibration is done iteratively as a two stage process after smearing of energy in MC (see Section 7.3.2)

- The wheel- and octant-wise calibration. For each octant of the barrel wheels BBE, CB1, CB2, CB3 and each forward wheel FB1 and FB2 one average calibration factor is derived.

- The z -wise calibration. The calibration factors determined in bins of Z_{imp} . The size of the bins is 1 cm for $Z_{\text{imp}} < 0$ cm, 10 cm for $0 \leq Z_{\text{imp}} < 90$ cm, 20 cm bins for $90 \leq Z_{\text{imp}} < 110$ cm and 50 cm bins for $Z_{\text{imp}} \geq 110$ in order to keep number of data events approximately the same for all bins.

These steps are iteratively repeated with narrowing of the “window” to $0.9 < E_e/E^{\text{DA}} < 1.1$.

After this procedure the fine ϕ -wise calibration is applied. It is derived for bins in ϕ of the electron cluster for each of the BBE, CB1, CB2-IF regions. The necessity of this additional correction is shown on Fig. 7.5 where the ϕ dependence of the energy scale for data and simulation is presented before and after the ϕ -wise calibration.

As the last step, in the region $-190 < Z_{\text{imp}} < -189$ (BBE part), the energy was corrected period-wise to about 2% in data and 1% in MC to compensate the slight discrepancy in the shapes of the E_e/E^{DA} distributions.

The results of the calibration on the NC sample for one period extracted with the wide “window” ($0.85 < E_e/E^{\text{DA}} < 1.15$) are presented on Fig. 7.4a, b. To check the calibration in the forward region the whole data sample was needed to reach statistical precision of one per cent, the result is shown in Fig. 7.4c.

7.3.2 Electron Energy Resolution

The energy resolution of the LAr calorimeter for the electromagnetic showers has been determined at CERN [46] test beam to be

$$\sigma(E)/E = 12\%/\sqrt{E/[\text{GeV}]} \oplus 1\%.$$

The electron energy resolution as a function of Z_{imp} determined using a root mean square of the ratio E_e/E^{DA} is shown in Fig. 7.6. For the NC event selection it is typically 4-6%. The resolution degrades at a z -cracks and reaching values of 8%. To improve the description of the resolution an additional energy smearing in MC is applied using a Gaussian function with $\sigma_{\text{smear}} = \sqrt{\sigma_{\text{Data}}^2 - \sigma_{\text{MC}}^2}$. This difference is determined for each z bin used in the z -wise calibration. Fig. 7.6 shows the resolution before and after this additional smearing. After smearing the simulation follows data very well.

7.3.3 Check of the Calibration with the Compton Events

The electromagnetic energy scale calibration was performed at high scattered electron energies. To verify calibration at low energies of the scattered electron a sample of the QED Compton events has been used. The whole HERA II data set was used to increase the statistical precision of the verification.

The topology of the QED Compton events is distinct and very different from the NC’s one. These events are characterized by two back-to-back electromagnetic clusters, one from the scattered electron with associated track and the other from a photon without a track, with no any other activity in the event.

These properties are utilized in the selection of the QED Compton events:

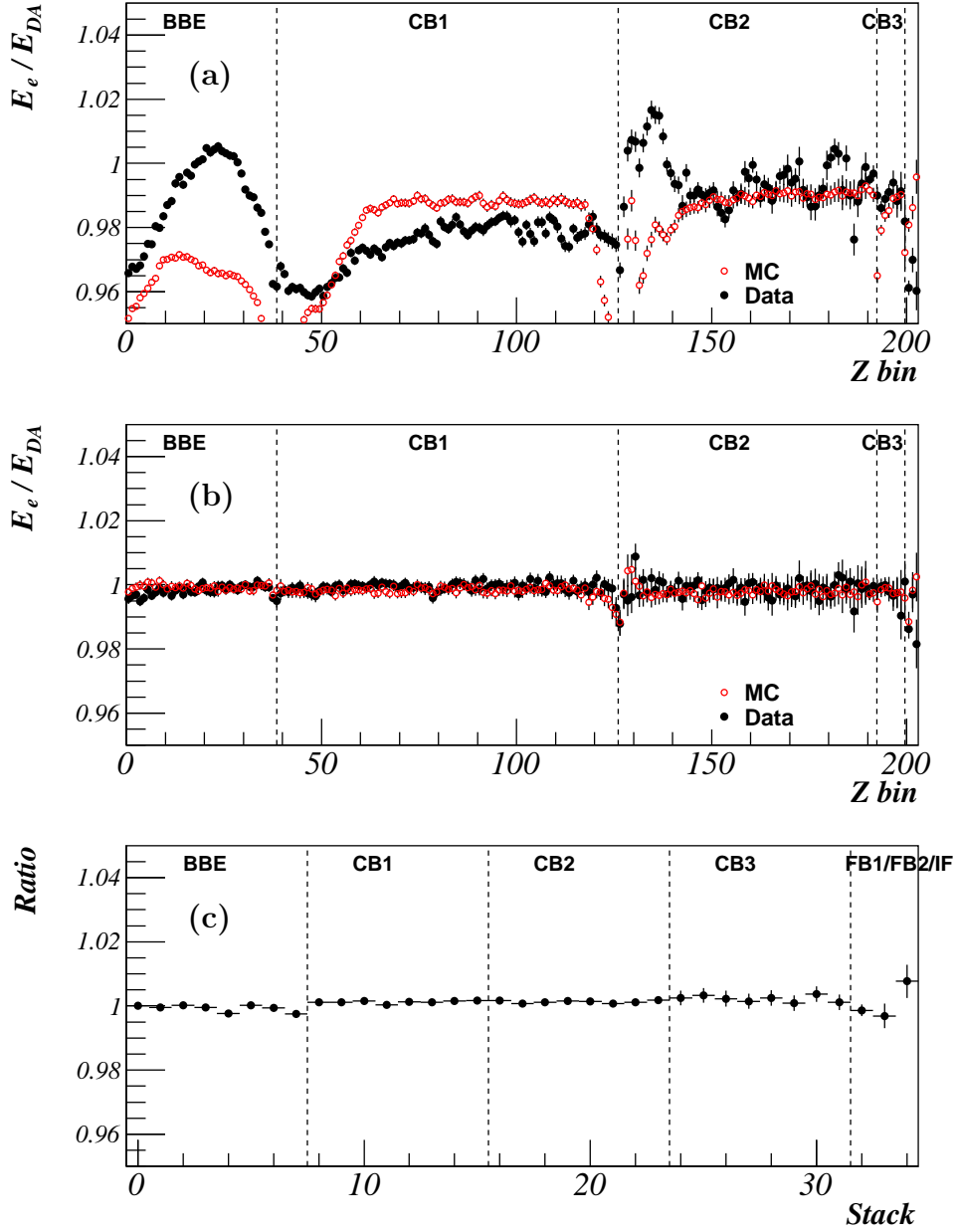


Figure 7.4: The mean of E_e/E^{DA} ratio extracted in Z_{imp} bins (a) before and (b) after the electromagnetic calibration for the Per0607RH period. (c) The double ratio $(E_e/E^{DA})_{data}/(E_e/E^{DA})_{MC}$ of the data to simulation is shown for entire HERA II data set as a function of the calorimetric stack number.

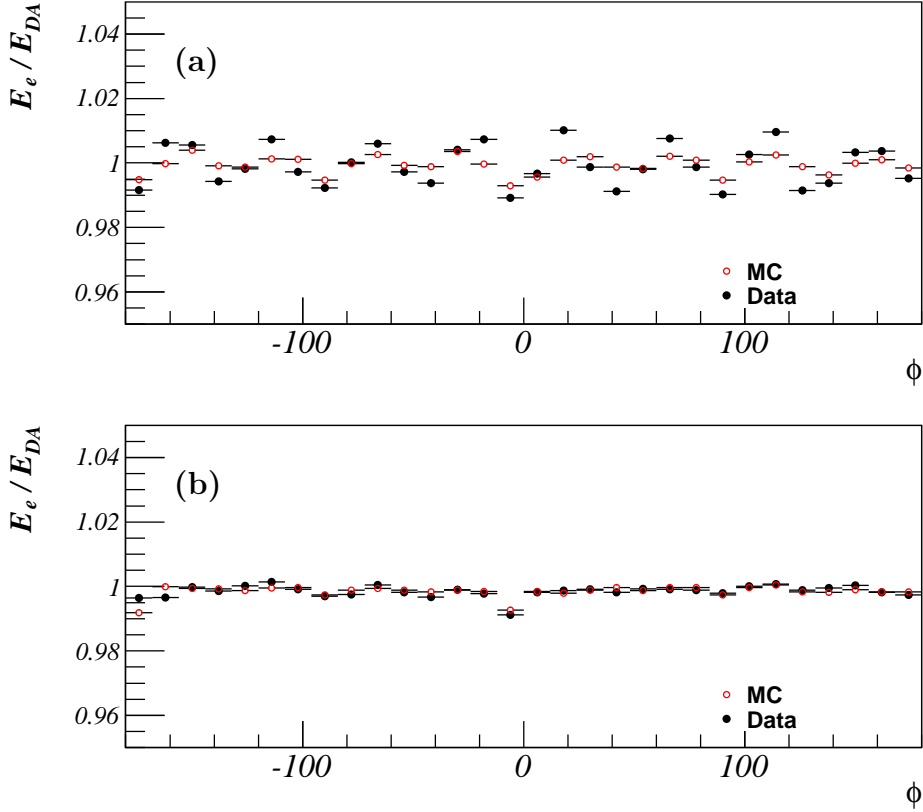


Figure 7.5: The mean of E_e/E^{DA} ratio determined in the ϕ bins after the wheel-octant-wise and z -wise calibrations **(a)** before and **(b)** after the ϕ -wise calibration.

- Number of electromagnetic candidates is two or three. The third candidate occurs in the case of hard radiation from the scattered electron.
- Accomplanarity, the ϕ angle between the first two electromagnetic candidates, is more than 160° .
- Number of reconstructed tracks is less than 3.
- Energy from hadrons is less than 1 GeV.
- Energy summed over muons is less than 1 GeV.
- Exclude z and ϕ cracks in LAr calorimeter: $15 < Z_{\text{imp}} < 25$ cm, $|\phi_e - 45^\circ \cdot n| < 2^\circ, n = 0, \dots, 7$.
- Background finders against halo and cosmics are applied.

The Compton sample is divided into two parts: scattered electron energy $E_e \in [6, 11]$ GeV and $E_e \in [11, 20]$ GeV. For these samples the $E_t^{\text{clus}}/P_t^{\text{track}}$ ratio of an electron transversal momentum calculated with the energy and position of the cluster (E_t^{clus}) and the same quantity calculated with the track information (P_t^{track}) is presented in Fig. 7.7. It shows a good agreement between data and MC. The first sample contains 270 data events under the peak and the peak values of the $E_t^{\text{clus}}/P_t^{\text{track}}$ distributions determined in Gaussian fits of the region $[0.9, 1.1]$ are 1.032 ± 0.005 for

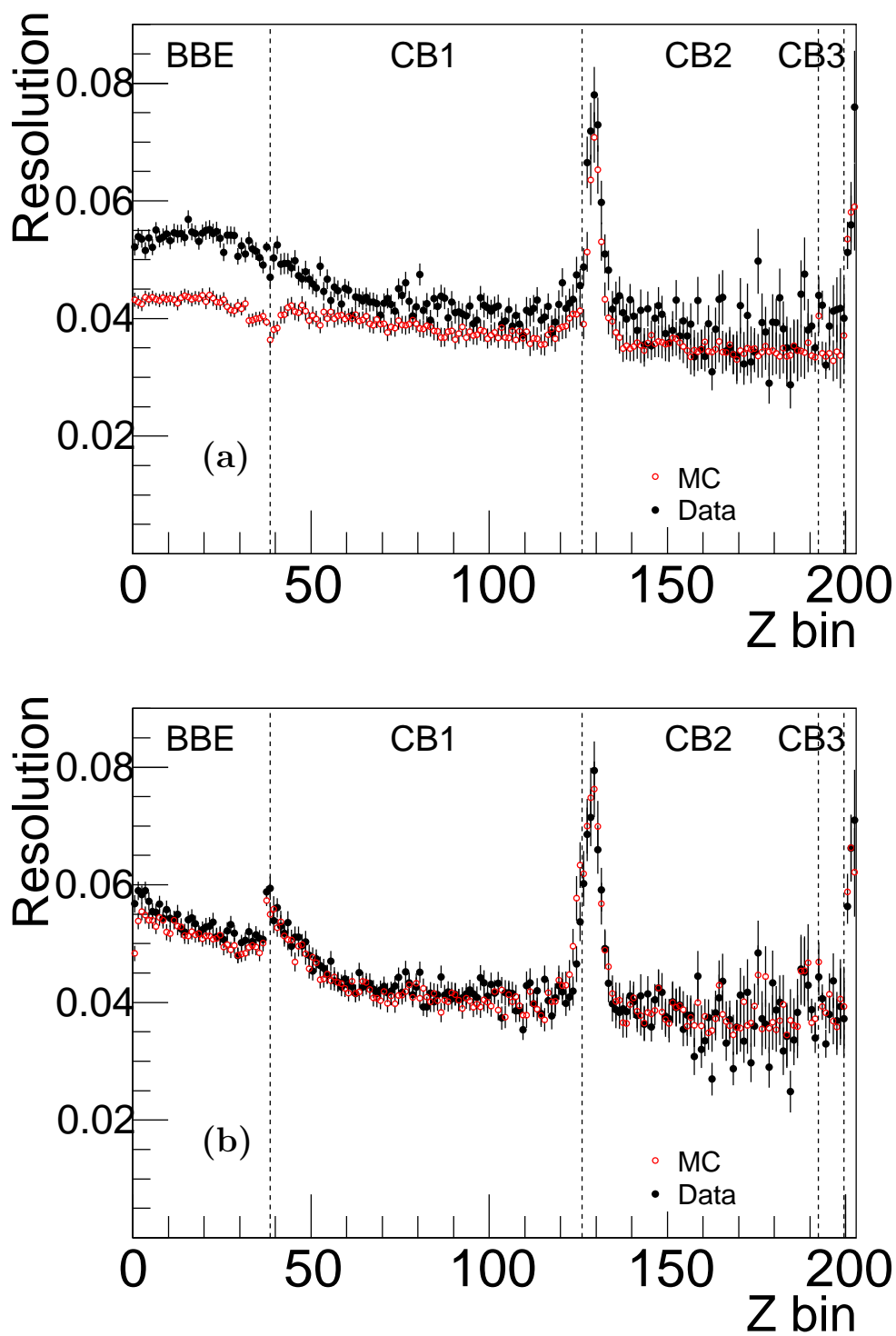


Figure 7.6: The resolution of the electron energy measurement as a function of z -position of the impact point (a) before and (b) after the Gaussian smearing of the energy in a simulation.

data and 1.030 ± 0.001 for simulation. The second sample contains 550 data events and the peak values are 1.031 ± 0.004 for data and 1.023 ± 0.001 for simulation.

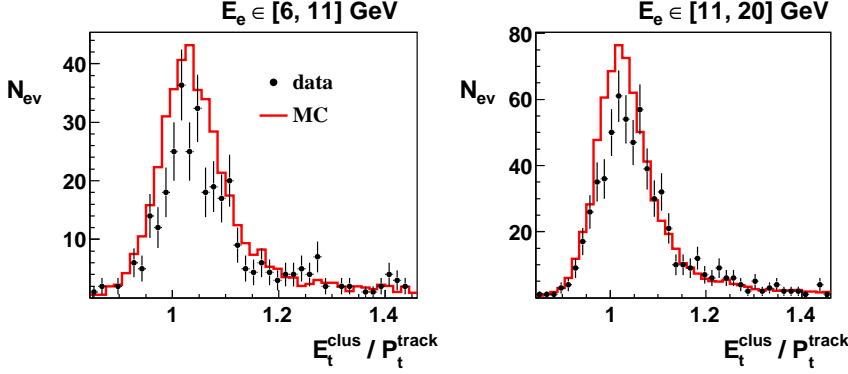


Figure 7.7: The $E_t^{\text{clus}}/P_t^{\text{track}}$ ratio for the sample of Compton events for **(left)** $E_e \in [6, 11]$ GeV and **(right)** $E_e \in [11, 20]$ GeV.

7.3.4 Electron Energy Scale Uncertainty

From the presented investigations the uncorrelated part of the uncertainty on the electron energy scale is estimated as shown in Table 7.1.

LAr part	BBE	CB1	CB2	CB3	FB+
Uncorrelated Unc. [%]	0.5	0.3	0.5	0.5	1.0

Table 7.1: The uncorrelated part of the electron energy scale uncertainty.

In addition at low electron energy $E_e < 11$ GeV, uncorrelated uncertainty of 0.5% related to possible deviations from a linearity of the electron energy response in the LAr calorimeter is added to other uncorrelated uncertainties in quadrature. This uncertainty estimation is based on the check of the calibration in Section 7.3.3.

A possible bias due to usage of the double angle method for energy calibration is taken into account in a correlated part of the uncertainty and is estimated to be of 0.5%. It was estimated from the ratio of a reconstructed electron energy using double angle method to a generated electron energy in simulation, $E^{\text{DA}}/E^{\text{gen}}$, shown in Fig. 7.8.

7.4 Electron Angles Measurement

A measurement of the polar angle of the scattered electron, Θ_e , is needed for calculation of the NC kinematic variables. It could be taken from the reconstructed track associated with the scattered electron (if it is reconstructed) or be calculated from the LAr calorimeter cluster position and position of the primary interaction vertex, measured using the tracker information. Below the track and vertex reconstruction

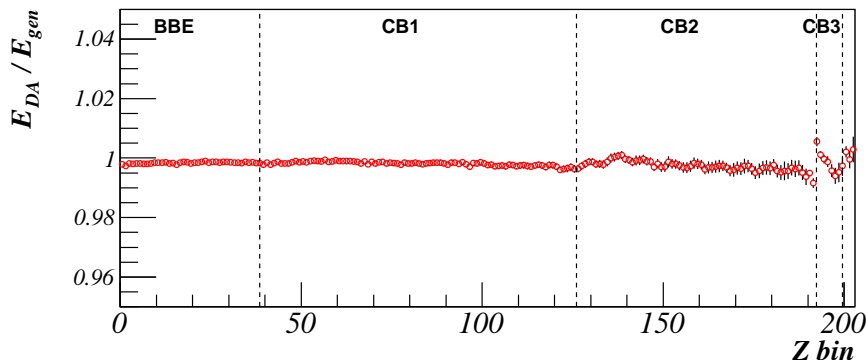


Figure 7.8: The $E^{\text{DA}}/E^{\text{gen}}$ ratio as a function of the Z_{bin} for the e^+p data set.

procedure as well as the precision of the angles measurement of the scattered electron are discussed.

For the polar angle measurement the vertex-cluster information is used for the reasons given below. For the azimuthal electron angle ϕ_e determination the tracker measurement is preferred if the track's quality satisfies the so-called LeeWest conditions [92] and the vertex position is not changed in the OptimalNC vertex procedure (see Section 7.5.1). Otherwise the vertex-cluster measurement is used. For selected in the analysis events in about 95% cases the tracker information is used for the azimuthal angle determination. Because of the design of the track detectors, the tracker resolution of the ϕ_e measurement is much better than the vertex-cluster one.

An uncertainty on the polar angle measurement is discussed in Section 7.4.4. The detector has an approximate axial symmetry such that the cross section measurement is almost not sensitive to the ϕ_e measurement, therefore no additional uncertainty due to the azimuthal angle determination is needed.

7.4.1 Track Reconstruction

For an ideal tracking detector with homogeneous magnetic field \mathbf{B}_z (magnetic field in z direction) the track parametrization is a helix with five parameters: the curvature κ , the distance d_{ca} and the angle ϕ_0 at the point of closest approach to the axis, the intercept z_0 and the slope parameter $\tan \lambda = \cot \Theta$ [93]. The helix is presented by the circle in the $r\phi$ plane

$$\frac{1}{2}\kappa(x_i^2 + y_i^2 + d_{\text{ca}}^2) - (1 + \kappa d_{\text{ca}})(x_i \sin \phi_0 - y_i \cos \phi_0) + d_{\text{ca}} = 0, \quad (7.1)$$

and by the straight line in the sz plane

$$z_i = z_0 + \tan \lambda \cdot s_i, \quad (7.2)$$

where index i enumerates detector planes at which the track measurement occurred, and s is the track length in Oxy (or, the same $r\phi$) plane. The track's curvature, strength of the magnetic field and the particle's transverse momentum are related via

$$P_t [\text{GeV}/c] = \frac{0.3 \cdot B_z [\text{T}]}{\kappa [\text{m}^{-1}]}. \quad (7.3)$$

Various effects can result in deviation from the ideal helix trajectory such as multiple scattering deflections, field inhomogeneity and continuous energy loss along the trajectory. To take this possible deviations into account the broken line fit technique [93, 94] is implemented for the track reconstruction.

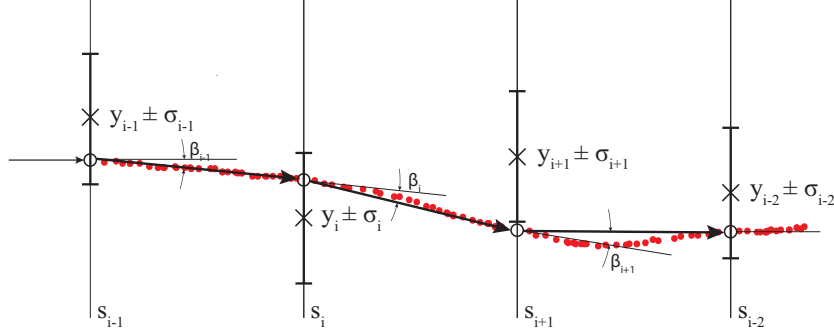


Figure 7.9: Particle trajectory in sz plane.

In Fig. 7.9 a particle trajectory in sz plane is shown. Without multiple scattering it should be a straight line (see (7.2)), and in presence of multiple scattering the trajectory has kinks. Vector $\{y_i\}$ presents the measured coordinates at detector planes with the uncertainties $\{\sigma_i\}$. Vector $\{\beta_i^{sz}\}$ presents the kink angles at which the particle deviates after each detector section. The variations $\{\sigma_{\beta^{sz},i}^2\}$ of the deviations between the i^{th} and $(i+1)^{\text{th}}$ planes due to multiple scattering are estimated from the amount of the material between planes, particle momentum, and velocity [32] obtained from a rough fast helix fit using preselected hits [95]. Vector $\{u_i\}$ presents the estimation of the z coordinates, where the particle actually crossed the detector planes. The values of β_i^{sz} and u_i, s_i are related as

$$\beta_i^{sz} = \frac{u_{i-1} - u_i}{s_i - s_{i-1}} - \frac{u_{i+1} - u_i}{s_{i+1} - s_i}. \quad (7.4)$$

In given notation the track reconstruction in the sz plane with n hits is the result of the minimization of the function $S[\mathbf{u}]$

$$S[\mathbf{u}] = \sum_{i=1}^n \frac{(y_i - u_i)^2}{\sigma_i^2} + \sum_{i=2}^{n-1} \frac{(\beta_i^{sz})^2}{\sigma_{\beta,i}^2} \xrightarrow{\mathbf{u}} \min \quad (7.5)$$

with respect to the values $\{u_i\}$. For the reconstruction in the $r\phi$ plane the same form of the minimization function is used with a correction of the kink angles for the influence of magnetic field

$$\beta_i^{r\phi} = [\dots] + (a_{i-1} + a_i) \frac{\Delta\kappa}{2}, \quad (7.6)$$

where a_i is the distance between the points i and $(i+1)$, and $[\dots]$ presented by the same expression as β_i^{sz} in (7.4), but for the discrepancies and kinks in the $r\phi$ plane⁴.

⁴In the latter case the curvature κ is an unknown and should be included to the set of the parameters for minimization: $S[\mathbf{u}, \kappa] \rightarrow \min$.

Because of the special form of the function (7.5) to be minimized, the procedure can be reduced to the solution of the equation of the form $C_{\mathbf{u}}\mathbf{u} = \mathbf{r}$, where $C_{\mathbf{u}}$ is a band symmetric matrix. This problem is solved with the Cholevsky decomposition in $\mathcal{O}(n)$ operations⁵.

In this fit the track parameters are extracted with the covariance matrix at each point of the trajectory.

Reconstruction of the tracks in H1 experiment starts from basic initial track finding with CJC hits, supplemented by FST and BST tracks. Using various methods [95] all CJC hits either are associated with tracks or removed as a noise, and the rough parameters of potential tracks are provided. Then the accurate parameters of the tracks with the procedure described above are estimated.

After the track reconstruction with the CJC information, the additional (precise) hits from CIP, COZ, and CST detectors are added and the fit is repeated.

To compare the tracker measurement with the calorimeter information, the track can be extrapolated to the surface of the calorimeter, approximated by octagon (for CB and FB) or 16-fold polygon (for BBE) with an inner radius of 105 cm. The z coordinate of the intersection of the extrapolation and the reference surface, Z_{imp} , is called z impact position. In the case when particle enters BBE through the front face of the BBE wheel, and not touching the CB wheel, the z impact position is set to $Z_{\text{imp}} = -152.5$ cm.

7.4.2 Vertex Reconstruction, DTRA and DTNV Tracks

The reconstructed tracks are used to determine position of the primary interaction vertex (x_v, y_v, z_v) and the time T_0 [95], when the interaction took place.

As a first step primary weight w_p , dependent on d_{ca} , radius of the first hit and track length is assigned to each track. Using median method central z_0 , T_0 values within acceptable ranges are determined on the basis of the w_p 's. On the basis of this selection the most populated cluster of z_0 values is determined and the tracks from this cluster are re-fitted in the $s - z$ and $r - \phi$ planes with additional constraint on a common vertex. Tracks which do not fit to this vertex candidate are removed from the vertex fit. Finally the T_0 is determined as the weighted mean over accepted primary tracks.

An outcome of the vertex-unconstrained fits are DTNV tracks. The vertex-constraint fits provide DTRA tracks⁶. A vertex name convention include the name of tracking device which provided the most precise information for this vertex reconstruction: mainly CJC, but also FTD, BST, FST vertices are possible. A DTNV vertex corresponds to a point of the closest approach on the beam line of a DTNV track propagated to the beam line.

7.4.3 Alignment of the LAr Calorimeter

To provide a measurement which exploits an information from both CTD and the LAr calorimeter, the relative alignment of these detectors has to be performed. For

⁵For the $r\phi$ plane the procedure is the same with minor technical complications.

⁶Notation DTRA and DTNV correspond to data banks where the relevant track information is stored.

this the scattered electrons from the NC sample are used. Electron tracks with COZ and CST hits which improve a precision in z , are propagated to a surface of the calorimeter. Track impact positions are compared then with positions of electron cluster projected to the calorimeter surface. Global fit is performed to minimize a difference in positions. In the fit the LAr calorimeter is allowed to move and rotate along all three spatial axis. In addition for each calorimeter wheel (BBE, CB1-3, FB) a shift along z direction is allowed. The procedure takes into account the calorimeter shrinkage due to cooling from room temperature down to 72° K of liquid argon. In total 10 parameters describe position of the calorimeter wheels [96].

An influence of the alignment on the measurement of the polar and azimuthal angles is shown in Fig. 7.10.

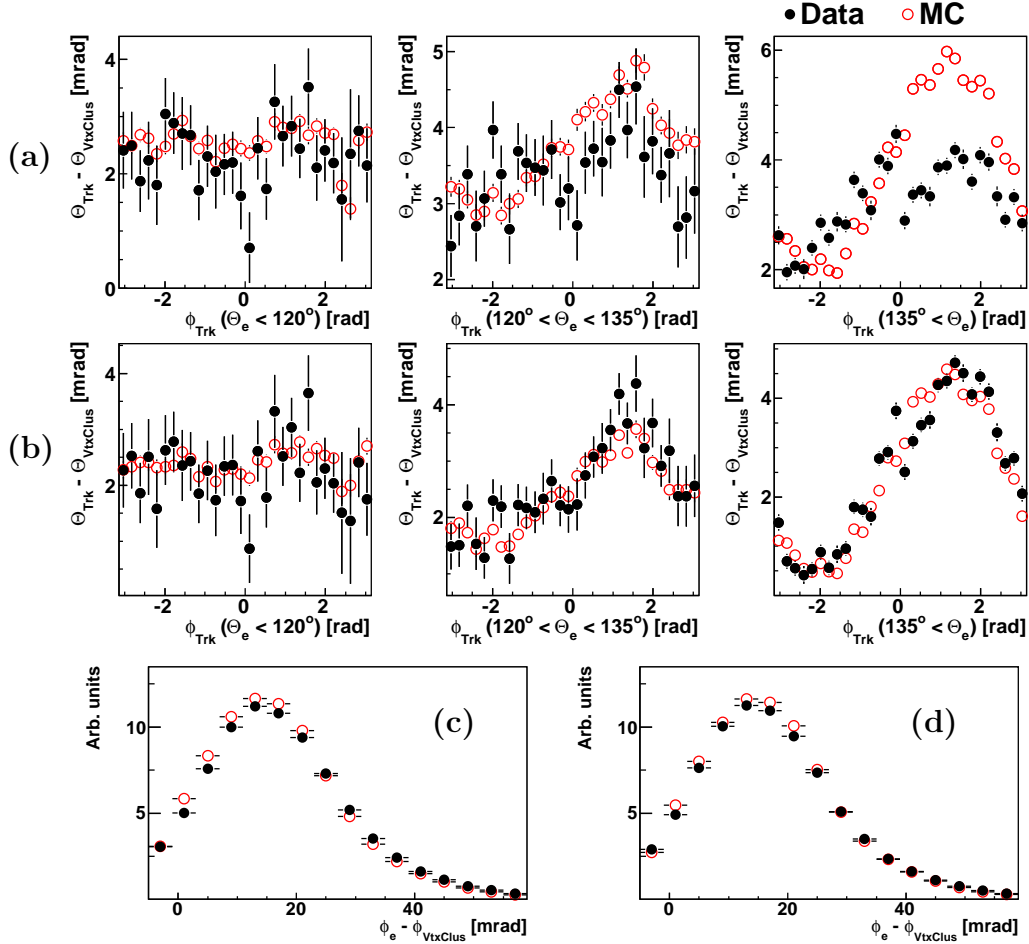


Figure 7.10: **(a, b)**: Difference between the scattered electron polar angle taken from the reconstructed track and from the straight line between the primary vertex and the electron cluster as a function of ϕ_e in different parts of the detector (a) before and (b) after the alignment of the LAr calorimeter. **(c, d)**: Distribution of the difference of azimuthal angles taken from the reconstructed track and a straight line between the primary vertex and the electron cluster (c) before and (d) after the alignment.

Beam Tilt Correction

The z -axis of the H1 coordinate system is not exactly a direction of the electron and proton beams. The beams have small inclination, the so-called “beam tilt”, of about 1 mrad. Beam tilt is accurately measured for each run. In the calculation of the polar and azimuthal angles of the scattered electron within the H1OO software a correction for the beam tilt is applied.

7.4.4 The Polar Angle Measurement

The best measurement of the polar angle of the scattered electron, in principle, is provided by the tracker. But in the H1 experiment the quality of the data from the tracker (and even the set of the tracking devices) and corresponding uncertainty on the tracker measurement vary considerably with the time. For example CST and FST information is not available for the Per06em period. Therefore, the polar angle, Θ_e , is taken from the electron cluster position and the primary vertex position. This measurement is stable over time.

An estimation of the uncertainty on the Θ_e measurement in the track detector is done comparing tracks reconstructed using CJC hits only and the same tracks reconstructed using CJC and CST hits. The CST hits provide an accuracy much better than 1 mrad, but they are available only for part of tracks. During reconstruction both track parametrizations are available and the comparison provides an estimation of the uncertainty for the whole set of CJC tracks. The discrepancy between these two parametrizations in the slope parameter $\tan \lambda$ (this parameter corresponds to the track’s Θ) is shown in Fig. 7.11 as a function of Θ . The blue lines show the effect of 1 mrad shift of the CJC track’s Θ . From this plot the uncertainty of the Θ track measurement in the tracker is considerably better than 1 mrad.

To estimate an uncertainty of the polar angle measurement from the cluster and vertex positions, Θ_{VtxClus} , the differences between the angle measured in the tracker, Θ_{Trk} , and Θ_{VtxClus} are compared for data and simulation (see Fig. 7.12).

The shapes of the distributions are very similar and the mean values, extracted from the Gaussian fits in the central regions of the distributions, are within 1 mrad. The uncertainty on the scattered electron polar angle measurement is taken to be 1 mrad.

7.5 Primary Interaction Vertex

For the reconstruction of the NC event kinematics a position of the primary interaction vertex should be measured. This information together with the measurement of the scattered electron cluster position gives the scattering angle Θ_e . The vertex position is also needed to measure polar angles of hadronic final state particles (which in turn give the values of Σ and P_t^{had}) using the HFS calorimetric measurement. Requirement on the interaction vertex to be within certain interval around the nominal vertex position improves quality of kinematics reconstruction and reduces a non- ep -collision background.

The output of the tracks reconstruction procedure is the sets of the DTRA and DTNV tracks and the primary interaction vertices (CJC, FST, BST, FTD) obtained

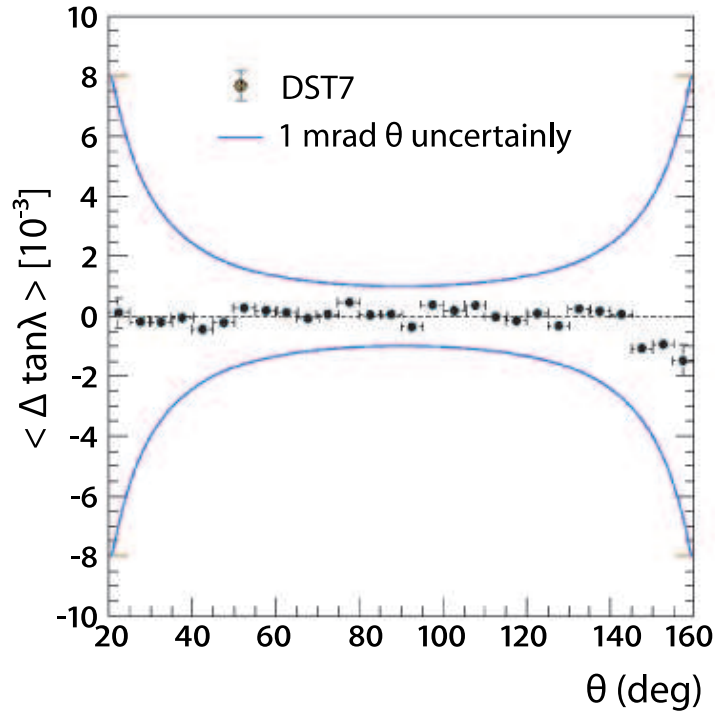


Figure 7.11: Comparison of the slope parameter $\tan \lambda$ obtained in the track reconstruction with the CJC hits only and in the reconstruction with the CJC and CST hits. The effect of 1 mrad shift of the track's Θ is shown by the blue line. The e^+p data sample is used, obtained in the year 2007 [95].

in the vertex fits (see Section 7.4.1). In some cases these vertices appear to be reconstructed very far away from the true primary ep collision position. This happens in the ep collisions at high x where the hadronic final state goes at small angle along the beam and interacts with the beam pipe or collimators. These secondary interactions in the forward part of the detector with high track multiplicity are sometimes taken as a primary interaction. A typical event of this kind is shown in Fig. 7.13. From the point of view of the tracks reconstruction program this case is indistinguishable from the case of the normal ep interaction in the forward part of the detector because tracker can't recognize the scattered electron.

For such events with wrongly reconstructed vertex the kinematics is spoiled completely. There is a danger also that these events will be lost because of the cut on the interaction vertex position. For these reasons one has to recognize such events and optimize an estimation of the interaction vertex position. At the higher level of the analysis the scattered electron information can help to distinguish and measure the true vertex position.

The corresponding procedure is called the NC Optimal Vertex. It is described below. It helps to measure correct primary vertex position, to recover kinematics, and to improve efficiency to find vertex from 90% [88] to almost 100%, and therefore to reduce the associated uncertainty.

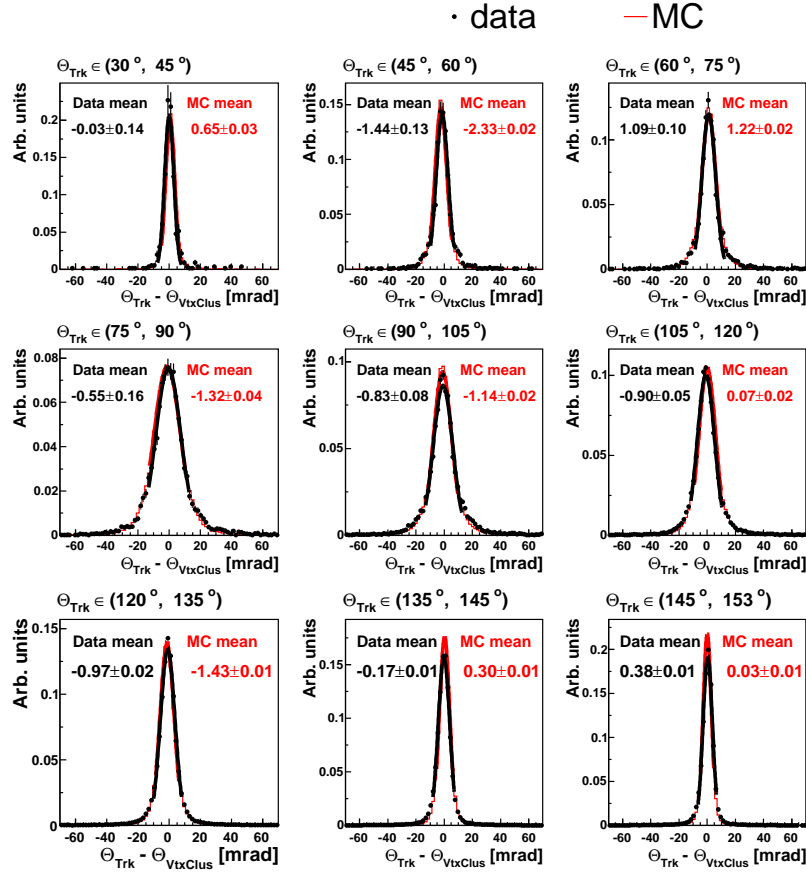


Figure 7.12: Difference between the polar angle measurement of the scattered electron from the track reconstruction and from the cluster and vertex positions in bins of Θ_{Trk} . The mean values are determined using Gaussian fits and shown in the plots on left for data and on right for simulation with the statistical uncertainties from the fits. The comparison is presented for the Per0607 period.

7.5.1 The NC Optimal Vertex

The NC optimal vertex approach is making use of information from the scattered electron candidate and aims for the best estimation of the primary interaction vertex position, $Z_{\text{OptimalNC}}$, and validation of the scattered electron measured in the calorimeter with the tracker information. For that the following information in general is available:

- The electron cluster. An identification efficiency for the scattered electron is very high (see Section 7.2) if the electron is in acceptance of the LAr calorimeter. The cluster position provides a good estimation of the position of the electron entry point on the surface of the calorimeter.
- The DTRA track linked to the electron cluster (see Fig. 7.14a). This track fitted to the reconstructed primary interaction vertex provides reliable estimation of the electron properties and indicates that one can trust the reconstructed vertex position, if the track points to the electron cluster.

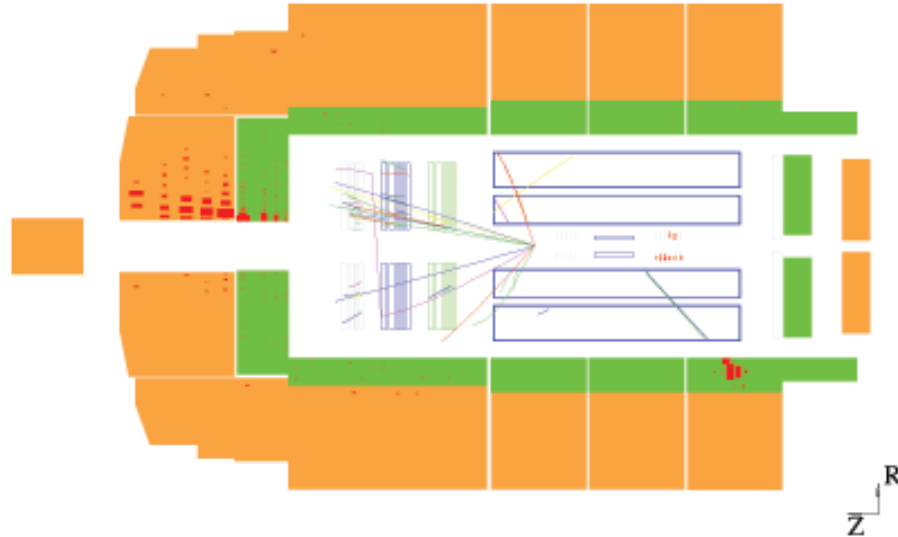


Figure 7.13: Example of the DTNV event. The scattered electron gives an isolated cluster of high energy in the calorimeter and a DTNV track. The HFS interacts with the beam pipe downstream to the proton beam direction providing multiple tracks and a fake primary vertex.

- The DTNV track linked to the electron cluster (see Fig. 7.14b). This track provides unbiased (but not the most precise) and robust estimation of the electron properties. The DTNV vertex is the point on the beam line most close to the propagation of the DTNV track to the beam line. The distance d_{ca} of the closest approach of this propagation to the beam line should be reasonably small: $d_{ca} < 2$ cm.
- The CJC vertex obtained in the vertex fit. It is the best estimation of the vertex position if it is not spoiled by the secondary interactions.
- The CIP hits. They can help for the electron verification if the electron track is completely lost (neither DTRA, nor DTNV electron tracks are reconstructed).

In general, the CJC vertex obtained in the vertex fit, which involves all reconstructed tracks in the event, is the best estimation of the primary vertex position. Therefore, if the vertex fit has converged and the DTRA track associated with the scattered electron points to the electron cluster in the LAr calorimeter, the vertex position is taken from the vertex fit. The matching between the DTRA track and the electron cluster is illustrated in Fig. 7.14a. If the distance D_{DTRA} is below 12 cm (12 cm is a characteristic size of a calorimetric cell in the LAr calorimeter), the electron cluster is considered to be validated by the DTRA track and the event is classified as Optimal—DTRA with $z_{\text{OptimalNC}} = z_{\text{CJC}}$.

If the vertex fit has failed or there is no DTRA track pointing to the electron cluster, a DTNV track pointing to the electron cluster within 12 cm, see Fig. 7.14b, is considered. If there is the DTNV vertex (and the CJC vertex is not constructed) and

the DTNV track, the event is classified as Optimal—DTNV with $z_{\text{OptimalNC}} = z_{\text{DTNV}}$. If the CJC vertex is available, the choice of the primary vertex relies on the analysis of the CJC and DTNV vertex positions.

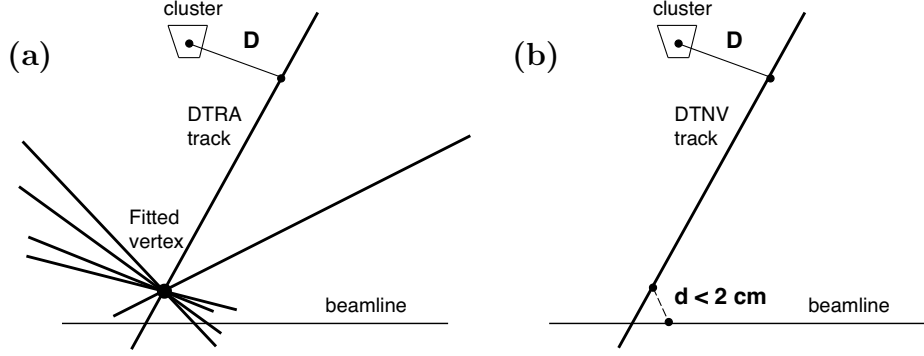


Figure 7.14: Schematic view of the (a) DTRA and (b) DTNV tracks, vertex and cluster with the essential parameters definition.

The CJC and DTNV vertices distributions for the cases, where the CJC was reconstructed but the DTRA track is missed, are shown in Fig. 7.15 together with the difference between these two. The CJC vertex has a big non-physical “tail” at large values of the Z_{CJC} . At the same time the DTNV vertex distribution demonstrates a good agreement between data and MC and follows the profile of the proton bunch.

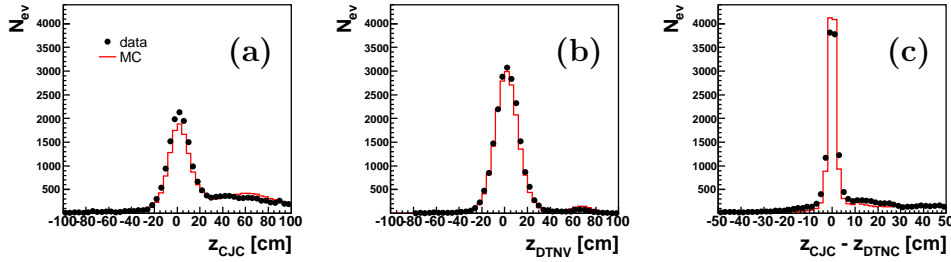


Figure 7.15: Distributions of the vertex z position of the (a) CJC vertices, (b) DTNV vertices and (c) difference between them for events without DTRA track pointing to the electron cluster.

The distributions for the CJC and DTNV vertices for different regions of the $\Delta Z_{\text{CJC-DTNV}} = Z_{\text{CJC}} - Z_{\text{DTNV}}$ distribution are shown in Fig. 7.16. In the case when the CJC and DTNV vertices are close, $-10 < \Delta Z_{\text{CJC-DTNV}} < 10$ cm (“central” region of $\Delta Z_{\text{CJC-DTNV}}$ distribution, Fig. 7.16 b, e) both vertices demonstrate good agreement between data and MC and centered around zero. Here one assumes that the vertex fit provides the right vertex position, and $Z_{\text{OptimalNC}} = Z_{\text{CJC}}$ is taken.

If the distance between the CJC and DTNV vertices is more than 10 cm, we generally rely on the DTNV vertex, and suppose that the CJC vertex was constructed with the tracks from the secondary interaction of the HFS particle with the beam

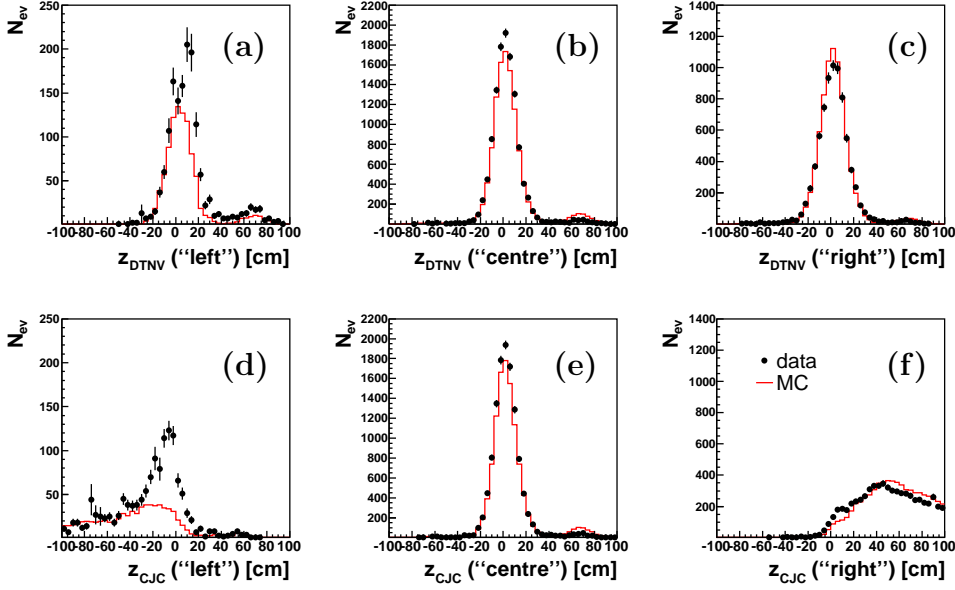


Figure 7.16: Distributions of the CJC and DTNV vertices for the different regions of the $\Delta Z_{\text{CJC-DTNV}}$ variable.

pipe. The region of $\Delta Z_{\text{CJC-DTNV}} > 10$ cm (marked as “right”, Fig. 7.16 c, f) is populated with the events where these nuclear interactions occurred. The CJC vertex is completely spoiled while DTNV vertex demonstrates good agreement between data and MC and peaks around zero. In this region one takes $Z_{\text{OptimalNC}} = Z_{\text{DTNV}}$.

In the region of $\Delta Z_{\text{CJC-DTNV}} < -10$ cm (marked as “left”, Fig. 7.16 a, d) if the DTNV vertex is reasonably close to the nominal interaction point (namely $Z_{\text{DTNV}} < 20$ cm) we rely on it and take $Z_{\text{OptimalNC}} = Z_{\text{DTNV}}$, otherwise the CJC vertex is taken. In Fig. 7.17 a typical event with far forward DTNV vertex ($Z_{\text{DTNV}} > 20$ cm) is shown with the distribution for the Z_{CJC} for such cases. The CJC vertex looks reasonable though the electron DTRA track is lost.

If an event is not classified as Optimal—DTRA or Optimal—DTNV, but the vertex fit has converged, one tries to validate this vertex with the CIP hits. It could happen that the electron track is lost in the reconstruction despite one measures correctly the electron cluster and the vertex. On the line between the vertex and the cluster one searches for hits in the CIP chamber which has a good segmentation in the z direction. If two or more such hits are found, the situation is recognized as the NC event with the electron track lost and one assumes $Z_{\text{OptimalNC}} = Z_{\text{CJC}}$. These events are classified as Optimal—CJC.

If none of the approaches above to get the vertex position is successful, the event is classified as NoVertex event and will not pass the NC selection.

After all, four classes of events are identified

- DTRA events where the vertex fit converged and the electron DTRA track matches well to the electron cluster.
- DTNV events where the vertex comes from the DTNV track reconstruction and the electron DTNV track matches well to the electron cluster. If the

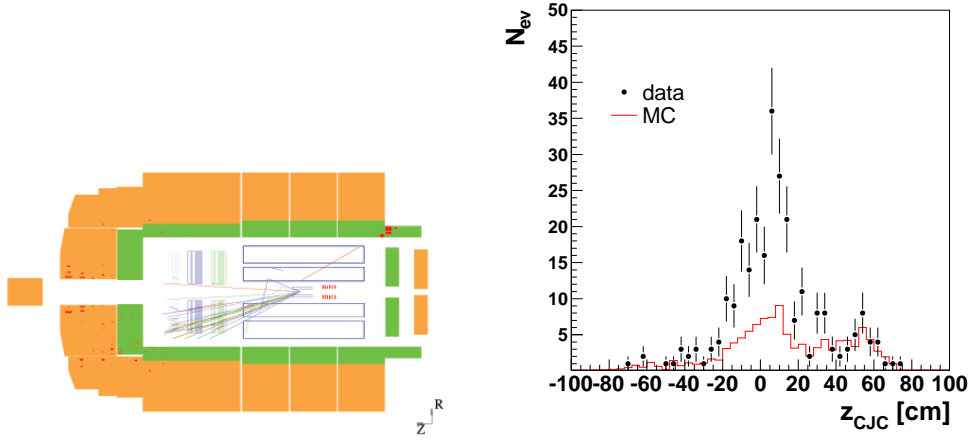


Figure 7.17: For the case $\Delta Z_{CJC-DTNV} < -10$ cm and $Z_{DTNV} > 20$ cm: event display with a typical event (**left plot**) and distribution of the CJC vertices for the whole HERA II sample (**right plot**).

primary vertex position is changed (DTNV vertex is taken), the hadronic final state variables, calculated with the reconstructed vertex position, should be re-calculated, see Section 7.6.5.

- CJC events where the DTRA and DTNV tracks are lost, but the CJC vertex is reliable and electron is verified by the CIP hits on the expected trajectory of the electron.
- NoVertex events where no Optimal vertex is found. In this subsample we require $\gamma_h < 30^\circ$ if the CJC vertex is not reconstructed. The rejected events (with $\gamma_h \geq 30^\circ$) were scanned visually and were identified as non- ep background with the $E - P_z$ distribution which does not peak around 55 GeV. Here we formally assume $Z_{OptimalNC} = 0$.

For these four classes the distributions of γ_h , $\log_{10}(x_{e\Sigma'})$, $E - P_z$, P_t^{had}/P_t^e , E_e/E^{DA} variables are shown in Fig. 7.18. These distributions for the DTRA, DTNV and CJC samples demonstrate a good agreement between data and MC. The NoVertex sample behaves as expected for the NC events with a peak in the $E - P_z$ distribution around 55 GeV. It causes an inefficiency of the Optimal Vertex procedure. Statistics of the DTRA sample is roughly forty times larger than that of the DTNV and CJC samples, and the NoVertex sample statistics is two times smaller.

The DTNV events are concentrate at a region of low γ_h or high x where the hadronic final state goes in the forward direction with the following nuclear interactions. They were restored with the Optimal Vertex procedure and pass now the NC selection cut $|Z_{vtx}| < 35$ cm.

7.5.2 Vertex and Track-Cluster Matching Efficiency

To determine an efficiency of the vertex finding and the track-cluster matching a clean NC events sample, close to that used for the cross-section measurement, is used. An event is classified as having the OptimalNC vertex if DTRA, DTNV or

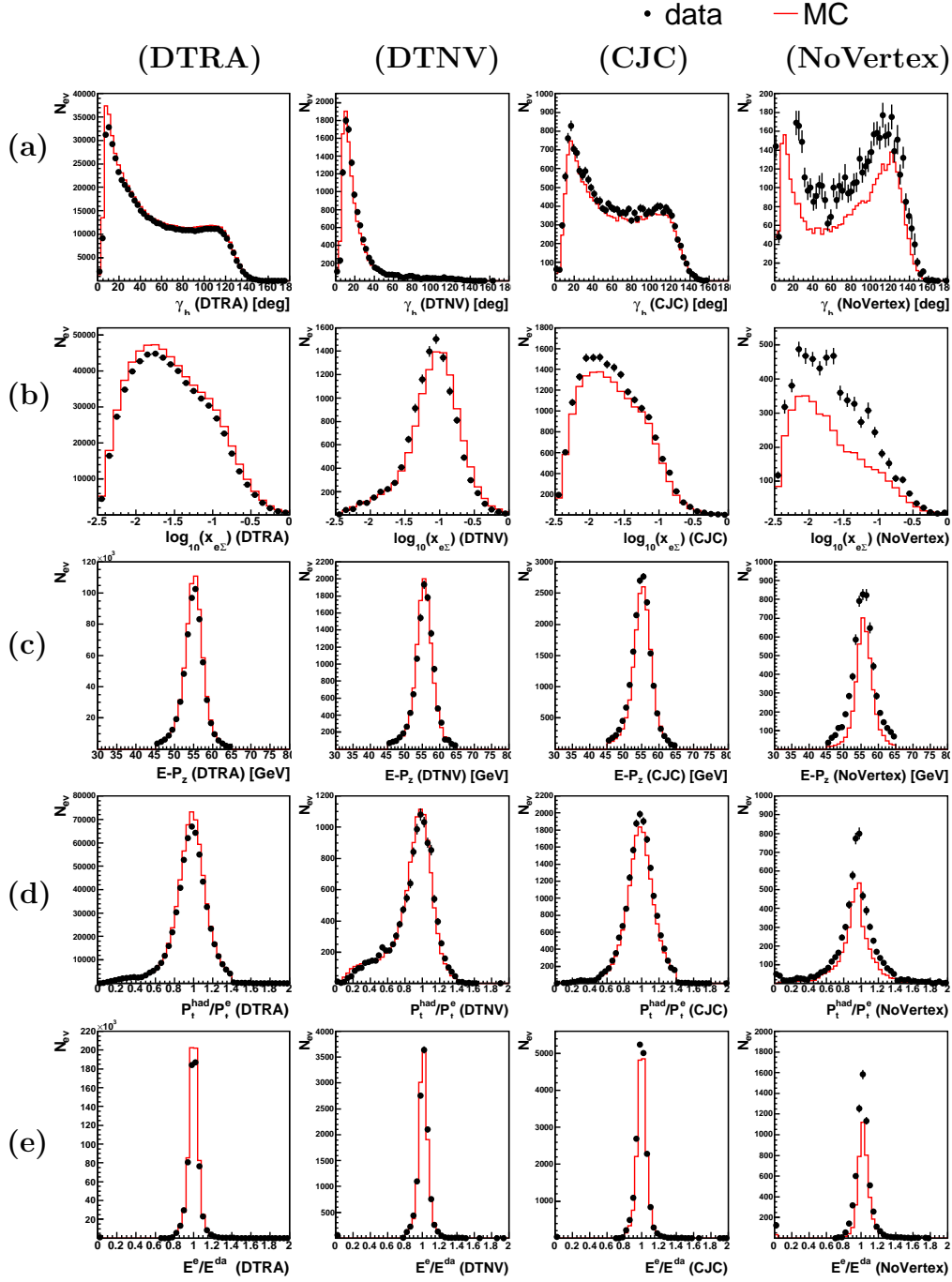


Figure 7.18: Distributions of the (a) γ_h , (b) $\log_{10}(x_{e\Sigma'})$, (c) $E - P_z$, (d) P_t^{had}/P_t^e , (e) E_e/E^{DA} variables for the DTRA, DTNV, CJC and NoVertex samples for the whole HERA II statistics.

CJC vertex (with verification of electron by tracking detectors) is found or $\Theta < 30^\circ$ and the CJC vertex is found. Events from the NoVertex sample give an inefficiency of the procedure. Cuts applied to the monitor sample are the following:

- Energy of the scattered electron candidate $E_e > 18$ GeV to eliminate the photoproduction background.
- $Q_e^2 > 133$ GeV² and $y_e < 0.9$.
- $45 < E - P_z < 65$ GeV.
- The OptimalNC Vertex z position is within 35 cm, if the vertex is reconstructed.
- In case of NoVertex event, if the CJC vertex is not reconstructed, γ_h has to be below 30° .
- Rejection of the events with the second electromagnetic cluster with the energy more than 6 GeV. In some cases energetic electromagnetic cluster from photon in hadronic final state is recognized as a scattered electron cluster causing the fake inefficiency. The real scattered electron in these events is presented also but has smaller P_t . In the region of small Θ the NC statistics is small and the contribution of such events is relatively large. This effect is suppressed by the requirement of the absence of the second electromagnetic cluster for efficiency determination.
- Exclude z and ϕ cracks in LAr calorimeter: $15 < Z_{imp} < 25$ cm, $|\phi_e - 45^\circ \cdot n| < 2^\circ$, $n = 0, \dots, 7$.
- Anti-Compton background cut is applied.
- Background finders are applied.

Fractions of the DTRA, DTNV, CJC and the overall fraction of OptimalNC events in the monitor sample are shown in Fig. 7.19 as a function of γ_h . The DTNV sample demonstrates rise of its rate at small γ_h values (the region where the secondary nuclear interactions occur).

The efficiency of the OptimalNC vertex is shown in Fig. 7.20 for data and MC. Generally the efficiency in MC is 0.3% higher than in data. The corresponding correction is applied to the MC.

The region of $\Theta_e < 30^\circ$ (at very high Q^2) is out of the central tracker acceptance and the electron track reconstruction is not efficient. On the other hand the electron identification in the LAr calorimeter is very reliable and verification of the electron with the tracker information is not needed. For this reasons in the analysis in this region the presence of the CJC vertex is required, but not obligatory the OptimalNC vertex. The check of this condition with the whole NC sample shows 100% efficiency with relatively large statistical error.

In the Nominal analysis, where the OptimalNC vertex and CJC vertex at $\Theta_e < 30^\circ$ are used, the systematic uncertainty is taken to be 0.2% for $\Theta_e > 50^\circ$ and 1% for $\Theta_e < 50^\circ$.

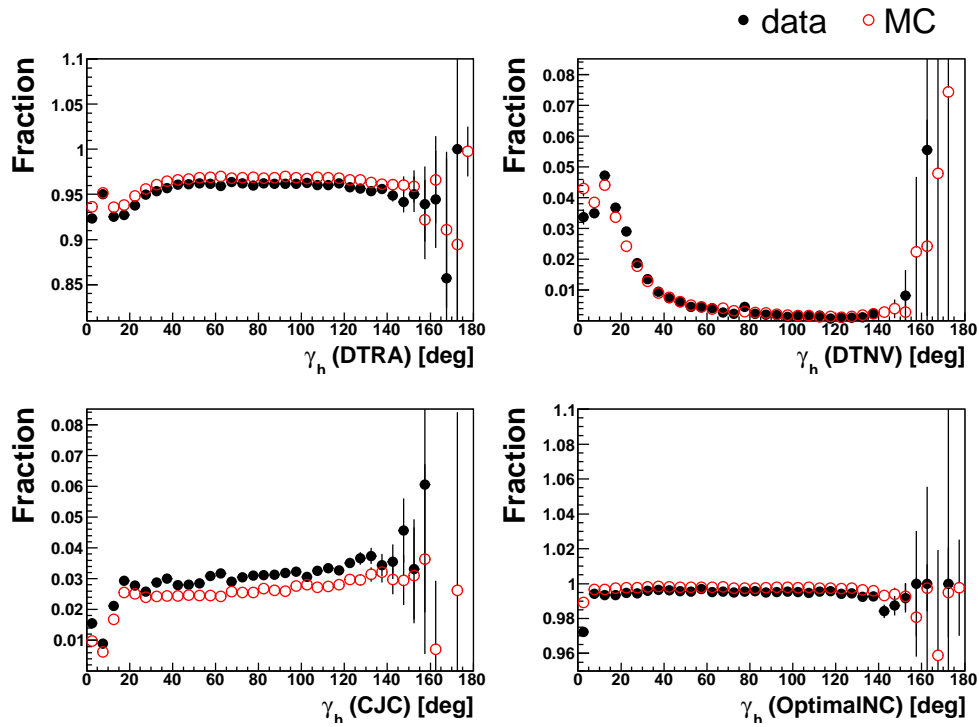


Figure 7.19: Fractions of the DTRA, DTNV, CJC components and the whole OptimalNC vertex sample in the monitor sample as a function of the γ_h variable.

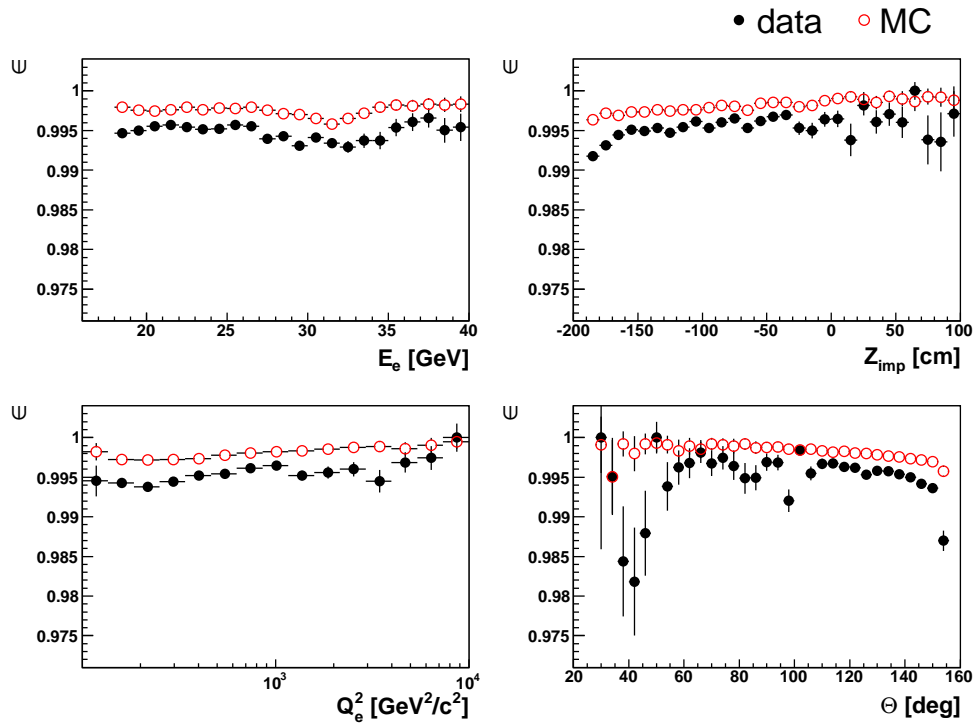


Figure 7.20: Efficiency OptimalNC vertex as a function of E_e , Z_{imp} , Q_e^2 and Θ variables.

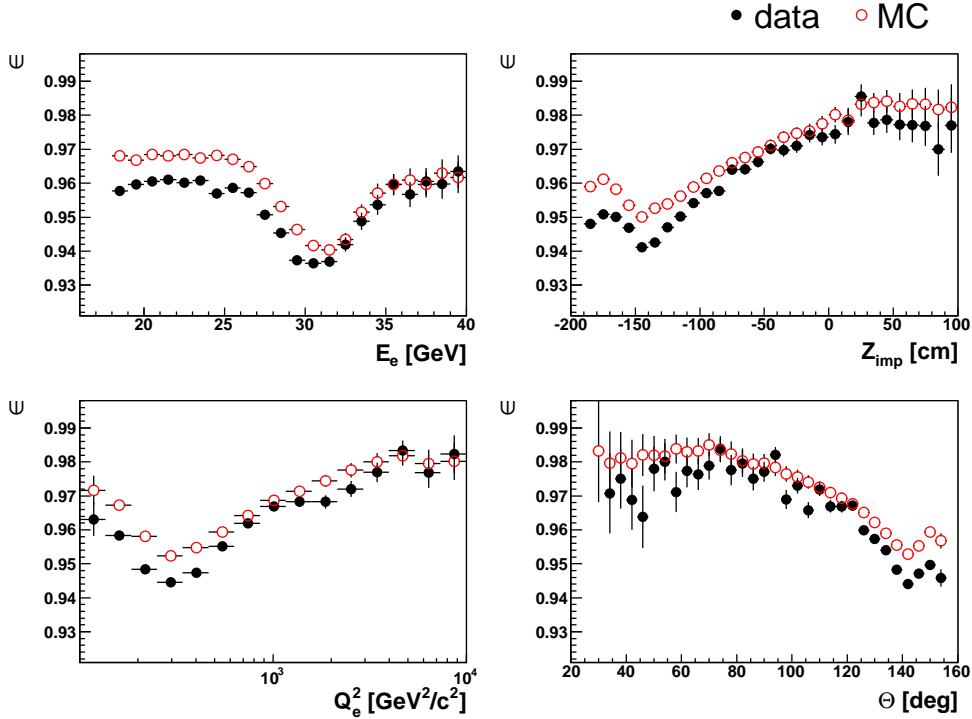


Figure 7.21: Efficiency of the DTRA vertex sample as a function of E_e , Z_{imp} , Q_e^2 and Θ variables.

For the HighY analysis the DTRA sample is used because the well measured charge of the track is needed for suppression and subtraction of the photoproduction background. The efficiency of this condition measured with the NC selection criteria described above (at high energy of the electron candidate) is presented in Fig. 7.21. Difference between data and MC vertex efficiency is generally about 1%. To check the efficiency at low scattered electron energy, neutral current events with hard initial state radiation (NC ISR) and QED Compton events are used. These samples are free from photoproduction background.

In the NC ISR sample a high energy photon in Photon Tagger ($E_{\gamma}^{\text{PhTag}} > 12$ GeV) is required. At the same time we ask for high total $(E - P_z)^{\text{Tot}} = (E - P_z)^{\text{had}} + (E - P_z)^{\text{em cand}} + 2E_{\gamma}^{\text{PhTag}} > 45$ GeV and low hadronic $(E - P_z)^{\text{had}} < 10$ GeV. Such cuts leave the photoproduction only with relatively high energy of fake candidate, and consequently small cross section. Other cuts for this sample are similar to the standard NC selection. Special topology of the Compton events allows selection of a clean Compton sample. The events with two back-to-back electromagnetic candidates, number of tracks $N_{\text{Trk}} < 3$ and very low activity in the LAr ($E^{\text{had}} < 1$ GeV) are selected.

To measure efficiency a monitor sample with all events with $|Z_{\text{OptimalNC}}| < 35$ cm from the NC ISR and QED Compton samples are taken. The signal events have to have $D_{\text{DTRA}} < 12$ cm (condition for the Optimal-DTRA vertex sample). The efficiency measured with this combined statistics is shown in Fig. 7.22. The results at low energy agree with the measurement at high energy of the scattered electron. To improve the simulation, 1% inefficiency correction is applied to MC. The remaining

differences between data and MC after this correction are within 1%. The uncertainty is taken to be 1%.

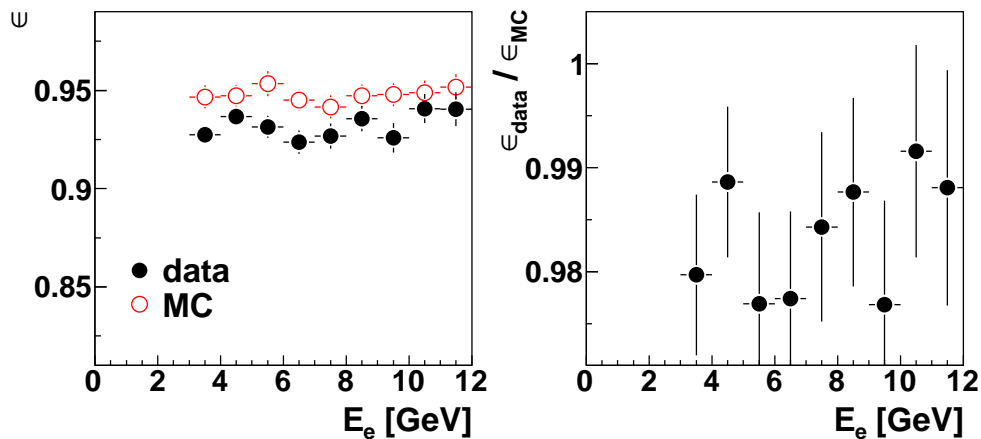


Figure 7.22: Efficiency of the DTRA vertex as a function of the scattered electron candidate energy E_e measured with the ISR and Compton events.

7.6 Hadronic Final State

For good reconstruction of the kinematic variables, accurate measurements of the inclusive hadronic quantities Σ and P_t^{had} are needed (see Section 5.1).

The reconstruction of the hadronic final state (HFS) uses the results of the clustering of the deposited energy in calorimetric cells with the clustering algorithm [97] and reconstruction of the tracks from the tracker information. The clusters obtained from the clustering procedure undergo the software compensation procedure [98] to equalize the response of the LAr calorimeter caused by electromagnetic and hadronic particles. The separation of the electromagnetic and hadronic clusters is done using a neural network. With the Hadroo2 algorithm [99] the information from the calorimeter and tracker is combined to provide the best measurement of the final state particles. Then the final calibration is applied to provide the best estimation of the energy of the hadronic final state (HFS).

Below the procedure for reconstruction of the hadronic part of the final state is described.

7.6.1 Separation of the Electromagnetic and Hadronic Showers

In the non-compensating calorimeters fluctuations of the electromagnetic component of hadronic showers is the reason for the energy spread in single hadron and jet measurements. Term “non-compensating” refers to difference in the response for hadronic and electromagnetic energy deposits. Assuming larger or smaller electromagnetic energy fraction in the shower in the HFS reconstruction for the non-compensated calorimeter, one varies the energy scale of the whole hadronic shower.

The H1 software weighing technique [98] aims to equalize the calorimeter response to electrons (photons) and hadrons by weighing of the cell energies in hadronic showers on the event by event basis. To do the proper weighing one has to estimate the fraction of the electromagnetic energy or the probability for each single cluster to originate from the electromagnetic particle. For this purpose the neural network is used [100] which allows to take into account possible non-trivial correlations between the input variables. As an input information the shower shape characteristics are taken. The training of the network is done separately for each calorimeter wheel.

The output of the neural network, the probability P_{em} for the cluster to be an electromagnetic, is used for the energy reconstruction. If the probability is more than 50%, the cluster is assumed to be an electromagnetic and its energy is taken as the electromagnetic energy E_{em} , otherwise the hadronic energy E_{had} from the software weighing [101] is used.

One defines the generated electromagnetic fraction of the jet as

$$f_{em}^{gen} = \frac{1}{E_{jet}^{gen}} \sum_{\{e,\gamma\}} E_{em} \quad (7.7)$$

and the reconstructed one as

$$f_{em}^{rec} = \frac{1}{E_{jet}^{rec}} \left(\sum_{\{em\ cand\}} E_{cand} + \sum_{\{clusters\}} P_{em}^i E_{cls}^i \right) \quad (7.8)$$

where the first sum runs over all candidates found by the electron finder (see Section 7.2) and the second sum runs over all remaining clusters of the jet. The results of the electromagnetic energy fraction determination are presented in Fig. 7.23 with the results from the standard H100 procedure for comparison.

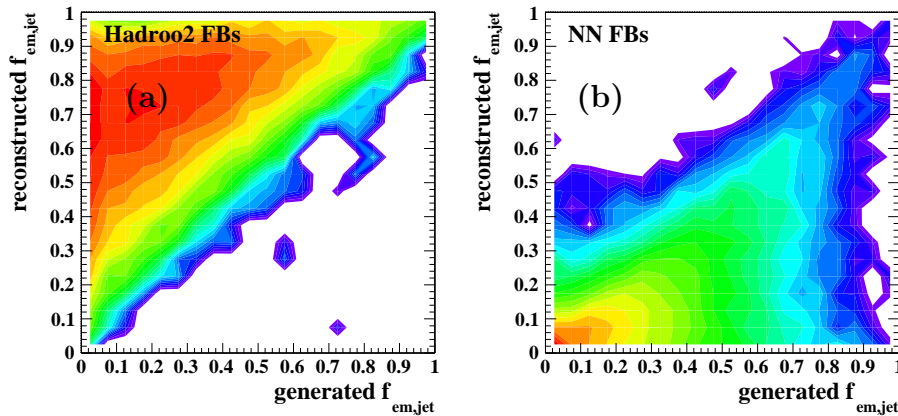


Figure 7.23: Generated and reconstructed electromagnetic fractions of jet in FB region for the (a) standard algorithm and (b) neural network algorithm [100].

7.6.2 The HADROOII Algorithm

From the clusters and reconstructed tracks information, reconstruction of the final state particles is provided with the HADROOII (Hadronic Reconstruction in

H100) routine [99], which anticipates the idea of energy flow algorithm: energy of the charged particles can be measured either by the curvature of the track in the tracker system or by the calorimetric measurement. At lower particle momenta and high curvature of the track, the track measurement surpasses in precision the calorimetric one. At high energy the calorimeter resolution is better. The point where the precisions of the calorimetric and track measurements is about the same is at approximately 25 GeV.

The HADROOII algorithm compares the track momentum and the calorimetric energy calculated within a “cylinder” which comprise an overlapping volume of 67.5° cone around straight line extrapolation of the track into the calorimeter (the cone vertex is situated at the impact point of the particle on the surface of the LAr) and two cylinders of radius 25 cm in the electromagnetic part of LAr and 50 cm in the hadronic part.

On the basis of the resolution estimation for two (track and cluster) measurements, one measurement is taken to provide the four-vector of the reconstructed candidate and the other one is discarded.

Each track in the HFS is supposed to originate from a pion, so

$$E_{\text{Trk}}^2 = P_{\text{Trk}}^2 + m_{\pi}^2 = P_{t,\text{Trk}}^2 / \sin^2 \Theta + m_{\pi}^2. \quad (7.9)$$

Assuming absence of the correlation between P_t and Θ , the error on the track’s energy is

$$\delta_{\text{Trk}} = \frac{\sigma(E_{\text{Trk}})}{E_{\text{Trk}}} = \frac{1}{E_{\text{Trk}}} \sqrt{\left(\frac{P_{t,\text{Trk}}^2}{\sin^4 \Theta} \cos^2 \Theta\right) \sigma_{\Theta}^2 + \left(\frac{1}{\sin^2 \Theta}\right) \sigma_{P_t}^2}, \quad (7.10)$$

where σ_{P_t} and σ_{Θ} are the errors on the $P_{t,\text{Trk}}$ and Θ measurements correspondingly.

An estimation of the corresponding error on the LAr energy measurement of the same particle is given by

$$\delta_{\text{Calo}} = \frac{\sigma_{\text{Calo}}}{E_{\text{Trk}}} = \frac{50\%}{\sqrt{E_{\text{Trk}}}}. \quad (7.11)$$

For the estimation the track’s energy measurement is used because a priori the number of clusters produced by the incident particle is not known.

If $\delta_{\text{Trk}} < \delta_{\text{Calo}}$ the track measurement is used. The corresponding energy deposit in the calorimeter E_{Calo} should be suppressed to avoid double counting. If

$$E_{\text{Calo}} < E_{\text{Trk}} \left(1 + 1.96 \sqrt{\delta_{\text{Trk}}^2 + \delta_{\text{Calo}}^2}\right), \quad (7.12)$$

the cluster energy is suppressed, otherwise the cluster’s energy excess is assumed to originate from a neutral particle or another track, and the track energy E_{Trk} is subtracted from E_{Calo} . This procedure takes into account possible fluctuation of both measurements within a 95% confidence interval.

If $\delta_{\text{Trk}} > \delta_{\text{Calo}}$ the energies E_{Calo} and E_{Trk} are compared. If

$$E_{\text{Calo}} - 1.96\sigma_{\text{Calo}} < E_{\text{Trk}}, \quad (7.13)$$

where $\sigma_{\text{Calo}} = 0.5\sqrt{E_{\text{Calo}}}$, the clusters are used to create HFS object and the track is removed. If $E_{\text{Trk}} < E_{\text{Calo}} - 1.96\sigma_{\text{Calo}}$ it is assumed that E_{Calo} originates from several particles. The track is then used and the track energy is subtracted from E_{Calo} .

Once all tracks have been considered, the remaining clusters are used to create HFS particles. These clusters are supposed to originate from neutral particles or charged particles with non-reconstructed tracks.

7.6.3 Calibration of the Hadronic Energy

Once all tracks and clusters have been assembled to hadronic objects, a suitable calibration procedure for the calorimeter clusters has to be applied to set proper energy scale for data and MC. The calibration exploits an independence of the double-angle measurements of the hadronic final state from the energy measured in the calorimetric cells (both for HFS and the scattered electron). For one-jet events (where the γ_h angle is well defined) with the cuts which ensure absence of the leakage of hadronic energy from the calorimeter and absence of hard ISR which could change the initial lepton beam energy, the P_t^{DA} agrees with P_t^{gen} (the transverse momentum in the event defined on the generator level) within 0.5% in the most part of the kinematical plane as it is shown in Fig. 7.24. Thus the double angle measurement can serve as a good estimation of the true value of transverse momentum.

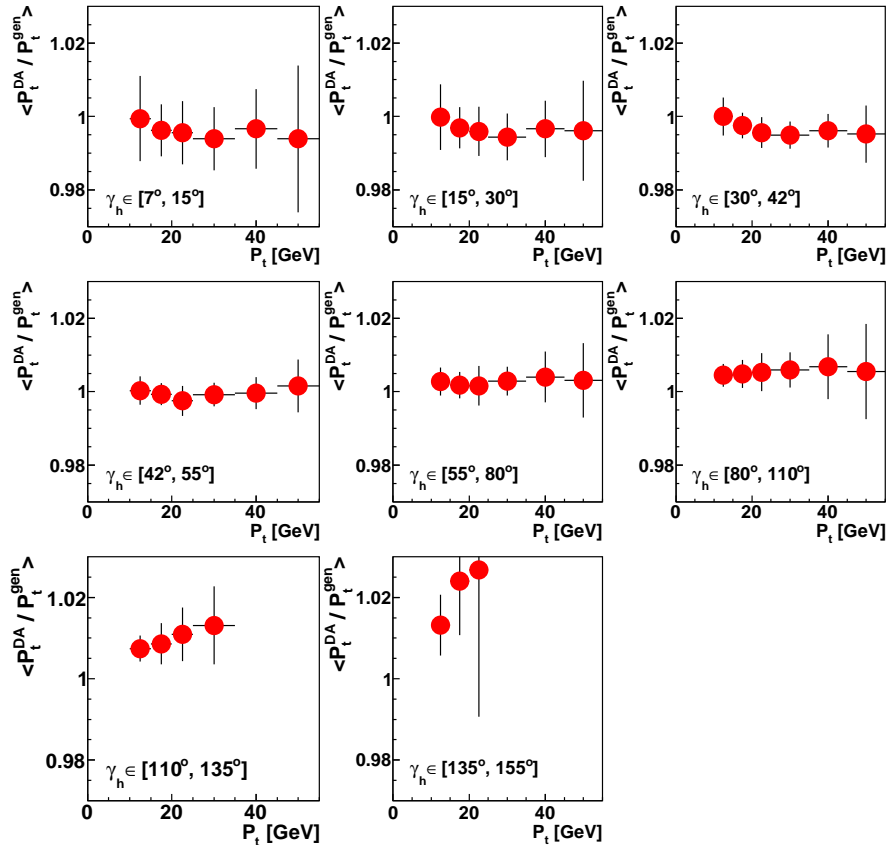


Figure 7.24: The $P_t^{\text{DA}}/P_t^{\text{gen}}$ ratio as a function of the P_t^{DA} in different regions of γ_h for the PerPos period.

The calibrated four-vector \mathbf{h} of the hadronic final state is given by

$$\mathbf{h} = \sum_{i \in \text{jet}} (\alpha^i \mathbf{c}_{\text{jet}}^i + \mathbf{t}_{\text{jet}}^i) + \sum_{j \in \text{out}} (\beta^j \mathbf{c}_{\text{out}}^j + \mathbf{t}_{\text{out}}^j), \quad (7.14)$$

where \mathbf{c} is a four-vector for the HFS object obtained from clusters and \mathbf{t} is a four-vector for the HFS object obtained from tracks. The sums run over all HFS objects inside and outside the jet. The calibration constants α, β are applied on the clusters energy only (tracks are supposed to be well measured) and have the form

$$\alpha, \beta = P_{\text{em}} g_e(\eta_{\text{cls}}, E_{\text{cls}}; \vec{v}_e) + (1 - P_{\text{em}}) g_h(\eta_{\text{cls}}, E_{\text{cls}}; \vec{v}_h), \quad (7.15)$$

where g_e and g_h are the two-dimensional functions of the cluster pseudorapidity, η_{cls} , and energy, E_{cls} , and vectors of free parameters \vec{v}_e, \vec{v}_h have to be determined during the calibration procedure.

The free parameters are obtained in the minimization of the χ^2 function calculated over the bins of the certain grid in $(\eta_{\text{jet}}, P_t^{\text{jet}})$ coordinates

$$\chi^2 = \sum_{\{\text{bins}\}} \frac{(m_{\text{bin}} - 1)^2}{\sigma_{\text{bin}}^2}, \quad (7.16)$$

where the mean m_{bin} and the width σ_{bin} are extracted from the transversal momentum balance $P_t^{\text{bal}} = P_t^{\text{had}}/P_t^{\text{DA}}$ distribution in the given bin.

To check the hadronic calibration the following event selection criteria have been applied

- All jets are in the acceptance of the calorimeter.
- $Q^2 > 60 \text{ GeV}^2$.
- The transverse momentum of the scattered electron $P_t^e > 10 \text{ GeV}$.
- $E - P_z > 42 \text{ GeV}$.
- The ratio $P_t^{\text{had}}/P_t^e > 0.35$.

These conditions ensure reasonable performance of the double angle method [100].

Control plots for the check of the hadronic energy scale in data and MC are shown in Fig. 7.25. The mean value of the P_t^{bal} is extracted for each bin of P_t^{had} and γ_h in a Gaussian fit as the peak value of the distribution. Agreement between data and simulation after calibration is within 1%. The overall shift of the mean value of the balance is due to hadronic energy leakage which is allowed for the calibration check.

The uncorrelated uncertainty on the hadronic energy scale is taken to be 1%. The correlated part of the uncertainty related to the double angle method and is supposed to be 0.5%.

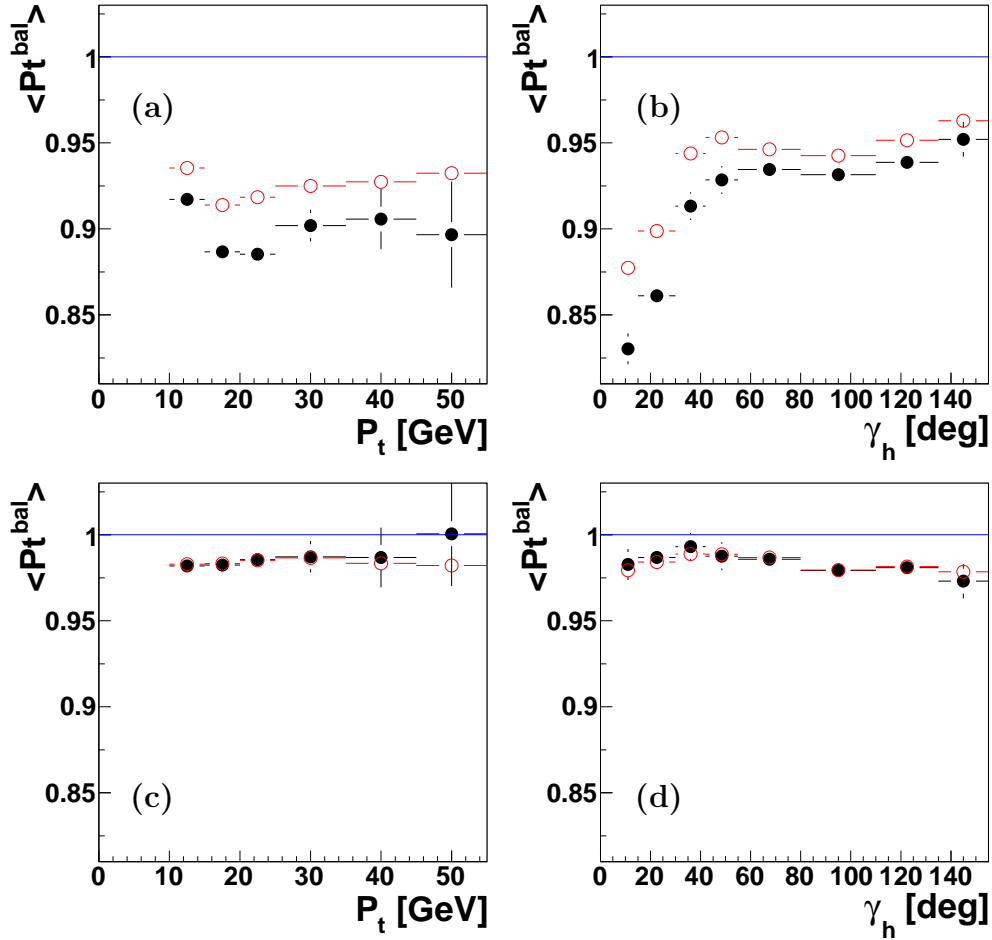


Figure 7.25: The mean P_t^{bal} values in different P_t^{had} and γ_h bins for data (closed circles) and MC (open circles) for the Per0607 period. Two upper plots (a, b) refer to the uncalibrated case, two bottom plots (c, d) are done after the hadronic calibration was applied.

7.6.4 Hadronic Energy in SpaCal

The high P_t jets calibration described above corrects the energy of the LAr clusters and improves reconstruction of the HFS. In the region of high y (where the hadronic final state could partially go in the backward direction) the contribution of the hadronic energy measured in the SpaCal calorimeter is also important. For this reason an additional calibration of the SpaCal calorimeter was applied separately for data and MC.

For calibration at high y we assume that the part of the HFS measured in the LAr and the tracker system are reconstructed well and the difference between the measured transverse momentum of the scattered electron and the HFS appears due to energy measurement in the SpaCal. The correction factors for the electromagnetic and hadron sections of the SpaCal are assumed to be dependent only on the energy measured in these sections.

The following procedure is applied. We select the event sample for the SpaCal calibration as follows:

- $E_e > 2$ GeV.
- $Q^2 > 60$ GeV².
- $E - P_z > 42$ GeV.
- $P_t^{\text{had}}/P_t^e > 0.35$.
- $P_t^{\text{SpaCal}}/P_t^{\text{DA}} > 0.05$.

Here the P_t^{SpaCal} is the transverse momentum of the HFS measured in the SpaCal calorimeter. For these events the momentum components P_x, P_y and energy E measured in the electromagnetic (SE) and hadronic (SH) parts of the SpaCal and in the LAr and tracker systems (LT) are compared with the transverse momentum of the scattered electron. With this information we minimize the function

$$\sum_{\{\text{events}\}} [(P_t^e)^2 - (P_x^{\text{LT}} + C^{\text{SE}}P_x^{\text{SE}} + C^{\text{SH}}P_x^{\text{SH}})^2 - (P_y^{\text{LT}} + C^{\text{SE}}P_y^{\text{SE}} + C^{\text{SH}}P_y^{\text{SH}})^2] \xrightarrow{A_e, B_e, C_e, A_h} \min, \quad (7.17)$$

where the correction factors $C^{\text{SE}}, C^{\text{SH}}$ depend on optimization parameters A_e, B_e, C_e, A_h :

$$\begin{aligned} C^{\text{SE}} &= A_e + B_e e^{C_e E^{\text{SE}}}, \\ C^{\text{SH}} &= A_h. \end{aligned} \quad (7.18)$$

The corrected energy in the SpaCal is calculated as

$$E_{\text{corr}}^{\text{SpaCal}} = (A_e + B_e e^{C_e E^{\text{SE}}})E^{\text{SE}} + A_h E^{\text{SH}}. \quad (7.19)$$

The calibration improves description of the HFS in the high y region, particularly the description of the $E - P_z$ variable which is used in the NC sample selection. The $E - P_z$ distributions before and after the SpaCal hadronic calibration are presented in Fig. 7.26. In addition the hadronic energy in the SpaCal was shifted in MC up by 5% to bring MC closer to the data, assuming this shift originates from the hadronic calibration of the SpaCal.

From the distributions for all data periods the uncertainty on the hadronic energy scale in the SpaCal is obtained to be 5% in the high y region.

7.6.5 The DTNV Sample

As it was mentioned in Section 7.5.1, in the DTNV event sample the DTNV vertex is used as a primary vertex. It means that the hadronic final state calculated assuming the old reconstructed vertex position (the CJC vertex) should be re-calculated. Moreover, tracks can not be used to form the HFS because most likely that they originate from the secondary nuclear interaction.

The hadronic final state is re-calculated using uncalibrated hadronic four-vector obtained from clusters in the LAr. Re-calculation is performed assuming that this vector is caused by single energy deposition in the LAr. Under this assumption the hadronic four-vector can be re-calculated to the new primary vertex position.

The calibration of the re-calculated HFS is done as a function of the angle of the hadronic final state. The calibration exploits the transversal momentum conservation

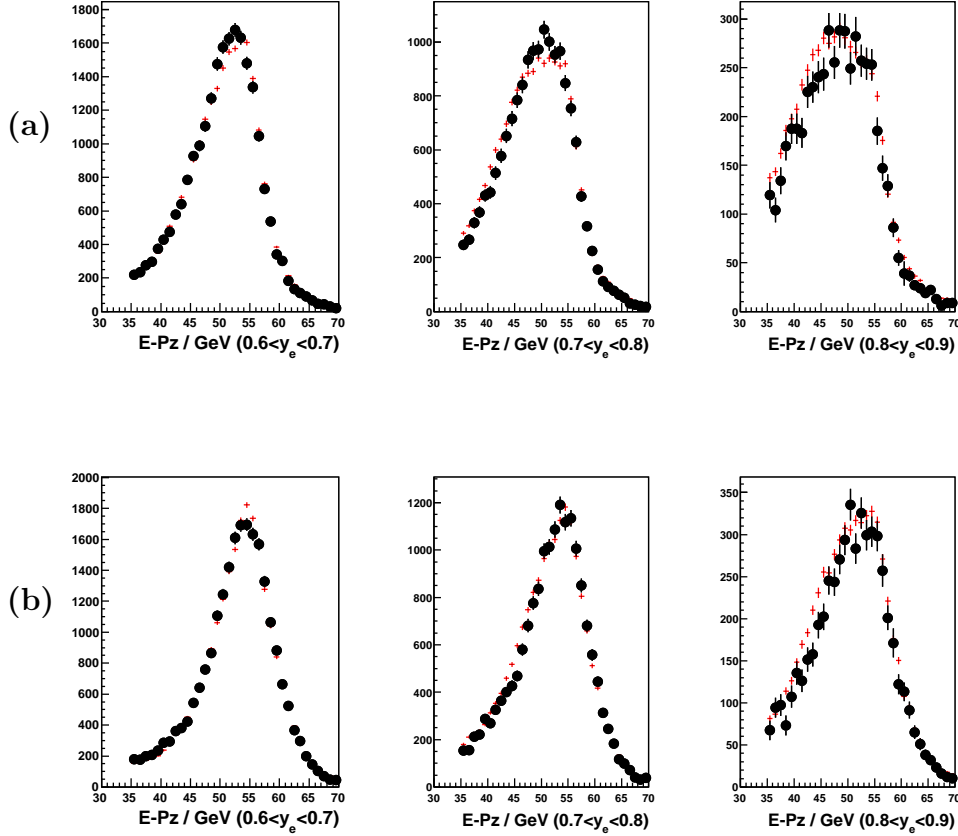


Figure 7.26: The $(E - P_z)$ distribution in different y bins for data (circles) and MC (error crosses) (a) before and (b) after the SpaCal calibration. Wrong charge subtraction procedure is applied to eliminate photoproduction background.

and is done period-wise separately for data and MC. The calibration procedure is similar to the “Step1” in the version of the HFS calibration described in [99]. The $P_t^{\text{bal}} = P_t^{\text{had}}/P_t^{\text{DA}}$ distributions are shown in Fig. 7.27 before and after calibration applied demonstrating an improvement of agreement between data and simulation.

To check re-calculation of DTNV HFS properties comparing them with the standard reconstruction procedure, where the hadrons undergo full reconstruction with proper calibration, the DTNV events were preselected and re-reconstructed with the special version of the H1REC, where the reconstruction program has a “hint”, where the “true” vertex position should be. About one third of the DTNV events migrated to the DTRA sample [102] after re-reconstruction. For these events the relative difference in the P_t^{had} and $(E - P_z)$ variables between standard reconstruction (marked as “VT”) and re-reconstruction (marked as “DP”) is shown in Fig. 7.28. The differences are within 15%. The overall influence on the cross section could be estimated from the ratio of the numbers of the data events in $x - Q^2$ bins passed the selection in the case of standard reconstruction and the case, where 2/3 of the DTNV sample was substituted by the duplicated re-reconstructed sample. The ratio is shown in Fig. 7.29. It overestimates the effect on the cross section measurement as

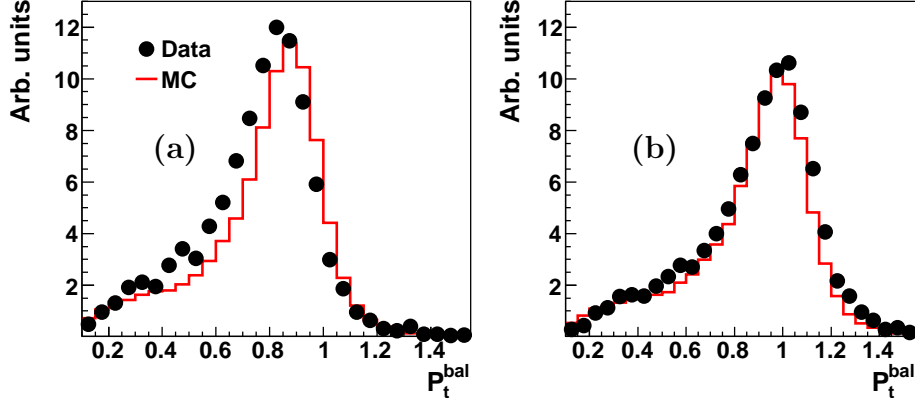


Figure 7.27: The influence of the DTNV calibration on the DTNV sample: the events distribution in P_t^{bal} variable (a) before and (b) after calibration.

soon as the simulation also has the DTNV events which lead to partial cancellation of the effect, but they were not re-reconstructed for this test. The overall conclusion is that the re-calculation of the HFS and energy calibration of the DTNV events work well and the residual effect is negligible.

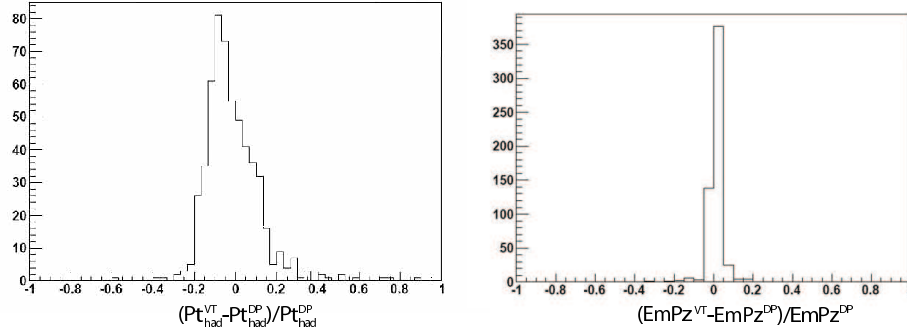


Figure 7.28: The relative difference in P_t^{had} and $(E - P_z)$ variables between the standard (VT) and new (DP) reconstructions for the events migrated from the DTNV (in VT) sample to DTRA (in DP) samples.

7.6.6 Noise Contribution to the HFS Measurement

The noise treatment described in Section 4.1.1 reduces the noise significantly. Still at the subsequent level of reconstruction further noise reduction is possible. Here not only the electronic noise but also the energy depositions from the beam halo and cosmic muons can be suppressed.

Four algorithms are applied for the high level noise suppression [103]. First, all clusters consisting of only one cell and energy of less than 0.2 GeV on the electromagnetic energy scale are removed. Then the FSCLUS and NEWSUP algorithms

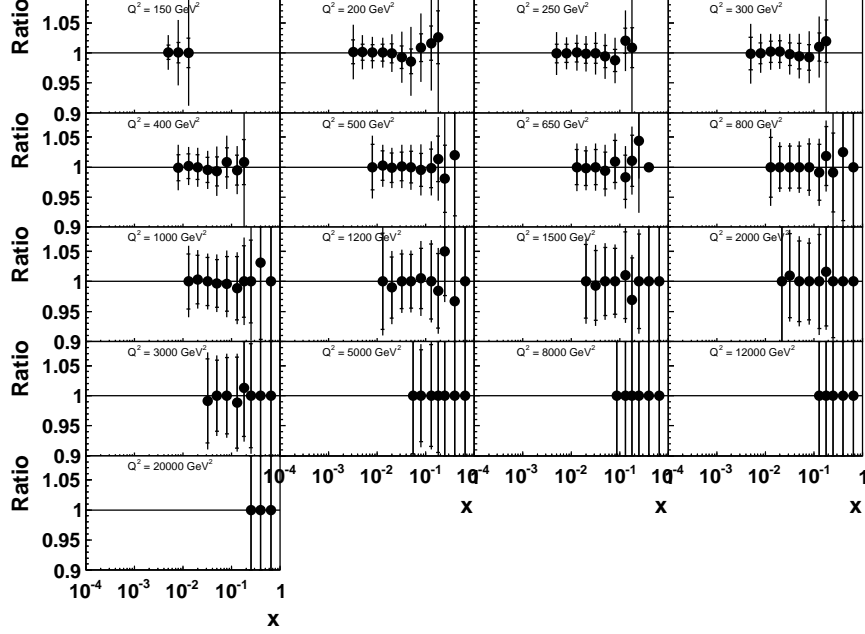


Figure 7.29: Influence of the re-calculation of the HFS for the DTNV sample on the number of the data events passed the NC selection in $x - Q^2$ bins (see explanations in the text). The inner error bars show the statistical uncertainty.

remove isolated low-energy clusters from electronic noise. The HALOID algorithm removes clusters from halo muons and the HNOISE algorithm suppress cluster from cosmic muons and coherent noise. The performance of the noise suppression procedure was studied [103] which shows a small loss of 0.2-1% for low energy signal clusters.

The noise contribution is especially dangerous in the region of low y or high x (see Section 5.1). For example, any noise cluster in the backward part of the detector contributes twice to Σ and cause migration of the high x events to the region of moderate x . The relative contributions⁷ from the LAr and SpaCal calorimeters, tracks and estimation of suppressed noise at the stage of the HFS reconstruction to y_h are shown as a function of y_h for data and Monte Carlo in Fig. 7.30.

Still some fraction of noise could remain unrecognized and could influence the HFS reconstruction. To estimate this effect a fraction f_n of recognized and suppressed noise was added to the total HFS, and the $P_t^{\text{bal}} = P_t^{\text{had}}/P_t^e$ distribution at high x values is studied. In Fig. 7.31 the effect is shown for $f_n = 20\%$. This value was found to be reasonable to restore the P_t^{bal} distributions at high x . The correlated uncertainty of 20% of the suppressed noise is assigned to the estimation of the noise energy in the LAr.

⁷Actually, these contributions are fractions of Σ , see (5.7)

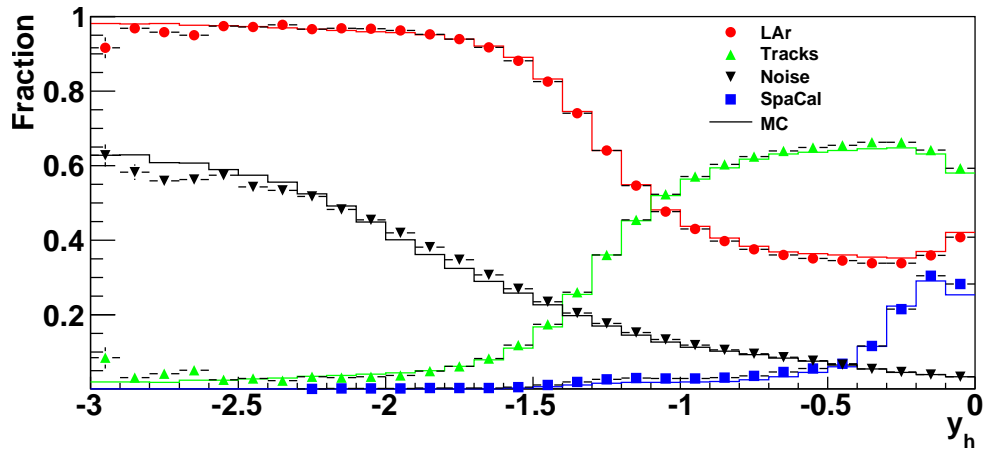


Figure 7.30: Relative contributions from the calorimeters, tracker and suppressed noise to the y measurement from data (point-like markers) and MC (solid lines) for all e^+p periods.

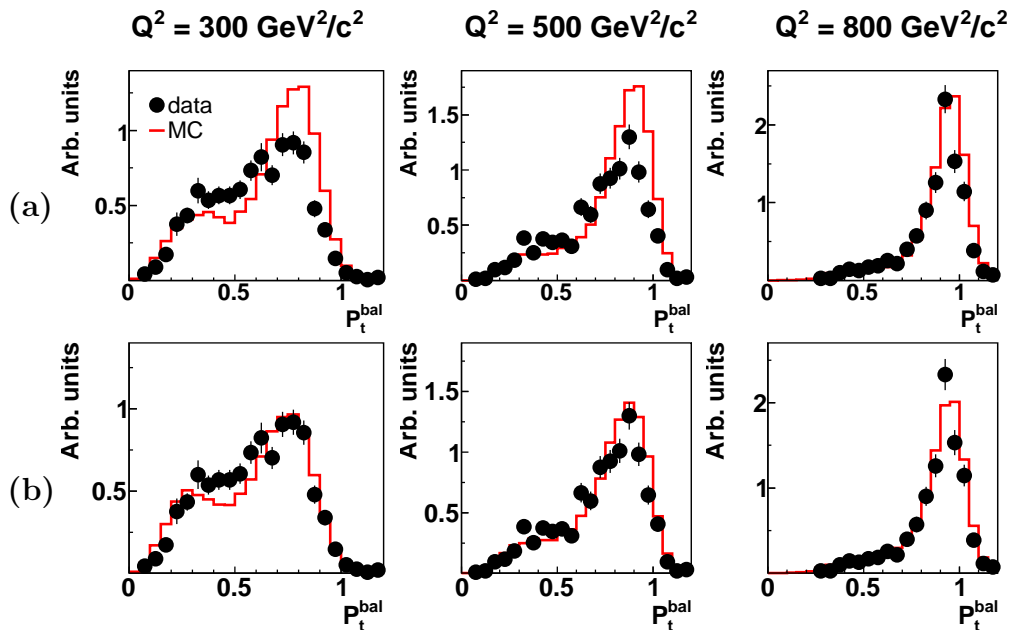


Figure 7.31: The effect of the noise addition to the HFS: P_t^{bal} distribution at $x = 0.25$ bins with (a) standard HFS and (b) HFS with a 20% fraction of noise.

7.7 Trigger Treatment

During the data taking a decision whether to write down an event on the tape or not is done by the trigger system. Generally each subtrigger used in this analysis consists of a main trigger component which fires on the energy deposition in the LAr calorimeter (either from an electron candidate or hadronic final state) and veto conditions, which suppress backgrounds.

If one measures an efficiency of a trigger element (TE) with a monitor trig-

s67	LAr_electron_1 !VETO_BG && !BToF_BG && !STof_BG FIT_IA !FIT_BG CIP_T0 (LAr_T0 && !CIP_T0_nextbc) !(CIP_mul > 7 && CIP_sig == 0)	energy condition ToF veto (I) ToF veto (II) time condition CIP veto
s75	LAr_electron_2 FTT_mul_Td > 0 !VETO_BG && !BToF_BG && !STof_BG FIT_IA !FIT_BG CIP_T0 !(CIP_mul > 7 && CIP_sig == 0) L2_LAr_electron	energy condition track condition ToF veto (I) ToF veto (II) time condition CIP veto L2 condition
s57	LAr_electron_1 CIP_T0 (LAr_T0 && !CIP_T0_nextbc)	energy condition time condition

Table 7.2: Trigger requirements for the subtriggers in use. Conditions from different rows supposed to be joint with the AND logical operator.

ger (MT) than the efficiency ε of this TE is

$$\varepsilon(TE) = \frac{\text{number of event triggered by } TE \text{ and } MT}{\text{number of events triggered by } MT}. \quad (7.20)$$

The inefficiency of the TE is $\bar{\varepsilon} = 1 - \varepsilon$.

For two mutually independent triggers A and B the efficiency of the condition $A||B$ is

$$\varepsilon(A||B) = 1 - (1 - \varepsilon(A))(1 - \varepsilon(B)). \quad (7.21)$$

The subtriggers used in this analysis to trigger NC events are **s67** and **s75**. For monitoring purposes the **s57** subtrigger is used. They trigger on the signal from the LAr calorimeter induced by a high energy electron or hadronic final state. This information is combined with the timing information from the LAr calorimeter and the central proportional chamber CIP as it shown in Table 7.2⁸.

During the HERA II period there were minor changes in the conditions quoted. Namely as a track condition for **s75** till year 2005 the DCRPh_THig element was used. In the year 2006 the ToF veto (II) condition was substituted by (!VETO_BG && (!BToF_BG && BToF_Gl && !BToF_IA)), and the time condition for the subtrigger **s75** was changed to CIP_T0 && (CIP_sig > 0). Since the end of 2006 for the subtrigger **s67** an additional muon condition (CIP_mul > 0) || (!Mu_BIEC) was used. These changes cause slight variations in the trigger efficiencies, but allow to use the same methods of the trigger efficiency measurements as for the quoted configuration.

The monitor subtrigger **s57** is a prescaled copy of the subtrigger **s67** without the veto requirement. It is used to study the CIP and ToF veto conditions.

⁸Symbols “&&”, “||” and “!” denote here logical operations AND, OR and NOT correspondingly.

7.7.1 Triggering of Electron in LAr

The trigger elements **LAr_electron_1** and **LAr_electron_2** trigger on the activity in the LAr calorimeter and can be fired either by the electron candidate (“electron” case) or by the hadronic final state (“hadron” case). To investigate an efficiency to trigger a neutral current event with one of the components, another component is used as a monitor trigger. These two are treated as mutually independent conditions as soon as the scattered electron is spatially isolated. This way we investigate the trigger efficiency for one part of the LAr calorimeter using as a monitor another part of the same calorimeter. An identification of the “electron” and “hadron” cases is done via matching of the positions of the fired calorimeter trigger towers and the direction of the scattered electron. Another possibility to measure the trigger efficiency is to use the SpaCal triggers, which react on the hadronic activity in the SpaCal at high y . Both methods give compatible results, so for investigation of the “electron” part, the “hadronic” part and the SpaCal triggers (**s0,s9**) are used together as a monitor in order to increase a statistical precision.

In the region of Nominal analysis the **LAr_electron_1** condition is almost 100% efficient (the minimum energy of the scattered electron for this y region is about 10 GeV and well above the threshold). As a trigger the subtrigger **s67** is used. The efficiency of the **LAr_electron_1** TE is calculated as a combination of the “electron” and “hadron” efficiencies.

The efficiency for the “electron” part is very high everywhere except several regions where the trigger cells were switched off due to high noise or malfunctioning of the hardware (an example is shown in Fig. 7.37). These regions are excluded from the analysis by the Fiducial Volume Cut (see Section 7.7.6). Finally the trigger efficiency for this TE in this region was measured in the $x - Q^2$ grid as it is shown in Fig. 7.32 and is applied to Monte Carlo separately for each helicity subperiod to follow possible time dependencies.

For the HighY part of the analysis the strategy is more complicated. To obtain the lowest common threshold (see Section 4.3.1), “electron” parts of the **LAr_electron_1** TE from **s67** and **LAr_electron_2** TE from **s75** were combined. The subtriggers **s67** and **s75**, apart from the thresholds of the electron TE, have different additional criteria. For combination, the events triggered by the “electron” part of the **LAr_electron_2** TE of **s75** but not by the **s67** subtrigger were weighed to the ratio of the efficiencies of these additional criteria, to have these events effectively on the same footing as events triggered by **s67**. Then these events are added to the events triggered by the “electron” part of the **LAr_electron_1** TE of the **s67**. In both cases an electron candidate is accepted inside the fiducial volume only.

The weights applied to the data events triggered by **s75** only are the prescales ratio, the ratio of the efficiencies for T0 conditions for **s67** and **s75** and track and L2 efficiencies for **s75**. The muon veto is present in **s67** only, but it is 100% efficient.

The efficiency of the unified effective “electron” trigger element is derived in the $E_e - Z_{\text{imp}}$ bins for each year separately and applied to the Monte Carlo. As a monitor trigger the “hadronic” part of the **s67** subtrigger and the SpaCal subtriggers were used. The threshold behavior at low scattered electron energy plays a crucial rôle: the efficiency drops as E_e decreases, as it is shown in Fig. 7.33. Efficiency of the “hadronic” part in this low E_e region is small and not suitable to improve overall

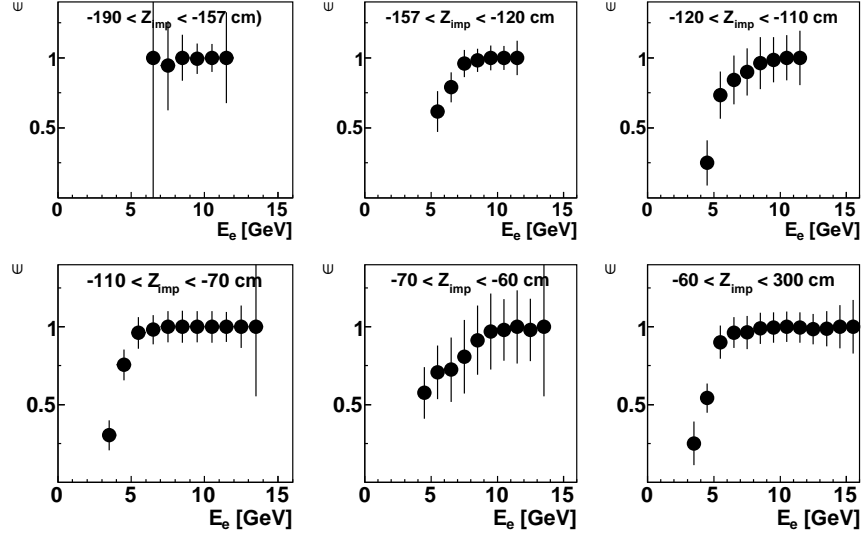


Figure 7.33: The threshold behavior of the unified effective “electron” TE efficiency in different Z_{imp} regions for the Per0607 period.

st67.

For the reweighing of the data collected with the **s75** subtrigger only, the ratio of the combined $T0$ efficiency to the CIP_ $T0$ efficiency is taken.

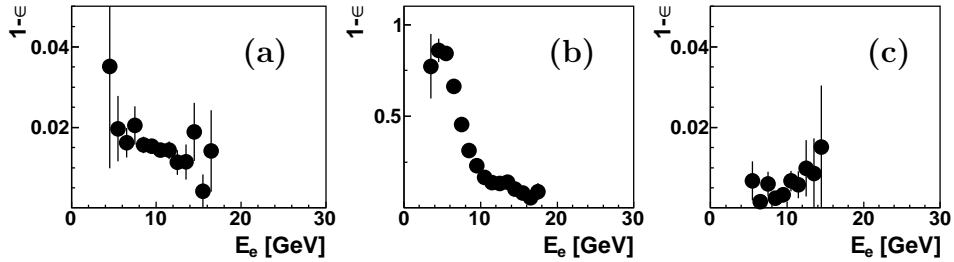


Figure 7.34: Inefficiency of the (a) CIP_ $T0$, (b) (LAr_ $T0$ && !CIP_ $T0_{\text{nextbc}}$) and (c) $Veto$ conditions as a function of scattered electron candidate energy E_e for the Per0607 period.

7.7.3 Veto Conditions

The veto conditions use time-of-flight (ToF) information to reject out of time background events and CIP information to veto background from the interaction of the beam particles with the collimators in the beam pipe (see Section 4.3.1).

To determine the inefficiency of these conditions for the most part of the subperiods the subtrigger **s57** is used as a monitor. The obtained inefficiency is shown in Fig. 7.34 (c) for the Per0607 period. The correction is applied to the MC events as an average single factor for each annual subperiod. The measured inefficiency decreases from 1.3% for Per0304 to 0.4% for Per0607 (see Appendix A).

Another possibility to determine the Veto efficiency is to use the Bethe-Heitler sample preselected with the **s61** subtrigger. For this sample the veto condition was modelled on the analysis level [105] and the fraction of events rejected by this constructed veto was calculated. The results are shown in Fig. 7.35 and are in a good agreement with the conventional measurement. For the beginning of the Per0304, where the **s57** had a veto condition and can not be used as a monitor for the veto efficiency measurement, the veto efficiency from this investigation is taken.

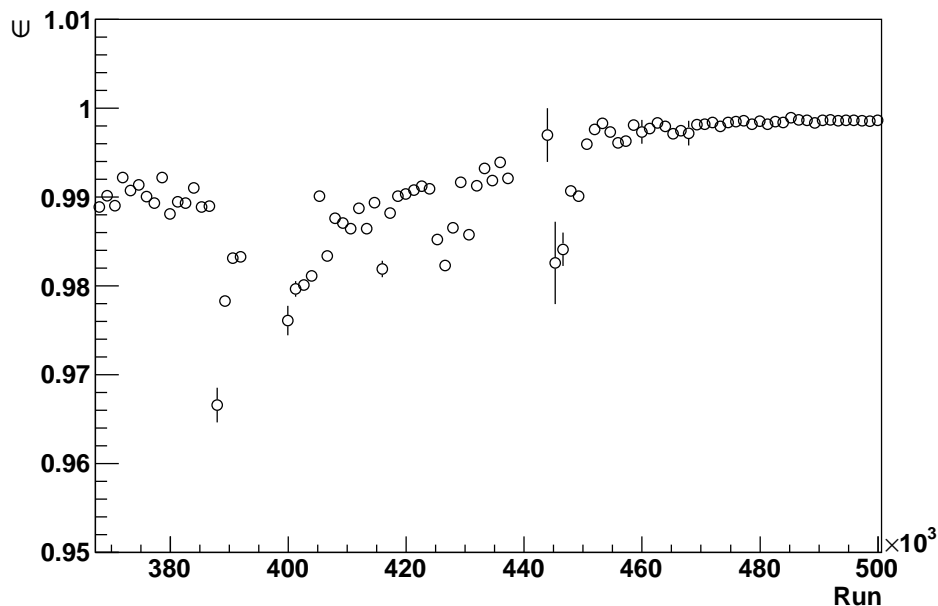


Figure 7.35: Inefficiency of the *Veto* condition determined with the Bethe-Heitler sample as a function of run number.

7.7.4 Track Conditions

For the subtrigger **s75** the level one FTT track condition is applied. The decision is based on the information from the CJC chambers and produced in analysis of the hits pattern in the $r - \phi$ plane [106]. During Per0304 period for the same purposes the DCRPh condition was used.

As a monitor for the investigation of this trigger condition the combination ((**s67** subtrigger) && LAr_electron_2 && CIP_T0) is used. The inefficiency of the *Track* condition demonstrates strong dependence on the number of central tracks for low multiplicities as it is shown in Fig. 7.36. The correction is applied as a function of the number of tracks separately for each annual subperiod.

7.7.5 Trigger Level 2 Condition

The level two topological trigger condition L2_LAr_electron is used for the **s75** subtrigger. In the analysis the efficiency of this subtrigger is important for events triggered by the LAr_electron_2 trigger element at low E_e . As a monitor the events with the **s67** and level one conditions from the **s75** are taken.

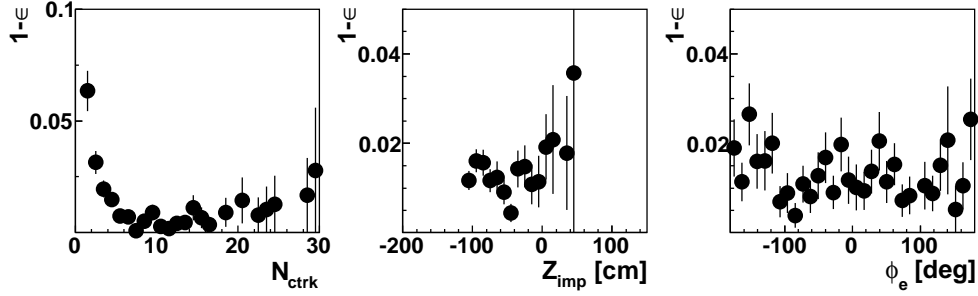


Figure 7.36: Inefficiency of the *Track* condition as a function of number of central tracks N_{ctrk} , Z_{imp} and ϕ_e for the Per0405 period.

The inefficiency is non-negligible only for the Per0304 ($\bar{\varepsilon} = 0.8\%$) and Per0405 ($\bar{\varepsilon} = 2\%$) periods (see Appendix A) with flat dependence on kinematic variables. The correction is applied as a single factor for each period.

7.7.6 Fiducial Volume Definition

The trigger decision is mainly based on information from the LAr. Due to technical reasons (like noise) several calorimeter cells and CIP pads were inefficient even for the high energy scattered electron (where the efficiency is supposed to be 100%). These regions were excluded from the analysis with the fiducial volume cut. This cut is applied as a function of ϕ and Z_{imp} of the scattered electron, where statistics is sufficient to identify inefficient regions (not very high Z_{imp}). It takes into account time variation of the inefficient regions map. The fiducial volume for the Per06em period is shown in Fig. 7.37

7.7.7 Trigger Efficiency Uncertainty

The uncertainty of the trigger efficiency determination consists of several components: a common part of all subtriggers from the T0 and Veto conditions, electron triggering for the Nominal and HighY parts of the analysis, and the reweighing of the “electron” part of **s75** subtrigger to **s67**.

An uncertainty $\sigma_{\text{CIP_T0}}$ on the inefficiency $\bar{\varepsilon}(\text{CIP_T0})$ is estimated to be 1% for Per0304 and 0.5% for other periods. For an uncertainty σ_{T0} for the whole T0 condition efficiency we take $\sigma_{\text{T0}} = \sigma_{\text{CIP_T0}} \cdot \bar{\varepsilon}(\text{LAr_T0} \ \&\& \ \text{!CIP_T0_nextbc})$. The Veto uncertainty σ_{Veto} is estimated for each annual period and is about 0.5% (see Appendix A).

For the triggering of the electron in the Nominal part of the analysis we take the uncertainty of the trigger efficiency to be 50% of the measured inefficiency.

As the electron trigger efficiency uncertainty in the HighY part of the analysis we take the statistical uncertainty of the trigger efficiency measurement

$$\sigma_{\varepsilon} = \sqrt{\frac{N_T}{N_M} \left(1 - \frac{N_T}{N_M}\right) \frac{1}{N_M}} = \sqrt{\frac{\varepsilon \bar{\varepsilon}}{N_M}}, \quad (7.22)$$

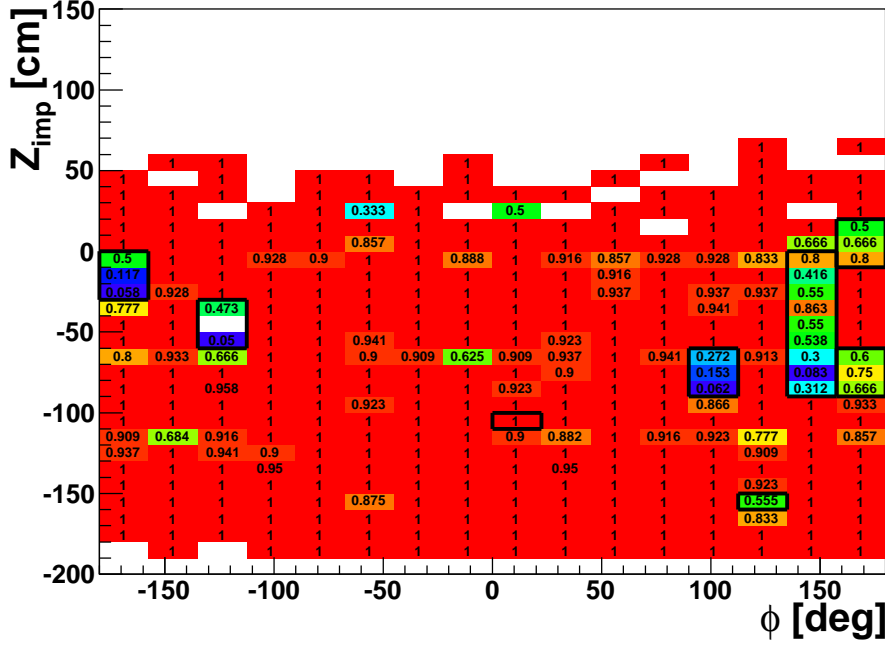


Figure 7.37: Efficiency of the “electron” part of the `LAr_electron_1` trigger element in the $Z_{\text{imp}} - \phi$ plane with the fiducial volume boundaries (black rectangles) for the Per06em period.

where N_M is the number of the events in a monitor sample, N_T denotes number of the events from the monitor sample passed the trigger condition criteria. In this notations the estimation of the efficiency $\varepsilon = N_T/N_M$.

If $\varepsilon > 1/2$ which is the case everywhere for the analysis, the inclusion of the additional subtrigger, which increase the trigger efficiency, will result in decrease of the trigger efficiency uncertainty. Despite the statistics will not increase significantly (and the statistical uncertainty will almost not decrease), the systematic uncertainty of the measurement will improve considerably. This is the reason for complication of the analysis with the usage of the trigger mix.

To estimate the uncertainty in the region of the HighY part of the analysis, we suppose that for each bin where we measure the efficiency the number of the monitor events $N_M = 100$ (this assumption overestimates N_M by a factor of 2 in some bins and is safe). Then the uncertainty is calculated as⁹

$$\sigma_\varepsilon^{\text{bin}} = \sqrt{\frac{\varepsilon^{\text{bin}} \cdot \bar{\varepsilon}^{\text{bin}}}{100}} \quad (7.23)$$

Finally for the data-to-data reweighing procedure of events triggered by `s75` only the uncertainty sources are from the CIP_T0, L2 and FTT trigger weights. The CIP_T0 uncertainty is not more than 1% (see above), the L2 condition uncertainty is about 0.1% and the the relative uncertainty of the FTT inefficiency is 50%. All these

⁹We apply also the additional protection conditions: if $\sigma_\varepsilon^{\text{bin}} > \varepsilon^{\text{bin}}$, then $\sigma_\varepsilon^{\text{bin}} = \varepsilon^{\text{bin}}$, and if $\sigma_\varepsilon^{\text{bin}} > \bar{\varepsilon}^{\text{bin}}$, then $\sigma_\varepsilon^{\text{bin}} = \bar{\varepsilon}^{\text{bin}}$

uncertainties summed together being propagated to the cross section uncertainty are well below 0.1%. For this reason these uncertainties are not taken into account.

To obtain the total trigger systematic uncertainty all sources are added in quadrature.

7.8 Background Treatment

As it was discussed in Section 7.1 two different background treatments are used in the analysis.

The HighY branch is characterized by relatively small energy of the scattered electron and suffers from the large background contamination. Almost all processes which produce fake NC candidates have approximately the same probability to provide an electron candidate of the “right” electric charge (charge of the candidate coincide with the charge of the beam’s lepton) and “wrong” charge (charge of the candidate is opposite to the charge of the beam’s lepton). At moderate candidate’s energy the track bends enough to ensure a reliable measurement of the charge of the candidate. The wrong charge candidates in data give an estimation of the amount of the background events among the selected right charge candidates. This contribution can be then statistically subtracted. In this way the acceptance and trigger efficiency for the background does not enter to the cross section measurement. Quality of the charge measurement and the ratio of the numbers of the wrong and right charge background events (charge asymmetry) contribute to the uncertainty of the measurement.

In the region of the Nominal analysis the charge determination is not reliable at high electron energy (the curvature of the candidate’s track is too small) and we accept all candidates. The backgrounds are simulated with the Monte Carlo (see Section 6). Generally MC background events which passed the selection criteria are very special¹⁰ and the relative uncertainty on the simulation is large. On the other hand the background contamination in this region is small, such that the absolute uncertainty is also small.

7.8.1 Charge Determination

In the HighY analysis only electron candidates with the “right” charge are selected. The “wrong” charge candidates are used for the statistical subtraction of the remaining background events.

To estimate an uncertainty on the charge measurement, the distributions of the wrong charge fraction of events at high scattered electron energies in data and signal MC are investigated as shown in Fig. 7.38.

At relatively small electron energy the fraction is large due to background events with the wrong charge (in data) and cases where the electron candidate from the HFS is recognized as a scattered electron (in data and simulation). With the rise of

¹⁰For example, for the case of photoproduction, to pass the selection cuts an event has to have a high energy isolated electron from the HFS. The probability to obtain such event depends on the hadronization model plugged into the MC generator.

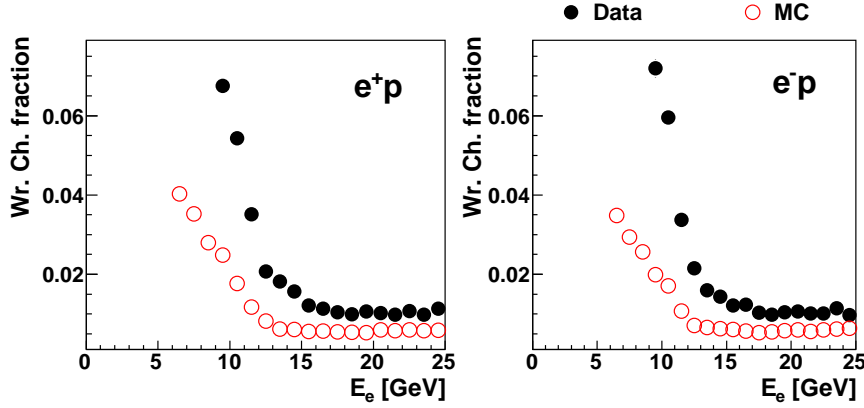


Figure 7.38: Fraction of wrong charge candidates in data and signal MC as a function of the scattered electron energy for the e^+p and e^-p data sets.

the energy both sources vanish and in the region of $E_e \in [15, 25]$ GeV the rate has a plateau, where only the wrong charge determination¹¹ contributes.

Each event with wrongly determined charge enters the cross section calculation twice: it does not appear in the data sample and is subtracted from the data sample in the background subtraction procedure then. Difference between data and MC in Fig. 7.38 is 0.5%. The correction applied to the cross section measurement is 1%. The uncertainty on the charge determination assumed to be 0.25% which leads to the 0.5% uncertainty on the cross section.

7.8.2 Background Charge Asymmetry

For the reliable application of the charge subtraction procedure in the HighY analysis possible difference between positively and negatively charged fake electron candidates from photoproduction background processes has to be taken into account. The full HERA II statistics accumulated in both e^+p and e^-p reactions was used to determine this asymmetry.

The source of the charge background asymmetry is the following. In the photoproduction a probability to obtain proton and antiproton of the same energy in the final state is the same. But for the proton energy released in the calorimeter it is just its kinetic energy while for the antiproton 2 GeV of additional energy from annihilation in the material of the detector should be added. Consequently antiprotons will deposit more energy in the calorimeter and more likely pass the energy requirement in the NC selection, producing more fake electrons.

To evaluate the charge asymmetry $A = N_{\gamma p}^- / N_{\gamma p}^+$ ¹², the ratio of negative and positive fake electron candidates in the photoproduction, the data from e^-p and e^+p periods have been used. Assuming that the efficiencies for the NC and photoproduction background are the same one can calculate

¹¹Due to the wrong reconstruction of the curvature's sign of the track.

¹²No asymmetry corresponds to $A = 1$.

$$A = \frac{N_{\gamma p}^-}{N_{\gamma p}^+} = \frac{N^-(e^+p)}{N^+(e^-p)} \cdot \frac{N(e^-p)}{N(e^+p)}, \quad (7.24)$$

where $N^\alpha(e^\beta p)$ is a number of the events in data with sign of the scattered candidate α obtained in $e^\beta p$ reaction, and $N = N^- + N^+$. The results for the background asymmetry as a function of the scattered electron energy E_e at low electron energy (where the background contribution dominates) is shown in Fig. 7.39a. The average value of the asymmetry is 1.02 with the statistical uncertainty of 0.02. The total numbers of events of both signs which represent the normalization factors in (7.24) depend also on the efficiency of the background registration.

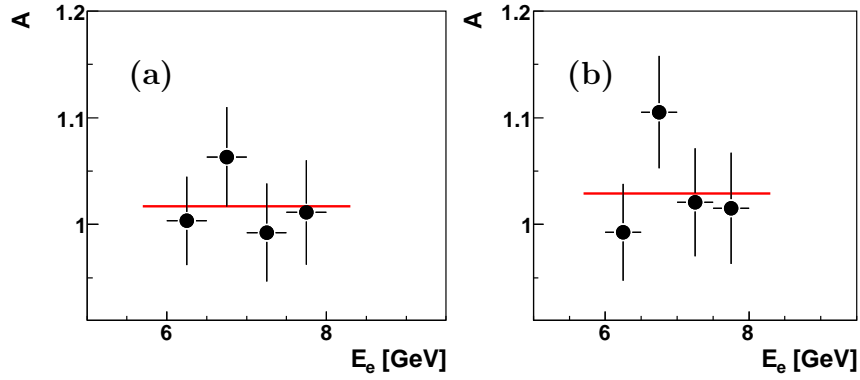


Figure 7.39: Charge asymmetry of the background measured using the e^+p and e^-p data sets with two methods (see in the text). The lines show the asymmetry values averaged over the bins.

A weak part of this method is a possible variation of the background and NC registration efficiencies from year to year. To avoid this, another method of the asymmetry calculation is used also: the event numbers in the ratio of the wrong charge background events are normalized to the numbers of the simulated NC events obtained taking into account annual variation of registration efficiency. The total uncertainty of the MC normalization is limited then by the knowledge of the luminosity of the data. To eliminate this uncertainty the MC distributions are normalized to the data:

$$A = \frac{N^-(e^+p)}{N^+(e^-p)} \cdot \frac{N_{MC}^{NC}(e^-p)}{N_{MC}^{NC}(e^+p)} \cdot \left[\frac{(N_{MC}^{NC}(e^+p) + N_{MC}^{bkg}(e^+p))/N(e^+p)}{(N_{MC}^{NC}(e^-p) + N_{MC}^{bkg}(e^-p))/N(e^-p)} \right]^{Tot}, \quad (7.25)$$

where index “tot” denote that all ratios are taken using total numbers of events accumulated in the histograms. Here we obtain a slight dependence on the simulation on the background contribution. The average asymmetry determined with this method is shown in Fig. 7.39b. The average value is 1.03 with the statistical uncertainty of 0.02.

The similar results were obtained using the photoproduction sample in data (see Section 7.8.3) where the background events of the “right” and “wrong” charges

for each period are directly tagged with the electron tagger (see also Section 7.8.3). The measured asymmetry value is 1.09 with the statistical uncertainty of 0.04.

From these measurements the value of the charge asymmetry is taken to be 1.03 with the uncertainty of 0.05.

The ratio of the numbers of the wrong charge candidates in Django for positron and electron runs was measured to be $A_{\text{wrch}} = 0.86$.

7.8.3 Photoproduction Background Using Pythia MC

In the Nominal part of the analysis Pythia MC is used to estimate photoproduction background. To check normalization of the photoproduction backgrounds simulated using Pythia, it was compared to the tagged photoproduction events in data. These data events were triggered using special photoproduction trigger element from ETag6 and are characterized by the electron in the electron tagger with the absence of the signal in the photon tagger. The cuts applied in data to select photoproduction events which satisfy the NC selection are

- Trigger element $TE115$ (electron tagger, ETag6) is fired, and $TE116$ (photon tagger, PhTag) is not fired.
- Cuts on the signal in the electron tagger to get the region where the acceptance is calculated: $4 < E^{\text{ETag}} < 20$ GeV and $-3 < X^{\text{ETag}} < 3$ cm.
- $20 < E - P_z < 45$ GeV.

The photoproduction which is detected by ETag6 and corresponds to the ETag6 acceptance calculation [107] occurs in the following kinematical region for Pythia MC

- $Q_{\text{gen}}^2 < 0.01$ GeV².
- $4 < E^{\text{gen}} < 12$ GeV.

The event weight of this MC is multiplied by the calculated acceptance of the ETag6. In addition, trigger efficiencies of **s67**, **s75** determined for NC events are applied to the γp Pythia events.

The general cuts for the NC selection applied to the data and MC (Django and Pythia) are:

- Scattered electron candidate with $E_e > 6$ GeV is found.
- The data events triggered with the subtriggers **s67** or **s75**.
- CJC vertex is reconstructed and electron DTRA track matches to the cluster ($D_{\text{DTRA}} < 12$ cm).
- $Q^2 > 75$ GeV².
- $|Z_{\text{vtx}}| < 35$ cm.
- $Z_{\text{imp}} > -190$ cm, cracks ($15 < Z_{\text{imp}} < 25$ cm, $|\phi_e - 45^\circ \cdot n| < 2^\circ, n = 0, \dots, 7$) are removed and the FidVol cut is applied.

- Cut on Compton events and background finders are applied.

To subtract the contribution of the genuine NC events in this γp sample the signal MC (Django) is used with the additional cut $E_\gamma^{\text{ISR}} < 6$ GeV which corresponds to the condition $E^{\text{PhTag}} < 6$ GeV in data (region where the $TE116$ is not sensitive). The $(E - P_z)$ distribution for the NC events peaks around $2E_e^0$ (see Fig. 7.40a). To normalize the MC contribution the kinematical region $52 < E - P_z < 62$ GeV which is free from photoproduction contribution is chosen. This normalized Django contribution then subtracted from the tagged events in data.

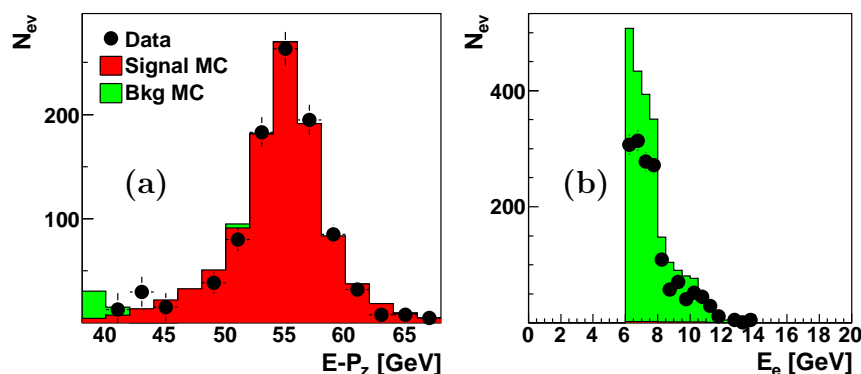


Figure 7.40: (a) The tagged data are combined with signal and background MCs after normalization of the Django contribution as a function of $E - P_z$. (b) Tagged photoproduction events in the HighY analysis domain. Both plots are for the e^+p period.

The distributions of the tagged photoproduction data events (with the subtracted estimation of the NC contribution) and simulation in the region of the Nominal analysis is shown in Fig. 7.41 as a function of the electron candidate energy. Data and simulation are found to be in good agreement. Thus no normalization correction for Pythia is needed.

The background simulation is checked also in the HighY region (see Fig. 7.40b). Here the discrepancy was observed up to 30%. The uncertainty on the background simulation normalization is taken for Nominal analysis to be 30%.

7.8.4 Rejection of Compton Events

The Compton events contribute to the NC sample and are treated as a background to the deep inelastic scattering process.

Two sets of the selection cuts against the Compton events are applied:

- Two electromagnetic candidates back to back in ϕ :
acoplanarity $\psi = \text{acos}(\cos(\phi_1 - \phi_2)) > 160^\circ$, where ϕ_1, ϕ_2 are azimuthal angles of the candidates.
- Number of tracks less than 3.

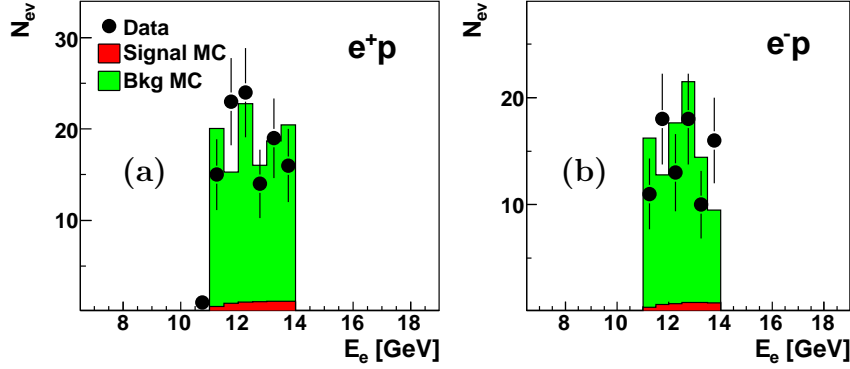


Figure 7.41: The tagged photoproduction events in the Nominal analysis domain for the (a) e^+p and (b) e^-p data sets.

- Veto on hadronic energy $E_{had} < 1$ GeV.
- Veto on muon energy $E_\mu < 1$ GeV.

for the case when the beam proton stays intact and another set

- Two electromagnetic candidates with $\psi > 170^\circ$.
- Number of tracks less than two.
- Cut on balance of transverse momentum $0.6 < P_t^{had}/P_t^e < 1.4$.
- Veto on muon energy $E_\mu < 1$ GeV.

with the tighter cut on the electromagnetic candidates allowing a larger contribution from HFS.

In Fig. 7.42 the fractions of the Compton events before and after application of these cuts in the selected NC sample are shown. The rate of true NC events rejected with the cut is also shown. This study was performed using simulated events. The WABGEN MC is used together with other background MCs only for the Nominal part of analysis. The rate of the elastic and quasi-elastic Compton events after the cut is below 0.5% and the loss of the NC events due to these cuts is found to be negligible. For this reasons no additional systematics related to the Compton contribution is applied.

7.8.5 Rejection of Non- ep Background

Small fraction of the NC candidates induced by non- ep interactions of cosmic muons, beam halo particles, self-excitation of electronics is recorded and passes the main selection cuts. This contribution is not simulated in Monte Carlo and is suppressed in data by special non- ep background finders [108] which are applied on the basis of the topology of these events.

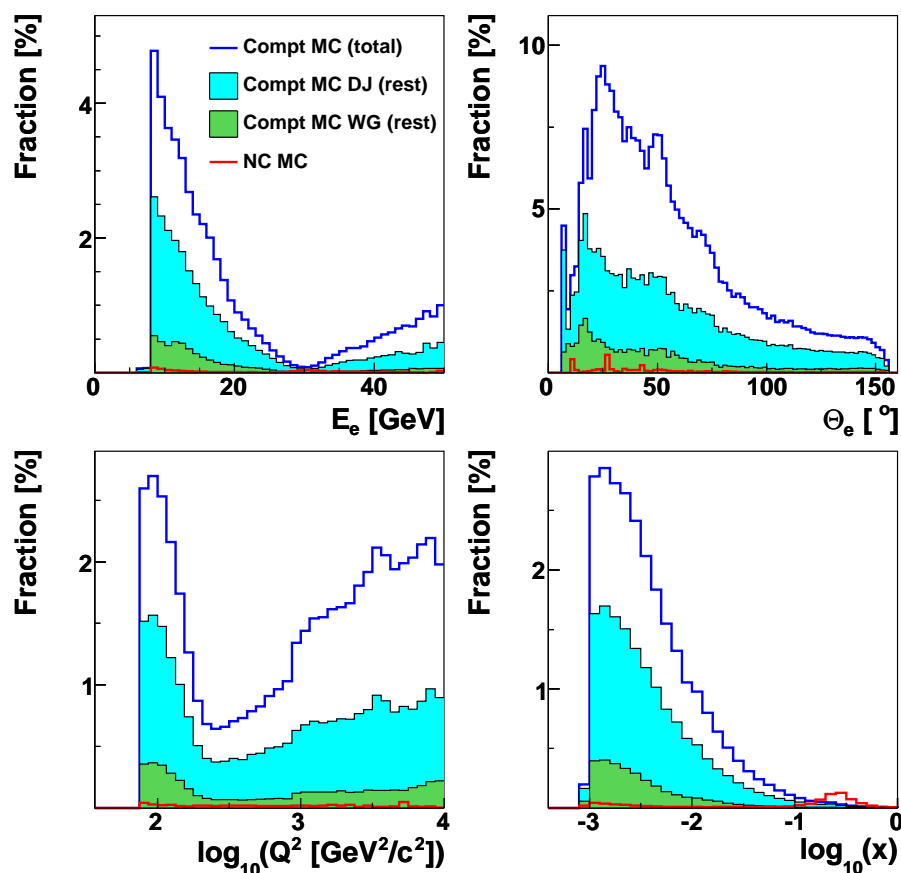


Figure 7.42: Fractions of events which passed the NC selection in simulation as a functions of E_e , Θ_e , $\log_{10}(Q^2 [\text{GeV}^2])$ and x . The samples are: (**deep blue line**) Compton events passed the NC selection before the anti-Compton cut, (**filled area**) Compton events after all the NC cuts including the anti-Compton cut, in particular (**light blue**) inelastic Compton events from Django generator and (**green**) elastic and quasi-elastic Compton events from WABGEN generator, (**red line**) true NC events rejected by the anti-Compton cut.

For each event in data and MC the background finder algorithms are applied and the flags “passed – not passed” are set up. Only several “safe” (Ibg) finders have been used for the analysis (see Table 7.3).

The cuts applied to identify the non- ep backgrounds are

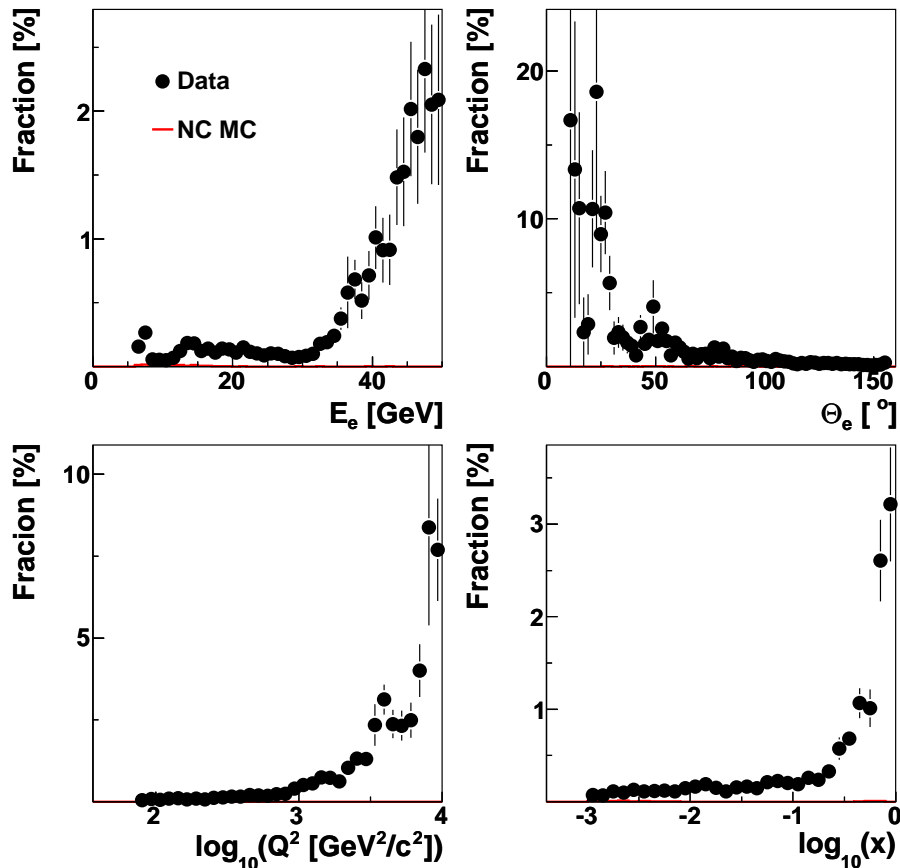
- $Ibg7$ and $P_t^{\text{had}}/P_t^e < 0.1$.
- $(Ibg0 \& \& Ibg1 || Ibg5 \& \& Ibg6 || Ibg6 \& \& Ibg7 || Ibg7 \& \& Ibg5)$ and $P_t^{\text{had}}/P_t^e > 0.1$.
- $Ibg5 || Ibg6$ and $P_t^{\text{had}}/P_t^e < 0.5$.

The fraction of the data and true NC events in MC which were rejected by these cuts is shown in Fig. 7.43.

In general non- ep background events contribute homogeneously along Z_{imp} , such that the relative fraction grows with the Q^2 . For the $Q^2 > 5000 \text{ GeV}^2$ the visual

Finder	Pattern	Ibg bit #
HALAR	High energetic cluster from halo without associated track	0
HAMULAR	High energetic cluster from halo without associated track	1
COSMUMU	Two opposite muon tracks matching in Θ and ϕ	5
COSMULAR	At least one muon with 90% of energy deposited in LAr	6
COSTALAR	Two opposite clusters in the Tail Catcher with 85% of energy deposited in LAr	7

Table 7.3: Background finding algorithms [108] used in the analysis.

Figure 7.43: Fractions of the data (black) and true NC events in MC (hardly visible line in red) were rejected by the non- ep cuts.

scan of the NC candidates has been done and the found non- ep background events were removed.

7.9 Vertex Reweighting in MC

The interaction vertex in the H1 experiment is simulated in accordance with the vertex distribution in real data. Each good or medium quality data run with its unique vertex distribution and other run-dependent conditions is represented in a Monte Carlo simulation. The number of the Monte Carlo events for the given run is proportional to the luminosity of the data collected in this run. If one excludes certain run range in the analysis from the data, the same run range is excluded also from MC.

Still the description of the vertex distribution in MC could be not perfect. The discrepancy in the vertex distribution along the z axis cause biases in the reconstruction of the Θ_e angle of the scattered electron. The imperfection of the description even after such a “data-like” simulation occurs from the differences in the lumi per run used for the vertex simulation during the MC processing and in the analysis with specific HV conditions.

For a fine tuning of the vertex distribution, an additional reweighting at the analysis level is performed. The reweighting procedure brings the MC vertex distribution as close as possible to the data within the region of interest¹³ for the selected runs in the analysis.

To achieve that the following procedure is applied. We obtain the Z_{vtx} distributions at reconstructed level for the data and MC with the full NC selection plus two additional criteria

- The polar angle of the scattered electron is required to be $\Theta_e < 145^\circ$ to avoid a bias due to geometrical acceptance for the scattered electron in the LAr calorimeter.
- Inelasticity $y_h > 0.1$ and number of reconstructed tracks $N_{\text{Trk}} > 1$ are required to ensure a good reconstruction of the hadronic final state and thus the interaction vertex.

The ratio of these distributions for data and MC is fitted within the Z_{vtx} range of the analysis with the polynomial function ensuring normalization of the result to unity, such that the reweighting function is

$$f_{\text{rew}}(z) = \frac{\sum_{i=0}^{10} A_i z^i}{A_{11}} . \quad (7.26)$$

This reweighting function is applied in MC using the generated vertex position. After that each time when the analysis starts, the H1OO software runs over the entire MC file (for all MC files used in the particular job), calculates the integral before and after the reweighting within the selected Z_{vtx} range at generated level and scales the MC weight such that the MC luminosity stays the same. This normalization is the product of three factors: correction for an exclusion of some runs on the analysis level due to run conditions, for the (small) change of the luminosity within the

¹³We take the region $|Z_{\text{vtx}}| < 35$ cm. See. Section 8

analysis range due to the reweighing¹⁴, and for the cut on the vertex position in the simulation.

The reconstructed Z_{vtx} distribution before and after the reweighing is shown in Fig. 7.44.

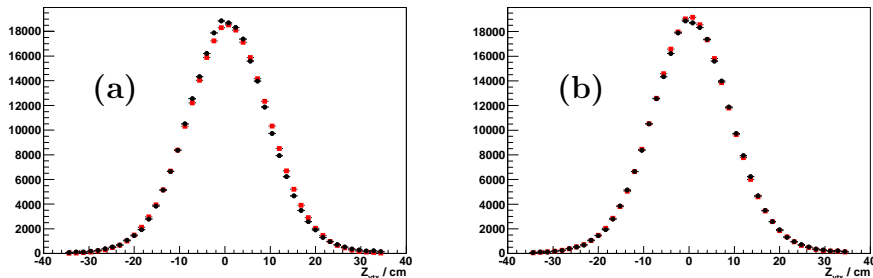


Figure 7.44: The distribution of interaction vertex Z_{vtx} for data (black) and MC (red) (a) before and (b) after the vertex reweighing in simulation.

7.10 QED Radiation Correction Uncertainty

The DJANGO14 generator used in the analysis takes into account QED radiative correction in one loop calculations. This allows to include an emission of one additional photon in the NC event generation. The implementation of this first order correction is checked with the analytical calculation by the HECTOR [29] package. The ratio of the NC cross sections obtained with these programs is shown in Fig. 7.45. The comparison is done in electron variables with the cut $E - P_z > 35$ GeV. Statistics of the Django event sample generated for the test is 50 mio. events. The two calculations are found to be in a good agreement.

The uncertainty on the QED radiative correction accounts for residual deviations of the ratio from unity and is taken to be 0.3% for $y < 0.63$ and $x < 0.1$ (central region), 2% for $x > 0.3$ (region of high x) and 1% otherwise.

7.11 Run Selection

During the data taking the data are collected in so-called runs — short time periods ($\lesssim 1$ hour) characterized by stable detector conditions. In one fill of the accelerator rings¹⁵ many runs are taken. The quality of a run was classified as good (all major detector components are worked well), medium (some components have problems) or poor (serious hardware problems).

For each detector the High Voltage (HV) status was checked. It shows whether the device is in operation at the certain moment. For example, tracker could be

¹⁴Originally the reweighing function is normalized to unity as it is described above, but after an exclusion of some runs the shape and therefore the normalization of the reweighed vertex distribution could be slightly changed.

¹⁵The lifetime of the beams at the HERA accelerator is about 10 h and is determined primarily by the lepton beam.

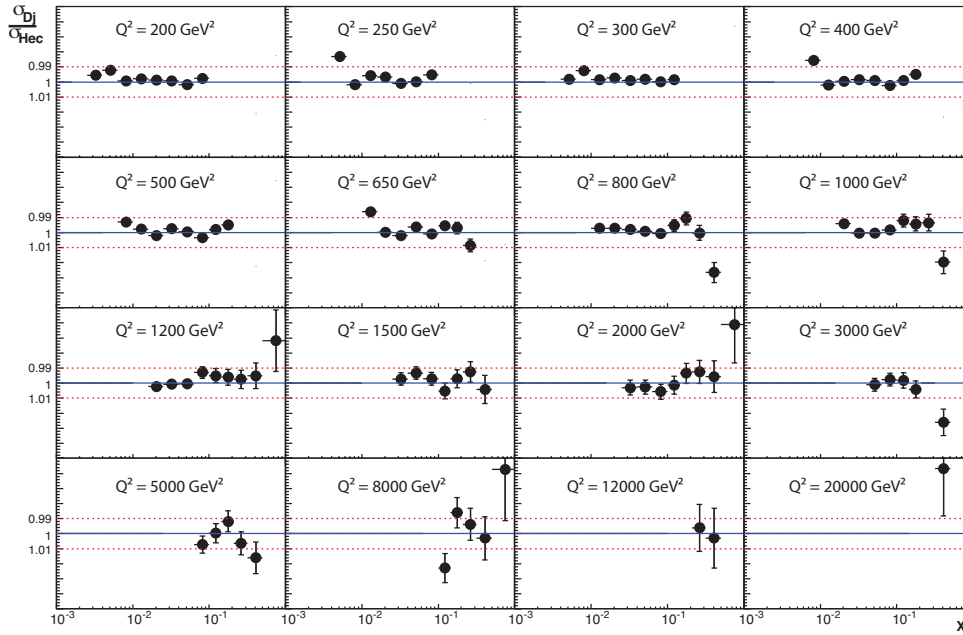


Figure 7.45: The ratio of the NC cross sections calculated with the DJANGO14 and HECTOR programs.

overloaded with the large flux of incoming particles from short beam instabilities and be switched off for several seconds (so-called “trip”) to avoid damage. The HV status of the detectors was inquired each ten seconds.

To select the data for the analysis the following run selection is applied

- The quality of the run is good or medium. Several run periods were excluded due to known problems with the hardware.
- Minimum luminosity of the run is 0.2 nb^{-1} (this corresponds to approximately 10 s of data taking).
- From each run only that part was taken, when the HV status is “ON” for the CJC, LAr, ToF, CIP devices, the LAr trigger and the Lumi system.
- The **s67** subtrigger is not prescaled.
- The polarization is measured. On the analysis level, runs with polarization less than 20% are excluded.

Chapter 8

Neutral Current Cross Section Measurement

8.1 Binning, Acceptance, Purity and Stability.

For the cross section measurement in the analysis the binning in the (x, Q^2) plane presented in Fig. 8.1 is used.

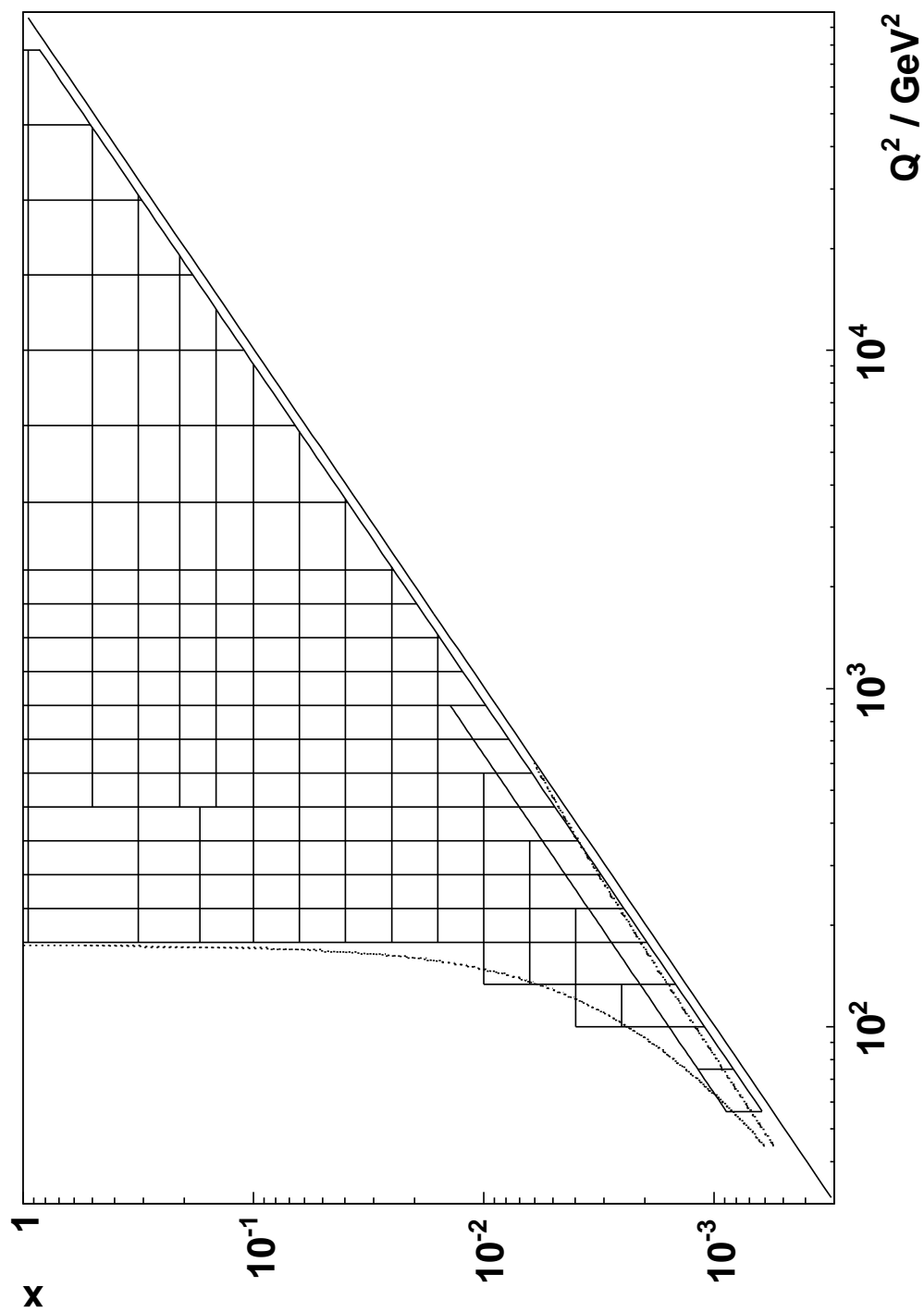
In general it consists of rectangular bins in the (x, Q^2) coordinates with an additional band at low y and moderate Q^2 where the bins are rectangular in the (y, Q^2) coordinates.

At low Q^2 the measurement is limited by the LAr acceptance and the energy measurement of the scattered electron (dotted lines in Fig. 8.1 correspond to $\Theta_e = 155^\circ$ and $E_e = 6$ GeV). At high y the y -band cuts several $x - Q^2$ bins such that only small “triangles” are left. These “triangles” are joined to the nearest $x - Q^2$ bins as it is shown in the plot. The bins at the highest values of x and $\log_{10}(Q^2 [\text{GeV}^2]) < 2.65$ are joined because of a degradation of a resolution in this region. The bin’s edges and bin’s centres are given in Table 8.1.

The y -band bins cover $y > 0.63$ with the bin centres at $y_{\text{centre}} = 0.75$ in the region $\log_{10}(Q^2 [\text{GeV}^2]) < 2.95$. The line $y_{\text{max}} = 0.95$ is shown in the plot. The actual upper boundary of the bins is determined by the analysis selection (varies from $y = 0.90$ to $y = 0.93$, see Section 8.4).

For the reconstruction of the kinematical variables electron and $e\Sigma'$ methods are used. The consistency of the cross section results using these two methods is demonstrated in Fig. 8.2. The resulting cross sections are combined to a final cross section. A choice of the certain method for the given point is done on the basis of the best obtained total error of the measurement shown in Fig. 8.3. The transition from one method to the other happens at $y = 0.19$. At smaller values of y one uses the electron method results, otherwise the $e\Sigma'$ method is used.

The bins accepted for the measurement should be in the regions, where imperfections of the Monte Carlo description of the experimental setup is not crucially important, so the MC correction is not very large. The bin sizes have to be taken such that the resolution effects do not spoil the measurement (far migrations between distant bins are difficult for simulation, and the uncertainty estimation becomes more complicated, see Section 5.2). The way to estimate reliability of the measurement in the bin is to calculate an acceptance (\mathcal{A}), purity (\mathcal{P}) and stability (\mathcal{S}) using

Figure 8.1: The binning scheme in (x, Q^2) plane.

$\log_{10}(Q_{\min}^2 [\text{GeV}^2])$	$\log_{10}(Q_{\max}^2 [\text{GeV}^2])$	$Q_{\text{centre}}^2 [\text{GeV}^2]$	$\log_{10}(x_{\min})$	$\log_{10}(x_{\max})$	x_{centre}
1.75	1.875	60	-3.0	-2.8	0.0013
1.875	2.00	90	-2.8	-2.6	0.0020
2.00	2.125	120	-2.6	-2.4	0.0032
2.125	2.25	150	-2.4	-2.2	0.0050
2.25	2.35	200	-2.2	-2.0	0.0080
2.35	2.45	250	-2.0	-1.8	0.0130
2.45	2.55	300	-1.8	-1.6	0.0200
2.55	2.65	400	-1.6	-1.4	0.0320
2.65	2.75	500	-1.4	-1.2	0.0500
2.75	2.85	650	-1.2	-1.0	0.0800
2.85	2.95	800	-1.0 ^h	-0.84 ^h	0.1300 ^h
2.95	3.05	1000	-1.0 ^l	-0.767 ^l	0.1300 ^l
3.05	3.15	1200	-0.84 ^h	-0.68 ^h	0.1800 ^h
3.15	3.25	1500	-0.767 ^l	-0.50 ^l	0.1800 ^l
3.25	3.35	2000	-0.68 ^h	-0.50 ^h	0.2500 ^h
3.35	3.55	3000	-0.50 ^h	-0.30 ^h	0.4000 ^h
3.55	3.78	5000	-0.50 ^l	-0.02 ^l	0.4000 ^l
3.78	4.00	8000	-0.30 ^h	-0.02 ^h	0.6500 ^h
4.00	4.222	12000			
4.222	4.444	20000			
4.444	4.666	30000			
4.666	4.888	50000			

Table 8.1: The Q^2 and x bin's edges and central values. Indices “ l ” and “ h ” denote the binning scheme below and above $\log_{10}(Q^2 [\text{GeV}^2]) = 2.65$.

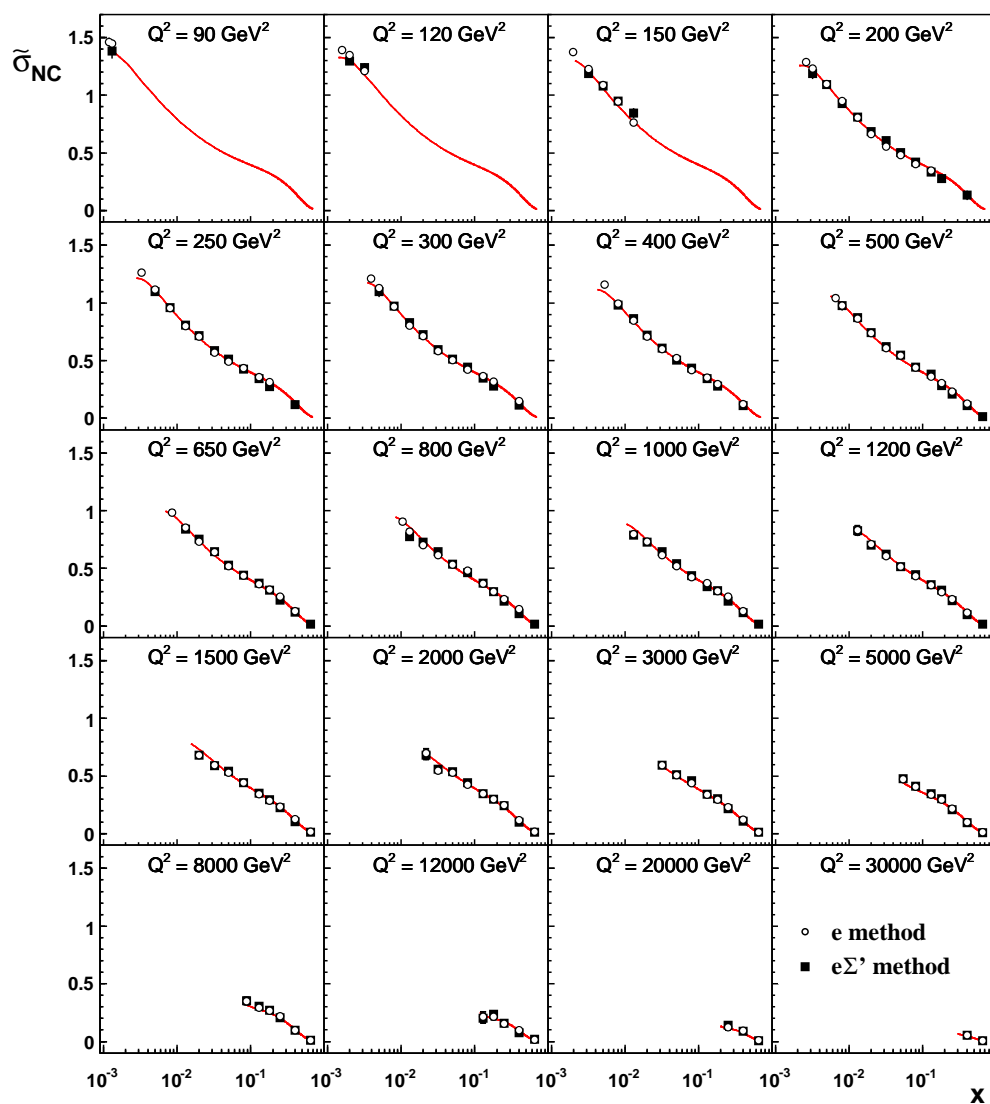


Figure 8.2: The NC cross section measured using the electron (open circles) and $e\Sigma'$ (filled squares) methods for the e^+p data period.

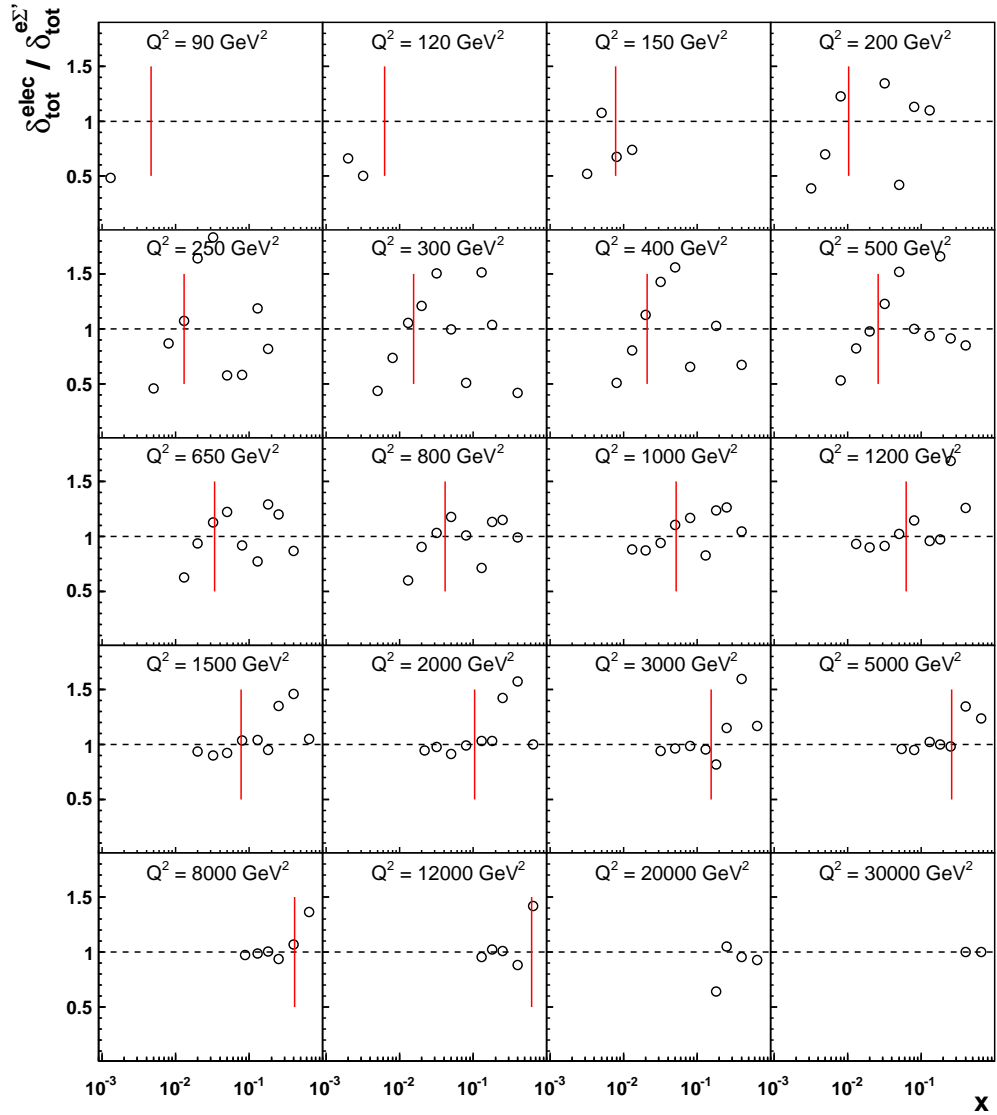


Figure 8.3: Ratio of the total uncertainties of the measurement obtained with the electron and $e\Sigma'$ methods. Vertical line marks $y = 0.19$ transition boundary (where it is applicable).

simulated events. One defines

- N_{gen}^i : the total number of events generated in bin i .
- N_{rec}^i : the total number of events reconstructed in bin i .
- N_{stay}^i : the number of events generated in bin i and reconstructed at the same bin i .
- N_{lost}^i : the number of events being generated in bin i are not reconstructed in any bin.

Then

$$\begin{aligned}\mathcal{A}^i &= \frac{N_{\text{rec}}^i}{N_{\text{gen}}^i}, \\ \mathcal{P}^i &= \frac{N_{\text{stay}}^i}{N_{\text{rec}}^i}, \\ \mathcal{S}^i &= \frac{N_{\text{stay}}^i}{N_{\text{gen}}^i - N_{\text{lost}}^i}.\end{aligned}\tag{8.1}$$

The acceptance shows the overall correction needed from the detector effects. If the MC describes the detector well, the true number of events in data $N_{\text{data}}^{\text{true}}$ occurred in a certain bin is

$$N_{\text{data}}^{\text{true}} = \frac{N_{\text{data}}^{\text{rec}}}{\mathcal{A}}.\tag{8.2}$$

Purity and stability quantify the smearing effects. Purity shows how many events reconstructed in a certain bin were generated in this bin. Stability is the ratio of the number of events which stay in a certain bin to the total number of events generated in this bin and passed the selection criteria. The $(1 - \mathcal{S})$ fraction of events migrates to the other bins.

For the analysis the bins with

$$\mathcal{A} > 0.2, \mathcal{P} > 0.3, \mathcal{S} > 0.3\tag{8.3}$$

are chosen.

The acceptance, purity and stability for the positron and electron data samples are shown in Fig. 8.4.

8.2 Cross Section Calculation

Using the number of reconstructed NC data events in the certain bin $N_{\text{NC data}}^{\text{rec}}$, luminosity of the data $\mathcal{L}_{\text{data}}$ and the acceptance correction \mathcal{A} , the measured cross section at a specific point (x_c, Q_c^2) which belongs to this bin is calculated as

$$\frac{d^2\sigma^{\text{meas}}}{dx dQ^2}(x_c, Q_c^2) = \frac{N_{\text{NC data}}^{\text{rec}}}{\mathcal{L}_{\text{data}} \cdot \mathcal{A}} \cdot \delta_{\text{cbc}}(x_c, Q_c^2).\tag{8.4}$$

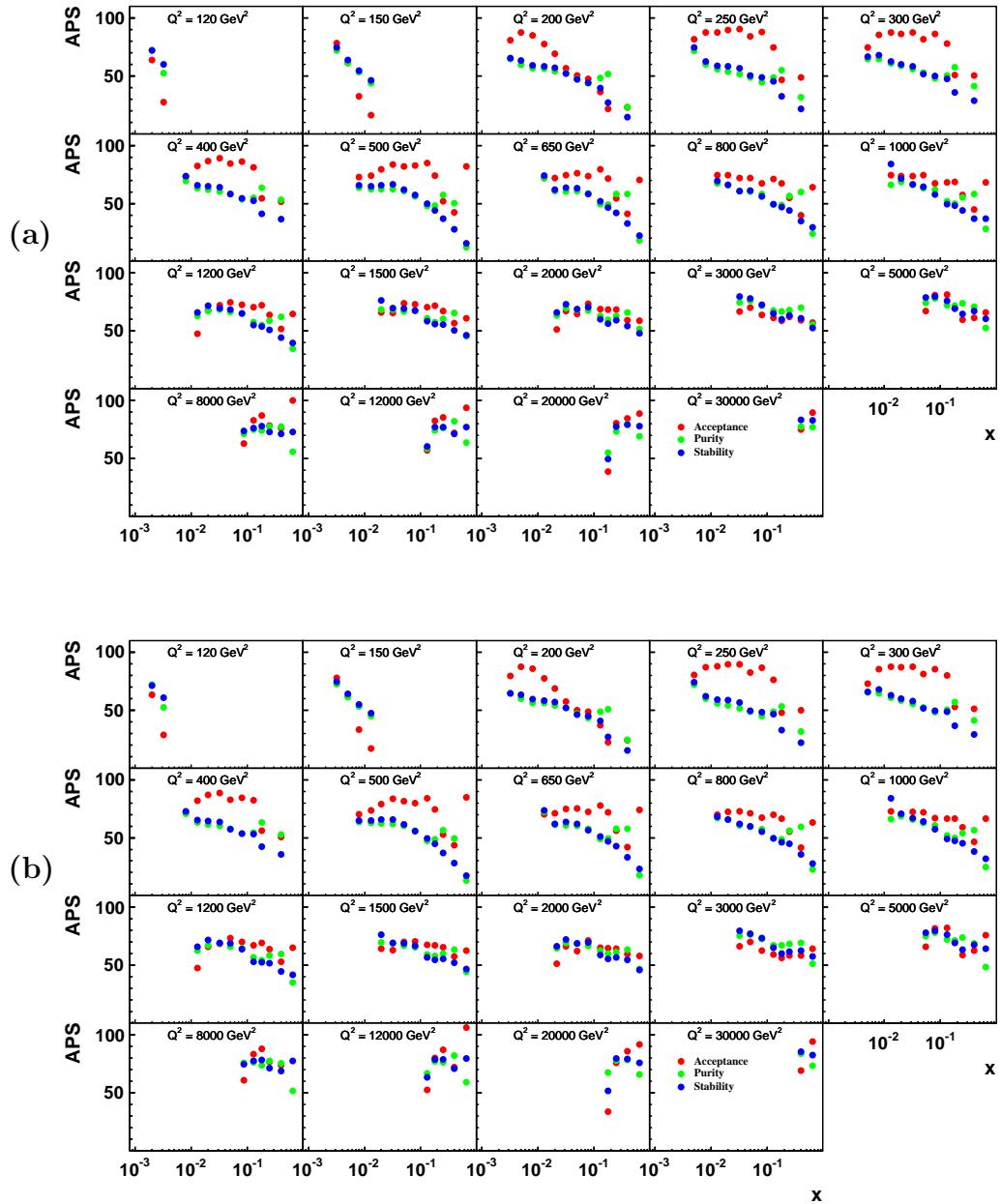


Figure 8.4: The acceptance, purity and stability for the (a) e^+p and (b) e^-p data periods.

Here the term δ_{cbc} is the so-called centre of bin correction which relates the double differential cross section at a point and the integral over the bin. It is calculated in theory as

$$\delta_{\text{cbc}}(x_c, Q_c^2) = \frac{\frac{d^2\sigma}{dx dQ^2}(x_c, Q_c^2)}{\int_{\text{bin}} \frac{d^2\sigma}{dx dQ^2}}. \quad (8.5)$$

Introducing the number of reconstructed events in MC $N_{\text{NC MC}}^{\text{rec}}$, the luminosity of the MC sample \mathcal{L}_{MC} , the equation (8.4) can be re-written as (see also the discussion in Section 8.3)

$$\frac{d^2\sigma^{\text{meas}}}{dx dQ^2}(x_c, Q_c^2) = \frac{N_{\text{NC data}}^{\text{rec}}}{N_{\text{NC MC}}^{\text{rec}}} \cdot \frac{\mathcal{L}_{\text{MC}}}{\mathcal{L}_{\text{data}}} \cdot \frac{d^2\sigma_{\text{Born}}^{\text{th}}}{dx dQ^2}(x_c, Q_c^2), \quad (8.6)$$

where the last term is the double differential cross section at the bin centre calculated at the Born level in the SM theory with the same proton structure functions as they are used for the MC generation.

$N_{\text{NC data}}^{\text{rec}}$ and $N_{\text{NC MC}}^{\text{rec}}$ are the numbers of a genuine NC events reconstructed in the given bin. They are obtained as a difference between the total number of the reconstructed events in the bin $N_{\text{data}}^{\text{rec}}$ and $N_{\text{MC}}^{\text{rec}}$ and the estimation of the number of background events in the same bin.

For the data

$$N_{\text{NC data}}^{\text{rec}} = N_{\text{data}}^{\text{rec}} - N_{\text{MC}}^{\text{bkg}} - A(N_{\text{data}}^{\text{wrch}} - N_{\text{MC}}^{\text{wrch}}) - A_{\text{wrch}} N_{\text{MC}}^{\text{wrch}}. \quad (8.7)$$

The first two subtracted terms are contributions from the background simulation ($N_{\text{MC}}^{\text{bkg}}$, used in the Nominal part of the analysis) and estimation of the background using wrong charge events (N^{wrch} , used for the HighY part of the analysis) corrected to the charge asymmetry¹. It is assumption that the wrong charge candidates are either from the photoproduction or from the fake electron in the genuine NC event; to take the latter into account we estimate this fraction in MC obtaining $N_{\text{MC}}^{\text{wrch}}$ and subtract it from the data. These background estimation techniques are applied in the non-intersecting regions of the phase space and therefore they can be summed.

Both for data and MC the wrong charge fraction coming from the genuine NC events is subtracted with the appropriate asymmetry factors. For the simulation one has

$$N_{\text{NC MC}}^{\text{rec}} = N_{\text{MC}}^{\text{rec}} - A_{\text{wrch}} N_{\text{MC}}^{\text{wrch}}. \quad (8.8)$$

It was checked that the neglect of the last term both for $N_{\text{NC data}}^{\text{rec}}$ and $N_{\text{NC MC}}^{\text{rec}}$ does not affect the measured cross section (the effect is below 0.1%).

8.3 Meaning of the Measurement

In the experiment we count the number of data events N_{data} registered in a $x - Q^2$ bin. This number corresponds to a convolution of the exact cross section for the NC

¹The asymmetry factors were determined as ratios of the numbers of the wrong charge candidates in positron and electron runs. Consequently for the Per0304 and Per0607 numbers for asymmetries from the Sections 7.8.2, 7.8.1 should be taken directly, and for Per0405 and Per06em these values should be inverted.

process Σ^e with the detector efficiency $\varepsilon_{\text{data}}$ (here we denote the cross section at a point as $\Sigma = d^2\sigma/dxdQ^2(x, Q^2)$)

$$N_{\text{data}} = \int_{\text{bin}} \Sigma^e \varepsilon_{\text{data}}. \quad (8.9)$$

The theoretical calculation can provide an approximate prediction for the cross section. Let us assume that we can calculate in theory the cross section in zero (Born) and n -th order in electroweak theory, using a certain model for the parametrization of the hadronic current (see for example, Section 2.3.2). Then the Born in EW Σ^0 (compare to Sections 2.4, 2.5) and n -th order Σ^n cross sections can be calculated. Using Σ^n for the simulation, one obtains a number of MC events in the bin N_{MC} similarly to (8.9).

Let us assume now that the electroweak and hadronic corrections are small. Then

$$\begin{aligned} \Sigma^e &= \Sigma^0(1 + \delta_{\text{EW}}^\infty)(1 + \delta_{\text{had}}) = \Sigma_{\text{had}}^0(1 + \delta_{\text{EW}}^\infty), \\ \Sigma^n &= \Sigma^0(1 + \delta_{\text{EW}}^n). \end{aligned} \quad (8.10)$$

where $\delta_{\text{EW}}^\infty$ (δ_{EW}^n) and δ_{had} are a correction to all higher orders electroweak effects (correction to the higher orders electroweak effects up to n -th order) and a correction to the “true” proton structure respectively. The Σ_{had}^0 denotes the NC cross section as it would be calculated with the true proton structure functions and in Born approximation in EW theory.

Then the formula (8.6) used in the analysis for the cross section calculation reads

$$\Sigma^{\text{meas}} = \frac{N_{\text{data}}}{N_{\text{MC}}} \frac{\mathcal{L}_{\text{MC}}}{\mathcal{L}_{\text{data}}} \Sigma^0 = \Sigma_{\text{had}}^0 \frac{1 + \delta_{\text{EW}}^\infty}{1 + \delta_{\text{EW}}^n}. \quad (8.11)$$

Here the correction from the integration over the bin was neglected, and we assume also $\varepsilon_{\text{data}} = \varepsilon_{\text{MC}}$ for simplicity. One sees that under such procedure the measured cross section Σ^{meas} is the Born NC cross section, multiplied by the ratio of the EW corrections. No matter which exactly proton structure was taken for the theoretical input (it could be even an empirical model obtained not in the perturbative calculations, like in [109]), the result would correspond to the “true” proton structure.

For the moment the full higher order corrections beyond the one photon emission for the NC process are not known. Let us remind, that the signal MC in the analysis (Django) takes into account one photon emission from the lepton line. The higher order QED corrections are not taken into account. This defines the meaning of the measured cross section.

There are several theoretical calculations which estimate the effect of the higher order corrections. To investigate the value of the last term in (8.11) the HECTOR program has been used.

This HECTOR program was used with two setups. The Standard (Std) setup is the one loop calculation. It is in use for the Django generator.

The Full setup includes the following parameters:

- IOPT = 1: allows the QED LLA radiative correction to be calculated in the first and higher orders (the HELIOS branch of HECTOR),
- IEXP = 1: soft photon exponentiation is allowed,

- IORD = 3: the QED corrections to $\mathcal{O}(\alpha L)$ and $\mathcal{O}((\alpha L)^2)$ are summed and the soft photon exponentiation is included,
- ICOR = 5: ISR, FSR and Compton peak contributions are included,
- ICMP = 1: a one-fold Compton integration is used for the Compton correction,

and follows the Django setup for the first order correction.

The ratio of the double differential cross sections $\sigma_{\text{Hec}}^{\text{Full}}/\sigma_{\text{Hec}}^{\text{Std}}(x_e, Q_e^2)$ is shown in Fig. 8.5. The prediction for the NC cross section is the same for the high y region and differ by several percent at low y region. Higher values of Q^2 lead to higher values of y at which the correction becomes significant. The general picture is stable against the variation of the condition under which the comparisons are done, like switching on/off the Compton contribution and cut on the W variable.

Another electromagnetic correction which is also not taken into account (see Section 6.1) is related to the possibility of a photon emission from the quark line. Such correction would depend on the quark mass m_q via terms like $\ln(Q^2/m_q^2)$ if calculated in the on-mass-shell scheme [29]. On one hand this means that the effect should be smaller for quarks than for electron, on the other hand it makes the theoretical estimation dependent on the quarks masses and on the scheme which is used for these masses extraction, etc. Absence of such correction modifies the exact meaning of (2.34) (and similarly for (2.44)). This should be taken into account in the usage of the measurements (for example, absorbed into the parton distributions or fragmentation functions, see [110]).

8.4 Neutral Current Event Selection

The Neutral Current selection criteria are described below.

- Run selection which ensure good quality of the data and reliable measurement of the polarization (Section 7.11).
- Scattered electron candidate found in the LAr calorimeter with the energy $E_e > 6$ GeV.
- $Q_e^2 > 75$ GeV².
- If $y_e > 0.63$ and $\log_{10}(Q_e^2 [\text{GeV}^2]) < 2.95$ specific HighY cuts are applied, otherwise specific Nominal cuts are applied.
 - Specific Nominal cuts
 - * Event is triggered by the *s67* subtrigger.
 - * OptimalNC vertex is found (this would ensure good track-cluster matching, see Section 7.5) or for $\Theta_e < 30^\circ$ the CJC vertex is found.
 - * $y_e < 0.93$.
 - Specific HighY cuts
 - * Event is triggered by the “electron part” (see Section 7.7.1) of *s67* or *s75* subtriggers.

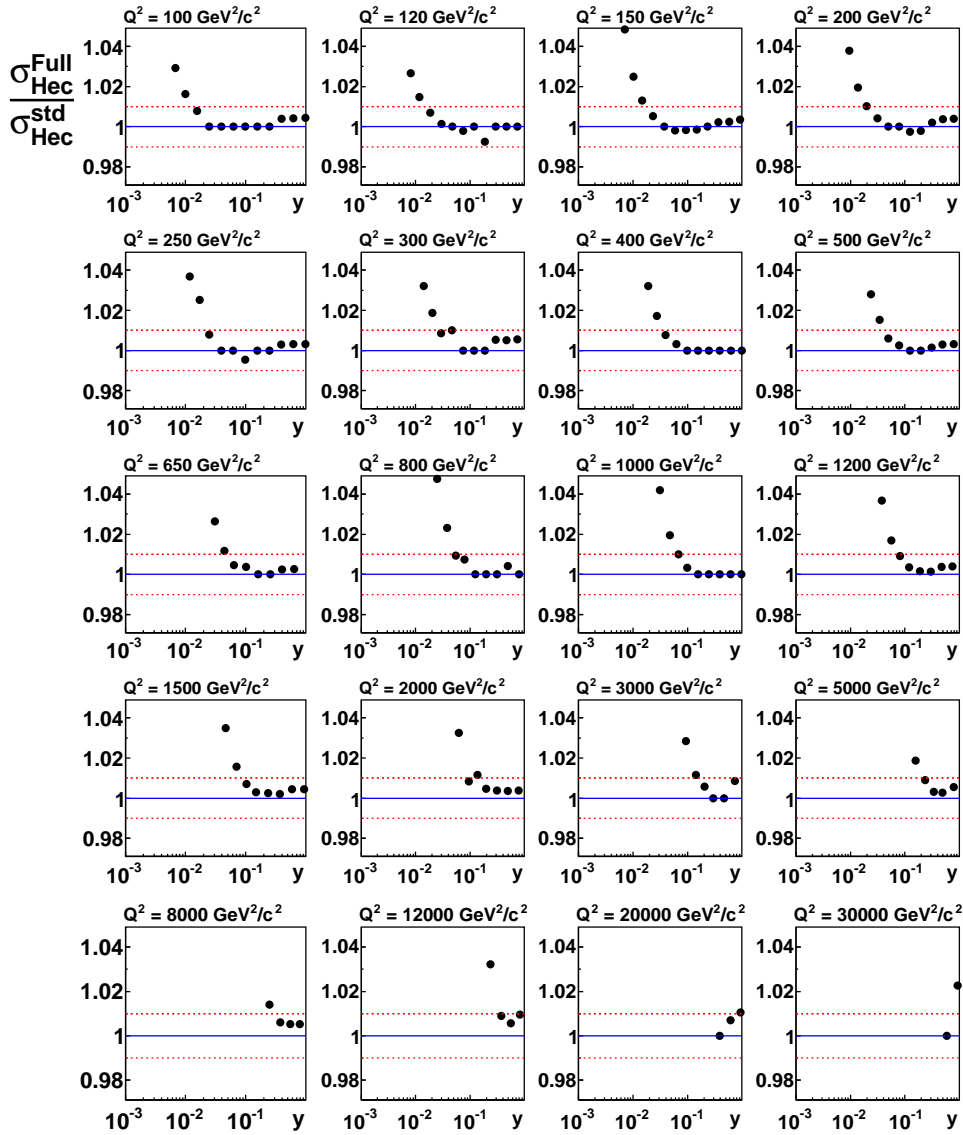


Figure 8.5: The effect of the higher orders radiative corrections estimated with the HECTOR program. For the setup definitions abbreviated as “Full” and “Std” see in the text.

* DTRA track with $d_{\text{DTRA}} < 12$ cm.

- $|Z_{\text{vtx}}| < 35$ cm.
- $E - P_z > 35$ GeV.
- Acceptance of the LAr calorimeter $Z_{\text{imp}} < -190$ cm.
- Exclude Z_{imp} and ϕ_e cracks: remove region $15 < Z_{\text{imp}} < 25$ cm and if $Z_{\text{imp}} < 300$ cm also regions $|\phi_e - 45^\circ \cdot n| < 2^\circ, n = 0, \dots, 7$.
- Rejection of Compton events (Section 7.8.4).
- Rejection of non- ep events (Section 7.8.5).
- Fiducial volume cut (Section 7.7.6).
- Rejection of visually found non- ep events in data at high Q^2 (Section 7.8.5).

8.5 Neutral Current Control Plots

To check an overall quality of the simulation after all the corrections discussed above distributions for an energy of a scattered electron E_e and a scattering angle Θ_e , ($E - P_z$), balance of a transversal momentum measured with the HFS and the scattered electron P_t^{had}/P_t^e , an impact position Z_{imp} and distributions for kinematical variables x and Q^2 are shown in Fig. 8.6 for the e^+p and in Fig. 8.7 for the e^-p scattering for data and simulation. The MC is normalized to a luminosity of the data samples.

The background contribution is obtained from the simulation and a wrong charge data sample as discussed in Section 7.8.

A good agreement between data and simulation is observed.

8.6 Systematic Uncertainties

An important part of the cross section measurements is the reliable estimation of the uncertainties. The significant part of Section 7 is devoted to the determination of the uncertainties on the quantities, like energies of scattered electron and HFS, efficiencies etc.

To propagate these uncertainties to the uncertainty of the measured cross section the following method is applied. For each quantity q with the systematic uncertainty σ_q three measurements of the cross section are obtained: with the central value of this quantity in simulation and shifted to $\pm\sigma_q$, corresponding to tree values for the final result (central and two “shifted”). The cross section shifts corresponding to the “up” and “down” shifts are associated with the uncertainty of the measured cross section related to the uncertainty of the given source q . All systematic errors are assumed to be symmetric (it is checked that in the analysis “up” and “down” shifts of the result are almost the same in modulo and have opposite signs). All the identified sources are supposed to be independent, and to obtain the total systematic uncertainty one has to add all uncertainties from the single sources in quadrature.

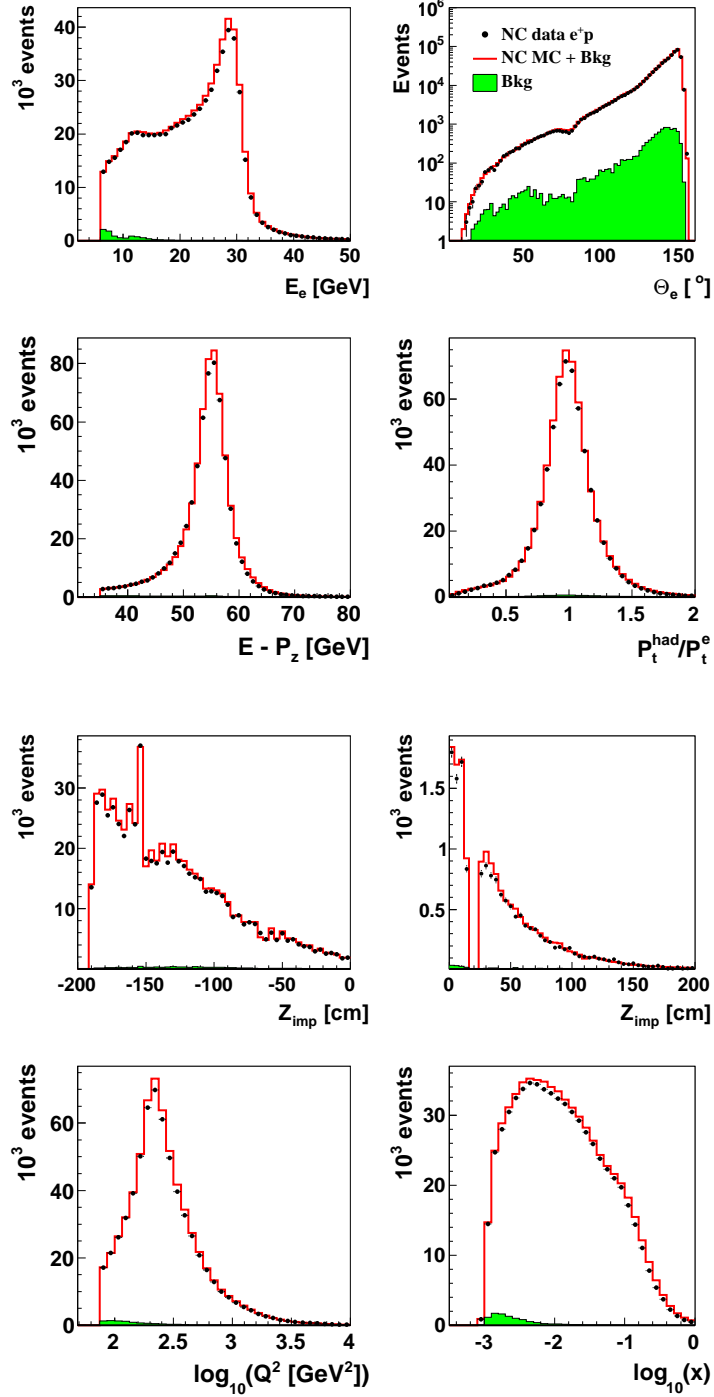


Figure 8.6: Distribution for an energy of a scattered electron E_e and a scattering angle Θ_e , $(E - P_z)$, balance of a transversal momentum measured with the HFS and the scattered electron P_t^{had}/P_t^e , an impact position Z_{imp} and distributions for kinematical variables x and Q^2 for the e^+p scattering.

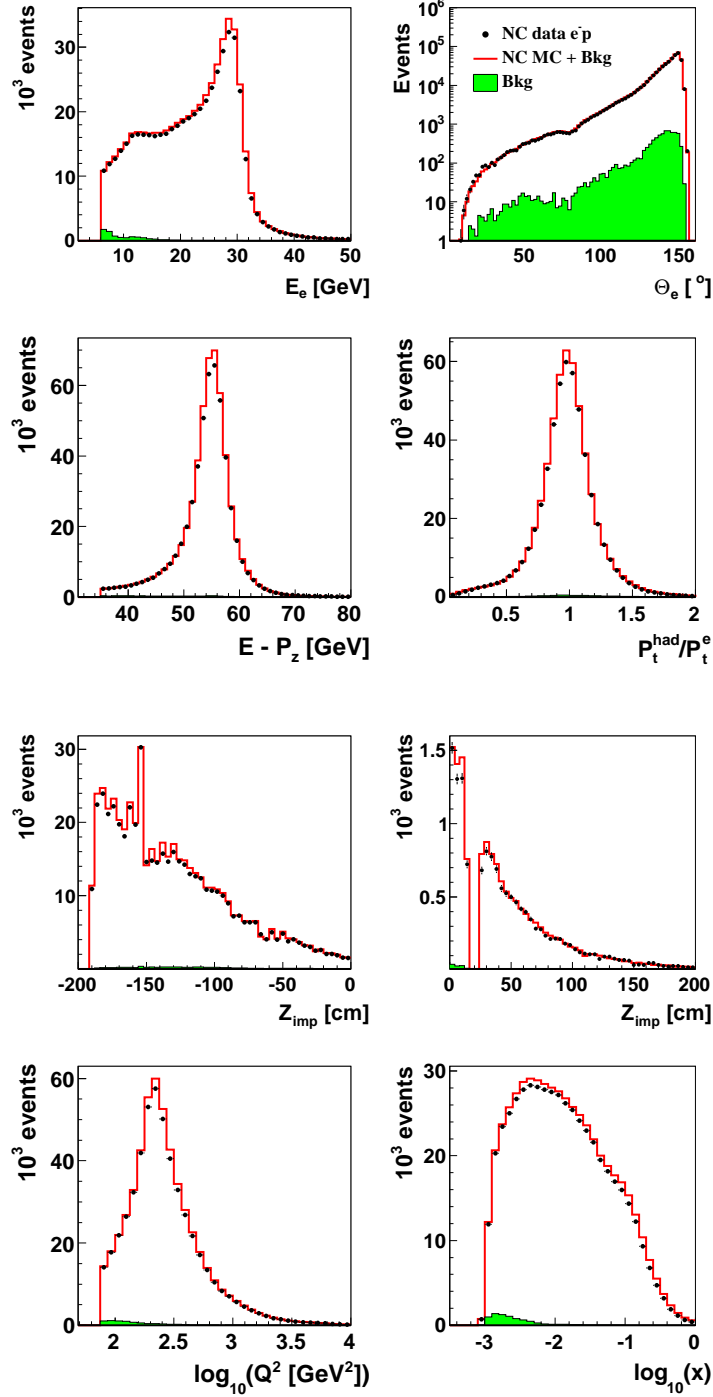


Figure 8.7: Distribution for an energy of a scattered electron E_e and a scattering angle Θ_e , $(E - P_z)$, balance of a transversal momentum measured with the HFS and the scattered electron P_t^{had}/P_t^e , an impact position Z_{imp} and distributions for kinematical variables x and Q^2 for the e^-p scattering.

For the whole measurement in the (x, Q^2) plane one has to take into account possible correlations between measurements at different points. For this purpose the systematic uncertainties are splitted into correlated and uncorrelated, where it is applicable. The correlated part occurs due to the sources which could shift certain quantity for all the cross section measurements at different points simultaneously. On the contrary, the uncorrelated part is related to the uncertainty unique for each point. For example, the measured electron energy has the correlated part related to the method used for the calibration (other words, the calibrated energy could be shifted everywhere in respect to the true one) and the uncorrelated part related to a quality of the calibration.

The list of systematic uncertainties identified in the measurement is given below.

- **Electron identification efficiency (Section 7.2).**

Uncorrelated: 0.2% in the Nominal analysis and 0.5% in the HighY analysis for $Z_{\text{imp}} < 20$ cm, and 1% for $Z_{\text{imp}} \geq 20$ cm.

- **Electromagnetic energy scale (Section 7.3).**

Correlated: 0.5%.

Uncorrelated: from 0.3% to 1% (see Table 7.1).

- **Hadronic energy scale (Section 7.6).**

- LAr calorimeter: correlated part is 0.5%, uncorrelated part is 1%.
- SpaCal calorimeter: uncorrelated, 5%.

- **Noise contribution (Section 7.6.6)**

Correlated: 20%.

- **Trigger efficiency (Section 7.7.7).**

- *Veto* condition: from 0.3% to 0.6%, see Appendix A.
- *T0* condition: for the *CIP_T0* condition, 1% for Per0304, 0.5% for other periods, combined with the uncertainty for the *LAr_T0* condition.
- Electron triggering
 - * Nominal part: 50% of the inefficiency.
 - * HighY part: estimation from the statistical uncertainty of the trigger efficiency measurement.

- **Track and Vertex-Cluster efficiency (Section 7.5.2).**

- OptimalNC vertex for Nominal part: uncorrelated, 0.2% for $\Theta_e > 50^\circ$ and 2% for $\Theta_e \leq 50^\circ$.
- DTRA vertex for HighY part: uncorrelated, 1%.

- **Electron Polar Angle (Section 7.4.4).**

Correlated: 1 mrad.

- **Charge determination (Section 7.8.1).**

Uncorrelated: 0.25%, applied for the HighY analysis only. This efficiency enters the analysis twice, thus the uncertainty on the cross section is 0.5%.

- **Background charge asymmetry (Section 7.8.2).**

Correlated: 0.05, for the HighY part of the analysis only.

- **Background simulation normalization (Section 7.8.3).**

Correlated: 30%, for the Nominal part of the analysis only.

- **QED radiative correction (Section 7.10).**

Uncorrelated: 0.3% for $y < 0.63$ and $x < 0.1$; 1% for $0.1 \leq x < 0.3$ or ($x < 0.3$ and $y \geq 0.63$); 2% for $x \geq 0.3$.

- **Luminosity (normalization) uncertainty (see [61], [111]).**

Correlated within subperiods: for the latest results see Table B.1.

- **Polarization uncertainty (see [112]).**

Correlated within subperiods: 2%.

Chapter 9

Results

The results of the analysis presented below are based on the full HERA II statistics. The double differential neutral current cross section $d^2\sigma/dxdQ^2$ is measured in the kinematical range $90 \leq Q^2 \leq 50000 \text{ GeV}^2$ and $0.0013 \leq x \leq 0.65$. The single differential neutral current cross section $d\sigma/dQ^2$ measured in the kinematical range $200 \leq Q^2 \leq 50000 \text{ GeV}^2$ for $y < 0.9$. These measurements are done for the e^+p and e^-p NC interactions with positive and negative longitudinal polarizations of the lepton beam and polarization equals to zero.

To obtain unpolarized e^+p and e^-p data samples with effectively zero polarization the polarized data samples are combined. A small correction for residual polarization is applied using the unpolarized theoretical Born cross section in (8.6). For the single differential measurement all selected events are used up to $y = 0.93$ (see Section 8.4), and the theoretical Born cross section in (8.6) is integrated up to $y = 0.9$.

The xF_3 proton structure function is extracted using the measured unpolarized double differential cross sections. The polarization asymmetry A is measured using the polarized cross sections.

The essence of this analysis is a significant reduction of the uncertainty of the measurement. Comparing to HERA I, the HERA II statistics of the e^-p data sample is increased by a factor of 7, and the statistics of the e^+p data set is doubled. Systematic uncertainties were carefully analysed. This allowed to improve a total uncertainty of the e^+p scattering cross section measurement by a factor of 2 with respect to the HERA I results. The comparison of the total uncertainties of this measurement and the HERA I results at the H1 experiment is shown in Fig. 9.1 for $Q^2 \leq 8000 \text{ GeV}^2$ (where a contribution from the systematic uncertainty is dominating) for the e^+p scattering. The systematic uncertainty was reduced by a factor of 2 in comparison with the preliminary HERA II measurement [113]. A ratio of the systematic uncertainties for this analysis and the preliminary analysis of the HERA II data is shown in Fig. 9.2 for the e^-p scattering. The rise of the ratio at high x is related to the re-estimation of the noise uncertainty.

9.1 Double Differential NC Cross Sections.

The measured reduced NC double differential polarized cross section is shown in Fig. 9.3 for e^+p and in Fig. 9.4 for e^-p scattering compared with the Standard Model

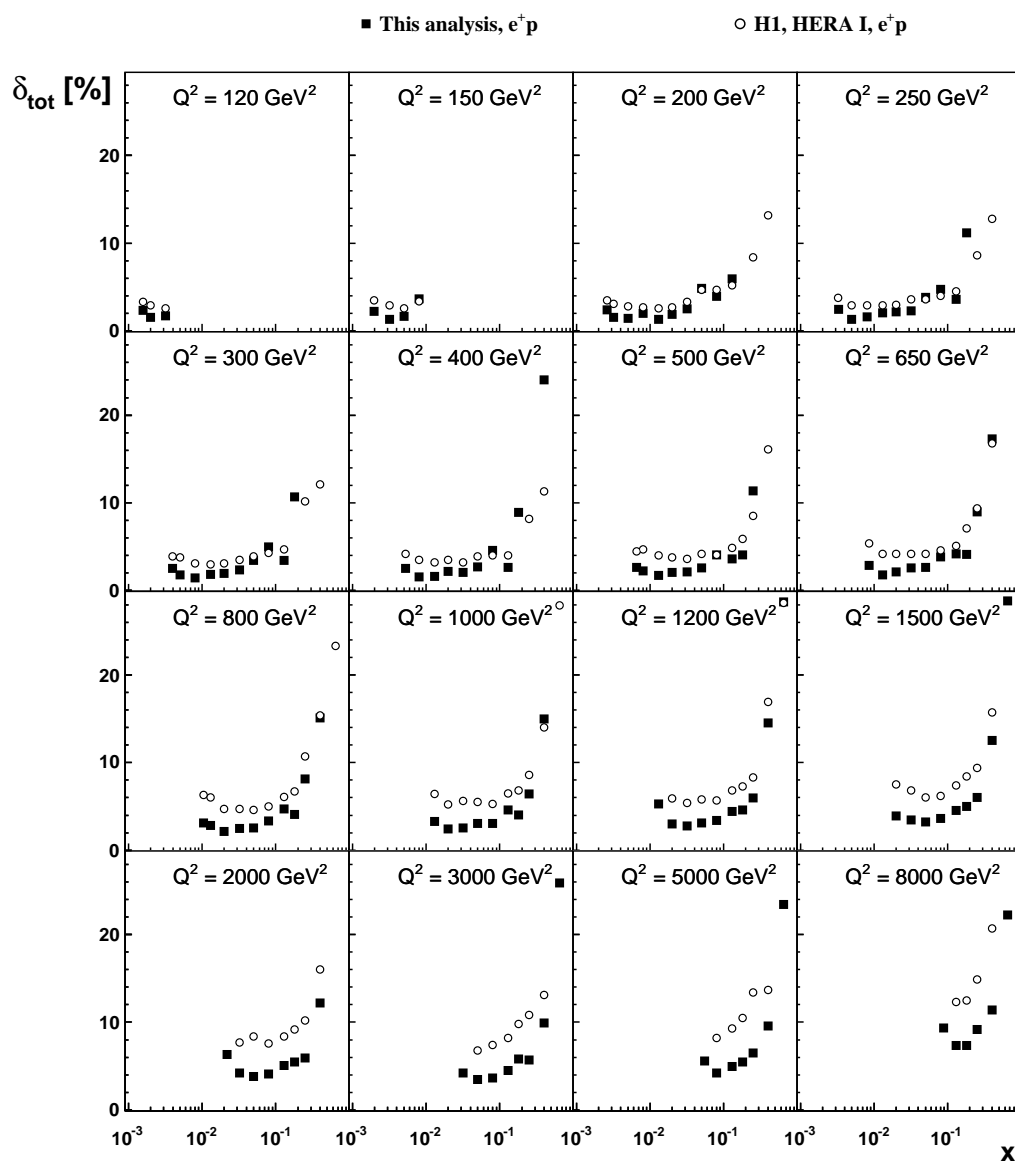


Figure 9.1: The comparison of the total uncertainty $\delta_{\text{tot}} [\%]$ obtained in this analysis (filled squares) and in the measurement using the HERA I data (open circles) for the e^+p NC scattering.

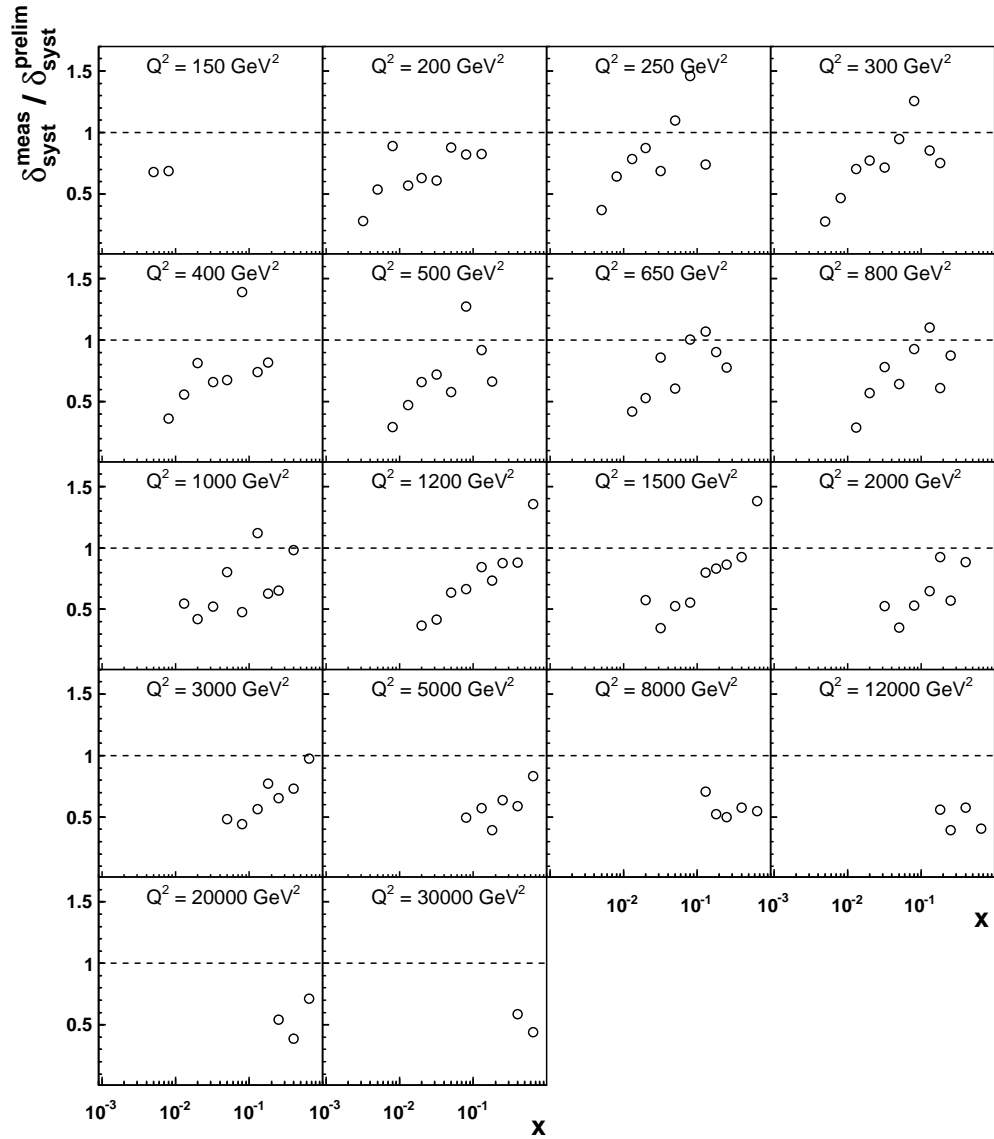


Figure 9.2: Ratio of the systematic uncertainty obtained in this measurement to the systematic uncertainty of the HERA II preliminary result for the e^-p NC scattering.

prediction based on PDFs from the HERAPDF1.0 QCD fit to the NC and CC HERA I measurements by H1 and ZEUS [81]. The measurement covers the range of $90 \leq Q^2 \leq 50000 \text{ GeV}^2$ and $0.0013 \leq x \leq 0.65$. The unpolarized cross section measurements compared to the theoretical prediction are shown in Fig. 9.5.

The polarized measured cross sections are listed in Table C.1, Table C.2 for e^+p scattering with positive ($P_e = +32.5\%$) and negative ($P_e = -37.6\%$) polarizations of the lepton beam, in Table C.3, Table C.4 for e^-p scattering with positive ($P_e = +36.9\%$) and negative ($P_e = -26.0\%$) polarizations of the lepton beam, and in Table C.5, Table C.6 for e^+p and e^-p unpolarized scattering, with statistical, systematic and total errors. Correlated and uncorrelated parts of the systematic uncertainty are given also with contributions from an electromagnetic and hadronic energy scales, polar angle measurement, noise contribution and background estimation. The statistical uncertainty of the measurement grows from 1% at lowest values of $Q^2 \approx 100 \text{ GeV}^2$ to several percent at Q^2 around 10000 GeV^2 . The systematic uncertainty is larger than the statistical one for $Q^2 \lesssim 500 \text{ GeV}^2$. It is increasing at the lowest y values due to uncertainty on the noise contribution. The systematic uncertainty slowly grows towards large Q^2 because of decrease of statistics available for efficiencies determination.

The cross section rises from high to low values of x . This rise is damped in the region of the highest y and low Q^2 (see bins with $Q^2 \leq 200 \text{ GeV}^2$) because of the F_L structure function contribution to the cross section.

In the region of high $Q^2 \approx M_Z^2$ a Z boson exchange starts to play a role. So for e^+p scattering with a positively polarized leptons the cross section is larger than that for a negatively polarized leptons, and vice versa for the e^-p scattering. The unpolarized cross section for the e^-p NC scattering is larger than that for the e^+p scattering because of the contribution of the $x\tilde{F}_3$ structure function, which enters with opposite signs.

In Fig. 9.6 the comparison of this measurement with the HERA I results at the H1 experiment for the e^+p NC unpolarized scattering is shown. The cross sections are found to be in a good agreement.

The NC double differential unpolarized cross section measurement at high y is important for the of the \tilde{F}_L structure function (see Section 2.3.5). In the present work it is measured in the $Q^2 - y$ grid at proton beam energy 920 GeV, with the aim of further combination with medium and low proton beam energy data sets. The results are presented in Tables (C.7), (C.8).

9.2 Single Differential NC Cross Sections.

The Q^2 dependence of the NC single differential cross section $d\sigma/dQ^2$ as well as the ratio of $d\sigma/dQ^2$ to the theoretical expectation is shown in Fig. 9.7 for the unpolarized $e^\pm p$ scattering, in Fig. 9.8 for polarized e^+p , and in Fig. 9.9 for polarized e^-p scattering. The Standard Model expectation is calculated with the HERAPDF1.0 PDFs [81]. The measured cross section values are listed in Table C.9, Table C.10 for e^+p scattering with positive ($P_e = +32.5\%$) and negative ($P_e = -37.6\%$) polarizations of the lepton beam, in Table C.11, Table C.12 for e^-p scattering with positive ($P_e = +36.9\%$) and negative ($P_e = -26.0\%$) polarizations of the lepton beam, and

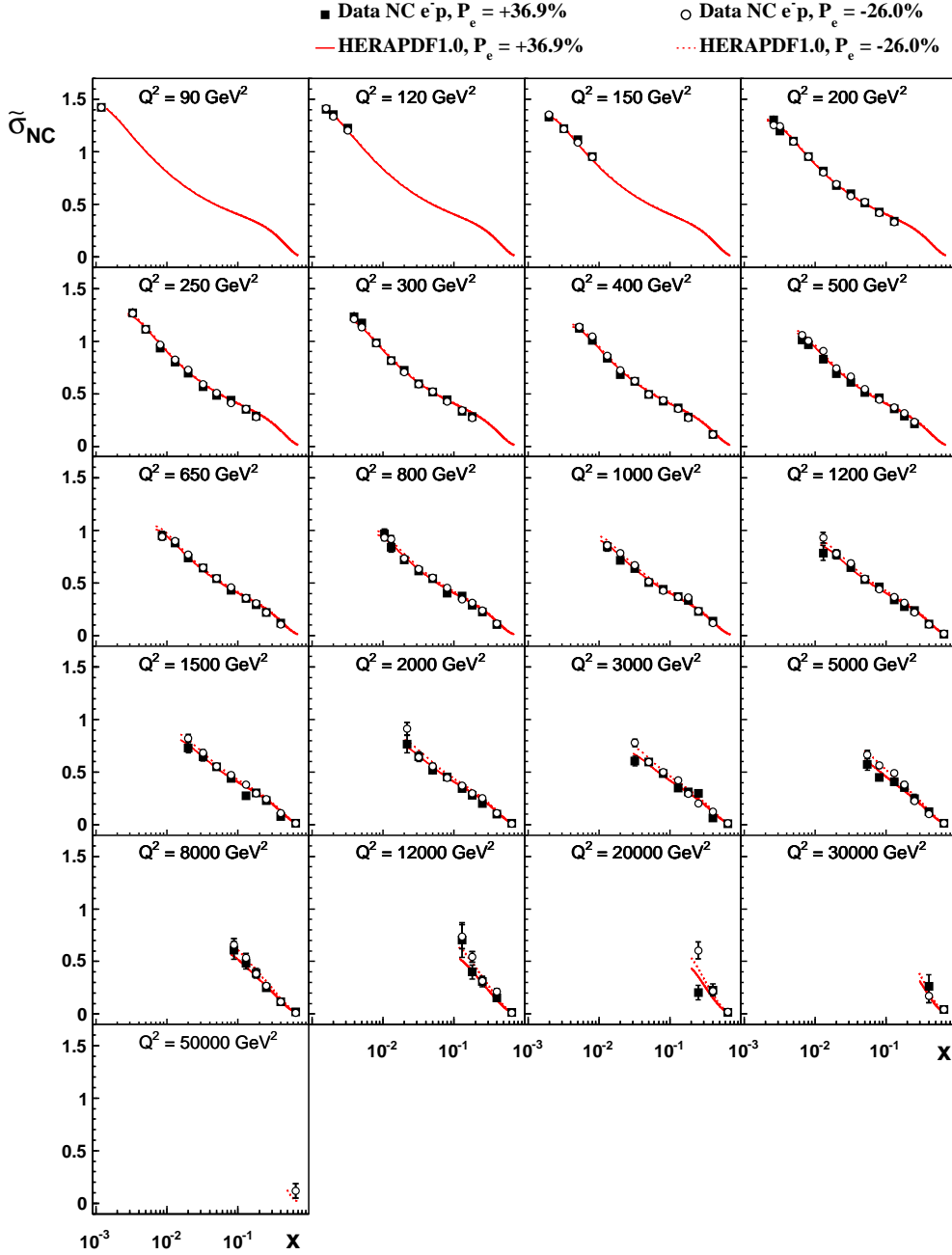


Figure 9.4: The e^-p NC reduced cross section $\tilde{\sigma}_{\text{NC}}(x, Q^2)$ for (full squares) positive and (open points) negative longitudinal polarization of the lepton beam. The inner and outer error bars represent the statistical and total uncertainty respectively. The normalization uncertainty is not included in the error bars. The data are compared to the Standard Model prediction based on HERAPDF1.0.

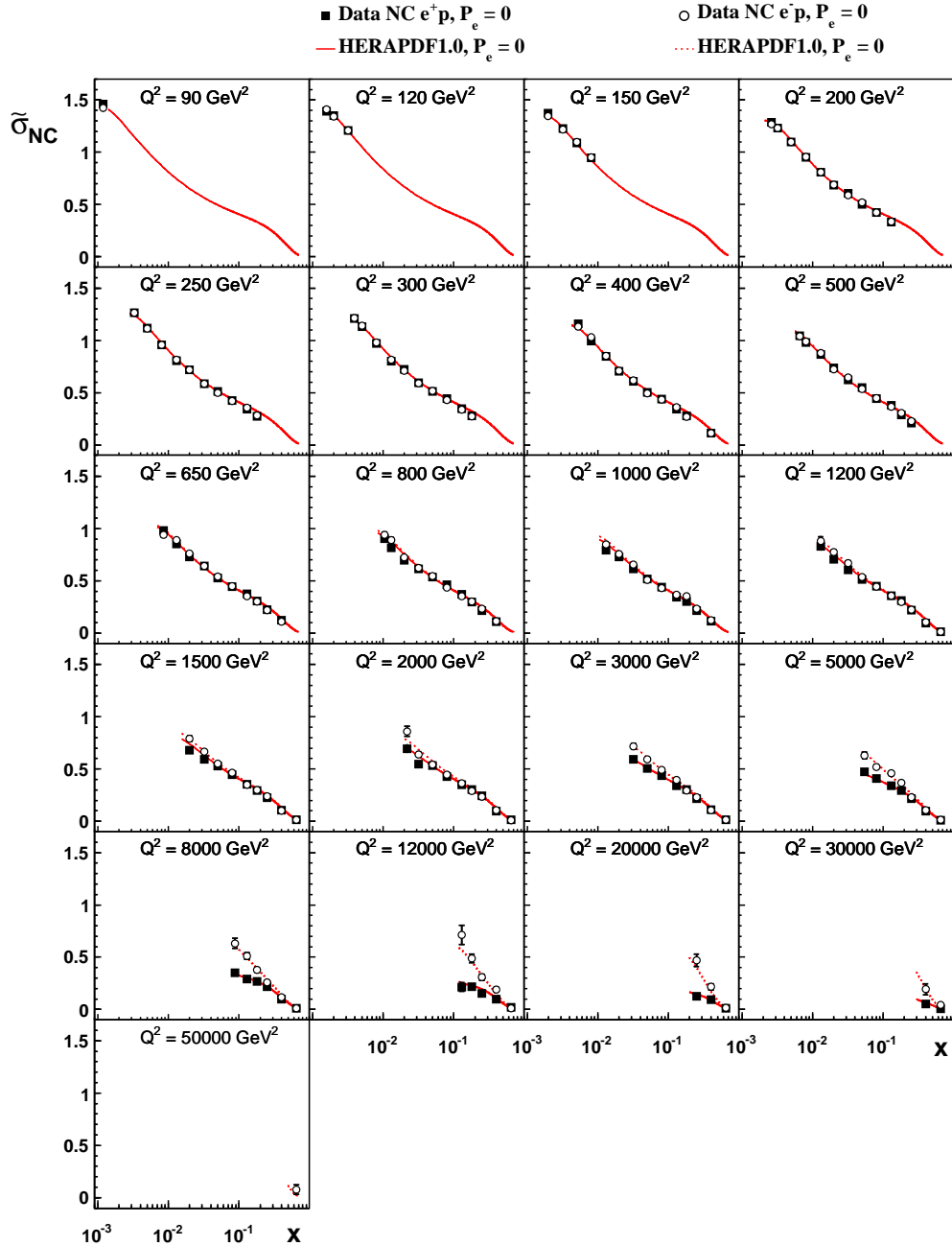


Figure 9.5: The NC reduced cross section $\tilde{\sigma}_{NC}(x, Q^2)$ in unpolarized $e^\pm p$ scattering. The inner and outer error bars represent the statistical and total uncertainty respectively. The normalization uncertainty is not included in the error bars. The data are compared to the Standard Model prediction based on HERAPDF1.0.

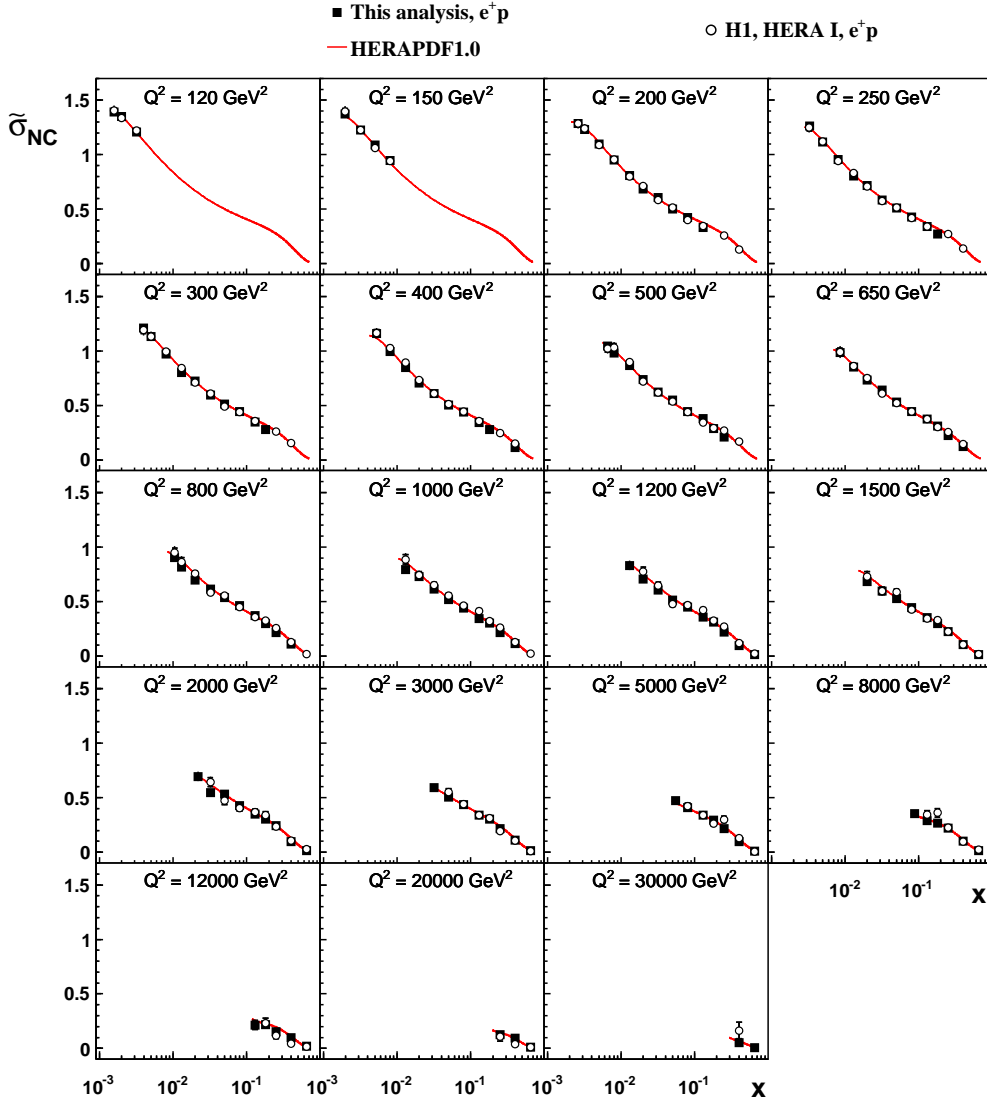


Figure 9.6: The unpolarized e^+p NC reduced cross sections $\tilde{\sigma}_{NC}(x, Q^2)$ measured in this analysis and the HERA I measurement. The inner and outer error bars represent the statistical and total uncertainty respectively. The data are compared to the Standard Model prediction based on HERAPDF1.0.

in Table C.13, Table C.14 for e^+p and e^-p unpolarized scattering.

Apart a normalization shift of about 2–3%, a good agreement between measurement and theoretical prediction over two orders of magnitude in Q^2 is observed. The e^+p and e^-p cross sections start to depart at $Q^2 \approx M_Z^2$ because of the Z boson exchange.

The systematic error of the measurement dominates at $Q^2 \lesssim 500 \text{ GeV}^2$. At high Q^2 the statistical uncertainty dominates.

9.3 The $x\tilde{F}_3$ Structure Function.

Combining the cross section results for the unpolarized electron- and positron-proton scattering, the generalized $x\tilde{F}_3$ structure function can be determined. From (2.38) one can write

$$x\tilde{F}_3 = \frac{Y_+}{2Y_-} (\tilde{\sigma}_{\text{NC}}^-(x, Q^2) - \tilde{\sigma}_{\text{NC}}^+(x, Q^2)). \quad (9.1)$$

The measured unpolarized NC cross sections at high Q^2 (the region where a contribution of the Z -boson exchange is sizable) are shown in Fig. 9.10.

The $x\tilde{F}_3$ structure function determined using relation (9.1) is shown in Fig. 9.11(a) together with the SM expectation using HERAPDF1.0 [81]. For $Q^2 \lesssim M_Z^2$ the contribution from the Z -boson exchange¹ is still small in compare with the pure γ exchange, such that an absolute small uncertainty on the cross section measurement at this region propagates to a relatively large uncertainty on the $x\tilde{F}_3$ structure function. For this reason several measurements at moderate Q^2 are left out of scale on the plots (but included into a further $xF_3^{\gamma Z}$ determination procedure).

The dominant contribution to the structure function $x\tilde{F}_3$ arises from the γZ interference term, since the pure Z boson exchange term is suppressed by an additional factor $Q^2/(Q^2 + M_Z^2)$ and by the small value of a vector coupling v_e . Thus one can extract the $xF_3^{\gamma Z}$ structure function as

$$xF_3^{\gamma Z} = x\tilde{F}_3 \frac{Q^2 + M_Z^2}{a_e \kappa Q^2}. \quad (9.2)$$

The $xF_3^{\gamma Z}$ structure function is shown in Fig. 9.11(b) as a function of x at different Q^2 .

Since the Standard Model predicts a weak dependence of $xF_3^{\gamma Z}$ on Q^2 , the measurements at different Q^2 could be combined to increase the statistical precision of the measurement. Measurements at all Q^2 are transformed to the single value of $Q^2 = 1500 \text{ GeV}^2$ and averaged then using the total uncertainties of the measurements. In such a procedure the statistical and total uncertainties are averaged supposing them to be independent from point to point. The result is shown in Fig. 9.12 and listed in Table C.15.

9.4 Polarization Asymmetry.

From the chiral structure of the weak interaction a difference in the cross sections for electrons and positrons with different polarizations on the proton arises. This differ-

¹To be precise, a contribution from the γZ interference term.

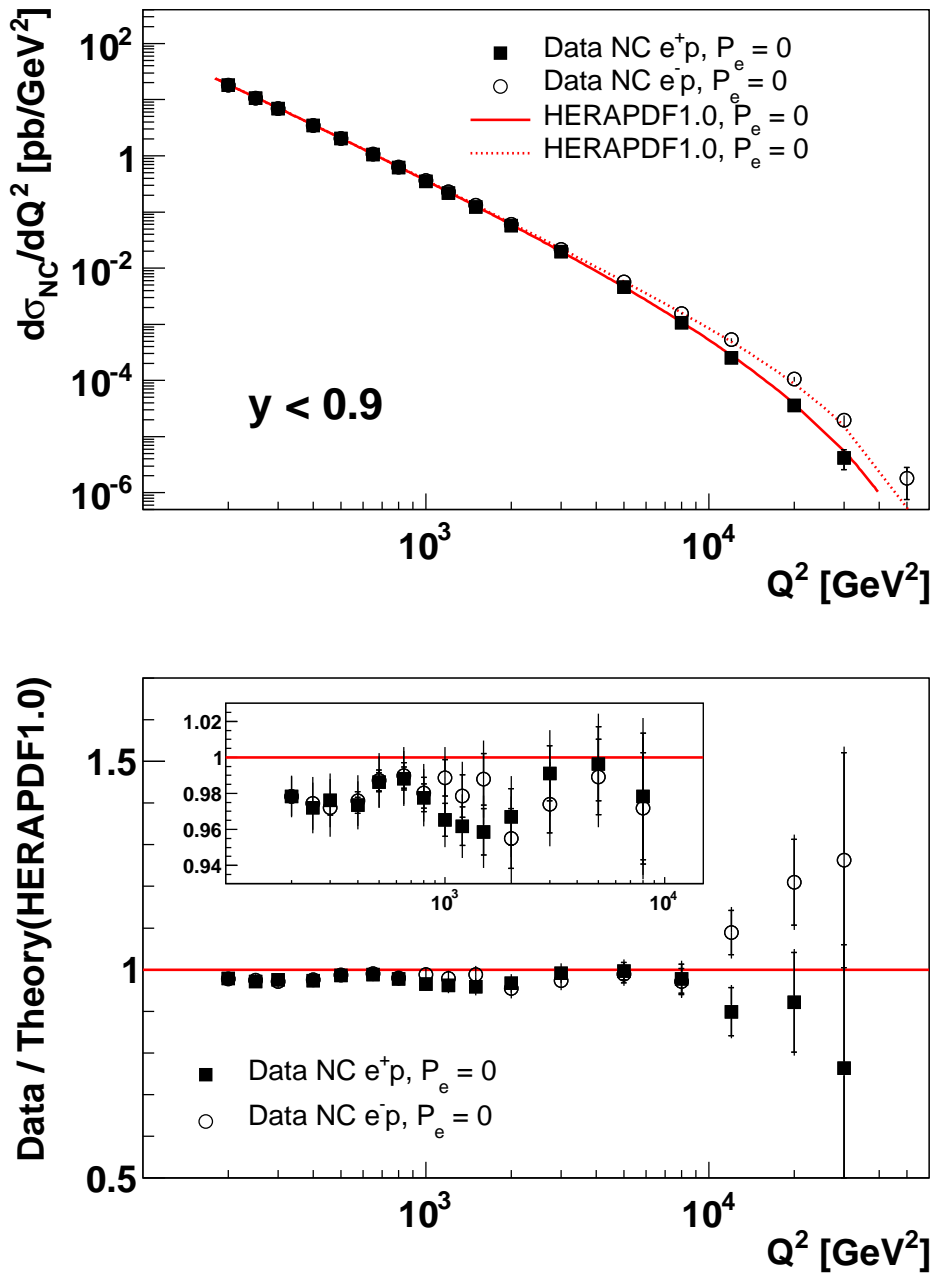


Figure 9.7: The Q^2 dependence of the NC cross section $d\sigma/dQ^2$ for unpolarized (solid squares) e^+p and (open circles) e^-p scattering. The data are compared to the Standard Model prediction from the HERAPDF1.0 fits.

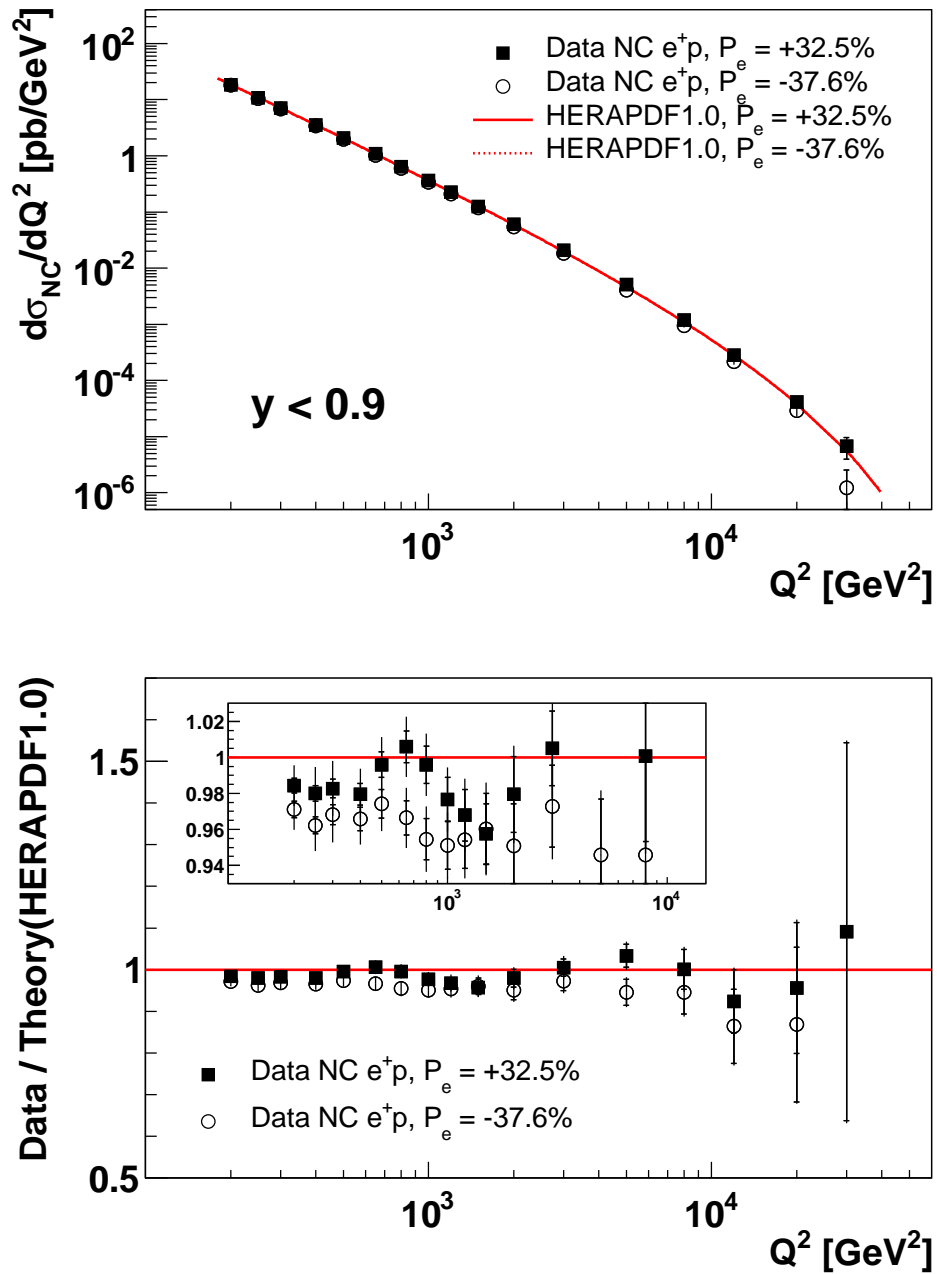


Figure 9.8: The Q^2 dependence of the NC cross section $d\sigma/dQ^2$ for e^+p scattering with the right handed (solid squares) and left handed (open circles) data sets. The data are compared to the Standard Model prediction from the HERAPDF1.0 fits.

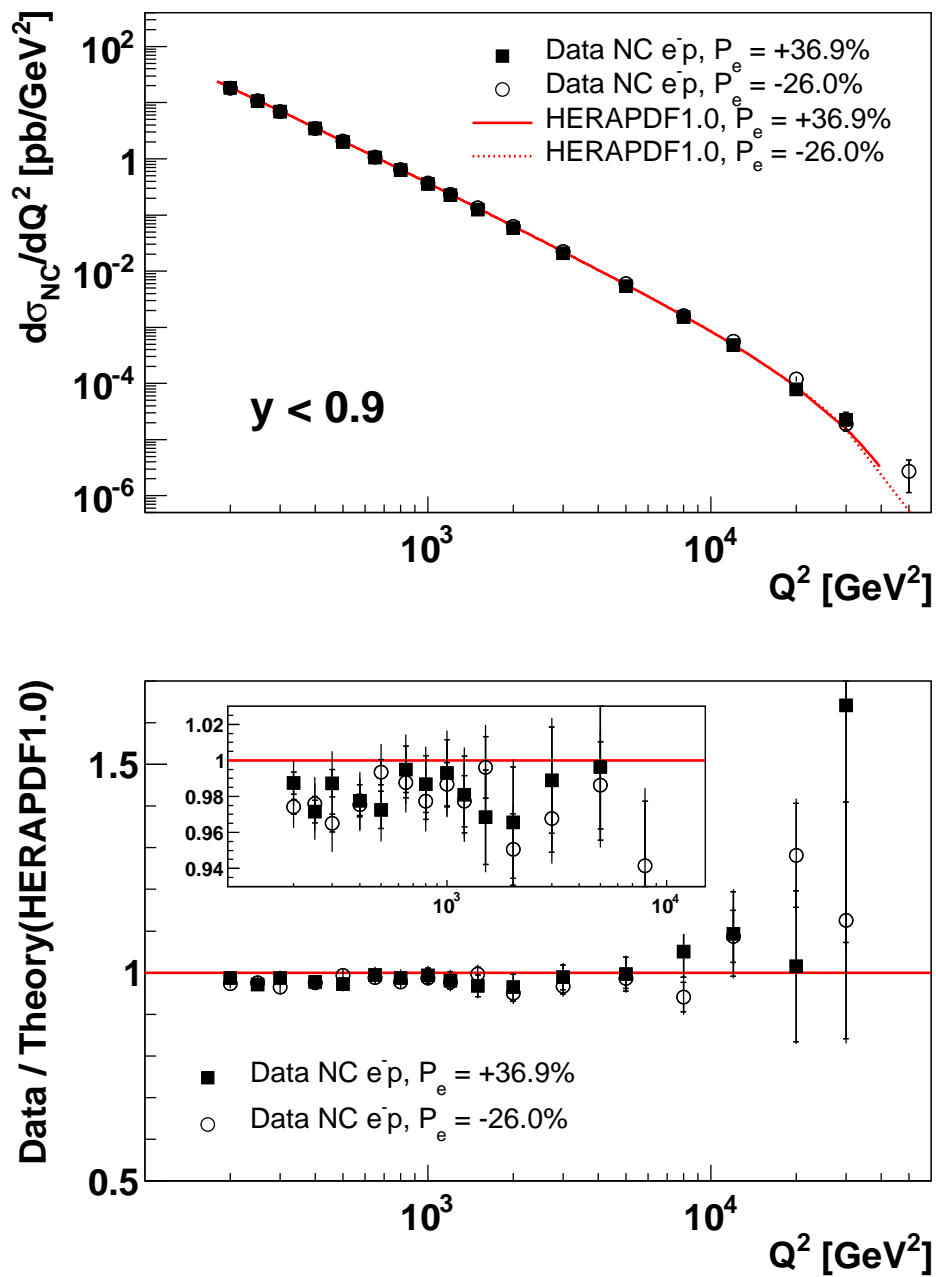


Figure 9.9: The Q^2 dependence of the NC cross section $d\sigma/dQ^2$ for e^-p scattering with the right handed (solid squares) and left handed (open circles) data sets. The data are compared to the Standard Model prediction from the HERAPDF1.0 fits.

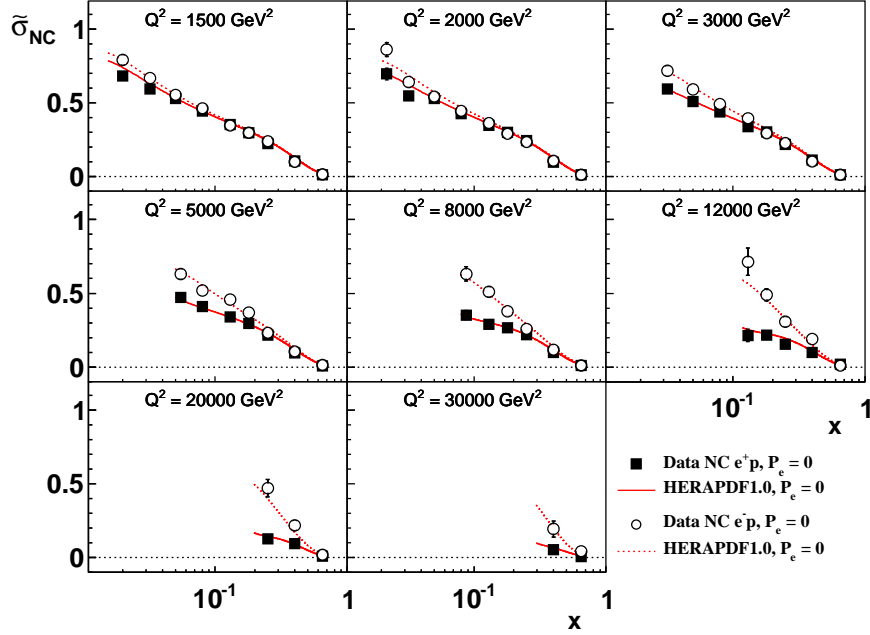


Figure 9.10: The reduced cross section $\tilde{\sigma}_{NC}$ in unpolarized $e^\pm p$ scattering using the HERA II data set for Q^2 above 1000 GeV^2 . The data are compared to the Standard Model prediction using HERAPDF1.0. The inner error bars represent the statistical uncertainty and the outer error bars represent the total errors. The normalization uncertainty is not included in the error bars.

ence is sizable in the region of $Q^2 \gtrsim M_Z^2$ where the Z -boson exchange significantly contributes to the cross section.

The influence of the lepton beam polarization on the cross section is quantified by the polarization asymmetry A defined as

$$A^\pm = \frac{2}{P_R - P_L} \frac{\sigma^\pm(P_R) - \sigma^\pm(P_L)}{\sigma^\pm(P_R) + \sigma^\pm(P_L)}, \quad (9.3)$$

where “ \pm ” sign refers to the sign of the lepton in the $e^\pm p$ scattering. To a good approximation this ratio can be expressed as

$$A^\pm \approx \mp \kappa a_e \frac{F_2^{\gamma Z}}{F_2}. \quad (9.4)$$

One expects A^+ to be positive and about equal to $(-A^-)$. At large x the polarization asymmetry depends on the d_v/u_v ratio of the valence quarks distributions [11]

$$A^\pm \approx \pm \kappa \frac{1 + d_v/u_v}{4 + d_v/u_v}. \quad (9.5)$$

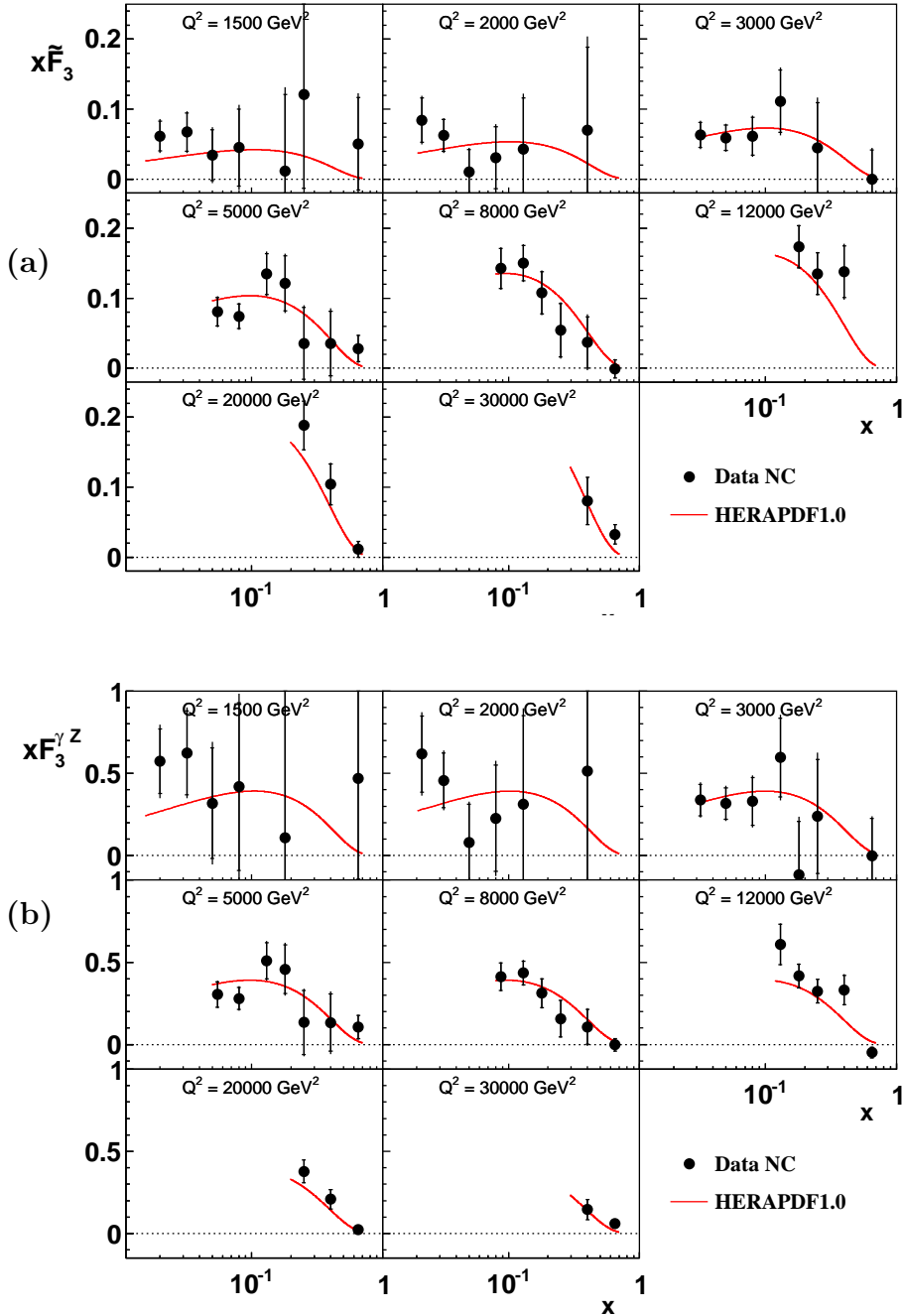


Figure 9.11: The structure functions (a) $x\tilde{F}_3$ and (b) $xF_3^{\gamma Z}$ evaluated using HERA II data set (solid points) is shown compared to Standard Model expectation from HERAPDF1.0 (solid curve). The inner error bars represent the statistical uncertainty and the outer error bars represent the total errors which includes the normalization uncertainty.

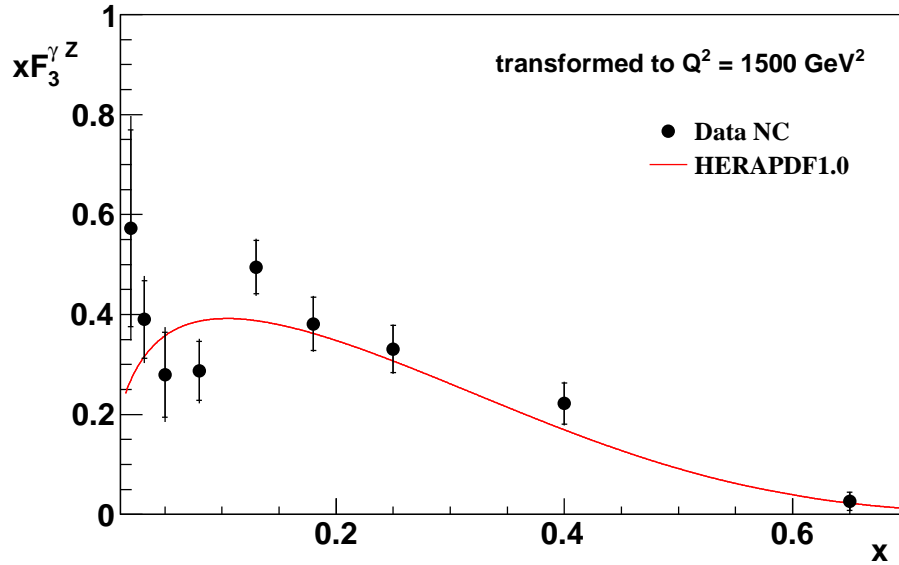


Figure 9.12: The structure function $xF_3^{\gamma Z}$ extracted from the HERA II data set (solid points) and transformed to $Q^2 = 1500 \text{ GeV}^2$ is shown together with the Standard Model expectation using HERAPDF1.0 (solid curve). The inner error bars represent the statistical uncertainty and the outer error bars represent the total errors which includes the normalization uncertainty of the measurement.

The polarization asymmetry A^\pm determined in the analysis is shown in Fig. 9.13. The correlated systematic uncertainties are supposed to cancel in the asymmetry calculation using (9.3).

The result of the measurement demonstrates the expected from the Standard Model properties: the polarization asymmetries for the e^+p and e^-p scattering have opposite signs and vanish at small values of Q^2 .

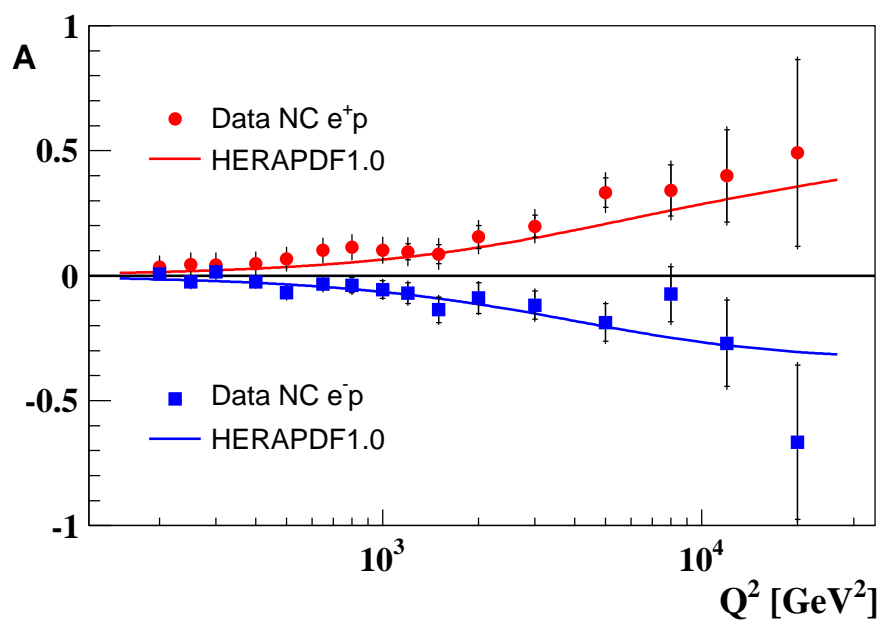


Figure 9.13: The Q^2 dependence of the polarization asymmetry A , for e^+p (red circles) and e^-p (blue squares). The data are compared to the Standard Model prediction (full lines). The inner error bars represent the statistical uncertainties and the outer error bars represent the total errors.

Chapter 10

Summary and Outlook

In this thesis new measurements of the $e^\pm p$ neutral current deep inelastic scattering with longitudinally polarized lepton beams using the H1 detector at the HERA collider are presented. The measurements are performed up to large values of the momentum transferred squared $Q^2 \lesssim 50000 \text{ GeV}^2$ making possible detailed investigations of QCD and the electroweak theory.

The data used for the analysis were taken at a centre-of-mass energy $\sqrt{s} = 319 \text{ GeV}$ in the years 2003-2007 with the absolute value of the polarization of the lepton beam about 30% and a total integrated luminosity of 330 pb^{-1} .

Double and single differential cross sections are measured:

- **Double differential cross section** $d^2\sigma/dxdQ^2$.

The $e^\pm p$ polarized double NC differential cross section for neutral current scattering in the kinematical region of $90 \leq Q^2 \leq 50000 \text{ GeV}^2$ and $0.0013 \leq x \leq 0.65$ is measured. The total uncertainty of the measurement at moderately high values of Q^2 is about 1%; in the region of high Q^2 the precision is limited by the statistical uncertainty of the measurement. The cross sections for positively and negatively polarized lepton beams are combined to obtain the unpolarized $e^\pm p$ cross section. The achieved systematic precision is in general twice better than that for the H1 analysis on the HERA I data set.

- **Single differential cross section** $d\sigma/dQ^2$.

The $e^\pm p$ polarized and unpolarized single differential cross sections for neutral currents are measured for $200 \leq Q^2 \leq 50000 \text{ GeV}^2$.

Using the NC cross section results the following quantities were determined

- The structure function xF_3 . The unpolarized double differential measurements with electron and positron beams allowed to extract the structure function $x\tilde{F}_3$. This structure function is dominated by the interference term $xF_3^{\gamma Z}$ being a sensitive probe of the valence quark content in the proton. The x distribution of the $xF_3^{\gamma Z}$ is determined at $Q^2 = 1500 \text{ GeV}^2$.
- The polarization asymmetry A . The inclusive single differential cross section measurements with positive and negative polarization of the lepton beams are used to extract the polarization asymmetry A^\pm in $e^\pm p$ scattering processes.

The theoretical prediction is found to be in good agreement with this result, which clearly demonstrates the chiral structure of the weak interactions.

The Standard Model predictions based on the QCD fit HERAPDF1.0 are found to be in good agreement with ep cross section measurements.

The unpolarized cross sections are compared to the H1 measurement obtained using the HERA I data sample, and found to be consistent with a significant improvement in precision.

The measured cross sections may be used for the following applications:

- The measurement done in this analysis will have a sizeable impact on the determination of the PDFs in future QCD fits [114].
- The measured NC process combined with the measurement of the CC process can be used for extraction of the axial and vector coupling constants of the light quarks u and d to the Z boson with a precision better than that at LEP and Tevatron [11].
- At high y the cross section is sensitive to the longitudinal proton structure function \tilde{F}_L , which could be extracted by comparison of the measured cross section and a QCD prediction for the \tilde{F}_2 structure function [87]. Combining the measured cross section at moderate y with measurements at lowered proton energy at high y at HERA one can extract \tilde{F}_L in a model independent way [115].
- The measurement of the single differential cross section allows to improve limits on possible contact interactions and on the quark radius [12].

Appendix A

Trigger Components Characteristics

Below the year dependent efficiencies and uncertainties (where applicable) for the CIP_T0, *Veto* and L2_LAr_electron trigger conditions are given.

Component	Data period			
	Per0304	Per0405	Per06em	Per0607
CIP_T0 inefficiency	0.0316	0.0244	0.0273	0.0141
CIP_T0 uncertainty	0.010	0.005	0.005	0.005
<i>Veto</i> efficiency	0.987	0.991	0.992	0.996
<i>Veto</i> uncertainty	0.005	0.006	0.005	0.003
L2_LAr_electron inefficiency	0.0076	0.0219	0.0	0.0

Table A.1: The trigger efficiencies and uncertainties for the CIP_T0, *Veto* and L2_LAr_electron conditions.

Appendix B

Luminosity Correction

Below the latest luminosity corrections [111] with corresponding uncertainties are given.

Period	Luminosity [pb^{-1}]	QED Compton Correction
PerPosRH	98.17	1.02179 ± 0.01025
PerPosLH	81.51	1.09545 ± 0.01264
PerNegRH	45.99	0.99686 ± 0.01516
PerNegLH	102.57	1.01329 ± 0.00998

Table B.1: The QED Compton correction for the luminosity.

Appendix C

Cross Section Tables

The double and single differential NC cross sections measured in this analysis as well as the extracted $x F_3^{\gamma Z}$ structure function are presented below. The total, statistical and systematic uncertainties are given. The systematic uncertainty is splitted into correlated and uncorrelated parts. Systematic uncertainties from several sources which influence on the measured cross section is non-trivial are given separately.

Q^2 [GeV ²]	x	y	$\bar{\sigma}_{NC}$	δ_{stat} [%]	δ_{syst} [%]	δ_{tot} [%]	δ_{unc} [%]	δ_{unc}^E [%]	δ_{unc}^{had} [%]	δ_{cor} [%]	δ_{cor}^E [%]	δ_{cor}^{\oplus} [%]	δ_{cor}^{had} [%]	δ_{cor}^{Noi} [%]	δ_{cor}^{Bkg} [%]	δ_{cor}^{WrCh} [%]
90	0.0012	0.7500	1.48040	0.95	2.49	2.66	2.37	0.28	0.24	0.77	0.37	0.49	0.06	0.18	0.00	0.42
120	0.0016	0.7500	1.40520	1.07	2.27	2.50	2.15	0.22	0.25	0.71	0.34	0.46	0.06	0.18	0.00	0.39
120	0.0020	0.5907	1.37070	0.87	1.40	1.65	0.82	0.32	0.09	1.14	0.33	0.70	0.03	0.19	0.81	0.00
120	0.0032	0.3692	1.20720	1.27	1.66	2.09	1.23	0.89	0.04	1.11	0.90	0.61	0.01	0.16	0.12	0.00
150	0.0020	0.7500	1.38770	1.20	2.10	2.42	1.97	0.28	0.20	0.71	0.46	0.39	0.05	0.18	0.00	0.31
150	0.0032	0.4615	1.24070	0.74	1.19	1.40	0.84	0.49	0.06	0.85	0.52	0.53	0.02	0.16	0.38	0.00
150	0.0050	0.2954	1.10920	0.88	1.48	1.73	1.06	0.78	0.00	1.04	0.81	0.66	0.00	0.03	0.03	0.00
150	0.0080	0.1846	0.96873	1.31	3.62	3.85	2.47	1.95	1.24	2.65	1.95	0.84	0.58	1.48	0.02	0.00
200	0.0026	0.7500	1.32990	1.54	2.19	2.68	2.11	0.59	0.21	0.59	0.08	0.48	0.05	0.19	0.00	0.25
200	0.0032	0.6154	1.23820	1.40	1.28	1.89	0.85	0.13	0.08	0.95	0.38	0.62	0.03	0.17	0.60	0.00
200	0.0050	0.3938	1.10600	0.97	1.30	1.62	0.89	0.54	0.04	0.94	0.71	0.61	0.02	0.12	0.07	0.00
200	0.0080	0.2461	0.96126	0.98	1.85	2.10	1.25	1.02	0.00	1.37	1.10	0.82	0.00	0.00	0.00	0.00
200	0.0130	0.1515	0.82357	1.10	1.02	1.50	0.87	0.19	0.36	0.54	0.28	0.32	0.12	0.31	0.00	0.00
200	0.0200	0.0985	0.69649	1.24	1.66	2.07	1.24	0.87	0.38	1.10	0.91	0.45	0.12	0.39	0.00	0.00
200	0.0320	0.0615	0.61550	1.45	2.28	2.70	1.65	1.25	0.63	1.57	1.27	0.67	0.31	0.53	0.00	0.00
200	0.0500	0.0394	0.50429	1.67	4.65	4.94	2.23	1.99	0.30	4.08	1.99	0.68	0.12	3.49	0.00	0.00
200	0.0800	0.0246	0.42545	1.90	3.91	4.35	2.45	2.11	0.58	3.05	2.11	0.85	0.27	2.01	0.00	0.00
200	0.1300	0.0151	0.32834	2.23	5.64	6.06	2.56	1.71	1.27	5.02	1.72	0.80	0.65	4.60	0.00	0.00
250	0.0033	0.7500	1.29370	1.75	2.20	2.81	2.13	0.33	0.27	0.55	0.30	0.31	0.09	0.20	0.00	0.27
250	0.0050	0.4923	1.13720	1.13	1.06	1.55	0.79	0.30	0.06	0.70	0.36	0.47	0.03	0.16	0.35	0.00
250	0.0080	0.3077	0.97191	1.10	1.40	1.78	0.97	0.64	0.01	1.01	0.90	0.45	0.00	0.03	0.01	0.00
250	0.0130	0.1893	0.82050	1.20	1.97	2.31	1.24	0.97	0.13	1.54	0.77	0.65	0.09	1.16	0.00	0.00
250	0.0200	0.1231	0.73902	1.21	2.03	2.36	1.23	0.96	0.02	1.62	0.67	0.64	0.06	1.32	0.00	0.00
250	0.0320	0.0769	0.59311	1.31	2.06	2.44	1.34	0.99	0.42	1.56	0.76	0.56	0.22	1.22	0.00	0.00
250	0.0500	0.0492	0.51802	1.43	3.84	4.10	1.16	0.75	0.21	3.67	0.44	0.58	0.09	3.59	0.00	0.00
250	0.0800	0.0308	0.42812	1.54	4.67	4.92	1.28	0.74	0.36	4.50	0.52	0.53	0.09	4.43	0.00	0.00
250	0.1300	0.0189	0.33628	1.80	3.43	3.88	1.97	1.24	0.81	2.81	1.08	0.58	0.46	2.49	0.00	0.00
250	0.1800	0.0137	0.27370	2.46	11.15	11.42	3.14	2.22	1.58	10.70	2.11	1.02	0.76	10.42	0.00	0.00
300	0.0039	0.7500	1.22900	1.90	2.18	2.89	2.12	0.04	0.24	0.52	0.27	0.31	0.06	0.20	0.00	0.24
300	0.0050	0.5907	1.15320	1.94	1.24	2.30	0.95	0.32	0.07	0.79	0.49	0.36	0.03	0.14	0.48	0.00
300	0.0080	0.3692	0.98997	1.29	1.12	1.71	0.77	0.24	0.02	0.82	0.53	0.61	0.01	0.09	0.05	0.00
300	0.0130	0.2272	0.81023	1.31	1.67	2.13	1.00	0.65	0.00	1.34	1.23	0.53	0.00	0.00	0.01	0.00
300	0.0200	0.1477	0.73553	1.40	1.65	2.17	1.04	0.67	0.11	1.29	0.64	0.50	0.05	0.99	0.01	0.00
300	0.0320	0.0923	0.60067	1.51	2.14	2.62	1.26	0.94	0.26	1.72	0.95	0.55	0.10	1.33	0.00	0.00
300	0.0500	0.0591	0.51697	1.64	3.16	3.56	1.33	0.98	0.28	2.87	0.83	0.55	0.06	2.69	0.00	0.00
300	0.0800	0.0369	0.45020	1.72	4.90	5.20	1.56	1.19	0.26	4.65	0.80	0.67	0.14	4.53	0.00	0.00
300	0.1300	0.0227	0.36051	1.86	2.92	3.47	2.13	1.53	0.73	2.01	1.35	0.74	0.35	1.23	0.00	0.00
300	0.1800	0.0164	0.27659	2.74	10.52	10.87	3.02	2.09	1.53	10.08	2.03	0.72	0.74	9.82	0.00	0.00
400	0.0053	0.7500	1.19500	2.07	2.10	2.95	2.05	0.20	0.23	0.45	0.11	0.32	0.07	0.20	0.00	0.21
400	0.0080	0.4923	0.99617	1.60	1.06	1.92	0.82	0.25	0.06	0.67	0.43	0.44	0.02	0.14	0.23	0.00
400	0.0130	0.3029	0.87648	1.49	1.18	1.90	0.88	0.42	0.01	0.79	0.62	0.50	0.00	0.03	0.01	0.00
400	0.0200	0.1969	0.71897	1.57	1.85	2.43	1.19	0.88	0.00	1.42	1.30	0.57	0.00	0.00	0.00	0.00
400	0.0320	0.1231	0.60852	1.65	1.74	2.40	1.04	0.60	0.23	1.39	0.92	0.41	0.08	0.96	0.00	0.00
400	0.0500	0.0788	0.51367	1.83	2.39	3.01	1.05	0.52	0.31	2.15	0.82	0.44	0.13	1.93	0.00	0.00
400	0.0800	0.0492	0.44323	1.92	4.45	4.85	1.04	0.35	0.13	4.33	0.61	0.26	0.12	4.27	0.00	0.00
400	0.1300	0.0303	0.34272	2.08	2.17	3.00	1.61	0.56	0.80	1.45	1.01	0.41	0.28	0.91	0.00	0.00
400	0.1800	0.0219	0.28687	2.94	8.55	9.04	2.52	1.35	1.46	8.17	1.94	0.74	0.80	7.86	0.00	0.00
400	0.4000	0.0098	0.10743	4.77	23.91	24.38	3.17	1.37	1.86	23.70	2.21	0.69	0.93	23.56	0.00	0.00
500	0.0066	0.7500	1.09270	2.39	2.04	3.14	1.98	0.19	0.21	0.52	0.39	0.24	0.06	0.19	0.00	0.15
500	0.0080	0.6154	0.99747	2.68	1.21	2.95	1.02	0.30	0.09	0.66	0.31	0.46	0.04	0.16	0.30	0.00
500	0.0130	0.3787	0.87251	1.85	1.02	2.11	0.83	0.20	0.02	0.60	0.39	0.44	0.01	0.08	0.04	0.00
500	0.0200	0.2461	0.75102	1.89	1.66	2.52	1.09	0.71	0.00	1.26	1.15	0.49	0.00	0.00	0.00	0.00
500	0.0320	0.1538	0.64110	1.91	1.63	2.51	0.92	0.36	0.06	1.34	0.70	0.31	0.05	1.11	0.00	0.00
500	0.0500	0.0985	0.55687	2.01	2.27	3.04	1.09	0.56	0.32	1.99	1.07	0.40	0.09	1.63	0.00	0.00
500	0.0800	0.0615	0.45554	2.19	3.36	4.01	1.06	0.40	0.09	3.19	0.72	0.48	0.05	3.07	0.00	0.00
500	0.1300	0.0379	0.38340	2.60	3.56	4.41	1.77	0.99	0.62	3.09	1.30	0.72	0.37	2.68	0.00	0.00
500	0.1800	0.0273	0.28501	3.13	3.65	4.81	2.09	0.99	1.08	2.99	1.72	0.40	0.54	2.35	0.00	0.00
500	0.2500	0.0197	0.21847	4.11	10.77	11.53	2.74	1.19	1.70	10.42	2.13	0.57	0.84	10.15	0.00	0.00

Q^2 [GeV ²]	x	y	$\tilde{\sigma}_{\text{NC}}$	δ_{stat} [%]	δ_{syst} [%]	δ_{tot} [%]	δ_{unc} [%]	δ_{Eunc} [%]	δ_{hadunc} [%]	δ_{cor} [%]	δ_{Ecor} [%]	$\delta_{\text{Θcor}}$ [%]	δ_{hadcor} [%]	$\delta_{\text{Noi cor}}$ [%]	$\delta_{\text{Bkg cor}}$ [%]	$\delta_{\text{WrCh cor}}$ [%]
650	0.0085	0.7500	1.02990	2.84	2.03	3.49	1.97	0.21	0.21	0.49	0.22	0.36	0.06	0.22	0.00	0.11
650	0.0130	0.4923	0.85142	2.14	0.96	2.35	0.85	0.09	0.05	0.43	0.11	0.36	0.02	0.14	0.14	0.00
650	0.0200	0.3200	0.73641	2.21	1.37	2.60	1.00	0.46	0.01	0.93	0.75	0.55	0.00	0.03	0.02	0.00
650	0.0320	0.2000	0.67421	2.28	2.13	3.12	1.37	1.00	0.00	1.63	1.53	0.56	0.00	0.00	0.00	0.00
650	0.0500	0.1280	0.54846	2.40	1.96	3.10	1.08	0.48	0.17	1.64	0.91	0.44	0.10	1.29	0.00	0.00
650	0.0800	0.0800	0.47289	2.64	3.26	4.19	1.38	0.81	0.37	2.95	1.18	0.40	0.16	2.67	0.00	0.00
650	0.1300	0.0492	0.38507	2.91	3.90	4.86	1.42	0.23	0.10	3.63	0.76	0.27	0.05	3.54	0.00	0.00
650	0.1800	0.0356	0.32652	3.51	3.46	4.93	2.15	1.02	1.09	2.71	1.49	0.52	0.71	2.08	0.00	0.00
650	0.2500	0.0256	0.22331	4.44	8.51	9.60	3.00	1.57	1.76	7.97	2.43	0.74	0.75	7.51	0.00	0.00
650	0.4000	0.0160	0.12666	6.41	16.86	18.04	3.62	1.43	2.05	16.47	2.71	0.49	1.06	16.20	0.00	0.00
800	0.0105	0.7500	0.94877	3.23	2.04	3.82	2.00	0.14	0.22	0.42	0.20	0.25	0.09	0.24	0.00	0.11
800	0.0130	0.6059	0.85363	3.47	1.35	3.72	1.23	0.17	0.09	0.54	0.18	0.41	0.04	0.15	0.26	0.00
800	0.0200	0.3938	0.71367	2.52	1.14	2.77	1.00	0.39	0.01	0.54	0.41	0.33	0.01	0.09	0.04	0.00
800	0.0320	0.2461	0.64274	2.60	1.68	3.09	1.27	0.78	0.00	1.10	0.93	0.58	0.00	0.00	0.00	0.00
800	0.0500	0.1575	0.54535	2.76	1.63	3.20	1.07	0.19	0.16	1.23	0.84	0.30	0.03	0.85	0.00	0.00
800	0.0800	0.0985	0.46251	3.01	2.59	3.97	1.20	0.25	0.22	2.30	0.95	0.29	0.02	2.07	0.00	0.00
800	0.1300	0.0606	0.39471	3.42	4.12	5.35	1.56	0.43	0.05	3.81	1.05	0.51	0.02	3.62	0.00	0.00
800	0.1800	0.0438	0.31180	3.94	2.79	4.83	2.10	0.81	1.01	1.83	1.58	0.48	0.51	0.60	0.00	0.00
800	0.2500	0.0315	0.22079	5.01	7.42	8.96	2.71	1.01	1.56	6.91	1.81	0.24	0.83	6.61	0.00	0.00
800	0.4000	0.0197	0.10908	7.91	14.36	16.40	4.03	1.78	2.24	13.79	4.04	0.67	0.84	13.14	0.00	0.00
1000	0.0130	0.7574	0.78806	3.63	2.19	4.24	1.69	0.20	0.18	1.39	0.08	0.24	0.06	0.20	1.35	0.00
1000	0.0200	0.4923	0.73700	2.96	1.14	3.17	0.99	0.29	0.06	0.56	0.30	0.43	0.03	0.15	0.14	0.00
1000	0.0320	0.3077	0.65070	2.87	1.37	3.18	1.15	0.68	0.00	0.74	0.67	0.32	0.00	0.02	0.00	0.00
1000	0.0500	0.1969	0.54654	3.09	1.89	3.62	1.48	1.10	0.00	1.17	1.04	0.55	0.00	0.00	0.00	0.00
1000	0.0800	0.1231	0.45586	3.40	1.81	3.85	1.18	0.37	0.29	1.37	0.69	0.19	0.17	1.15	0.00	0.00
1000	0.1300	0.0757	0.33689	4.26	3.76	5.68	1.48	0.04	0.17	3.46	0.40	0.11	0.12	3.43	0.00	0.00
1000	0.1800	0.0547	0.32817	4.32	2.51	4.99	2.00	0.71	0.99	1.51	1.33	0.45	0.52	0.18	0.00	0.00
1000	0.2500	0.0394	0.22649	5.39	4.96	7.33	2.63	1.21	1.43	4.21	1.94	0.43	0.55	3.66	0.00	0.00
1000	0.4000	0.0246	0.12660	9.65	13.53	16.62	3.65	1.43	2.07	13.02	2.02	0.46	1.04	12.82	0.00	0.00
1200	0.0130	0.9088	0.88398	5.76	3.25	6.61	2.52	0.18	0.27	2.05	0.16	0.12	0.08	0.24	2.02	0.00
1200	0.0200	0.5907	0.75378	3.64	1.20	3.84	1.12	0.24	0.08	0.43	0.24	0.24	0.03	0.12	0.23	0.00
1200	0.0320	0.3692	0.59432	3.51	1.09	3.67	0.93	0.41	0.02	0.56	0.41	0.39	0.01	0.07	0.01	0.00
1200	0.0500	0.2363	0.51973	3.52	1.74	3.93	1.34	1.02	0.00	1.11	1.02	0.43	0.00	0.00	0.01	0.00
1200	0.0800	0.1477	0.47246	3.87	2.02	4.36	1.43	0.96	0.33	1.42	0.98	0.36	0.12	0.96	0.00	0.00
1200	0.1300	0.0909	0.39472	4.75	2.68	5.45	1.48	0.69	0.06	2.23	0.73	0.29	0.08	2.08	0.00	0.00
1200	0.1800	0.0656	0.32661	5.18	2.72	5.85	1.76	0.91	0.49	2.08	0.98	0.29	0.16	1.80	0.00	0.00
1200	0.2500	0.0473	0.20944	6.05	4.27	7.40	2.78	1.77	1.37	3.24	1.89	0.39	0.68	2.52	0.00	0.00
1200	0.4000	0.0295	0.09758	9.14	13.54	16.33	4.48	3.01	2.36	12.78	3.19	0.46	1.26	12.30	0.00	0.00
1200	0.6500	0.0182	0.01609	15.27	24.88	29.19	5.65	3.73	2.86	24.23	3.86	0.54	1.20	23.89	0.00	0.00
1500	0.0200	0.7384	0.71137	4.61	2.07	5.06	1.83	0.25	0.22	0.96	0.27	0.32	0.08	0.19	0.84	0.00
1500	0.0320	0.4615	0.60822	4.29	1.22	4.46	1.05	0.45	0.05	0.62	0.45	0.40	0.03	0.13	0.02	0.00
1500	0.0500	0.2954	0.54341	4.00	1.31	4.21	1.11	0.62	0.00	0.70	0.62	0.33	0.00	0.02	0.00	0.00
1500	0.0800	0.1846	0.45048	4.27	1.74	4.61	1.28	0.80	0.14	1.18	0.81	0.15	0.04	0.84	0.00	0.00
1500	0.1300	0.1136	0.37523	5.06	2.59	5.69	1.77	0.98	0.22	1.89	0.98	0.13	0.11	1.61	0.00	0.00
1500	0.1800	0.0820	0.30766	5.50	2.60	6.09	1.70	0.82	0.19	1.96	0.82	0.24	0.11	1.76	0.00	0.00
1500	0.2500	0.0591	0.21073	6.62	3.79	7.63	2.77	1.76	1.30	2.59	1.79	0.24	0.80	1.68	0.00	0.00
1500	0.4000	0.0369	0.11000	9.18	10.21	13.72	3.95	2.41	2.04	9.41	2.43	0.22	0.95	9.04	0.00	0.00
1500	0.6500	0.0227	0.01221	20.45	25.24	32.49	7.86	5.49	4.39	23.99	5.49	0.54	2.00	23.26	0.00	0.00

Q^2 [GeV ²]	x	y	$\tilde{\sigma}_{\text{NC}}$	δ_{stat} [%]	δ_{syst} [%]	δ_{tot} [%]	δ_{unc} [%]	$\delta_{\text{unc}}^{\text{E}}$ [%]	$\delta_{\text{unc}}^{\text{had}}$ [%]	δ_{cor} [%]	$\delta_{\text{cor}}^{\text{E}}$ [%]	$\delta_{\text{cor}}^{\ominus}$ [%]	$\delta_{\text{cor}}^{\text{had}}$ [%]	$\delta_{\text{cor}}^{\text{Noi}}$ [%]	$\delta_{\text{cor}}^{\text{Bkg}}$ [%]	$\delta_{\text{cor}}^{\text{WrCh}}$ [%]
2000	0.0219	0.9000	0.73938	7.45	3.51	8.24	3.02	0.75	0.22	1.79	0.67	0.20	0.10	0.21	1.64	0.00
2000	0.0320	0.6154	0.56165	5.24	1.55	5.46	1.47	0.27	0.09	0.50	0.27	0.38	0.05	0.11	0.16	0.00
2000	0.0500	0.3938	0.55793	4.84	1.27	5.01	1.21	0.25	0.01	0.40	0.25	0.31	0.01	0.03	0.00	0.00
2000	0.0800	0.2461	0.43212	5.01	1.98	5.39	1.54	1.10	0.00	1.24	1.10	0.59	0.00	0.00	0.00	0.00
2000	0.1300	0.1515	0.36522	5.96	2.44	6.44	1.95	1.18	0.53	1.46	1.19	0.29	0.23	0.75	0.00	0.00
2000	0.1800	0.1094	0.32694	6.25	2.83	6.86	1.74	0.68	0.30	2.23	0.68	0.20	0.14	2.11	0.00	0.00
2000	0.2500	0.0788	0.27446	6.49	3.23	7.25	2.58	1.65	0.92	1.94	1.66	0.37	0.61	0.71	0.00	0.00
2000	0.4000	0.0492	0.09996	10.67	9.62	14.37	4.33	2.91	2.03	8.59	2.91	0.21	1.10	8.00	0.00	0.00
2000	0.6500	0.0303	0.01486	21.86	25.91	33.90	7.47	4.64	4.43	24.81	4.66	0.51	1.90	24.29	0.00	0.00
3000	0.0320	0.9230	0.61381	5.01	2.09	5.43	1.85	0.25	0.14	0.97	0.20	0.25	0.06	0.13	0.90	0.00
3000	0.0500	0.5907	0.54630	4.21	1.53	4.48	1.43	0.48	0.06	0.56	0.43	0.34	0.02	0.08	0.06	0.00
3000	0.0800	0.3692	0.47198	4.45	1.41	4.66	1.25	0.49	0.01	0.64	0.49	0.41	0.01	0.02	0.00	0.00
3000	0.1300	0.2272	0.35452	5.54	1.80	5.83	1.62	0.70	0.00	0.79	0.70	0.37	0.00	0.00	0.00	0.00
3000	0.1800	0.1641	0.33256	7.20	2.94	7.78	2.15	1.48	0.33	2.00	1.48	0.09	0.27	1.32	0.00	0.00
3000	0.2500	0.1181	0.22699	6.38	2.95	7.03	2.40	1.56	0.71	1.73	1.56	0.13	0.25	0.69	0.00	0.00
3000	0.4000	0.0738	0.11234	8.59	7.28	11.26	3.91	2.57	1.78	6.15	2.57	0.12	0.85	5.51	0.00	0.00
3000	0.6500	0.0454	0.01256	20.04	22.59	30.20	8.09	5.78	4.52	21.09	5.78	0.10	2.31	20.15	0.00	0.00
5000	0.0547	0.9000	0.51914	6.62	2.49	7.07	2.22	0.70	0.13	1.14	0.35	0.43	0.09	0.11	0.98	0.00
5000	0.0800	0.6154	0.46953	4.99	1.66	5.26	1.59	0.30	0.05	0.48	0.32	0.33	0.03	0.07	0.11	0.00
5000	0.1300	0.3787	0.36967	6.01	1.96	6.32	1.85	0.49	0.00	0.66	0.49	0.44	0.00	0.02	0.00	0.00
5000	0.1800	0.2735	0.32921	6.59	2.15	6.94	2.00	0.72	0.00	0.79	0.72	0.34	0.00	0.00	0.00	0.00
5000	0.2500	0.1969	0.21291	8.44	2.16	8.71	2.11	0.46	0.00	0.47	0.46	0.12	0.00	0.00	0.00	0.00
5000	0.4000	0.1231	0.10810	10.56	4.99	11.68	3.79	2.14	1.65	3.25	2.15	0.13	0.69	2.33	0.00	0.00
5000	0.6500	0.0757	0.01173	22.99	14.88	27.39	6.66	4.04	3.71	13.31	4.04	0.38	2.13	12.49	0.00	0.00
8000	0.0875	0.9000	0.44120	10.51	3.39	11.04	3.06	0.68	0.09	1.47	0.29	0.25	0.04	0.09	1.41	0.00
8000	0.1300	0.6059	0.32478	8.97	2.57	9.33	2.54	0.33	0.06	0.42	0.23	0.23	0.04	0.08	0.24	0.00
8000	0.1800	0.4376	0.29665	8.98	2.53	9.33	2.42	0.32	0.00	0.75	0.39	0.64	0.00	0.01	0.00	0.00
8000	0.2500	0.3151	0.22290	13.24	2.53	13.48	2.50	0.25	0.00	0.38	0.28	0.26	0.00	0.00	0.00	0.00
8000	0.4000	0.1969	0.10110	13.63	5.19	14.59	4.30	2.87	0.00	2.90	2.87	0.41	0.00	0.00	0.00	0.00
8000	0.6500	0.1212	0.01346	24.29	12.80	27.46	7.53	4.68	4.02	10.36	4.68	0.65	2.06	8.98	0.00	0.00
12000	0.1300	0.9088	0.22254	27.62	5.79	28.22	5.19	0.99	0.09	2.58	1.50	0.66	0.03	0.09	1.99	0.00
12000	0.1800	0.6564	0.22604	15.02	2.59	15.24	2.51	0.68	0.07	0.61	0.26	0.48	0.03	0.08	0.27	0.00
12000	0.2500	0.4726	0.17032	15.33	2.57	15.55	2.47	0.86	0.03	0.71	0.63	0.32	0.01	0.03	0.00	0.00
12000	0.4000	0.2954	0.12357	16.94	5.08	17.68	4.44	3.40	0.00	2.46	2.43	0.39	0.00	0.00	0.00	0.00
12000	0.6500	0.1818	0.02780	24.28	9.09	25.93	6.78	5.20	2.87	6.06	4.38	0.34	1.54	3.87	0.00	0.00
20000	0.2500	0.7876	0.14265	25.85	3.89	26.14	3.63	2.39	0.10	1.41	1.33	0.33	0.09	0.11	0.27	0.00
20000	0.4000	0.4923	0.11140	23.67	4.32	24.06	4.12	2.91	0.02	1.27	1.26	0.20	0.01	0.03	0.00	0.00
20000	0.6500	0.3029	0.00726	71.00	16.66	72.92	14.76	14.26	0.00	7.72	7.35	2.38	0.00	0.00	0.00	0.00
30000	0.4000	0.7384	0.08242	51.24	5.33	51.52	5.07	2.86	0.07	1.64	1.54	0.55	0.06	0.06	0.19	0.00
30000	0.6500	0.4544	0.01415	70.93	10.88	71.76	9.95	8.65	0.00	4.40	4.23	1.21	0.00	0.00	0.00	0.00

Table C.1: The NC e^+p double differential reduced cross section $\tilde{\sigma}_{\text{NC}}$ for positively polarized ($P_e = +32.5\%$) leptons with the statistical δ_{stat} , systematic δ_{syst} and total δ_{tot} errors. The quantities shown are total uncorrelated systematic δ_{unc} with the contributions from the electron energy scale uncertainty $\delta_{\text{unc}}^{\text{E}}$ and hadronic energy scale uncertainty $\delta_{\text{unc}}^{\text{had}}$. The effect of other uncorrelated systematic uncertainties is included into δ_{unc} . The correlated systematic error δ_{cor} is shown with the contributions from electron energy scale $\delta_{\text{cor}}^{\text{E}}$, polar angle measurement $\delta_{\text{cor}}^{\ominus}$, hadronic energy scale $\delta_{\text{cor}}^{\text{had}}$, noise subtraction $\delta_{\text{cor}}^{\text{Noi}}$, simulated background $\delta_{\text{cor}}^{\text{Bkg}}$, wrong charge data subtraction $\delta_{\text{cor}}^{\text{WrCh}}$. The normalization and polarization errors are not included into the errors.

Q^2 [GeV ²]	x	y	$\bar{\sigma}_{NC}$	δ_{stat} [%]	δ_{syst} [%]	δ_{tot} [%]	δ_{unc} [%]	δ_{unc}^E [%]	δ_{unc}^{had} [%]	δ_{cor} [%]	δ_{cor}^E [%]	δ_{cor}^{\oplus} [%]	δ_{cor}^{had} [%]	δ_{cor}^{Noi} [%]	δ_{cor}^{Bkg} [%]	δ_{cor}^{WrCh} [%]
90	0.0012	0.7500	1.44090	1.06	2.51	2.73	2.38	0.20	0.24	0.82	0.36	0.57	0.05	0.18	0.00	0.43
120	0.0016	0.7500	1.37870	1.19	2.22	2.52	2.10	0.18	0.23	0.74	0.39	0.44	0.06	0.19	0.00	0.40
120	0.0020	0.5907	1.32800	0.97	1.49	1.78	0.93	0.55	0.09	1.16	0.58	0.58	0.04	0.17	0.80	0.00
120	0.0032	0.3692	1.21400	1.38	1.34	1.93	0.97	0.49	0.03	0.93	0.49	0.76	0.01	0.20	0.07	0.00
150	0.0020	0.7500	1.35950	1.33	2.05	2.44	1.96	0.51	0.23	0.59	0.11	0.43	0.06	0.19	0.00	0.33
150	0.0032	0.4615	1.21240	0.82	1.25	1.49	0.83	0.47	0.06	0.93	0.58	0.54	0.03	0.19	0.45	0.00
150	0.0050	0.2954	1.06430	1.00	1.69	1.96	1.22	0.98	0.00	1.17	0.98	0.64	0.00	0.04	0.02	0.00
150	0.0080	0.1846	0.92332	1.46	3.57	3.86	2.49	2.12	0.98	2.56	2.14	0.45	0.35	1.27	0.03	0.00
200	0.0026	0.7500	1.23700	1.76	2.11	2.74	2.02	0.44	0.20	0.62	0.24	0.47	0.04	0.16	0.00	0.28
200	0.0032	0.6154	1.22760	1.55	1.24	1.98	0.84	0.13	0.08	0.90	0.25	0.64	0.03	0.19	0.56	0.00
200	0.0050	0.3938	1.08920	1.08	1.25	1.66	0.87	0.50	0.02	0.90	0.65	0.62	0.01	0.11	0.07	0.00
200	0.0080	0.2461	0.93867	1.09	1.94	2.23	1.32	1.10	0.00	1.42	1.18	0.78	0.00	0.00	0.01	0.00
200	0.0130	0.1515	0.79118	1.24	1.29	1.79	0.83	0.27	0.17	0.99	0.36	0.46	0.06	0.79	0.01	0.00
200	0.0200	0.0985	0.67016	1.40	1.71	2.21	1.31	0.92	0.48	1.10	0.95	0.52	0.19	0.03	0.00	0.00
200	0.0320	0.0615	0.59552	1.65	2.44	2.95	1.76	1.38	0.64	1.69	1.40	0.68	0.37	0.55	0.00	0.00
200	0.0500	0.0394	0.50003	1.91	4.83	5.19	2.35	2.11	0.31	4.22	2.10	0.75	0.24	3.57	0.00	0.00
200	0.0800	0.0246	0.41908	2.20	3.55	4.17	2.24	1.74	0.88	2.75	1.78	0.87	0.39	1.87	0.00	0.00
200	0.1300	0.0151	0.34030	2.55	5.83	6.36	2.44	1.58	1.18	5.29	1.57	0.93	0.65	4.93	0.00	0.00
250	0.0033	0.7500	1.22920	1.96	2.12	2.88	2.04	0.25	0.27	0.54	0.18	0.37	0.08	0.20	0.00	0.28
250	0.0050	0.4923	1.09570	1.25	1.06	1.64	0.78	0.29	0.05	0.72	0.49	0.43	0.02	0.15	0.25	0.00
250	0.0080	0.3077	0.93750	1.24	1.38	1.86	0.93	0.58	0.00	1.02	0.85	0.57	0.00	0.03	0.03	0.00
250	0.0130	0.1893	0.78958	1.34	1.85	2.29	1.20	0.93	0.06	1.41	0.76	0.66	0.07	0.98	0.02	0.00
250	0.0200	0.1231	0.69003	1.36	2.03	2.44	1.30	1.04	0.03	1.56	0.74	0.59	0.05	1.24	0.00	0.00
250	0.0320	0.0769	0.57574	1.47	2.25	2.68	1.29	0.98	0.28	1.84	0.71	0.55	0.16	1.59	0.00	0.00
250	0.0500	0.0492	0.50499	1.56	3.59	3.91	1.08	0.62	0.23	3.42	0.39	0.34	0.02	3.38	0.00	0.00
250	0.0800	0.0308	0.42496	1.83	4.54	4.89	1.30	0.74	0.41	4.35	0.56	0.59	0.20	4.27	0.00	0.00
250	0.1300	0.0189	0.35096	1.96	3.37	3.90	1.99	1.18	0.94	2.72	1.03	0.57	0.48	2.41	0.00	0.00
250	0.1800	0.0137	0.26846	2.66	10.98	11.30	2.87	1.93	1.46	10.60	1.88	0.82	0.64	10.38	0.00	0.00
300	0.0039	0.7500	1.19050	2.14	2.10	3.00	2.04	0.02	0.28	0.51	0.26	0.29	0.08	0.22	0.00	0.22
300	0.0050	0.5907	1.10200	2.13	1.19	2.44	0.94	0.25	0.08	0.73	0.37	0.39	0.03	0.16	0.47	0.00
300	0.0080	0.3692	0.94668	1.45	1.19	1.87	0.83	0.39	0.02	0.86	0.64	0.55	0.01	0.10	0.05	0.00
300	0.0130	0.2272	0.79435	1.45	1.59	2.15	0.97	0.61	0.00	1.26	1.10	0.61	0.00	0.00	0.01	0.00
300	0.0200	0.1477	0.71040	1.56	1.74	2.33	1.04	0.67	0.11	1.39	0.74	0.48	0.03	1.07	0.02	0.00
300	0.0320	0.0923	0.58805	1.64	2.17	2.72	1.32	1.00	0.30	1.72	0.96	0.69	0.19	1.23	0.00	0.00
300	0.0500	0.0591	0.50839	1.78	3.41	3.85	1.39	1.06	0.27	3.12	0.83	0.61	0.08	2.94	0.00	0.00
300	0.0800	0.0369	0.43636	1.89	4.69	5.06	1.55	1.14	0.39	4.43	0.87	0.59	0.11	4.30	0.00	0.00
300	0.1300	0.0227	0.32990	2.14	3.46	4.06	2.29	1.69	0.85	2.59	1.47	0.82	0.41	1.93	0.00	0.00
300	0.1800	0.0164	0.28222	3.00	10.51	10.93	2.99	2.05	1.53	10.08	2.05	0.68	0.73	9.82	0.00	0.00
400	0.0053	0.7500	1.11390	2.33	2.08	3.12	2.03	0.33	0.24	0.42	0.03	0.31	0.06	0.21	0.00	0.19
400	0.0080	0.4923	0.99566	1.77	1.04	2.05	0.83	0.28	0.05	0.63	0.39	0.42	0.02	0.14	0.21	0.00
400	0.0130	0.3029	0.80995	1.71	1.25	2.11	0.91	0.49	0.00	0.85	0.70	0.48	0.00	0.03	0.01	0.00
400	0.0200	0.1969	0.69221	1.77	1.96	2.64	1.15	0.83	0.00	1.59	1.47	0.61	0.00	0.00	0.00	0.00
400	0.0320	0.1231	0.60591	1.85	1.72	2.52	1.00	0.56	0.16	1.39	0.87	0.46	0.10	0.98	0.00	0.00
400	0.0500	0.0788	0.49336	2.03	2.31	3.08	1.07	0.51	0.37	2.05	0.74	0.44	0.12	1.86	0.00	0.00
400	0.0800	0.0492	0.43110	2.14	4.32	4.82	1.07	0.45	0.13	4.19	0.56	0.44	0.02	4.13	0.00	0.00
400	0.1300	0.0303	0.34426	2.24	2.28	3.19	1.67	0.75	0.76	1.55	1.19	0.55	0.39	0.73	0.00	0.00
400	0.1800	0.0219	0.26790	3.12	8.87	9.41	2.54	1.38	1.47	8.50	1.99	0.64	0.72	8.21	0.00	0.00
400	0.4000	0.0098	0.11510	5.21	23.56	24.13	3.23	1.59	1.80	23.34	2.55	0.91	0.93	23.16	0.00	0.00
500	0.0066	0.7500	0.98404	2.76	2.00	3.41	1.95	0.05	0.19	0.47	0.32	0.26	0.07	0.17	0.00	0.14
500	0.0080	0.6154	0.95615	2.93	1.20	3.17	1.03	0.31	0.07	0.62	0.33	0.37	0.02	0.15	0.34	0.00
500	0.0130	0.3787	0.85487	2.10	1.24	2.44	0.91	0.41	0.02	0.84	0.69	0.47	0.01	0.10	0.04	0.00
500	0.0200	0.2461	0.72241	2.09	1.50	2.57	1.01	0.57	0.00	1.11	0.94	0.59	0.00	0.00	0.00	0.00
500	0.0320	0.1538	0.60304	2.13	1.70	2.73	1.00	0.55	0.04	1.37	0.77	0.34	0.06	1.08	0.00	0.00
500	0.0500	0.0985	0.53678	2.32	1.92	3.01	1.03	0.50	0.20	1.62	0.87	0.38	0.12	1.31	0.00	0.00
500	0.0800	0.0615	0.42846	2.43	4.22	4.87	1.03	0.27	0.16	4.09	0.66	0.38	0.01	4.02	0.00	0.00
500	0.1300	0.0379	0.37816	2.77	2.66	3.84	1.59	0.70	0.54	2.13	1.10	0.47	0.24	1.75	0.00	0.00
500	0.1800	0.0273	0.28487	3.42	3.11	4.62	1.90	0.72	0.93	2.46	1.34	0.46	0.48	1.96	0.00	0.00
500	0.2500	0.0197	0.19734	4.73	11.21	12.17	3.30	1.79	2.12	10.71	2.77	0.66	1.16	10.26	0.00	0.00

Q^2 [GeV ²]	x	y	$\bar{\sigma}_{NC}$	δ_{stat} [%]	δ_{syst} [%]	δ_{tot} [%]	δ_{unc} [%]	δ_{unc}^E [%]	δ_{unc}^{had} [%]	δ_{cor} [%]	δ_{cor}^E [%]	δ_{cor}^{\ominus} [%]	δ_{cor}^{had} [%]	δ_{cor}^{Noi} [%]	δ_{cor}^{Bkg} [%]	δ_{cor}^{WrCh} [%]
650	0.0085	0.7500	0.92715	3.17	2.02	3.76	1.97	0.26	0.19	0.45	0.19	0.34	0.08	0.18	0.00	0.10
650	0.0130	0.4923	0.85193	2.35	1.04	2.57	0.90	0.29	0.04	0.52	0.34	0.37	0.02	0.09	0.08	0.00
650	0.0200	0.3200	0.72283	2.47	1.52	2.90	1.15	0.73	0.00	0.99	0.85	0.51	0.00	0.02	0.02	0.00
650	0.0320	0.2000	0.60507	2.56	1.82	3.14	1.17	0.70	0.00	1.40	1.26	0.61	0.00	0.00	0.00	0.00
650	0.0500	0.1280	0.50382	2.70	2.06	3.39	1.19	0.64	0.33	1.68	1.21	0.54	0.12	1.02	0.00	0.00
650	0.0800	0.0800	0.40609	2.95	3.44	4.53	1.17	0.51	0.12	3.23	0.90	0.40	0.06	3.08	0.00	0.00
650	0.1300	0.0492	0.35966	3.46	3.28	4.76	1.57	0.56	0.46	2.87	0.85	0.25	0.25	2.72	0.00	0.00
650	0.1800	0.0356	0.28670	3.93	3.13	5.02	1.94	0.88	0.76	2.45	1.54	0.67	0.38	1.74	0.00	0.00
650	0.2500	0.0256	0.22324	5.40	8.18	9.80	3.14	1.55	2.01	7.55	2.55	0.36	1.05	7.02	0.00	0.00
650	0.4000	0.0160	0.11664	7.28	16.41	17.95	3.71	1.91	1.83	15.98	2.87	0.73	1.01	15.67	0.00	0.00
800	0.0105	0.7500	0.85043	3.78	2.10	4.33	2.06	0.47	0.26	0.44	0.18	0.27	0.10	0.24	0.00	0.13
800	0.0130	0.6059	0.77462	3.94	1.22	4.12	1.15	0.17	0.08	0.40	0.20	0.29	0.03	0.13	0.14	0.00
800	0.0200	0.3938	0.68205	2.84	1.26	3.11	1.07	0.50	0.02	0.67	0.55	0.37	0.01	0.05	0.06	0.00
800	0.0320	0.2461	0.57702	3.09	1.46	3.42	1.20	0.67	0.00	0.83	0.77	0.33	0.00	0.00	0.00	0.00
800	0.0500	0.1575	0.52534	3.09	1.71	3.53	1.07	0.19	0.17	1.34	0.92	0.42	0.07	0.88	0.01	0.00
800	0.0800	0.0985	0.46642	3.30	2.61	4.20	1.24	0.39	0.22	2.29	0.97	0.42	0.06	2.03	0.00	0.00
800	0.1300	0.0606	0.34199	4.03	3.91	5.62	1.61	0.51	0.30	3.56	1.23	0.66	0.21	3.27	0.00	0.00
800	0.1800	0.0438	0.28205	4.58	3.09	5.52	2.20	1.01	1.04	2.17	1.84	0.51	0.33	0.97	0.00	0.00
800	0.2500	0.0315	0.20434	5.78	7.11	9.16	2.74	1.15	1.53	6.56	2.22	0.48	0.86	6.09	0.00	0.00
800	0.4000	0.0197	0.10831	8.61	13.63	16.12	3.64	1.41	1.84	13.13	2.57	0.48	0.58	12.86	0.00	0.00
1000	0.0130	0.7574	0.80449	3.90	1.97	4.37	1.59	0.13	0.26	1.17	0.14	0.35	0.11	0.19	1.08	0.00
1000	0.0200	0.4923	0.72058	3.28	1.12	3.47	0.99	0.34	0.05	0.51	0.35	0.35	0.02	0.10	0.10	0.00
1000	0.0320	0.3077	0.56954	3.38	1.34	3.63	1.11	0.59	0.00	0.76	0.57	0.50	0.00	0.01	0.02	0.00
1000	0.0500	0.1969	0.48459	3.58	2.20	4.21	1.70	1.37	0.00	1.40	1.34	0.40	0.00	0.00	0.00	0.00
1000	0.0800	0.1231	0.41876	3.88	1.75	4.25	1.15	0.29	0.26	1.31	0.69	0.31	0.14	1.07	0.01	0.00
1000	0.1300	0.0757	0.35107	4.59	3.07	5.52	1.49	0.33	0.14	2.68	0.47	0.25	0.10	2.63	0.00	0.00
1000	0.1800	0.0547	0.27607	5.19	2.43	5.73	1.86	0.48	0.84	1.56	1.06	0.26	0.36	1.05	0.00	0.00
1000	0.2500	0.0394	0.20531	6.29	5.16	8.14	2.59	1.18	1.36	4.46	1.85	0.44	0.67	3.98	0.00	0.00
1000	0.4000	0.0246	0.10188	9.29	13.18	16.13	3.63	1.44	2.09	12.67	2.03	0.27	1.04	12.46	0.00	0.00
1200	0.0130	0.9088	0.76875	6.75	3.37	7.55	2.52	0.03	0.28	2.23	0.03	0.34	0.06	0.22	2.19	0.00
1200	0.0200	0.5907	0.65281	4.32	1.19	4.48	1.09	0.15	0.10	0.47	0.15	0.35	0.04	0.13	0.24	0.00
1200	0.0320	0.3692	0.62074	3.75	1.15	3.92	0.97	0.48	0.01	0.62	0.48	0.38	0.01	0.06	0.00	0.00
1200	0.0500	0.2363	0.50852	3.95	1.69	4.30	1.29	0.95	0.00	1.09	0.95	0.53	0.00	0.00	0.00	0.00
1200	0.0800	0.1477	0.41694	4.29	1.78	4.64	1.17	0.70	0.14	1.34	0.72	0.28	0.17	1.08	0.00	0.00
1200	0.1300	0.0909	0.31784	5.35	2.61	5.95	1.60	0.85	0.37	2.06	0.94	0.28	0.10	1.81	0.00	0.00
1200	0.1800	0.0656	0.29382	5.50	2.61	6.08	1.79	0.94	0.51	1.91	1.00	0.33	0.43	1.53	0.00	0.00
1200	0.2500	0.0473	0.22915	6.33	3.92	7.44	2.44	1.32	1.23	3.06	1.42	0.35	0.56	2.63	0.00	0.00
1200	0.4000	0.0295	0.09804	10.06	12.07	15.71	4.35	2.83	2.34	11.26	3.00	0.45	0.98	10.80	0.00	0.00
1200	0.6500	0.0182	0.01340	18.61	27.00	32.79	5.42	3.31	2.91	26.45	3.49	0.61	1.46	26.17	0.00	0.00
1500	0.0200	0.7384	0.64748	5.31	1.94	5.66	1.75	0.19	0.17	0.84	0.21	0.21	0.07	0.18	0.76	0.00
1500	0.0320	0.4615	0.57808	5.22	1.01	5.32	0.95	0.07	0.04	0.33	0.07	0.30	0.02	0.11	0.05	0.00
1500	0.0500	0.2954	0.51209	4.55	1.38	4.76	1.10	0.61	0.00	0.82	0.61	0.55	0.00	0.01	0.00	0.00
1500	0.0800	0.1846	0.43726	4.75	1.95	5.14	1.47	1.07	0.23	1.28	1.08	0.22	0.05	0.66	0.00	0.00
1500	0.1300	0.1136	0.32734	6.01	2.44	6.49	1.59	0.81	0.06	1.85	0.80	0.19	0.05	1.66	0.00	0.00
1500	0.1800	0.0820	0.28359	6.36	3.10	7.08	1.84	0.98	0.48	2.50	0.99	0.23	0.30	2.27	0.00	0.00
1500	0.2500	0.0591	0.23962	6.88	3.75	7.83	2.63	1.69	1.11	2.67	1.69	0.20	0.48	1.99	0.00	0.00
1500	0.4000	0.0369	0.10280	10.61	10.78	15.13	4.27	2.61	2.39	9.90	2.61	0.10	1.16	9.48	0.00	0.00
1500	0.6500	0.0227	0.01555	19.64	24.10	31.09	6.11	4.05	3.10	23.31	4.12	0.89	1.77	22.85	0.00	0.00

Q^2 [GeV ²]	x	y	$\tilde{\sigma}_{\text{NC}}$	δ_{stat} [%]	δ_{syst} [%]	δ_{tot} [%]	δ_{unc} [%]	$\delta_{\text{unc}}^{\text{E}}$ [%]	$\delta_{\text{unc}}^{\text{had}}$ [%]	δ_{cor} [%]	$\delta_{\text{cor}}^{\text{E}}$ [%]	$\delta_{\text{cor}}^{\ominus}$ [%]	$\delta_{\text{cor}}^{\text{had}}$ [%]	$\delta_{\text{cor}}^{\text{Noi}}$ [%]	$\delta_{\text{cor}}^{\text{Bkg}}$ [%]	$\delta_{\text{cor}}^{\text{WrCh}}$ [%]
2000	0.0219	0.9000	0.64484	8.56	3.24	9.15	2.85	0.55	0.22	1.55	0.33	0.09	0.07	0.17	1.50	0.00
2000	0.0320	0.6154	0.53147	5.99	1.58	6.19	1.47	0.21	0.08	0.59	0.22	0.47	0.03	0.11	0.26	0.00
2000	0.0500	0.3938	0.49948	5.63	1.40	5.80	1.22	0.64	0.01	0.68	0.64	0.21	0.00	0.05	0.00	0.00
2000	0.0800	0.2461	0.42189	5.55	1.53	5.76	1.25	0.63	0.00	0.88	0.63	0.61	0.00	0.00	0.00	0.00
2000	0.1300	0.1515	0.32713	6.93	2.43	7.35	1.79	1.03	0.19	1.64	1.03	0.26	0.06	1.25	0.00	0.00
2000	0.1800	0.1094	0.27088	7.55	2.70	8.02	1.85	0.97	0.08	1.97	0.97	0.30	0.10	1.68	0.00	0.00
2000	0.2500	0.0788	0.20767	8.10	3.21	8.71	2.63	1.58	1.17	1.85	1.58	0.20	0.59	0.73	0.00	0.00
2000	0.4000	0.0492	0.09882	11.88	8.89	14.84	3.98	2.48	1.89	7.95	2.49	0.20	0.88	7.50	0.00	0.00
2000	0.6500	0.0303	0.01083	26.77	23.88	35.87	8.43	5.78	4.92	22.34	5.78	0.77	2.30	21.44	0.00	0.00
3000	0.0320	0.9230	0.57054	5.60	2.14	5.99	1.92	0.22	0.11	0.93	0.24	0.28	0.05	0.12	0.84	0.00
3000	0.0500	0.5907	0.46247	5.01	1.39	5.20	1.34	0.12	0.05	0.36	0.13	0.31	0.02	0.10	0.06	0.00
3000	0.0800	0.3692	0.39748	5.36	1.49	5.56	1.29	0.57	0.01	0.75	0.57	0.49	0.00	0.03	0.02	0.00
3000	0.1300	0.2272	0.32218	6.38	1.85	6.64	1.63	0.73	0.00	0.87	0.73	0.47	0.00	0.00	0.00	0.00
3000	0.1800	0.1641	0.26877	6.98	2.59	7.45	1.84	1.03	0.16	1.82	1.04	0.12	0.18	1.48	0.00	0.00
3000	0.2500	0.1181	0.20680	7.31	3.32	8.03	2.64	1.87	0.84	2.01	1.87	0.18	0.43	0.57	0.00	0.00
3000	0.4000	0.0738	0.11037	9.42	8.12	12.44	4.51	3.12	2.27	6.75	3.12	0.05	1.19	5.87	0.00	0.00
3000	0.6500	0.0454	0.01453	20.04	20.62	28.76	7.24	4.86	4.21	19.31	4.86	0.14	2.15	18.56	0.00	0.00
5000	0.0547	0.9000	0.41901	7.87	2.72	8.33	2.37	0.21	0.07	1.33	0.12	0.19	0.05	0.09	1.31	0.00
5000	0.0800	0.6154	0.34121	6.38	1.61	6.58	1.57	0.03	0.06	0.38	0.05	0.32	0.04	0.07	0.19	0.00
5000	0.1300	0.3787	0.30441	7.32	1.93	7.57	1.83	0.34	0.00	0.59	0.34	0.49	0.00	0.01	0.00	0.00
5000	0.1800	0.2735	0.25498	8.19	2.14	8.46	1.97	0.66	0.00	0.83	0.66	0.51	0.00	0.00	0.00	0.00
5000	0.2500	0.1969	0.21858	8.93	2.54	9.28	2.30	1.06	0.00	1.06	1.06	0.06	0.00	0.00	0.00	0.00
5000	0.4000	0.1231	0.08410	12.94	5.22	13.95	3.62	1.96	1.57	3.75	1.96	0.10	0.82	3.09	0.00	0.00
5000	0.6500	0.0757	0.00737	31.73	13.67	34.55	6.60	3.81	3.87	11.97	3.81	0.53	1.77	11.20	0.00	0.00
8000	0.0875	0.9000	0.25054	15.61	4.56	16.26	3.63	0.36	0.12	2.76	0.22	0.24	0.09	0.08	2.74	0.00
8000	0.1300	0.6059	0.25236	11.14	2.66	11.45	2.57	0.55	0.06	0.71	0.49	0.47	0.04	0.04	0.20	0.00
8000	0.1800	0.4376	0.23028	11.24	2.41	11.49	2.41	0.22	0.01	0.18	0.12	0.13	0.00	0.02	0.00	0.00
8000	0.2500	0.3151	0.21529	11.01	2.98	11.40	2.71	1.08	0.00	1.23	1.13	0.49	0.00	0.00	0.00	0.00
8000	0.4000	0.1969	0.09891	15.10	5.64	16.12	4.57	3.28	0.00	3.31	3.28	0.41	0.00	0.00	0.00	0.00
8000	0.6500	0.1212	0.01142	28.93	11.95	31.30	7.61	4.94	3.88	9.21	4.94	0.47	1.77	7.56	0.00	0.00
12000	0.1300	0.9088	0.20408	28.56	8.95	29.93	8.90	0.13	0.10	0.93	0.78	0.22	0.05	0.09	0.44	0.00
12000	0.1800	0.6564	0.20415	17.54	3.39	17.87	3.05	0.72	0.06	1.49	0.29	0.41	0.02	0.07	1.40	0.00
12000	0.2500	0.4726	0.13797	18.70	2.55	18.87	2.48	0.90	0.02	0.60	0.52	0.29	0.01	0.04	0.00	0.00
12000	0.4000	0.2954	0.06951	24.35	5.07	24.87	4.43	3.36	0.00	2.47	2.44	0.32	0.00	0.00	0.00	0.00
12000	0.6500	0.1818	0.01132	40.96	9.78	42.11	7.17	5.44	3.32	6.64	4.98	0.22	1.68	4.06	0.00	0.00
20000	0.2500	0.7876	0.10679	32.87	3.35	33.04	3.16	1.63	0.09	1.13	1.05	0.35	0.05	0.09	0.20	0.00
20000	0.4000	0.4923	0.07405	31.82	4.89	32.19	4.52	3.42	0.03	1.88	1.88	0.12	0.02	0.03	0.00	0.00
20000	0.6500	0.3029	0.01367	57.87	15.81	59.99	14.23	13.73	0.00	6.89	6.63	1.87	0.00	0.00	0.00	0.00
30000	0.4000	0.7384	0.02124	108.71	6.31	108.90	6.06	3.53	0.06	1.74	1.67	0.41	0.00	0.06	0.22	0.00

Table C.2: The NC e^+p double differential reduced cross section $\tilde{\sigma}_{\text{NC}}$ for negatively polarized ($P_e = -37.6\%$) leptons with the statistical δ_{stat} , systematic δ_{syst} and total δ_{tot} errors. The quantities shown are total uncorrelated systematic δ_{unc} with the contributions from the electron energy scale uncertainty $\delta_{\text{unc}}^{\text{E}}$ and hadronic energy scale uncertainty $\delta_{\text{unc}}^{\text{had}}$. The effect of other uncorrelated systematic uncertainties is included into δ_{unc} . The correlated systematic error δ_{cor} is shown with the contributions from electron energy scale $\delta_{\text{cor}}^{\text{E}}$, polar angle measurement $\delta_{\text{cor}}^{\ominus}$, hadronic energy scale $\delta_{\text{cor}}^{\text{had}}$, noise subtraction $\delta_{\text{cor}}^{\text{Noi}}$, simulated background $\delta_{\text{cor}}^{\text{Bkg}}$, wrong charge data subtraction $\delta_{\text{cor}}^{\text{WrCh}}$. The normalization and polarization errors are not included into the errors.

Q^2 [GeV ²]	x	y	$\bar{\sigma}_{\text{NC}}$	δ_{stat} [%]	δ_{syst} [%]	δ_{tot} [%]	δ_{unc} [%]	$\delta_{\text{unc}}^{\text{E}}$ [%]	$\delta_{\text{unc}}^{\text{had}}$ [%]	δ_{cor} [%]	$\delta_{\text{cor}}^{\text{E}}$ [%]	$\delta_{\text{cor}}^{\text{e}}$ [%]	$\delta_{\text{cor}}^{\text{had}}$ [%]	$\delta_{\text{cor}}^{\text{Noi}}$ [%]	$\delta_{\text{cor}}^{\text{Bkg}}$ [%]	$\delta_{\text{cor}}^{\text{WrCh}}$ [%]
90	0.0012	0.7500	1.42300	1.44	2.39	2.79	2.25	0.25	0.24	0.81	0.38	0.51	0.05	0.17	0.00	0.46
120	0.0016	0.7500	1.40720	1.58	2.22	2.72	2.09	0.27	0.27	0.73	0.30	0.46	0.06	0.18	0.00	0.44
120	0.0020	0.5907	1.35470	1.29	1.45	1.94	0.95	0.38	0.09	1.09	0.38	0.67	0.04	0.19	0.76	0.00
120	0.0032	0.3692	1.22450	1.78	1.63	2.41	1.24	0.77	0.05	1.07	0.78	0.67	0.03	0.22	0.16	0.00
150	0.0020	0.7500	1.32980	1.82	2.10	2.77	1.99	0.34	0.23	0.66	0.32	0.39	0.05	0.17	0.00	0.39
150	0.0032	0.4615	1.21990	1.09	1.24	1.65	0.89	0.36	0.07	0.86	0.44	0.58	0.03	0.20	0.41	0.00
150	0.0050	0.2954	1.11580	1.29	1.84	2.24	1.30	0.99	0.00	1.29	1.01	0.81	0.00	0.05	0.03	0.00
150	0.0080	0.1846	0.95614	1.92	3.39	3.89	2.36	1.88	1.06	2.42	1.89	0.86	0.47	1.16	0.03	0.00
200	0.0026	0.7500	1.30470	2.27	2.17	3.14	2.10	0.47	0.19	0.54	0.18	0.41	0.07	0.19	0.00	0.23
200	0.0032	0.6154	1.20090	2.06	1.22	2.39	0.95	0.15	0.07	0.77	0.30	0.51	0.02	0.16	0.45	0.00
200	0.0050	0.3938	1.10180	1.46	1.31	1.97	0.96	0.48	0.02	0.89	0.60	0.65	0.01	0.12	0.09	0.00
200	0.0080	0.2461	0.95698	1.44	1.86	2.35	1.35	1.04	0.00	1.29	1.07	0.72	0.00	0.00	0.00	0.00
200	0.0130	0.1515	0.81663	1.66	1.20	2.05	0.95	0.06	0.32	0.73	0.13	0.56	0.13	0.44	0.01	0.00
200	0.0200	0.0985	0.68205	1.84	1.64	2.47	1.26	0.78	0.36	1.06	0.83	0.55	0.15	0.31	0.00	0.00
200	0.0320	0.0615	0.60352	2.24	2.05	3.04	1.55	0.93	0.74	1.34	0.95	0.80	0.41	0.29	0.00	0.00
200	0.0500	0.0394	0.51457	2.46	4.81	5.40	2.18	1.88	0.22	4.29	1.90	0.41	0.04	3.82	0.00	0.00
200	0.0800	0.0246	0.42889	2.65	3.92	4.73	2.45	2.05	0.61	3.07	2.05	0.51	0.31	2.20	0.00	0.00
200	0.1300	0.0151	0.33902	3.12	5.15	6.02	2.36	1.41	1.18	4.57	1.40	0.83	0.65	4.22	0.00	0.00
250	0.0033	0.7500	1.27130	2.59	2.17	3.38	2.09	0.16	0.22	0.58	0.31	0.29	0.06	0.19	0.00	0.34
250	0.0050	0.4923	1.11400	1.68	1.20	2.07	0.94	0.39	0.07	0.75	0.58	0.34	0.02	0.17	0.28	0.00
250	0.0080	0.3077	0.93569	1.64	1.57	2.27	1.09	0.68	0.00	1.13	0.98	0.55	0.00	0.03	0.03	0.00
250	0.0130	0.1893	0.80230	1.75	2.12	2.74	1.34	0.99	0.14	1.64	0.72	0.75	0.08	1.27	0.03	0.00
250	0.0200	0.1231	0.69729	1.87	2.05	2.77	1.35	1.01	0.15	1.54	0.66	0.45	0.04	1.31	0.00	0.00
250	0.0320	0.0769	0.56719	1.94	1.95	2.75	1.26	0.83	0.25	1.49	0.57	0.47	0.10	1.29	0.00	0.00
250	0.0500	0.0492	0.48293	2.20	3.84	4.43	1.24	0.72	0.26	3.64	0.49	0.50	0.09	3.57	0.00	0.00
250	0.0800	0.0308	0.43772	2.36	4.57	5.14	1.33	0.77	0.16	4.37	0.57	0.63	0.09	4.28	0.00	0.00
250	0.1300	0.0189	0.35265	2.52	3.09	3.99	2.22	1.40	1.05	2.16	1.24	0.58	0.44	1.61	0.00	0.00
250	0.1800	0.0137	0.28916	3.52	11.39	11.92	2.94	2.08	1.33	11.00	1.93	0.92	0.71	10.77	0.00	0.00
300	0.0039	0.7500	1.23410	2.84	2.18	3.58	2.13	0.30	0.25	0.49	0.16	0.28	0.05	0.18	0.00	0.32
300	0.0050	0.5907	1.17490	2.76	1.32	3.06	1.02	0.24	0.07	0.84	0.53	0.54	0.04	0.19	0.30	0.00
300	0.0080	0.3692	0.98443	1.89	1.15	2.22	0.88	0.20	0.02	0.74	0.45	0.58	0.01	0.11	0.05	0.00
300	0.0130	0.2272	0.81694	1.92	1.56	2.47	1.05	0.58	0.00	1.16	0.95	0.67	0.00	0.00	0.00	0.00
300	0.0200	0.1477	0.72471	2.04	2.00	2.86	1.24	0.83	0.17	1.57	0.98	0.69	0.11	1.00	0.00	0.00
300	0.0320	0.0923	0.59602	2.18	1.96	2.93	1.28	0.87	0.12	1.49	0.70	0.55	0.08	1.19	0.00	0.00
300	0.0500	0.0591	0.51593	2.45	3.23	4.06	1.65	1.22	0.51	2.78	1.12	0.74	0.20	2.43	0.00	0.00
300	0.0800	0.0369	0.44454	2.54	4.68	5.33	1.58	1.14	0.26	4.41	0.80	0.58	0.11	4.29	0.00	0.00
300	0.1300	0.0227	0.33257	2.83	2.78	3.96	2.02	1.35	0.64	1.91	1.18	0.65	0.29	1.33	0.00	0.00
300	0.1800	0.0164	0.28045	3.94	9.93	10.68	3.11	2.14	1.59	9.43	2.27	0.75	0.81	9.09	0.00	0.00
400	0.0053	0.7500	1.12310	3.21	2.12	3.85	2.06	0.10	0.22	0.50	0.19	0.35	0.05	0.17	0.00	0.25
400	0.0080	0.4923	1.00690	2.41	1.21	2.70	0.97	0.35	0.06	0.73	0.51	0.47	0.02	0.15	0.18	0.00
400	0.0130	0.3029	0.83819	2.24	1.41	2.64	1.04	0.55	0.00	0.94	0.83	0.44	0.00	0.02	0.01	0.00
400	0.0200	0.1969	0.68057	2.36	2.08	3.14	1.31	0.93	0.00	1.62	1.55	0.47	0.00	0.00	0.00	0.00
400	0.0320	0.1231	0.61693	2.40	1.63	2.90	1.01	0.39	0.05	1.28	0.70	0.39	0.06	1.00	0.00	0.00
400	0.0500	0.0788	0.49292	2.72	2.17	3.48	1.15	0.49	0.36	1.84	0.92	0.45	0.17	1.51	0.00	0.00
400	0.0800	0.0492	0.42873	2.97	4.39	5.30	1.18	0.47	0.18	4.23	0.57	0.45	0.09	4.17	0.00	0.00
400	0.1300	0.0303	0.36577	3.18	2.65	4.14	1.74	0.75	0.78	2.00	1.15	0.52	0.32	1.52	0.00	0.00
400	0.1800	0.0219	0.27822	4.01	8.48	9.38	2.63	1.36	1.58	8.06	2.02	0.80	0.82	7.72	0.00	0.00
400	0.4000	0.0098	0.11329	6.45	25.74	26.53	3.09	1.40	1.62	25.55	2.15	0.72	0.78	25.44	0.00	0.00
500	0.0066	0.7500	1.01150	3.67	2.05	4.21	2.00	0.01	0.26	0.43	0.28	0.22	0.08	0.21	0.00	0.09
500	0.0080	0.6154	0.96767	3.92	1.23	4.11	1.10	0.22	0.09	0.53	0.31	0.37	0.04	0.15	0.17	0.00
500	0.0130	0.3787	0.83009	2.79	1.22	3.05	1.00	0.36	0.02	0.71	0.54	0.45	0.01	0.09	0.06	0.00
500	0.0200	0.2461	0.69316	2.80	1.75	3.30	1.19	0.73	0.00	1.28	1.15	0.57	0.00	0.00	0.01	0.00
500	0.0320	0.1538	0.60807	2.82	1.89	3.40	1.13	0.57	0.19	1.52	0.99	0.44	0.16	1.05	0.00	0.00
500	0.0500	0.0985	0.51095	3.03	1.90	3.58	1.23	0.67	0.32	1.45	0.91	0.44	0.20	1.02	0.00	0.00
500	0.0800	0.0615	0.45925	3.32	4.11	5.28	1.17	0.45	0.12	3.94	0.93	0.41	0.05	3.80	0.00	0.00
500	0.1300	0.0379	0.35563	3.85	3.08	4.93	1.55	0.56	0.31	2.66	0.94	0.53	0.16	2.43	0.00	0.00
500	0.1800	0.0273	0.28904	4.49	3.81	5.89	2.25	1.06	1.23	3.08	1.79	0.57	0.54	2.38	0.00	0.00
500	0.2500	0.0197	0.21493	6.05	10.04	11.72	2.91	1.32	1.84	9.61	2.36	0.54	0.92	9.25	0.00	0.00

Q^2 [GeV ²]	x	y	$\tilde{\sigma}_{\text{NC}}$	δ_{stat} [%]	δ_{syst} [%]	δ_{tot} [%]	δ_{unc} [%]	$\delta_{\text{unc}}^{\text{E}}$ [%]	$\delta_{\text{unc}}^{\text{had}}$ [%]	δ_{cor} [%]	$\delta_{\text{cor}}^{\text{E}}$ [%]	$\delta_{\text{cor}}^{\Theta}$ [%]	$\delta_{\text{cor}}^{\text{had}}$ [%]	$\delta_{\text{cor}}^{\text{Noi}}$ [%]	$\delta_{\text{cor}}^{\text{Bkg}}$ [%]	$\delta_{\text{cor}}^{\text{WrCh}}$ [%]
650	0.0085	0.7500	0.94803	4.25	2.03	4.71	2.00	0.15	0.22	0.34	0.07	0.26	0.05	0.17	0.00	0.09
650	0.0130	0.4923	0.87973	3.13	1.09	3.32	1.00	0.26	0.07	0.44	0.24	0.31	0.04	0.14	0.12	0.00
650	0.0200	0.3200	0.73837	3.26	1.57	3.62	1.19	0.64	0.01	1.02	0.88	0.52	0.01	0.02	0.01	0.00
650	0.0320	0.2000	0.64292	3.33	2.10	3.94	1.37	0.89	0.00	1.59	1.47	0.62	0.00	0.00	0.00	0.00
650	0.0500	0.1280	0.54143	3.49	1.98	4.01	1.18	0.53	0.10	1.59	0.91	0.31	0.09	1.26	0.00	0.00
650	0.0800	0.0800	0.43134	4.19	2.93	5.11	1.24	0.43	0.18	2.65	0.96	0.34	0.11	2.45	0.00	0.00
650	0.1300	0.0492	0.35311	4.53	3.19	5.54	1.63	0.55	0.43	2.75	1.02	0.27	0.07	2.54	0.00	0.00
650	0.1800	0.0356	0.29434	5.13	2.85	5.87	2.01	0.89	0.79	2.02	1.68	0.51	0.33	0.94	0.00	0.00
650	0.2500	0.0256	0.21983	6.50	8.94	11.05	3.13	1.59	1.93	8.37	2.72	0.54	1.03	7.83	0.00	0.00
650	0.4000	0.0160	0.11788	9.63	15.71	18.43	3.46	1.61	1.54	15.32	2.65	0.74	0.71	15.06	0.00	0.00
800	0.0105	0.7500	0.96812	4.70	2.06	5.13	2.03	0.22	0.21	0.35	0.13	0.24	0.06	0.20	0.00	0.07
800	0.0130	0.6059	0.83771	5.19	1.64	5.45	1.42	0.68	0.07	0.82	0.69	0.39	0.02	0.17	0.16	0.00
800	0.0200	0.3938	0.71821	3.75	1.33	3.98	1.16	0.53	0.02	0.64	0.58	0.28	0.01	0.08	0.02	0.00
800	0.0320	0.2461	0.61627	3.87	1.63	4.20	1.38	0.84	0.00	0.87	0.81	0.32	0.00	0.00	0.00	0.00
800	0.0500	0.1575	0.54236	4.06	1.75	4.43	1.19	0.19	0.29	1.28	0.77	0.39	0.09	0.95	0.01	0.00
800	0.0800	0.0985	0.40266	4.74	2.42	5.32	1.30	0.31	0.22	2.04	0.78	0.51	0.09	1.81	0.01	0.00
800	0.1300	0.0606	0.37664	5.79	3.54	6.79	1.61	0.30	0.25	3.15	0.83	0.22	0.16	3.02	0.00	0.00
800	0.1800	0.0438	0.28860	6.95	2.77	7.49	2.00	0.68	0.77	1.92	1.35	0.43	0.56	1.16	0.00	0.00
800	0.2500	0.0315	0.22600	7.30	6.86	10.02	3.11	1.41	1.89	6.12	2.54	0.67	0.95	5.45	0.00	0.00
800	0.4000	0.0197	0.10707	11.48	16.18	19.84	3.78	1.47	2.01	15.73	2.89	0.30	1.05	15.42	0.00	0.00
1000	0.0130	0.7574	0.84527	5.17	2.04	5.56	1.70	0.28	0.20	1.13	0.18	0.20	0.08	0.17	1.09	0.00
1000	0.0200	0.4923	0.71594	4.48	1.22	4.64	1.10	0.37	0.05	0.53	0.37	0.35	0.02	0.09	0.08	0.00
1000	0.0320	0.3077	0.63735	4.66	1.42	4.87	1.19	0.58	0.00	0.77	0.61	0.47	0.00	0.01	0.00	0.00
1000	0.0500	0.1969	0.50617	4.74	1.79	5.06	1.42	0.90	0.00	1.08	0.89	0.61	0.00	0.00	0.00	0.00
1000	0.0800	0.1231	0.44213	5.10	1.89	5.44	1.30	0.47	0.28	1.37	0.80	0.28	0.18	1.06	0.00	0.00
1000	0.1300	0.0757	0.36879	6.04	3.40	6.93	1.59	0.45	0.19	3.01	0.67	0.46	0.15	2.89	0.00	0.00
1000	0.1800	0.0547	0.33597	6.27	2.75	6.85	2.00	0.85	0.73	1.89	1.33	0.37	0.45	1.21	0.00	0.00
1000	0.2500	0.0394	0.22803	7.79	4.05	8.78	2.55	1.01	1.36	3.14	1.56	0.12	0.44	2.69	0.00	0.00
1000	0.4000	0.0246	0.13527	10.86	14.27	17.93	3.92	1.75	2.25	13.72	2.37	0.54	1.20	13.45	0.00	0.00
1200	0.0130	0.9088	0.78612	8.93	3.67	9.66	2.79	0.17	0.23	2.38	0.20	0.12	0.08	0.18	2.36	0.00
1200	0.0200	0.5907	0.77254	5.36	1.24	5.50	1.17	0.10	0.06	0.42	0.10	0.32	0.03	0.10	0.24	0.00
1200	0.0320	0.3692	0.64543	5.03	1.32	5.20	1.13	0.55	0.01	0.68	0.55	0.40	0.00	0.05	0.01	0.00
1200	0.0500	0.2363	0.53135	5.21	1.51	5.43	1.24	0.75	0.00	0.87	0.75	0.44	0.00	0.00	0.00	0.00
1200	0.0800	0.1477	0.46142	5.57	1.91	5.88	1.31	0.76	0.17	1.39	0.80	0.22	0.05	1.11	0.00	0.00
1200	0.1300	0.0909	0.33837	7.08	2.73	7.59	1.63	0.85	0.13	2.18	0.87	0.23	0.07	1.99	0.00	0.00
1200	0.1800	0.0656	0.27601	7.70	2.44	8.08	1.84	0.87	0.61	1.60	0.97	0.11	0.29	1.23	0.00	0.00
1200	0.2500	0.0473	0.23942	8.28	3.29	8.92	2.40	1.38	0.96	2.26	1.41	0.49	0.51	1.62	0.00	0.00
1200	0.4000	0.0295	0.11051	12.32	11.84	17.09	4.22	2.48	2.47	11.06	2.62	0.23	1.08	10.69	0.00	0.00
1200	0.6500	0.0182	0.01124	26.77	26.73	37.83	6.60	4.81	3.16	25.90	4.98	0.44	1.41	25.38	0.00	0.00
1500	0.0200	0.7384	0.73155	6.67	1.87	6.93	1.76	0.38	0.18	0.63	0.22	0.31	0.07	0.18	0.47	0.00
1500	0.0320	0.4615	0.64648	6.21	1.17	6.31	1.09	0.23	0.03	0.40	0.23	0.31	0.02	0.11	0.04	0.00
1500	0.0500	0.2954	0.55160	5.99	1.68	6.23	1.37	0.89	0.00	0.98	0.89	0.42	0.00	0.01	0.00	0.00
1500	0.0800	0.1846	0.44335	7.53	1.78	7.73	1.34	0.76	0.16	1.16	0.77	0.16	0.04	0.86	0.00	0.00
1500	0.1300	0.1136	0.27631	8.93	2.30	9.22	1.58	0.61	0.13	1.67	0.62	0.16	0.17	1.54	0.00	0.00
1500	0.1800	0.0820	0.30352	8.40	2.69	8.82	1.95	1.10	0.39	1.85	1.08	0.31	0.24	1.45	0.00	0.00
1500	0.2500	0.0591	0.23139	9.50	3.46	10.11	2.68	1.62	1.21	2.19	1.64	0.21	0.68	1.28	0.00	0.00
1500	0.4000	0.0369	0.07776	16.04	9.97	18.88	4.49	3.01	2.22	8.90	3.01	0.36	1.06	8.30	0.00	0.00
1500	0.6500	0.0227	0.01522	26.77	28.18	38.87	6.81	4.51	3.75	27.35	4.51	0.41	2.13	26.88	0.00	0.00

Q^2 [GeV ²]	x	y	$\tilde{\sigma}_{\text{NC}}$	δ_{stat} [%]	δ_{syst} [%]	δ_{tot} [%]	δ_{unc} [%]	$\delta_{\text{unc}}^{\text{E}}$ [%]	$\delta_{\text{unc}}^{\text{had}}$ [%]	δ_{cor} [%]	$\delta_{\text{cor}}^{\text{E}}$ [%]	$\delta_{\text{cor}}^{\ominus}$ [%]	$\delta_{\text{cor}}^{\text{had}}$ [%]	$\delta_{\text{cor}}^{\text{Noi}}$ [%]	$\delta_{\text{cor}}^{\text{Bkg}}$ [%]	$\delta_{\text{cor}}^{\text{WrCh}}$ [%]
2000	0.0219	0.9000	0.76767	10.56	2.82	10.93	2.45	0.46	0.22	1.40	0.17	0.20	0.08	0.22	1.35	0.00
2000	0.0320	0.6154	0.64794	7.26	1.67	7.45	1.57	0.27	0.10	0.55	0.25	0.33	0.06	0.11	0.33	0.00
2000	0.0500	0.3938	0.51758	7.57	1.37	7.69	1.25	0.50	0.01	0.57	0.50	0.27	0.00	0.03	0.00	0.00
2000	0.0800	0.2461	0.45464	7.37	1.59	7.54	1.37	0.69	0.00	0.80	0.69	0.41	0.00	0.00	0.00	0.00
2000	0.1300	0.1515	0.34418	9.23	2.36	9.52	1.97	1.16	0.42	1.29	1.16	0.22	0.21	0.48	0.00	0.00
2000	0.1800	0.1094	0.28184	10.17	2.90	10.58	1.96	1.03	0.21	2.14	1.03	0.26	0.14	1.85	0.00	0.00
2000	0.2500	0.0788	0.20123	11.49	3.07	11.89	2.61	1.52	1.08	1.62	1.52	0.17	0.44	0.31	0.00	0.00
2000	0.4000	0.0492	0.10026	15.64	8.38	17.74	4.18	2.65	2.00	7.26	2.66	0.16	1.10	6.67	0.00	0.00
2000	0.6500	0.0303	0.01375	31.67	24.14	39.82	7.36	4.59	4.37	22.99	4.59	0.65	1.54	22.46	0.00	0.00
3000	0.0320	0.9230	0.60711	7.45	2.11	7.74	1.90	0.10	0.13	0.93	0.07	0.26	0.05	0.13	0.88	0.00
3000	0.0500	0.5907	0.59895	5.95	1.50	6.13	1.43	0.28	0.06	0.44	0.23	0.35	0.04	0.09	0.08	0.00
3000	0.0800	0.3692	0.48869	6.63	1.43	6.78	1.30	0.38	0.00	0.58	0.38	0.44	0.00	0.01	0.02	0.00
3000	0.1300	0.2272	0.35167	8.44	1.99	8.67	1.75	0.85	0.00	0.95	0.85	0.41	0.00	0.00	0.00	0.00
3000	0.1800	0.1641	0.31189	8.96	2.88	9.41	2.26	1.52	0.49	1.78	1.51	0.08	0.33	0.88	0.00	0.00
3000	0.2500	0.1181	0.29750	8.59	2.56	8.96	2.12	1.19	0.15	1.44	1.21	0.09	0.06	0.77	0.00	0.00
3000	0.4000	0.0738	0.06700	16.30	7.01	17.74	4.35	2.90	2.17	5.50	2.90	0.23	1.09	4.53	0.05	0.00
3000	0.6500	0.0454	0.00783	35.50	22.25	41.90	8.37	5.84	4.94	20.62	5.84	0.18	2.47	19.62	0.00	0.00
5000	0.0547	0.9000	0.57591	9.53	2.25	9.79	2.13	0.38	0.10	0.71	0.26	0.32	0.05	0.11	0.57	0.00
5000	0.0800	0.6154	0.44820	7.67	1.67	7.85	1.61	0.24	0.05	0.43	0.25	0.29	0.03	0.08	0.19	0.00
5000	0.1300	0.3787	0.40735	8.49	1.93	8.70	1.84	0.42	0.02	0.55	0.42	0.36	0.00	0.02	0.04	0.00
5000	0.1800	0.2735	0.35463	9.47	1.94	9.67	1.90	0.26	0.00	0.40	0.26	0.31	0.00	0.00	0.00	0.00
5000	0.2500	0.1969	0.24910	16.81	2.91	17.06	2.53	1.43	0.00	1.44	1.43	0.10	0.00	0.00	0.00	0.00
5000	0.4000	0.1231	0.12302	14.45	4.47	15.13	3.52	1.78	1.48	2.75	1.80	0.10	0.65	1.98	0.00	0.00
5000	0.6500	0.0757	0.01228	31.69	15.68	35.36	7.21	4.22	4.50	13.93	4.22	0.24	2.51	13.03	0.00	0.00
8000	0.0875	0.9000	0.60712	13.91	3.09	14.25	2.78	0.22	0.16	1.34	0.17	0.41	0.06	0.16	1.25	0.00
8000	0.1300	0.6059	0.48396	11.13	2.45	11.39	2.39	0.26	0.08	0.54	0.42	0.25	0.04	0.09	0.20	0.00
8000	0.1800	0.4376	0.38911	11.74	2.35	11.97	2.31	0.19	0.00	0.42	0.29	0.31	0.00	0.02	0.00	0.00
8000	0.2500	0.3151	0.24935	14.04	2.68	14.29	2.56	0.79	0.00	0.82	0.81	0.12	0.00	0.00	0.00	0.00
8000	0.4000	0.1969	0.11609	18.93	6.64	20.06	5.18	4.13	0.00	4.14	4.13	0.32	0.00	0.00	0.00	0.00
8000	0.6500	0.1212	0.01885	28.90	11.17	30.99	7.10	4.45	3.60	8.62	4.46	0.33	1.68	7.17	0.00	0.00
12000	0.1300	0.9088	0.70623	23.39	3.48	23.65	3.19	1.06	0.09	1.39	0.67	0.41	0.05	0.08	1.14	0.00
12000	0.1800	0.6564	0.39901	16.73	2.38	16.89	2.34	0.54	0.09	0.39	0.14	0.29	0.05	0.10	0.20	0.00
12000	0.2500	0.4726	0.30921	16.71	2.69	16.93	2.59	1.19	0.01	0.71	0.70	0.12	0.01	0.03	0.00	0.00
12000	0.4000	0.2954	0.15341	21.86	5.57	22.56	4.78	3.82	0.00	2.86	2.79	0.62	0.00	0.00	0.00	0.00
12000	0.6500	0.1818	0.01521	44.81	8.75	45.66	6.49	4.84	2.79	5.87	4.41	0.45	1.32	3.62	0.00	0.00
20000	0.2500	0.7876	0.20360	34.08	2.76	34.20	2.67	1.18	0.07	0.71	0.67	0.18	0.03	0.08	0.07	0.00
20000	0.4000	0.4923	0.22881	24.30	4.89	24.79	4.61	3.59	0.02	1.62	1.62	0.07	0.01	0.02	0.00	0.00
20000	0.6500	0.3029	0.01419	70.89	16.08	72.69	14.44	13.96	0.00	7.07	6.55	2.64	0.00	0.00	0.00	0.00
30000	0.4000	0.7384	0.26197	43.33	6.64	43.83	5.94	2.99	0.11	2.97	1.57	0.55	0.04	0.06	2.46	0.00
30000	0.6500	0.4544	0.04199	57.80	11.47	58.93	10.10	9.27	0.00	5.42	5.16	1.67	0.00	0.00	0.00	0.00

Table C.3: The NC e^-p double differential reduced cross section $\tilde{\sigma}_{\text{NC}}$ for positively polarized ($P_e = +36.9\%$) leptons with the statistical δ_{stat} , systematic δ_{syst} and total δ_{tot} errors. The quantities shown are total uncorrelated systematic δ_{unc} with the contributions from the electron energy scale uncertainty $\delta_{\text{unc}}^{\text{E}}$ and hadronic energy scale uncertainty $\delta_{\text{unc}}^{\text{had}}$. The effect of other uncorrelated systematic uncertainties is included into δ_{unc} . The correlated systematic error δ_{cor} is shown with the contributions from electron energy scale $\delta_{\text{cor}}^{\text{E}}$, polar angle measurement $\delta_{\text{cor}}^{\ominus}$, hadronic energy scale $\delta_{\text{cor}}^{\text{had}}$, noise subtraction $\delta_{\text{cor}}^{\text{Noi}}$, simulated background $\delta_{\text{cor}}^{\text{Bkg}}$, wrong charge data subtraction $\delta_{\text{cor}}^{\text{WrCh}}$. The normalization and polarization errors are not included into the errors.

Q^2 [GeV ²]	x	y	$\bar{\sigma}_{NC}$	δ_{stat} [%]	δ_{syst} [%]	δ_{tot} [%]	δ_{unc} [%]	δ_{unc}^E [%]	δ_{unc}^{had} [%]	δ_{cor} [%]	δ_{cor}^E [%]	δ_{cor}^{\oplus} [%]	δ_{cor}^{had} [%]	δ_{cor}^{Noi} [%]	δ_{cor}^{Bkg} [%]	δ_{cor}^{WrCh} [%]
90	0.0012	0.7500	1.42250	0.95	2.42	2.60	2.27	0.34	0.27	0.85	0.49	0.48	0.05	0.18	0.00	0.45
120	0.0016	0.7500	1.41230	1.04	2.19	2.43	2.09	0.31	0.24	0.66	0.25	0.41	0.06	0.20	0.00	0.39
120	0.0020	0.5907	1.33660	0.87	1.55	1.78	1.02	0.54	0.08	1.17	0.57	0.62	0.03	0.18	0.80	0.00
120	0.0032	0.3692	1.20300	1.24	1.59	2.01	1.21	0.77	0.05	1.02	0.77	0.63	0.03	0.19	0.15	0.00
150	0.0020	0.7500	1.35720	1.20	2.09	2.41	1.99	0.39	0.21	0.64	0.32	0.42	0.06	0.16	0.00	0.32
150	0.0032	0.4615	1.21650	0.73	1.27	1.47	0.91	0.43	0.06	0.89	0.48	0.59	0.03	0.19	0.41	0.00
150	0.0050	0.2954	1.08910	0.88	1.66	1.88	1.20	0.86	0.00	1.14	0.89	0.71	0.00	0.04	0.04	0.00
150	0.0080	0.1846	0.95209	1.29	3.52	3.75	2.37	1.82	1.18	2.61	1.86	0.86	0.55	1.52	0.07	0.00
200	0.0026	0.7500	1.25500	1.56	2.15	2.66	2.07	0.37	0.22	0.59	0.30	0.38	0.06	0.18	0.00	0.27
200	0.0032	0.6154	1.24420	1.35	1.22	1.82	0.94	0.18	0.07	0.78	0.28	0.50	0.03	0.15	0.51	0.00
200	0.0050	0.3938	1.09750	0.96	1.31	1.62	0.99	0.54	0.02	0.86	0.62	0.58	0.01	0.14	0.08	0.00
200	0.0080	0.2461	0.95503	0.99	1.94	2.17	1.39	1.10	0.00	1.35	1.16	0.69	0.00	0.00	0.00	0.00
200	0.0130	0.1515	0.80370	1.12	1.21	1.65	0.93	0.24	0.20	0.78	0.32	0.40	0.08	0.58	0.01	0.00
200	0.0200	0.0985	0.69577	1.24	1.78	2.17	1.38	0.93	0.45	1.13	0.99	0.42	0.21	0.27	0.01	0.00
200	0.0320	0.0615	0.58031	1.44	2.24	2.66	1.68	1.19	0.69	1.48	1.19	0.68	0.33	0.45	0.00	0.00
200	0.0500	0.0394	0.52574	1.69	4.09	4.43	2.05	1.71	0.43	3.54	1.74	0.78	0.22	2.98	0.00	0.00
200	0.0800	0.0246	0.41836	1.94	4.08	4.52	2.28	1.88	0.54	3.38	1.89	0.87	0.18	2.66	0.00	0.00
200	0.1300	0.0151	0.33359	2.30	5.40	5.87	2.40	1.52	1.12	4.84	1.54	0.95	0.56	4.45	0.00	0.00
250	0.0033	0.7500	1.26350	1.73	2.16	2.77	2.09	0.29	0.26	0.53	0.23	0.36	0.05	0.20	0.00	0.24
250	0.0050	0.4923	1.11480	1.12	1.17	1.62	0.89	0.30	0.06	0.76	0.54	0.42	0.02	0.18	0.27	0.00
250	0.0080	0.3077	0.96757	1.10	1.46	1.83	1.01	0.55	0.00	1.06	0.90	0.57	0.00	0.04	0.00	0.00
250	0.0130	0.1893	0.82418	1.16	1.96	2.28	1.26	0.91	0.14	1.51	0.69	0.58	0.11	1.20	0.00	0.00
250	0.0200	0.1231	0.72722	1.20	2.17	2.48	1.41	1.09	0.17	1.65	0.83	0.76	0.07	1.20	0.00	0.00
250	0.0320	0.0769	0.59163	1.31	2.07	2.45	1.39	0.99	0.36	1.54	0.77	0.49	0.05	1.24	0.00	0.00
250	0.0500	0.0492	0.50823	1.48	3.72	4.00	1.27	0.81	0.21	3.49	0.61	0.63	0.16	3.38	0.00	0.00
250	0.0800	0.0308	0.41126	1.56	4.64	4.90	1.15	0.43	0.20	4.50	0.18	0.33	0.03	4.48	0.00	0.00
250	0.1300	0.0189	0.35480	1.76	3.20	3.65	2.14	1.31	1.03	2.38	1.17	0.65	0.49	1.90	0.00	0.00
250	0.1800	0.0137	0.27933	2.37	10.74	10.99	2.84	1.82	1.50	10.35	1.67	0.83	0.86	10.15	0.00	0.00
300	0.0039	0.7500	1.20760	1.93	2.16	2.90	2.09	0.08	0.23	0.52	0.22	0.33	0.06	0.20	0.00	0.26
300	0.0050	0.5907	1.12970	1.89	1.19	2.23	1.00	0.17	0.08	0.66	0.24	0.45	0.04	0.15	0.38	0.00
300	0.0080	0.3692	0.97946	1.28	1.20	1.75	0.92	0.36	0.02	0.77	0.54	0.53	0.01	0.10	0.08	0.00
300	0.0130	0.2272	0.81699	1.28	1.74	2.15	1.18	0.80	0.00	1.27	1.17	0.50	0.00	0.00	0.00	0.00
300	0.0200	0.1477	0.70571	1.39	1.73	2.21	1.09	0.62	0.06	1.34	0.67	0.50	0.05	1.05	0.00	0.00
300	0.0320	0.0923	0.59175	1.49	2.04	2.53	1.28	0.89	0.18	1.59	0.75	0.62	0.12	1.24	0.00	0.00
300	0.0500	0.0591	0.52072	1.61	3.08	3.47	1.39	0.97	0.29	2.74	0.84	0.52	0.10	2.56	0.00	0.00
300	0.0800	0.0369	0.42642	1.73	4.85	5.15	1.62	1.22	0.21	4.57	0.90	0.79	0.15	4.41	0.00	0.00
300	0.1300	0.0227	0.34056	1.82	3.20	3.68	2.16	1.50	0.78	2.36	1.38	0.72	0.34	1.74	0.00	0.00
300	0.1800	0.0164	0.27053	2.73	9.29	9.69	3.14	2.28	1.48	8.75	2.29	0.97	0.67	8.36	0.00	0.00
400	0.0053	0.7500	1.13680	2.23	2.12	3.08	2.06	0.21	0.28	0.51	0.06	0.36	0.09	0.23	0.00	0.26
400	0.0080	0.4923	1.04310	1.54	1.20	1.96	0.96	0.38	0.05	0.72	0.53	0.41	0.02	0.16	0.22	0.00
400	0.0130	0.3029	0.85855	1.50	1.37	2.04	0.97	0.42	0.00	0.98	0.78	0.59	0.00	0.03	0.02	0.00
400	0.0200	0.1969	0.72302	1.54	1.93	2.46	1.28	0.91	0.00	1.44	1.35	0.50	0.00	0.00	0.00	0.00
400	0.0320	0.1231	0.62201	1.61	1.71	2.35	1.06	0.52	0.16	1.35	0.75	0.43	0.09	1.03	0.01	0.00
400	0.0500	0.0788	0.49273	1.83	2.26	2.91	1.08	0.42	0.28	1.99	0.67	0.36	0.06	1.83	0.00	0.00
400	0.0800	0.0492	0.44062	1.92	4.45	4.85	1.07	0.23	0.14	4.32	0.54	0.28	0.07	4.28	0.00	0.00
400	0.1300	0.0303	0.35664	2.06	2.34	3.11	1.73	0.86	0.68	1.57	1.16	0.57	0.34	0.82	0.00	0.00
400	0.1800	0.0219	0.26813	2.76	8.80	9.22	2.63	1.29	1.67	8.40	1.92	0.51	0.87	8.11	0.00	0.00
400	0.4000	0.0098	0.11469	4.28	23.80	24.18	3.31	1.52	1.98	23.57	2.43	0.71	0.96	23.41	0.00	0.00
500	0.0066	0.7500	1.05590	2.45	2.03	3.18	1.98	0.05	0.20	0.44	0.33	0.12	0.08	0.19	0.00	0.15
500	0.0080	0.6154	1.00520	2.57	1.16	2.82	1.05	0.16	0.07	0.51	0.19	0.39	0.03	0.15	0.20	0.00
500	0.0130	0.3787	0.90577	1.85	1.24	2.22	0.96	0.31	0.03	0.79	0.61	0.49	0.01	0.09	0.06	0.00
500	0.0200	0.2461	0.73991	1.83	1.69	2.49	1.15	0.69	0.00	1.24	1.17	0.40	0.00	0.00	0.00	0.00
500	0.0320	0.1538	0.66201	1.81	1.68	2.47	1.04	0.44	0.09	1.32	0.83	0.32	0.04	0.98	0.00	0.00
500	0.0500	0.0985	0.54497	2.01	2.07	2.89	1.25	0.69	0.40	1.65	1.14	0.44	0.19	1.09	0.00	0.00
500	0.0800	0.0615	0.44269	2.26	3.94	4.54	1.16	0.46	0.14	3.76	0.72	0.49	0.10	3.66	0.00	0.00
500	0.1300	0.0379	0.36759	2.60	2.73	3.77	1.52	0.52	0.41	2.27	0.88	0.34	0.16	2.06	0.00	0.00
500	0.1800	0.0273	0.31244	3.04	2.99	4.27	1.92	0.82	0.84	2.30	1.40	0.51	0.51	1.67	0.00	0.00
500	0.2500	0.0197	0.23222	4.35	8.70	9.73	2.93	1.34	1.90	8.19	2.29	0.57	0.95	7.79	0.00	0.00

Q^2 [GeV ²]	x	y	$\bar{\sigma}_{NC}$	δ_{stat} [%]	δ_{syst} [%]	δ_{tot} [%]	δ_{unc} [%]	δ_{unc}^E [%]	δ_{unc}^{had} [%]	δ_{cor} [%]	δ_{cor}^E [%]	δ_{cor}^{\ominus} [%]	δ_{cor}^{had} [%]	δ_{cor}^{Noi} [%]	δ_{cor}^{Bkg} [%]	δ_{cor}^{WfCh} [%]
650	0.0085	0.7500	0.94159	2.88	2.02	3.51	1.97	0.15	0.21	0.42	0.15	0.32	0.07	0.20	0.00	0.10
650	0.0130	0.4923	0.89847	2.08	1.23	2.41	1.06	0.48	0.05	0.62	0.50	0.31	0.02	0.14	0.13	0.00
650	0.0200	0.3200	0.77150	2.14	1.34	2.52	1.05	0.41	0.00	0.82	0.64	0.52	0.00	0.03	0.00	0.00
650	0.0320	0.2000	0.64474	2.23	2.09	3.05	1.43	1.01	0.00	1.52	1.45	0.45	0.00	0.00	0.00	0.00
650	0.0500	0.1280	0.54348	2.38	1.77	2.97	1.11	0.42	0.06	1.39	0.76	0.36	0.06	1.11	0.00	0.00
650	0.0800	0.0800	0.45800	2.59	3.19	4.11	1.24	0.49	0.24	2.94	0.98	0.30	0.11	2.75	0.00	0.00
650	0.1300	0.0492	0.35507	3.02	3.18	4.38	1.63	0.71	0.31	2.73	1.12	0.61	0.14	2.41	0.00	0.00
650	0.1800	0.0356	0.30727	3.67	3.22	4.88	2.10	0.94	1.01	2.44	1.66	0.38	0.39	1.71	0.00	0.00
650	0.2500	0.0256	0.22186	4.34	9.01	10.00	3.03	1.61	1.79	8.48	2.32	0.63	1.03	8.07	0.00	0.00
650	0.4000	0.0160	0.10314	6.91	15.13	16.63	3.62	1.47	2.08	14.69	2.94	0.41	0.99	14.35	0.00	0.00
800	0.0105	0.7500	0.93306	3.24	2.03	3.82	1.99	0.06	0.19	0.37	0.23	0.16	0.09	0.21	0.00	0.08
800	0.0130	0.6059	0.91796	3.50	1.27	3.72	1.20	0.14	0.08	0.42	0.13	0.33	0.05	0.19	0.10	0.00
800	0.0200	0.3938	0.73332	2.51	1.26	2.81	1.11	0.46	0.02	0.61	0.48	0.36	0.01	0.08	0.06	0.00
800	0.0320	0.2461	0.63068	2.67	1.80	3.22	1.40	0.90	0.00	1.14	1.00	0.53	0.00	0.00	0.00	0.00
800	0.0500	0.1575	0.55173	2.72	1.71	3.21	1.11	0.11	0.10	1.30	0.61	0.26	0.02	1.11	0.01	0.00
800	0.0800	0.0985	0.45189	3.00	2.65	4.01	1.36	0.53	0.38	2.28	1.08	0.46	0.15	1.95	0.00	0.00
800	0.1300	0.0606	0.34288	3.62	2.93	4.66	1.68	0.55	0.49	2.39	1.26	0.41	0.29	1.97	0.00	0.00
800	0.1800	0.0438	0.31276	3.89	2.32	4.53	1.81	0.34	0.60	1.45	1.08	0.39	0.22	0.85	0.00	0.00
800	0.2500	0.0315	0.23658	5.15	6.10	7.99	2.80	1.30	1.54	5.42	2.29	0.53	0.87	4.81	0.00	0.00
800	0.4000	0.0197	0.11591	7.22	14.07	15.81	3.99	1.77	2.32	13.49	2.93	0.45	1.12	13.11	0.00	0.00
1000	0.0130	0.7574	0.85675	3.45	2.17	4.07	1.68	0.28	0.23	1.38	0.26	0.20	0.08	0.20	1.32	0.00
1000	0.0200	0.4923	0.78261	2.87	1.18	3.10	1.06	0.32	0.06	0.51	0.31	0.37	0.02	0.12	0.12	0.00
1000	0.0320	0.3077	0.66968	2.82	1.36	3.13	1.17	0.58	0.00	0.71	0.56	0.43	0.00	0.01	0.00	0.00
1000	0.0500	0.1969	0.51222	3.15	2.16	3.82	1.58	1.17	0.00	1.47	1.31	0.68	0.00	0.00	0.00	0.00
1000	0.0800	0.1231	0.42502	3.49	1.77	3.92	1.23	0.35	0.29	1.28	0.65	0.26	0.19	1.05	0.00	0.00
1000	0.1300	0.0757	0.36637	4.08	3.21	5.19	1.56	0.33	0.24	2.81	0.77	0.37	0.04	2.68	0.00	0.00
1000	0.1800	0.0547	0.36254	4.08	2.17	4.62	1.76	0.49	0.45	1.27	0.99	0.40	0.28	0.64	0.00	0.00
1000	0.2500	0.0394	0.23394	5.23	4.48	6.88	2.72	1.25	1.54	3.56	1.99	0.52	0.68	2.82	0.00	0.00
1000	0.4000	0.0246	0.11988	9.27	12.95	15.93	3.58	1.52	1.97	12.45	2.17	0.29	1.01	12.21	0.00	0.00
1200	0.0130	0.9088	0.93182	5.42	2.65	6.03	2.20	0.21	0.30	1.47	0.24	0.23	0.10	0.24	1.41	0.00
1200	0.0200	0.5907	0.78049	3.59	1.32	3.83	1.22	0.29	0.08	0.51	0.29	0.26	0.04	0.12	0.31	0.00
1200	0.0320	0.3692	0.68838	3.27	1.12	3.45	0.97	0.27	0.02	0.55	0.27	0.47	0.01	0.06	0.01	0.00
1200	0.0500	0.2363	0.54070	3.48	1.57	3.82	1.27	0.82	0.00	0.93	0.83	0.42	0.00	0.00	0.00	0.00
1200	0.0800	0.1477	0.44107	3.79	1.93	4.25	1.37	0.87	0.26	1.36	0.88	0.29	0.12	1.00	0.00	0.00
1200	0.1300	0.0909	0.36706	4.97	2.50	5.56	1.57	0.75	0.23	1.95	0.83	0.14	0.04	1.76	0.00	0.00
1200	0.1800	0.0656	0.30945	4.89	2.57	5.53	1.68	0.72	0.37	1.94	0.79	0.36	0.15	1.73	0.00	0.00
1200	0.2500	0.0473	0.21843	5.81	4.34	7.25	2.89	1.84	1.46	3.23	1.95	0.23	0.73	2.46	0.00	0.00
1200	0.4000	0.0295	0.10507	8.62	11.51	14.38	3.93	2.34	2.12	10.82	2.61	0.57	1.16	10.42	0.00	0.00
1200	0.6500	0.0182	0.01657	14.76	26.12	30.00	5.71	3.56	3.17	25.49	3.70	0.51	1.38	25.18	0.00	0.00
1500	0.0200	0.7384	0.82286	4.25	2.12	4.75	1.77	0.09	0.15	1.17	0.08	0.24	0.07	0.15	1.12	0.00
1500	0.0320	0.4615	0.68415	4.06	1.22	4.24	1.12	0.41	0.06	0.50	0.41	0.25	0.02	0.13	0.06	0.00
1500	0.0500	0.2954	0.55689	4.02	1.51	4.30	1.25	0.74	0.00	0.85	0.74	0.42	0.00	0.01	0.00	0.00
1500	0.0800	0.1846	0.47495	4.16	1.80	4.53	1.36	0.85	0.12	1.18	0.85	0.21	0.10	0.79	0.00	0.00
1500	0.1300	0.1136	0.38211	5.09	2.49	5.67	1.76	0.98	0.33	1.76	0.98	0.24	0.15	1.44	0.00	0.00
1500	0.1800	0.0820	0.29879	5.65	2.68	6.25	1.92	1.08	0.44	1.87	1.09	0.09	0.26	1.49	0.00	0.00
1500	0.2500	0.0591	0.24315	6.16	3.08	6.89	2.47	1.42	1.06	1.83	1.43	0.26	0.36	1.05	0.00	0.00
1500	0.4000	0.0369	0.11051	11.81	10.49	15.80	4.51	2.93	2.45	9.47	2.94	0.32	1.38	8.89	0.00	0.00
1500	0.6500	0.0227	0.01656	17.18	24.52	29.94	5.51	3.38	2.81	23.90	3.38	0.31	1.43	23.61	0.00	0.00

Q^2 [GeV ²]	x	y	$\tilde{\sigma}_{\text{NC}}$	δ_{stat} [%]	δ_{syst} [%]	δ_{tot} [%]	δ_{unc} [%]	$\delta_{\text{unc}}^{\text{E}}$ [%]	$\delta_{\text{unc}}^{\text{had}}$ [%]	δ_{cor} [%]	$\delta_{\text{cor}}^{\text{E}}$ [%]	$\delta_{\text{cor}}^{\ominus}$ [%]	$\delta_{\text{cor}}^{\text{had}}$ [%]	$\delta_{\text{cor}}^{\text{Noi}}$ [%]	$\delta_{\text{cor}}^{\text{Bkg}}$ [%]	$\delta_{\text{cor}}^{\text{WrCh}}$ [%]
2000	0.0219	0.9000	0.91358	6.57	3.06	7.25	2.47	0.21	0.20	1.81	0.33	0.20	0.08	0.19	1.76	0.00
2000	0.0320	0.6154	0.64380	4.89	1.58	5.13	1.49	0.20	0.10	0.51	0.20	0.41	0.05	0.15	0.15	0.00
2000	0.0500	0.3938	0.55740	4.87	1.30	5.05	1.19	0.43	0.02	0.54	0.43	0.33	0.01	0.04	0.03	0.00
2000	0.0800	0.2461	0.44422	5.02	1.71	5.30	1.42	0.83	0.00	0.95	0.83	0.46	0.00	0.00	0.00	0.00
2000	0.1300	0.1515	0.37325	5.97	2.13	6.33	1.70	0.78	0.17	1.28	0.76	0.19	0.11	1.00	0.00	0.00
2000	0.1800	0.1094	0.29730	6.63	3.03	7.29	2.10	1.30	0.36	2.18	1.32	0.28	0.18	1.70	0.00	0.00
2000	0.2500	0.0788	0.25220	6.91	2.77	7.44	2.34	1.32	0.73	1.48	1.32	0.27	0.34	0.51	0.00	0.00
2000	0.4000	0.0492	0.11020	10.01	8.88	13.38	4.44	2.86	2.33	7.69	2.86	0.10	1.24	7.03	0.00	0.00
2000	0.6500	0.0303	0.01061	25.06	24.12	34.78	7.50	5.22	3.91	22.92	5.22	0.51	2.03	22.22	0.00	0.00
3000	0.0320	0.9230	0.78025	4.42	1.97	4.84	1.83	0.24	0.11	0.74	0.20	0.30	0.05	0.12	0.64	0.00
3000	0.0500	0.5907	0.59764	4.01	1.45	4.27	1.40	0.15	0.05	0.39	0.15	0.34	0.03	0.08	0.05	0.00
3000	0.0800	0.3692	0.49903	4.37	1.48	4.61	1.32	0.54	0.00	0.67	0.54	0.39	0.00	0.01	0.00	0.00
3000	0.1300	0.2272	0.42102	5.17	1.94	5.53	1.72	0.84	0.00	0.90	0.84	0.34	0.00	0.00	0.00	0.00
3000	0.1800	0.1641	0.29231	6.17	2.68	6.72	2.05	1.28	0.36	1.72	1.28	0.07	0.23	1.13	0.00	0.00
3000	0.2500	0.1181	0.20141	6.95	3.08	7.60	2.51	1.70	0.72	1.79	1.71	0.16	0.34	0.39	0.00	0.00
3000	0.4000	0.0738	0.12254	8.09	6.06	10.11	3.64	2.31	1.54	4.85	2.31	0.13	0.66	4.21	0.00	0.00
3000	0.6500	0.0454	0.01605	29.82	20.99	36.47	7.88	5.19	4.98	19.46	5.19	0.29	2.86	18.53	0.00	0.00
5000	0.0547	0.9000	0.66803	5.98	2.14	6.35	2.01	0.17	0.14	0.71	0.07	0.38	0.07	0.13	0.58	0.00
5000	0.0800	0.6154	0.56384	4.65	1.61	4.92	1.57	0.15	0.06	0.35	0.20	0.27	0.02	0.06	0.08	0.00
5000	0.1300	0.3787	0.49111	5.23	1.86	5.55	1.79	0.32	0.01	0.50	0.31	0.39	0.00	0.01	0.00	0.00
5000	0.1800	0.2735	0.38378	6.13	1.91	6.42	1.86	0.25	0.00	0.43	0.25	0.35	0.00	0.00	0.00	0.00
5000	0.2500	0.1969	0.22693	8.02	2.44	8.38	2.24	0.95	0.00	0.97	0.95	0.20	0.00	0.00	0.00	0.00
5000	0.4000	0.1231	0.10067	10.62	5.06	11.77	3.75	2.15	1.66	3.41	2.17	0.18	0.78	2.50	0.00	0.00
5000	0.6500	0.0757	0.01520	19.28	15.40	24.68	7.44	4.77	4.41	13.48	4.77	0.18	2.40	12.38	0.00	0.00
8000	0.0875	0.9000	0.65903	8.85	2.91	9.31	2.71	0.57	0.06	1.06	0.40	0.33	0.03	0.08	0.93	0.00
8000	0.1300	0.6059	0.53559	7.10	2.39	7.49	2.35	0.25	0.03	0.46	0.21	0.30	0.01	0.05	0.27	0.00
8000	0.1800	0.4376	0.38171	8.01	2.31	8.33	2.27	0.17	0.04	0.44	0.23	0.38	0.01	0.02	0.00	0.00
8000	0.2500	0.3151	0.26779	9.07	2.85	9.51	2.63	1.12	0.00	1.10	1.10	0.05	0.00	0.00	0.00	0.00
8000	0.4000	0.1969	0.11826	12.62	5.29	13.68	4.31	3.03	0.00	3.07	3.02	0.55	0.00	0.00	0.00	0.00
8000	0.6500	0.1212	0.00988	25.88	12.51	28.75	7.88	5.24	4.36	9.72	5.24	0.25	2.53	7.78	0.00	0.00
12000	0.1300	0.9088	0.73632	15.44	4.89	16.20	4.62	0.69	0.15	1.60	0.59	0.26	0.07	0.14	1.45	0.00
12000	0.1800	0.6564	0.54337	9.58	2.29	9.85	2.25	0.11	0.07	0.40	0.09	0.32	0.04	0.10	0.19	0.00
12000	0.2500	0.4726	0.31513	11.15	2.57	11.44	2.48	0.97	0.02	0.66	0.64	0.15	0.02	0.03	0.00	0.00
12000	0.4000	0.2954	0.21341	12.42	5.54	13.60	4.79	3.85	0.00	2.77	2.72	0.54	0.00	0.00	0.00	0.00
12000	0.6500	0.1818	0.01090	35.46	8.20	36.39	6.28	4.52	2.91	5.27	3.70	0.41	1.43	3.44	0.00	0.00
20000	0.2500	0.7876	0.60341	13.33	3.21	13.71	2.92	1.14	0.09	1.34	0.72	0.17	0.05	0.05	1.11	0.00
20000	0.4000	0.4923	0.21815	16.55	4.76	17.22	4.47	3.39	0.03	1.65	1.64	0.09	0.01	0.03	0.16	0.00
20000	0.6500	0.3029	0.02011	40.89	17.73	44.56	15.82	15.41	0.00	8.00	7.60	2.51	0.00	0.00	0.00	0.00
30000	0.4000	0.7384	0.16984	35.96	7.25	36.69	6.88	3.38	0.15	2.31	1.61	0.17	0.06	0.11	1.64	0.00
30000	0.6500	0.4544	0.04519	37.83	12.96	39.99	11.51	10.82	0.00	5.94	5.66	1.80	0.00	0.02	0.00	0.00
50000	0.6500	0.7574	0.11790	57.78	10.48	58.72	9.89	7.09	0.00	3.48	3.27	1.18	0.00	0.00	0.00	0.00

Table C.4: The NC e^-p double differential reduced cross section $\tilde{\sigma}_{\text{NC}}$ for negatively polarized ($P_e = -26.0\%$) leptons with the statistical δ_{stat} , systematic δ_{syst} and total δ_{tot} errors. The quantities shown are total uncorrelated systematic δ_{unc} with the contributions from the electron energy scale uncertainty $\delta_{\text{unc}}^{\text{E}}$ and hadronic energy scale uncertainty $\delta_{\text{unc}}^{\text{had}}$. The effect of other uncorrelated systematic uncertainties is included into δ_{unc} . The correlated systematic error δ_{cor} is shown with the contributions from electron energy scale $\delta_{\text{cor}}^{\text{E}}$, polar angle measurement $\delta_{\text{cor}}^{\ominus}$, hadronic energy scale $\delta_{\text{cor}}^{\text{had}}$, noise subtraction $\delta_{\text{cor}}^{\text{Noi}}$, simulated background $\delta_{\text{cor}}^{\text{Bkg}}$, wrong charge data subtraction $\delta_{\text{cor}}^{\text{WrCh}}$. The normalization and polarization errors are not included into the errors.

Q^2 [GeV ²]	x	y	$\bar{\sigma}_{NC}$	δ_{stat} [%]	δ_{syst} [%]	δ_{tot} [%]	δ_{unc} [%]	δ_{unc}^E [%]	δ_{unc}^{had} [%]	δ_{cor} [%]	δ_{cor}^E [%]	δ_{cor}^{\oplus} [%]	δ_{cor}^{had} [%]	δ_{cor}^{Noi} [%]	δ_{cor}^{Bkg} [%]	δ_{cor}^{WrCh} [%]
90	0.0012	0.7500	1.46240	0.71	2.48	2.58	2.35	0.25	0.24	0.79	0.37	0.53	0.05	0.18	0.00	0.43
120	0.0016	0.7500	1.39310	0.79	2.22	2.36	2.10	0.20	0.24	0.72	0.36	0.45	0.06	0.18	0.00	0.39
120	0.0020	0.5907	1.35120	0.65	1.39	1.53	0.80	0.42	0.09	1.14	0.44	0.65	0.03	0.18	0.80	0.00
120	0.0032	0.3692	1.21020	0.94	1.43	1.71	1.02	0.71	0.03	1.01	0.72	0.68	0.01	0.18	0.10	0.00
150	0.0020	0.7500	1.37480	0.89	2.03	2.22	1.93	0.39	0.22	0.63	0.30	0.41	0.05	0.18	0.00	0.32
150	0.0032	0.4615	1.22780	0.55	1.19	1.31	0.80	0.48	0.06	0.89	0.55	0.53	0.03	0.18	0.41	0.00
150	0.0050	0.2954	1.08880	0.66	1.55	1.68	1.09	0.87	0.00	1.10	0.88	0.65	0.00	0.04	0.02	0.00
150	0.0080	0.1846	0.94810	0.97	3.56	3.69	2.43	2.03	1.13	2.60	2.04	0.66	0.47	1.39	0.02	0.00
200	0.0026	0.7500	1.28730	1.16	2.11	2.41	2.03	0.52	0.21	0.59	0.14	0.48	0.05	0.18	0.00	0.27
200	0.0032	0.6154	1.23320	1.04	1.19	1.58	0.74	0.13	0.08	0.93	0.32	0.63	0.03	0.18	0.58	0.00
200	0.0050	0.3938	1.09830	0.72	1.25	1.44	0.84	0.52	0.03	0.93	0.68	0.61	0.01	0.12	0.07	0.00
200	0.0080	0.2461	0.95092	0.73	1.87	2.00	1.25	1.06	0.00	1.39	1.13	0.80	0.00	0.00	0.01	0.00
200	0.0130	0.1515	0.80880	0.82	1.06	1.34	0.77	0.23	0.27	0.73	0.31	0.38	0.09	0.53	0.00	0.00
200	0.0200	0.0985	0.68453	0.93	1.62	1.87	1.21	0.89	0.43	1.07	0.93	0.48	0.15	0.21	0.00	0.00
200	0.0320	0.0615	0.60641	1.09	2.31	2.55	1.64	1.31	0.64	1.62	1.33	0.68	0.34	0.54	0.00	0.00
200	0.0500	0.0394	0.50231	1.26	4.70	4.86	2.22	2.04	0.29	4.14	2.04	0.71	0.09	3.53	0.00	0.00
200	0.0800	0.0246	0.42252	1.44	3.70	3.97	2.28	1.94	0.71	2.91	1.96	0.86	0.33	1.95	0.00	0.00
200	0.1300	0.0151	0.33365	1.68	5.68	5.93	2.43	1.65	1.23	5.14	1.65	0.86	0.65	4.75	0.00	0.00
250	0.0033	0.7500	1.26410	1.30	2.12	2.49	2.05	0.29	0.27	0.54	0.25	0.34	0.08	0.20	0.00	0.27
250	0.0050	0.4923	1.11820	0.84	1.01	1.31	0.73	0.30	0.06	0.71	0.42	0.45	0.02	0.16	0.31	0.00
250	0.0080	0.3077	0.95621	0.82	1.36	1.59	0.90	0.61	0.01	1.01	0.88	0.50	0.00	0.03	0.02	0.00
250	0.0130	0.1893	0.80635	0.89	1.89	2.09	1.17	0.95	0.10	1.48	0.77	0.65	0.08	1.08	0.01	0.00
250	0.0200	0.1231	0.71676	0.90	2.00	2.19	1.21	0.99	0.01	1.59	0.70	0.62	0.06	1.29	0.00	0.00
250	0.0320	0.0769	0.58518	0.98	2.10	2.32	1.27	0.99	0.36	1.68	0.74	0.56	0.20	1.39	0.00	0.00
250	0.0500	0.0492	0.51204	1.06	3.71	3.85	1.05	0.69	0.22	3.55	0.42	0.47	0.06	3.50	0.00	0.00
250	0.0800	0.0308	0.42663	1.18	4.59	4.74	1.21	0.74	0.39	4.43	0.54	0.56	0.14	4.36	0.00	0.00
250	0.1300	0.0189	0.34285	1.33	3.37	3.63	1.92	1.22	0.87	2.77	1.05	0.58	0.47	2.45	0.00	0.00
250	0.1800	0.0137	0.27129	1.81	11.06	11.20	2.96	2.09	1.53	10.65	2.00	0.93	0.70	10.40	0.00	0.00
300	0.0039	0.7500	1.21130	1.42	2.10	2.54	2.04	0.03	0.26	0.52	0.27	0.30	0.07	0.21	0.00	0.23
300	0.0050	0.5907	1.12970	1.43	1.11	1.82	0.82	0.29	0.08	0.76	0.43	0.37	0.03	0.15	0.48	0.00
300	0.0080	0.3692	0.97016	0.96	1.11	1.47	0.73	0.31	0.02	0.83	0.58	0.58	0.01	0.10	0.05	0.00
300	0.0130	0.2272	0.80291	0.97	1.60	1.87	0.93	0.63	0.00	1.30	1.17	0.56	0.00	0.00	0.01	0.00
300	0.0200	0.1477	0.72409	1.04	1.65	1.95	0.97	0.67	0.11	1.33	0.69	0.49	0.04	1.03	0.02	0.00
300	0.0320	0.0923	0.59487	1.11	2.11	2.39	1.23	0.96	0.28	1.72	0.95	0.61	0.14	1.29	0.00	0.00
300	0.0500	0.0591	0.51300	1.21	3.24	3.46	1.27	1.01	0.17	2.98	0.83	0.58	0.05	2.80	0.00	0.00
300	0.0800	0.0369	0.44388	1.27	4.79	4.96	1.49	1.16	0.32	4.55	0.83	0.63	0.13	4.43	0.00	0.00
300	0.1300	0.0227	0.34650	1.40	3.12	3.42	2.15	1.60	0.79	2.26	1.41	0.78	0.38	1.55	0.00	0.00
300	0.1800	0.0164	0.27911	2.02	10.50	10.69	2.94	2.07	1.53	10.08	2.04	0.70	0.74	9.82	0.00	0.00
400	0.0053	0.7500	1.15770	1.55	2.04	2.56	1.99	0.26	0.23	0.43	0.05	0.31	0.07	0.20	0.00	0.20
400	0.0080	0.4923	0.99568	1.19	0.99	1.54	0.74	0.26	0.06	0.65	0.41	0.43	0.02	0.14	0.22	0.00
400	0.0130	0.3029	0.84626	1.12	1.16	1.61	0.82	0.45	0.01	0.82	0.65	0.49	0.00	0.03	0.01	0.00
400	0.0200	0.1969	0.70666	1.17	1.86	2.20	1.11	0.86	0.00	1.50	1.38	0.59	0.00	0.00	0.00	0.00
400	0.0320	0.1231	0.60721	1.23	1.68	2.08	0.94	0.58	0.20	1.39	0.90	0.43	0.09	0.97	0.00	0.00
400	0.0500	0.0788	0.50438	1.36	2.32	2.69	0.97	0.51	0.34	2.10	0.78	0.44	0.12	1.90	0.00	0.00
400	0.0800	0.0492	0.43764	1.43	4.37	4.60	0.95	0.40	0.13	4.26	0.59	0.34	0.07	4.21	0.00	0.00
400	0.1300	0.0303	0.34335	1.52	2.16	2.64	1.57	0.64	0.78	1.49	1.09	0.47	0.33	0.83	0.00	0.00
400	0.1800	0.0219	0.27819	2.14	8.68	8.94	2.46	1.37	1.47	8.32	1.96	0.69	0.76	8.02	0.00	0.00
400	0.4000	0.0098	0.11080	3.52	23.74	24.00	3.07	1.47	1.83	23.54	2.36	0.79	0.93	23.39	0.00	0.00
500	0.0066	0.7500	1.04310	1.81	1.97	2.67	1.90	0.11	0.20	0.50	0.36	0.25	0.06	0.18	0.00	0.14
500	0.0080	0.6154	0.97850	1.98	1.08	1.25	0.87	0.31	0.08	0.64	0.32	0.42	0.03	0.15	0.32	0.00
500	0.0130	0.3787	0.86428	1.39	1.04	1.73	0.77	0.29	0.02	0.70	0.52	0.45	0.01	0.09	0.04	0.00
500	0.0200	0.2461	0.73785	1.40	1.53	2.08	0.97	0.65	0.00	1.19	1.06	0.54	0.00	0.00	0.00	0.00
500	0.0320	0.1538	0.62369	1.42	1.60	2.14	0.85	0.44	0.02	1.36	0.73	0.32	0.05	1.10	0.00	0.00
500	0.0500	0.0985	0.54765	1.52	2.07	2.57	0.96	0.53	0.27	1.83	0.98	0.39	0.10	1.49	0.00	0.00
500	0.0800	0.0615	0.44317	1.63	3.71	4.05	0.93	0.34	0.10	3.59	0.69	0.43	0.03	3.49	0.00	0.00
500	0.1300	0.0379	0.38095	1.90	3.09	3.63	1.59	0.86	0.58	2.65	1.21	0.61	0.31	2.26	0.00	0.00
500	0.1800	0.0273	0.28490	2.31	3.34	4.06	1.90	0.87	1.01	2.75	1.55	0.43	0.51	2.17	0.00	0.00
500	0.2500	0.0197	0.20882	3.10	10.93	11.36	2.87	1.46	1.89	10.55	2.42	0.61	0.98	10.20	0.00	0.00

Q^2 [GeV ²]	x	y	$\tilde{\sigma}_{\text{NC}}$	δ_{stat} [%]	δ_{syst} [%]	δ_{tot} [%]	δ_{unc} [%]	δ_{Eunc} [%]	δ_{hadunc} [%]	δ_{cor} [%]	δ_{Ecor} [%]	$\delta_{\text{Θcor}}$ [%]	δ_{hadcor} [%]	$\delta_{\text{Noi cor}}$ [%]	$\delta_{\text{Bkg cor}}$ [%]	$\delta_{\text{WrCh cor}}$ [%]
650	0.0085	0.7500	0.98280	2.12	1.95	2.88	1.89	0.23	0.20	0.47	0.21	0.35	0.07	0.20	0.00	0.11
650	0.0130	0.4923	0.85133	1.58	0.88	1.81	0.76	0.18	0.05	0.45	0.21	0.37	0.02	0.12	0.11	0.00
650	0.0200	0.3200	0.72998	1.65	1.35	2.13	0.95	0.58	0.00	0.96	0.80	0.53	0.00	0.02	0.02	0.00
650	0.0320	0.2000	0.64243	1.70	1.92	2.57	1.17	0.87	0.00	1.53	1.41	0.59	0.00	0.00	0.00	0.00
650	0.0500	0.1280	0.52814	1.79	1.92	2.63	1.00	0.55	0.24	1.65	1.05	0.49	0.10	1.17	0.00	0.00
650	0.0800	0.0800	0.44227	1.97	3.28	3.82	1.14	0.67	0.23	3.07	1.05	0.40	0.10	2.85	0.00	0.00
650	0.1300	0.0492	0.37342	2.23	3.54	4.18	1.33	0.38	0.26	3.28	0.80	0.26	0.09	3.17	0.00	0.00
650	0.1800	0.0356	0.30839	2.62	3.22	4.15	1.93	0.96	0.94	2.58	1.51	0.59	0.56	1.93	0.00	0.00
650	0.2500	0.0256	0.22320	3.45	8.31	9.00	2.93	1.56	1.87	7.78	2.48	0.57	0.88	7.29	0.00	0.00
650	0.4000	0.0160	0.12206	4.81	16.61	17.29	3.42	1.64	1.95	16.25	2.78	0.60	1.04	15.97	0.00	0.00
800	0.0105	0.7500	0.90396	2.46	1.95	3.14	1.91	0.24	0.23	0.39	0.08	0.26	0.09	0.24	0.00	0.12
800	0.0130	0.6059	0.81718	2.60	1.07	2.81	0.96	0.17	0.08	0.48	0.19	0.36	0.04	0.14	0.21	0.00
800	0.0200	0.3938	0.69907	1.89	1.08	2.17	0.90	0.44	0.02	0.59	0.47	0.35	0.01	0.08	0.05	0.00
800	0.0320	0.2461	0.61247	1.99	1.48	2.48	1.11	0.73	0.00	0.98	0.85	0.47	0.00	0.00	0.00	0.00
800	0.0500	0.1575	0.53608	2.06	1.55	2.57	0.88	0.19	0.07	1.28	0.87	0.35	0.03	0.86	0.00	0.00
800	0.0800	0.0985	0.46408	2.22	2.51	3.35	1.02	0.31	0.21	2.29	0.96	0.35	0.03	2.05	0.00	0.00
800	0.1300	0.0606	0.37070	2.61	3.94	4.73	1.38	0.46	0.12	3.69	1.13	0.57	0.10	3.47	0.00	0.00
800	0.1800	0.0438	0.29827	2.99	2.79	4.08	1.98	0.90	1.02	1.96	1.69	0.49	0.43	0.73	0.00	0.00
800	0.2500	0.0315	0.21331	3.79	7.21	8.14	2.54	1.07	1.55	6.75	1.99	0.35	0.84	6.39	0.00	0.00
800	0.4000	0.0197	0.10872	5.83	13.93	15.10	3.55	1.61	2.06	13.47	3.38	0.58	0.72	13.01	0.00	0.00
1000	0.0130	0.7574	0.79532	2.66	1.93	3.29	1.45	0.14	0.21	1.28	0.04	0.29	0.08	0.20	1.23	0.00
1000	0.0200	0.4923	0.72922	2.20	1.01	2.42	0.85	0.32	0.05	0.54	0.32	0.39	0.02	0.13	0.12	0.00
1000	0.0320	0.3077	0.61371	2.18	1.26	2.52	1.02	0.64	0.00	0.74	0.63	0.40	0.00	0.01	0.01	0.00
1000	0.0500	0.1969	0.51811	2.34	1.95	3.05	1.48	1.22	0.00	1.27	1.17	0.48	0.00	0.00	0.00	0.00
1000	0.0800	0.1231	0.43879	2.56	1.67	3.05	1.00	0.33	0.28	1.34	0.69	0.25	0.13	1.11	0.01	0.00
1000	0.1300	0.0757	0.34314	3.12	3.36	4.59	1.27	0.13	0.05	3.11	0.42	0.17	0.10	3.08	0.00	0.00
1000	0.1800	0.0547	0.30449	3.32	2.26	4.02	1.78	0.60	0.92	1.39	1.21	0.37	0.45	0.36	0.00	0.00
1000	0.2500	0.0394	0.21688	4.09	4.97	6.44	2.46	1.19	1.40	4.32	1.90	0.44	0.60	3.80	0.00	0.00
1000	0.4000	0.0246	0.11512	6.85	13.31	14.96	3.40	1.44	2.08	12.86	2.02	0.38	1.04	12.66	0.00	0.00
1200	0.0130	0.9088	0.83090	4.38	2.98	5.30	2.09	0.11	0.27	2.12	0.10	0.22	0.07	0.23	2.10	0.00
1200	0.0200	0.5907	0.70768	2.78	1.07	2.98	0.98	0.12	0.08	0.41	0.12	0.29	0.03	0.13	0.23	0.00
1200	0.0320	0.3692	0.60609	2.56	1.03	2.76	0.85	0.44	0.02	0.59	0.44	0.39	0.01	0.06	0.01	0.00
1200	0.0500	0.2363	0.51428	2.63	1.66	3.11	1.25	0.99	0.00	1.10	0.99	0.47	0.00	0.00	0.01	0.00
1200	0.0800	0.1477	0.44710	2.88	1.84	3.41	1.21	0.85	0.25	1.38	0.86	0.32	0.14	1.02	0.00	0.00
1200	0.1300	0.0909	0.35956	3.56	2.57	4.40	1.42	0.76	0.20	2.15	0.82	0.29	0.02	1.96	0.00	0.00
1200	0.1800	0.0656	0.31163	3.78	2.60	4.59	1.67	0.93	0.50	1.99	0.99	0.31	0.28	1.68	0.00	0.00
1200	0.2500	0.0473	0.21831	4.37	4.05	5.96	2.53	1.57	1.31	3.16	1.68	0.37	0.63	2.57	0.00	0.00
1200	0.4000	0.0295	0.09773	6.76	12.86	14.53	4.32	2.93	2.35	12.11	3.11	0.46	1.14	11.64	0.00	0.00
1200	0.6500	0.0182	0.01488	11.80	25.75	28.32	5.28	3.55	2.88	25.20	3.70	0.57	1.32	24.89	0.00	0.00
1500	0.0200	0.7384	0.68195	3.48	1.84	3.94	1.62	0.13	0.20	0.88	0.13	0.27	0.07	0.19	0.81	0.00
1500	0.0320	0.4615	0.59422	3.33	0.95	3.46	0.84	0.24	0.04	0.45	0.24	0.35	0.03	0.12	0.03	0.00
1500	0.0500	0.2954	0.52885	3.00	1.25	3.25	0.99	0.62	0.00	0.75	0.62	0.43	0.00	0.02	0.00	0.00
1500	0.0800	0.1846	0.44422	3.18	1.75	3.63	1.26	0.92	0.18	1.21	0.92	0.18	0.02	0.76	0.00	0.00
1500	0.1300	0.1136	0.35344	3.87	2.43	4.57	1.56	0.91	0.15	1.87	0.90	0.15	0.05	1.63	0.00	0.00
1500	0.1800	0.0820	0.29661	4.16	2.73	4.98	1.63	0.89	0.31	2.19	0.89	0.23	0.16	1.98	0.00	0.00
1500	0.2500	0.0591	0.22351	4.77	3.69	6.03	2.61	1.73	1.22	2.61	1.75	0.22	0.66	1.82	0.00	0.00
1500	0.4000	0.0369	0.10669	6.94	10.41	12.51	3.96	2.49	2.19	9.62	2.51	0.16	1.04	9.23	0.00	0.00
1500	0.6500	0.0227	0.01374	14.16	24.63	28.41	6.78	4.85	3.82	23.68	4.88	0.70	1.90	23.08	0.00	0.00

Q^2 [GeV ²]	x	y	$\tilde{\sigma}_{\text{NC}}$	δ_{stat} [%]	δ_{syst} [%]	δ_{tot} [%]	δ_{unc} [%]	$\delta_{\text{unc}}^{\text{E}}$ [%]	$\delta_{\text{unc}}^{\text{had}}$ [%]	δ_{cor} [%]	$\delta_{\text{cor}}^{\text{E}}$ [%]	$\delta_{\text{cor}}^{\ominus}$ [%]	$\delta_{\text{cor}}^{\text{had}}$ [%]	$\delta_{\text{cor}}^{\text{Noi}}$ [%]	$\delta_{\text{cor}}^{\text{Bkg}}$ [%]	$\delta_{\text{cor}}^{\text{WrCh}}$ [%]
2000	0.0219	0.9000	0.69554	5.62	2.93	6.34	2.40	0.55	0.22	1.68	0.52	0.15	0.09	0.19	1.58	0.00
2000	0.0320	0.6154	0.54741	3.94	1.43	4.19	1.33	0.22	0.09	0.53	0.23	0.41	0.04	0.11	0.20	0.00
2000	0.0500	0.3938	0.53101	3.67	1.13	3.84	1.01	0.42	0.01	0.50	0.42	0.27	0.00	0.04	0.00	0.00
2000	0.0800	0.2461	0.42717	3.72	1.67	4.08	1.28	0.89	0.00	1.07	0.89	0.60	0.00	0.00	0.00	0.00
2000	0.1300	0.1515	0.34770	4.52	2.31	5.07	1.74	1.11	0.38	1.52	1.12	0.28	0.16	0.97	0.00	0.00
2000	0.1800	0.1094	0.30133	4.81	2.65	5.49	1.61	0.81	0.20	2.10	0.81	0.25	0.04	1.92	0.00	0.00
2000	0.2500	0.0788	0.24372	5.06	3.10	5.94	2.47	1.62	1.03	1.87	1.62	0.29	0.60	0.64	0.00	0.00
2000	0.4000	0.0492	0.09935	7.94	9.24	12.18	4.03	2.73	1.97	8.31	2.73	0.20	1.00	7.78	0.00	0.00
2000	0.6500	0.0303	0.01295	16.93	24.83	30.06	7.57	5.17	4.65	23.65	5.18	0.45	2.09	22.98	0.00	0.00
3000	0.0320	0.9230	0.59372	3.73	1.96	4.22	1.72	0.20	0.13	0.94	0.14	0.27	0.06	0.13	0.87	0.00
3000	0.0500	0.5907	0.50769	3.22	1.32	3.48	1.26	0.22	0.06	0.39	0.19	0.33	0.02	0.09	0.06	0.00
3000	0.0800	0.3692	0.43780	3.42	1.34	3.67	1.15	0.53	0.01	0.69	0.53	0.44	0.01	0.02	0.01	0.00
3000	0.1300	0.2272	0.33950	4.18	1.70	4.52	1.49	0.71	0.00	0.82	0.71	0.41	0.00	0.00	0.00	0.00
3000	0.1800	0.1641	0.30333	5.14	2.67	5.79	1.87	1.29	0.12	1.90	1.29	0.10	0.08	1.39	0.00	0.00
3000	0.2500	0.1181	0.21763	4.81	3.02	5.68	2.39	1.69	0.77	1.85	1.69	0.15	0.33	0.64	0.00	0.00
3000	0.4000	0.0738	0.11138	6.35	7.58	9.89	4.06	2.81	1.99	6.40	2.81	0.09	1.00	5.67	0.00	0.00
3000	0.6500	0.0454	0.01347	14.17	21.64	25.86	7.47	5.38	4.38	20.30	5.38	0.12	2.24	19.45	0.00	0.00
5000	0.0547	0.9000	0.47254	5.07	2.34	5.58	2.01	0.49	0.11	1.20	0.24	0.33	0.07	0.10	1.12	0.00
5000	0.0800	0.6154	0.41041	3.93	1.50	4.20	1.44	0.16	0.05	0.41	0.20	0.32	0.03	0.07	0.14	0.00
5000	0.1300	0.3787	0.33964	4.64	1.78	4.97	1.68	0.36	0.00	0.58	0.36	0.46	0.00	0.02	0.00	0.00
5000	0.1800	0.2735	0.29506	5.14	1.85	5.46	1.75	0.47	0.00	0.60	0.47	0.38	0.00	0.00	0.00	0.00
5000	0.2500	0.1969	0.21561	6.13	2.10	6.48	1.98	0.72	0.00	0.72	0.72	0.07	0.00	0.00	0.00	0.00
5000	0.4000	0.1231	0.09700	8.18	4.94	9.56	3.54	2.06	1.61	3.45	2.07	0.11	0.74	2.66	0.00	0.00
5000	0.6500	0.0757	0.00973	18.62	14.20	23.41	6.27	3.94	3.78	12.74	3.94	0.34	1.98	11.94	0.00	0.00
8000	0.0875	0.9000	0.35273	8.72	3.33	9.34	2.68	0.27	0.10	1.98	0.08	0.25	0.06	0.09	1.96	0.00
8000	0.1300	0.6059	0.29135	6.99	2.34	7.37	2.29	0.34	0.06	0.47	0.25	0.33	0.04	0.07	0.22	0.00
8000	0.1800	0.4376	0.26610	7.01	2.23	7.36	2.17	0.28	0.01	0.51	0.26	0.43	0.00	0.01	0.00	0.00
8000	0.2500	0.3151	0.21889	8.86	2.40	9.18	2.31	0.59	0.00	0.67	0.62	0.25	0.00	0.00	0.00	0.00
8000	0.4000	0.1969	0.09996	10.12	5.18	11.37	4.17	3.04	0.00	3.07	3.04	0.41	0.00	0.00	0.00	0.00
8000	0.6500	0.1212	0.01251	18.60	12.19	22.24	7.15	4.79	3.96	9.87	4.78	0.52	1.94	8.39	0.00	0.00
12000	0.1300	0.9088	0.21480	19.87	5.28	20.55	4.98	0.60	0.10	1.73	1.00	0.47	0.04	0.09	1.32	0.00
12000	0.1800	0.6564	0.21572	11.41	2.59	11.70	2.43	0.58	0.07	0.88	0.19	0.45	0.03	0.08	0.72	0.00
12000	0.2500	0.4726	0.15532	11.86	2.48	12.11	2.39	0.88	0.02	0.66	0.58	0.31	0.01	0.04	0.00	0.00
12000	0.4000	0.2954	0.09854	13.91	5.01	14.78	4.36	3.38	0.00	2.46	2.44	0.36	0.00	0.00	0.00	0.00
12000	0.6500	0.1818	0.02016	20.89	9.27	22.85	6.80	5.30	3.06	6.30	4.63	0.29	1.60	3.95	0.00	0.00
20000	0.2500	0.7876	0.12606	20.32	3.47	20.61	3.23	2.10	0.10	1.27	1.22	0.20	0.07	0.11	0.24	0.00
20000	0.4000	0.4923	0.09422	18.99	4.45	19.50	4.18	3.11	0.02	1.50	1.50	0.08	0.01	0.03	0.00	0.00
20000	0.6500	0.3029	0.01006	44.86	16.22	47.70	14.44	14.05	0.00	7.40	7.07	2.18	0.00	0.00	0.00	0.00
30000	0.4000	0.7384	0.05340	46.36	5.08	46.64	4.81	3.13	0.07	1.63	1.59	0.25	0.03	0.06	0.20	0.00
30000	0.6500	0.4544	0.00810	71.12	10.33	71.87	9.36	8.45	0.00	4.38	4.22	1.20	0.00	0.00	0.00	0.00

Table C.5: The NC e^+p unpolarized double differential reduced cross section $\tilde{\sigma}_{\text{NC}}$ with the statistical δ_{stat} , systematic δ_{syst} and total δ_{tot} errors. The quantities shown are total uncorrelated systematic δ_{unc} with the contributions from the electron energy scale uncertainty $\delta_{\text{unc}}^{\text{E}}$ and hadronic energy scale uncertainty $\delta_{\text{unc}}^{\text{had}}$. The effect of other uncorrelated systematic uncertainties is included into δ_{unc} . The correlated systematic error δ_{cor} is shown with the contributions from electron energy scale $\delta_{\text{cor}}^{\text{E}}$, polar angle measurement $\delta_{\text{cor}}^{\ominus}$, hadronic energy scale $\delta_{\text{cor}}^{\text{had}}$, noise subtraction $\delta_{\text{cor}}^{\text{Noi}}$, simulated background $\delta_{\text{cor}}^{\text{Bkg}}$, wrong charge data subtraction $\delta_{\text{cor}}^{\text{WrCh}}$. The normalization and polarization errors are not included into the errors.

Q^2 [GeV ²]	x	y	$\bar{\sigma}_{NC}$	δ_{stat} [%]	δ_{syst} [%]	δ_{tot} [%]	δ_{unc} [%]	δ_{unc}^E [%]	δ_{unc}^{had} [%]	δ_{cor} [%]	δ_{cor}^E [%]	δ_{cor}^{\oplus} [%]	δ_{cor}^{had} [%]	δ_{cor}^{Noi} [%]	δ_{cor}^{Bkg} [%]	δ_{cor}^{WrCh} [%]
90	0.0012	0.7500	1.42200	0.80	2.39	2.52	2.24	0.31	0.26	0.83	0.46	0.49	0.05	0.17	0.00	0.46
120	0.0016	0.7500	1.40990	0.87	2.18	2.35	2.07	0.30	0.25	0.68	0.27	0.43	0.06	0.20	0.00	0.41
120	0.0020	0.5907	1.34140	0.72	1.49	1.65	0.95	0.49	0.09	1.15	0.51	0.63	0.03	0.18	0.79	0.00
120	0.0032	0.3692	1.20930	1.02	1.55	1.85	1.15	0.77	0.05	1.04	0.77	0.64	0.03	0.20	0.16	0.00
150	0.0020	0.7500	1.34770	1.00	2.07	2.30	1.97	0.38	0.22	0.65	0.32	0.41	0.06	0.17	0.00	0.34
150	0.0032	0.4615	1.21670	0.61	1.24	1.38	0.88	0.41	0.06	0.88	0.47	0.59	0.03	0.19	0.41	0.00
150	0.0050	0.2954	1.09680	0.73	1.69	1.84	1.20	0.90	0.00	1.19	0.93	0.74	0.00	0.04	0.04	0.00
150	0.0080	0.1846	0.95275	1.07	3.45	3.61	2.33	1.84	1.14	2.54	1.87	0.86	0.53	1.40	0.05	0.00
200	0.0026	0.7500	1.26900	1.29	2.12	2.48	2.04	0.40	0.21	0.57	0.26	0.39	0.06	0.18	0.00	0.26
200	0.0032	0.6154	1.22960	1.13	1.16	1.62	0.86	0.14	0.07	0.78	0.29	0.51	0.03	0.15	0.49	0.00
200	0.0050	0.3938	1.09770	0.80	1.29	1.52	0.95	0.52	0.02	0.87	0.61	0.60	0.01	0.13	0.09	0.00
200	0.0080	0.2461	0.95469	0.81	1.89	2.06	1.35	1.08	0.00	1.33	1.13	0.70	0.00	0.00	0.00	0.00
200	0.0130	0.1515	0.80699	0.93	1.15	1.48	0.87	0.18	0.24	0.76	0.26	0.45	0.09	0.54	0.01	0.00
200	0.0200	0.0985	0.69079	1.03	1.70	1.98	1.29	0.88	0.42	1.10	0.94	0.46	0.19	0.28	0.00	0.00
200	0.0320	0.0615	0.58707	1.22	2.13	2.45	1.58	1.11	0.71	1.43	1.12	0.72	0.35	0.40	0.00	0.00
200	0.0500	0.0394	0.52174	1.39	4.28	4.50	2.04	1.76	0.36	3.77	1.79	0.66	0.15	3.25	0.00	0.00
200	0.0800	0.0246	0.42136	1.57	3.99	4.29	2.28	1.94	0.56	3.27	1.94	0.75	0.22	2.52	0.00	0.00
200	0.1300	0.0151	0.33508	1.85	5.29	5.60	2.31	1.49	1.14	4.75	1.50	0.91	0.59	4.38	0.00	0.00
250	0.0033	0.7500	1.26430	1.44	2.13	2.57	2.06	0.25	0.24	0.54	0.26	0.34	0.05	0.20	0.00	0.27
250	0.0050	0.4923	1.11320	0.93	1.15	1.48	0.86	0.32	0.06	0.76	0.56	0.40	0.02	0.18	0.27	0.00
250	0.0080	0.3077	0.95647	0.91	1.47	1.73	1.00	0.59	0.00	1.08	0.92	0.56	0.00	0.03	0.01	0.00
250	0.0130	0.1893	0.81639	0.97	1.99	2.21	1.25	0.93	0.12	1.55	0.70	0.63	0.10	1.22	0.01	0.00
250	0.0200	0.1231	0.71709	1.01	2.10	2.33	1.35	1.07	0.10	1.60	0.78	0.67	0.05	1.23	0.00	0.00
250	0.0320	0.0769	0.58335	1.08	2.00	2.28	1.30	0.94	0.33	1.52	0.71	0.49	0.07	1.25	0.00	0.00
250	0.0500	0.0492	0.49976	1.23	3.74	3.93	1.20	0.78	0.23	3.54	0.57	0.59	0.14	3.44	0.00	0.00
250	0.0800	0.0308	0.41906	1.30	4.59	4.77	1.13	0.53	0.19	4.45	0.30	0.42	0.03	4.42	0.00	0.00
250	0.1300	0.0189	0.35375	1.44	3.14	3.45	2.12	1.34	1.04	2.31	1.19	0.63	0.47	1.81	0.00	0.00
250	0.1800	0.0137	0.28213	1.96	10.93	11.10	2.82	1.90	1.45	10.56	1.75	0.86	0.81	10.34	0.00	0.00
300	0.0039	0.7500	1.21400	1.60	2.13	2.66	2.06	0.15	0.23	0.51	0.20	0.32	0.06	0.19	0.00	0.28
300	0.0050	0.5907	1.14200	1.56	1.15	1.94	0.91	0.19	0.07	0.70	0.33	0.48	0.04	0.16	0.35	0.00
300	0.0080	0.3692	0.97954	1.06	1.15	1.56	0.86	0.31	0.02	0.76	0.51	0.55	0.01	0.10	0.07	0.00
300	0.0130	0.2272	0.81574	1.06	1.65	1.96	1.10	0.73	0.00	1.23	1.10	0.55	0.00	0.00	0.00	0.00
300	0.0200	0.1477	0.71055	1.15	1.77	2.11	1.08	0.69	0.08	1.40	0.76	0.56	0.05	1.04	0.00	0.00
300	0.0320	0.0923	0.59222	1.23	1.98	2.33	1.23	0.89	0.16	1.55	0.74	0.60	0.10	1.23	0.00	0.00
300	0.0500	0.0591	0.51851	1.35	3.09	3.37	1.41	1.05	0.35	2.75	0.92	0.58	0.13	2.52	0.00	0.00
300	0.0800	0.0369	0.43145	1.43	4.78	4.99	1.56	1.20	0.22	4.52	0.87	0.72	0.14	4.37	0.00	0.00
300	0.1300	0.0227	0.33766	1.53	3.04	3.41	2.08	1.46	0.74	2.23	1.32	0.70	0.32	1.62	0.00	0.00
300	0.1800	0.0164	0.27323	2.25	9.47	9.73	3.08	2.24	1.51	8.95	2.28	0.90	0.71	8.58	0.00	0.00
400	0.0053	0.7500	1.13040	1.83	2.08	2.77	2.02	0.18	0.26	0.50	0.10	0.35	0.07	0.21	0.00	0.26
400	0.0080	0.4923	1.02990	1.30	1.16	1.74	0.91	0.37	0.05	0.72	0.53	0.43	0.02	0.16	0.20	0.00
400	0.0130	0.3029	0.85058	1.25	1.35	1.83	0.94	0.46	0.00	0.96	0.79	0.54	0.00	0.03	0.02	0.00
400	0.0200	0.1969	0.70846	1.29	1.94	2.33	1.25	0.92	0.00	1.49	1.41	0.49	0.00	0.00	0.00	0.00
400	0.0320	0.1231	0.61928	1.33	1.65	2.12	0.98	0.48	0.13	1.33	0.73	0.41	0.07	1.02	0.01	0.00
400	0.0500	0.0788	0.49189	1.52	2.19	2.66	1.03	0.44	0.30	1.93	0.75	0.39	0.07	1.73	0.00	0.00
400	0.0800	0.0492	0.43616	1.61	4.41	4.70	1.02	0.30	0.15	4.29	0.55	0.33	0.06	4.24	0.00	0.00
400	0.1300	0.0303	0.35887	1.73	2.38	2.94	1.68	0.83	0.71	1.68	1.16	0.56	0.33	1.03	0.00	0.00
400	0.1800	0.0219	0.27086	2.27	8.68	8.97	2.57	1.31	1.64	8.29	1.95	0.60	0.85	7.99	0.00	0.00
400	0.4000	0.0098	0.11408	3.56	24.37	24.63	3.14	1.48	1.87	24.17	2.35	0.71	0.90	24.03	0.00	0.00
500	0.0066	0.7500	1.03950	2.04	1.98	2.84	1.94	0.03	0.22	0.43	0.31	0.15	0.08	0.20	0.00	0.13
500	0.0080	0.6154	0.99117	2.15	1.07	2.40	0.94	0.18	0.08	0.51	0.22	0.39	0.03	0.15	0.19	0.00
500	0.0130	0.3787	0.88016	1.54	1.18	1.94	0.90	0.33	0.03	0.76	0.59	0.47	0.01	0.09	0.06	0.00
500	0.0200	0.2461	0.72377	1.53	1.67	2.27	1.11	0.70	0.00	1.25	1.17	0.45	0.00	0.00	0.00	0.00
500	0.0320	0.1538	0.64382	1.52	1.70	2.28	0.99	0.48	0.12	1.38	0.88	0.35	0.07	1.00	0.00	0.00
500	0.0500	0.0985	0.53315	1.68	1.97	2.59	1.18	0.69	0.38	1.58	1.07	0.44	0.19	1.07	0.00	0.00
500	0.0800	0.0615	0.44682	1.87	3.97	4.38	1.08	0.46	0.14	3.82	0.78	0.47	0.09	3.70	0.00	0.00
500	0.1300	0.0379	0.36312	2.15	2.79	3.53	1.45	0.54	0.38	2.39	0.89	0.39	0.16	2.17	0.00	0.00
500	0.1800	0.0273	0.30448	2.52	3.19	4.06	1.93	0.89	0.96	2.54	1.52	0.53	0.52	1.89	0.00	0.00
500	0.2500	0.0197	0.22646	3.55	9.07	9.74	2.83	1.34	1.88	8.62	2.31	0.56	0.94	8.23	0.00	0.00

Q^2 [GeV ²]	x	y	$\bar{\sigma}_{NC}$	δ_{stat} [%]	δ_{syst} [%]	δ_{tot} [%]	δ_{unc} [%]	δ_{unc}^E [%]	δ_{unc}^{had} [%]	δ_{cor} [%]	δ_{cor}^E [%]	δ_{cor}^{\ominus} [%]	δ_{cor}^{had} [%]	δ_{cor}^{Noi} [%]	δ_{cor}^{Bkg} [%]	δ_{cor}^{WfCh} [%]
650	0.0085	0.7500	0.94074	2.38	1.96	3.08	1.92	0.15	0.22	0.39	0.11	0.30	0.06	0.19	0.00	0.09
650	0.0130	0.4923	0.88992	1.73	1.11	2.06	0.96	0.41	0.06	0.56	0.42	0.31	0.03	0.14	0.13	0.00
650	0.0200	0.3200	0.75893	1.79	1.34	2.23	1.01	0.48	0.00	0.88	0.71	0.52	0.00	0.03	0.01	0.00
650	0.0320	0.2000	0.64226	1.85	2.04	2.76	1.34	0.98	0.00	1.54	1.46	0.50	0.00	0.00	0.00	0.00
650	0.0500	0.1280	0.54125	1.97	1.77	2.65	1.03	0.45	0.06	1.45	0.80	0.34	0.06	1.15	0.00	0.00
650	0.0800	0.0800	0.44855	2.20	3.07	3.78	1.13	0.47	0.23	2.85	0.98	0.31	0.11	2.66	0.00	0.00
650	0.1300	0.0492	0.35349	2.51	3.13	4.01	1.52	0.66	0.35	2.73	1.09	0.51	0.12	2.45	0.00	0.00
650	0.1800	0.0356	0.30248	3.00	3.02	4.26	1.97	0.93	0.94	2.30	1.67	0.42	0.37	1.48	0.00	0.00
650	0.2500	0.0256	0.22067	3.61	8.95	9.65	2.96	1.60	1.83	8.45	2.44	0.60	1.03	8.00	0.00	0.00
650	0.4000	0.0160	0.10746	5.61	15.26	16.26	3.37	1.52	1.91	14.88	2.85	0.51	0.90	14.57	0.00	0.00
800	0.0105	0.7500	0.94055	2.67	1.95	3.30	1.92	0.08	0.19	0.35	0.17	0.19	0.08	0.21	0.00	0.08
800	0.0130	0.6059	0.88967	2.90	1.15	3.12	1.05	0.21	0.08	0.47	0.22	0.35	0.04	0.18	0.12	0.00
800	0.0200	0.3938	0.72600	2.09	1.20	2.40	1.03	0.48	0.02	0.62	0.51	0.34	0.01	0.08	0.05	0.00
800	0.0320	0.2461	0.62400	2.20	1.67	2.76	1.30	0.88	0.00	1.05	0.94	0.47	0.00	0.00	0.00	0.00
800	0.0500	0.1575	0.54693	2.26	1.62	2.79	0.99	0.13	0.16	1.29	0.66	0.30	0.04	1.06	0.01	0.00
800	0.0800	0.0985	0.43509	2.54	2.51	3.57	1.20	0.46	0.33	2.20	0.99	0.47	0.13	1.91	0.00	0.00
800	0.1300	0.0606	0.35204	3.09	2.99	4.30	1.51	0.47	0.42	2.58	1.13	0.35	0.19	2.29	0.00	0.00
800	0.1800	0.0438	0.30429	3.42	2.33	4.14	1.71	0.45	0.65	1.59	1.16	0.40	0.33	0.95	0.00	0.00
800	0.2500	0.0315	0.23261	4.22	6.27	7.56	2.75	1.33	1.64	5.63	2.37	0.57	0.89	5.00	0.00	0.00
800	0.4000	0.0197	0.11290	6.11	14.62	15.85	3.71	1.68	2.23	14.15	2.92	0.41	1.10	13.79	0.00	0.00
1000	0.0130	0.7574	0.84926	2.87	2.02	3.51	1.54	0.28	0.22	1.30	0.20	0.20	0.08	0.19	1.25	0.00
1000	0.0200	0.4923	0.75852	2.42	1.10	2.66	0.97	0.33	0.06	0.52	0.33	0.37	0.02	0.11	0.11	0.00
1000	0.0320	0.3077	0.65675	2.42	1.30	2.75	1.08	0.58	0.00	0.72	0.57	0.44	0.00	0.01	0.00	0.00
1000	0.0500	0.1969	0.50815	2.63	1.98	3.29	1.45	1.09	0.00	1.35	1.18	0.66	0.00	0.00	0.00	0.00
1000	0.0800	0.1231	0.42855	2.88	1.72	3.36	1.12	0.38	0.28	1.30	0.70	0.27	0.19	1.05	0.00	0.00
1000	0.1300	0.0757	0.36568	3.38	3.19	4.65	1.41	0.33	0.20	2.87	0.74	0.40	0.03	2.74	0.00	0.00
1000	0.1800	0.0547	0.35288	3.42	2.17	4.05	1.68	0.60	0.54	1.36	1.09	0.39	0.33	0.63	0.00	0.00
1000	0.2500	0.0394	0.23125	4.34	4.26	6.08	2.54	1.18	1.49	3.42	1.86	0.39	0.61	2.78	0.00	0.00
1000	0.4000	0.0246	0.12401	7.18	13.29	15.10	3.48	1.59	2.05	12.82	2.23	0.36	1.06	12.58	0.00	0.00
1200	0.0130	0.9088	0.88167	4.63	2.66	5.34	2.03	0.10	0.28	1.72	0.13	0.16	0.09	0.22	1.69	0.00
1200	0.0200	0.5907	0.77399	2.98	1.19	3.21	1.11	0.17	0.08	0.45	0.17	0.28	0.03	0.12	0.29	0.00
1200	0.0320	0.3692	0.67158	2.74	1.10	2.95	0.94	0.36	0.02	0.57	0.35	0.45	0.01	0.06	0.01	0.00
1200	0.0500	0.2363	0.53513	2.90	1.50	3.26	1.19	0.80	0.00	0.91	0.80	0.43	0.00	0.00	0.00	0.00
1200	0.0800	0.1477	0.44506	3.13	1.87	3.65	1.28	0.84	0.24	1.37	0.85	0.27	0.10	1.03	0.00	0.00
1200	0.1300	0.0909	0.35648	4.08	2.52	4.79	1.50	0.78	0.20	2.02	0.84	0.17	0.05	1.83	0.00	0.00
1200	0.1800	0.0656	0.29770	4.13	2.45	4.80	1.64	0.77	0.45	1.83	0.85	0.28	0.19	1.58	0.00	0.00
1200	0.2500	0.0473	0.22394	4.76	3.96	6.19	2.66	1.70	1.31	2.93	1.79	0.31	0.67	2.21	0.00	0.00
1200	0.4000	0.0295	0.10638	7.06	11.58	13.56	3.92	2.38	2.23	10.90	2.61	0.47	1.14	10.51	0.00	0.00
1200	0.6500	0.0182	0.01486	12.93	26.24	29.26	5.75	3.94	3.17	25.61	4.08	0.49	1.39	25.24	0.00	0.00
1500	0.0200	0.7384	0.78950	3.58	1.92	4.07	1.65	0.10	0.16	0.98	0.05	0.26	0.07	0.16	0.93	0.00
1500	0.0320	0.4615	0.66828	3.40	1.11	3.57	1.01	0.35	0.05	0.46	0.35	0.27	0.02	0.12	0.05	0.00
1500	0.0500	0.2954	0.55193	3.34	1.50	3.66	1.20	0.78	0.00	0.89	0.78	0.42	0.00	0.01	0.00	0.00
1500	0.0800	0.1846	0.46241	3.68	1.73	4.06	1.27	0.82	0.11	1.17	0.83	0.19	0.07	0.81	0.00	0.00
1500	0.1300	0.1136	0.34730	4.42	2.35	5.01	1.60	0.87	0.27	1.72	0.87	0.21	0.06	1.47	0.00	0.00
1500	0.1800	0.0820	0.29857	4.69	2.61	5.37	1.83	1.09	0.43	1.86	1.09	0.15	0.23	1.48	0.00	0.00
1500	0.2500	0.0591	0.23823	5.17	3.11	6.04	2.44	1.48	1.10	1.93	1.49	0.24	0.46	1.12	0.00	0.00
1500	0.4000	0.0369	0.09989	9.77	10.29	14.19	4.41	2.96	2.39	9.30	2.96	0.34	1.28	8.72	0.00	0.00
1500	0.6500	0.0227	0.01606	14.46	25.55	29.36	5.62	3.72	3.09	24.93	3.72	0.34	1.64	24.59	0.00	0.00

Q^2 [GeV ²]	x	y	$\bar{\sigma}_{\text{NC}}$	δ_{stat} [%]	δ_{syst} [%]	δ_{tot} [%]	δ_{unc} [%]	$\delta_{\text{unc}}^{\text{E}}$ [%]	$\delta_{\text{unc}}^{\text{had}}$ [%]	δ_{cor} [%]	$\delta_{\text{cor}}^{\text{E}}$ [%]	$\delta_{\text{cor}}^{\Theta}$ [%]	$\delta_{\text{cor}}^{\text{had}}$ [%]	$\delta_{\text{cor}}^{\text{Noi}}$ [%]	$\delta_{\text{cor}}^{\text{Bkg}}$ [%]	$\delta_{\text{cor}}^{\text{WrCh}}$ [%]
2000	0.0219	0.9000	0.86100	5.58	2.74	6.22	2.17	0.25	0.20	1.67	0.20	0.20	0.08	0.20	1.64	0.00
2000	0.0320	0.6154	0.64007	4.05	1.50	4.32	1.41	0.20	0.10	0.50	0.20	0.39	0.05	0.14	0.20	0.00
2000	0.0500	0.3938	0.54086	4.10	1.21	4.27	1.08	0.45	0.02	0.55	0.45	0.31	0.01	0.04	0.02	0.00
2000	0.0800	0.2461	0.44419	4.15	1.58	4.44	1.30	0.79	0.00	0.91	0.79	0.45	0.00	0.00	0.00	0.00
2000	0.1300	0.1515	0.36162	5.01	2.06	5.42	1.65	0.89	0.24	1.24	0.88	0.20	0.04	0.85	0.00	0.00
2000	0.1800	0.1094	0.29048	5.56	2.90	6.27	1.92	1.22	0.27	2.16	1.24	0.28	0.16	1.75	0.00	0.00
2000	0.2500	0.0788	0.23475	5.92	2.75	6.53	2.29	1.38	0.84	1.52	1.38	0.24	0.37	0.45	0.00	0.00
2000	0.4000	0.0492	0.10643	8.43	8.67	12.09	4.24	2.79	2.23	7.56	2.80	0.12	1.20	6.92	0.00	0.00
2000	0.6500	0.0303	0.01157	19.65	24.03	31.04	7.15	5.02	4.05	22.94	5.02	0.55	1.87	22.30	0.00	0.00
3000	0.0320	0.9230	0.71845	3.80	1.91	4.26	1.74	0.17	0.12	0.79	0.13	0.28	0.05	0.12	0.71	0.00
3000	0.0500	0.5907	0.59204	3.33	1.39	3.61	1.34	0.18	0.05	0.40	0.17	0.34	0.03	0.08	0.06	0.00
3000	0.0800	0.3692	0.49075	3.65	1.38	3.90	1.23	0.49	0.00	0.64	0.49	0.40	0.00	0.01	0.00	0.00
3000	0.1300	0.2272	0.39566	4.41	1.87	4.79	1.62	0.84	0.00	0.92	0.84	0.36	0.00	0.00	0.00	0.00
3000	0.1800	0.1641	0.29547	5.08	2.66	5.73	2.01	1.35	0.40	1.73	1.35	0.06	0.26	1.06	0.00	0.00
3000	0.2500	0.1181	0.22876	5.40	2.80	6.08	2.28	1.56	0.53	1.63	1.57	0.14	0.23	0.37	0.00	0.00
3000	0.4000	0.0738	0.10435	7.25	6.27	9.59	3.74	2.48	1.72	5.03	2.48	0.16	0.79	4.30	0.01	0.00
3000	0.6500	0.0454	0.01345	25.40	21.28	33.14	7.84	5.37	4.97	19.79	5.37	0.25	2.75	18.84	0.00	0.00
5000	0.0547	0.9000	0.63060	5.06	2.03	5.45	1.90	0.12	0.13	0.70	0.02	0.36	0.06	0.13	0.58	0.00
5000	0.0800	0.6154	0.52053	3.97	1.54	4.26	1.50	0.17	0.06	0.37	0.21	0.28	0.02	0.07	0.11	0.00
5000	0.1300	0.3787	0.45893	4.46	1.76	4.79	1.70	0.28	0.01	0.47	0.27	0.38	0.00	0.02	0.01	0.00
5000	0.1800	0.2735	0.36999	5.15	1.80	5.45	1.75	0.25	0.00	0.42	0.25	0.34	0.00	0.00	0.00	0.00
5000	0.2500	0.1969	0.23092	7.73	2.44	8.10	2.18	1.08	0.00	1.09	1.08	0.12	0.00	0.00	0.00	0.00
5000	0.4000	0.1231	0.10620	8.56	4.79	9.81	3.55	2.05	1.61	3.22	2.07	0.10	0.75	2.35	0.00	0.00
5000	0.6500	0.0757	0.01412	16.47	15.36	22.52	7.12	4.61	4.44	13.61	4.61	0.20	2.43	12.57	0.00	0.00
8000	0.0875	0.9000	0.63216	7.47	2.73	7.95	2.48	0.40	0.09	1.13	0.34	0.35	0.04	0.10	1.02	0.00
8000	0.1300	0.6059	0.51121	5.98	2.27	6.40	2.23	0.25	0.04	0.45	0.23	0.29	0.02	0.06	0.25	0.00
8000	0.1800	0.4376	0.37816	6.61	2.17	6.96	2.14	0.16	0.03	0.37	0.09	0.36	0.01	0.02	0.00	0.00
8000	0.2500	0.3151	0.25804	7.62	2.65	8.07	2.45	1.03	0.00	1.02	1.02	0.03	0.00	0.00	0.00	0.00
8000	0.4000	0.1969	0.11587	10.50	5.53	11.87	4.38	3.34	0.00	3.36	3.33	0.49	0.00	0.00	0.00	0.00
8000	0.6500	0.1212	0.01232	19.28	11.97	22.70	7.39	5.03	4.16	9.42	5.03	0.20	2.30	7.62	0.00	0.00
12000	0.1300	0.9088	0.71368	12.89	4.00	13.49	3.70	0.51	0.14	1.52	0.58	0.30	0.06	0.12	1.37	0.00
12000	0.1800	0.6564	0.48971	8.32	2.23	8.61	2.20	0.20	0.08	0.39	0.06	0.31	0.04	0.10	0.20	0.00
12000	0.2500	0.4726	0.30788	9.27	2.55	9.62	2.46	1.03	0.02	0.67	0.66	0.14	0.01	0.03	0.00	0.00
12000	0.4000	0.2954	0.19150	10.80	5.51	12.12	4.74	3.85	0.00	2.79	2.74	0.56	0.00	0.00	0.00	0.00
12000	0.6500	0.1818	0.01203	27.81	8.25	29.01	6.21	4.60	2.88	5.43	3.90	0.42	1.40	3.49	0.00	0.00
20000	0.2500	0.7876	0.47019	12.41	3.00	12.77	2.79	1.15	0.08	1.11	0.71	0.18	0.05	0.06	0.83	0.00
20000	0.4000	0.4923	0.21703	13.68	4.74	14.48	4.45	3.44	0.03	1.64	1.63	0.09	0.01	0.03	0.12	0.00
20000	0.6500	0.3029	0.01790	35.42	17.19	39.37	15.35	15.01	0.00	7.74	7.30	2.55	0.00	0.00	0.00	0.00
30000	0.4000	0.7384	0.19384	27.67	6.14	28.35	5.62	3.28	0.14	2.47	1.60	0.27	0.05	0.09	1.86	0.00
30000	0.6500	0.4544	0.04334	31.66	12.41	34.00	10.97	10.39	0.00	5.80	5.52	1.77	0.00	0.01	0.00	0.00
50000	0.6500	0.7574	0.07829	57.79	11.10	58.85	10.21	8.49	0.00	4.34	4.20	1.11	0.00	0.00	0.00	0.00

Table C.6: The NC e^-p unpolarized double differential reduced cross section $\bar{\sigma}_{\text{NC}}$ with the statistical δ_{stat} , systematic δ_{syst} and total δ_{tot} errors. The quantities shown are total uncorrelated systematic δ_{unc} with the contributions from the electron energy scale uncertainty $\delta_{\text{unc}}^{\text{E}}$ and hadronic energy scale uncertainty $\delta_{\text{unc}}^{\text{had}}$. The effect of other uncorrelated systematic uncertainties is included into δ_{unc} . The correlated systematic error δ_{cor} is shown with the contributions from electron energy scale $\delta_{\text{cor}}^{\text{E}}$, polar angle measurement $\delta_{\text{cor}}^{\Theta}$, hadronic energy scale $\delta_{\text{cor}}^{\text{had}}$, noise subtraction $\delta_{\text{cor}}^{\text{Noi}}$, simulated background $\delta_{\text{cor}}^{\text{Bkg}}$, wrong charge data subtraction $\delta_{\text{cor}}^{\text{WrCh}}$. The normalization and polarization errors are not included into the errors.

Q^2 [GeV ²]	x	y	$\bar{\sigma}_{\text{NC}}$	δ_{stat} [%]	δ_{syst} [%]	δ_{tot} [%]	δ_{unc} [%]	$\delta_{\text{unc}}^{\text{E}}$ [%]	$\delta_{\text{unc}}^{\text{had}}$ [%]	δ_{cor} [%]	$\delta_{\text{cor}}^{\text{E}}$ [%]	$\delta_{\text{cor}}^{\text{S}}$ [%]	$\delta_{\text{cor}}^{\text{had}}$ [%]	$\delta_{\text{cor}}^{\text{Noi}}$ [%]	$\delta_{\text{cor}}^{\text{Bkg}}$ [%]	$\delta_{\text{cor}}^{\text{WrCh}}$ [%]
90	0.0015	0.5950	1.40280	1.21	1.84	2.20	1.10	0.56	0.10	1.48	0.16	0.69	0.04	0.20	1.29	0.00
90	0.0012	0.7500	1.42200	0.80	2.39	2.52	2.24	0.31	0.26	0.83	0.46	0.49	0.05	0.17	0.00	0.46
120	0.0028	0.4250	1.27990	1.53	1.46	2.11	1.13	0.55	0.05	0.92	0.56	0.69	0.03	0.20	0.11	0.00
120	0.0025	0.4750	1.25500	1.32	1.60	2.08	1.21	0.76	0.06	1.05	0.75	0.64	0.02	0.18	0.32	0.00
120	0.0022	0.5300	1.34160	1.14	1.39	1.80	0.97	0.37	0.07	1.00	0.40	0.68	0.03	0.16	0.59	0.00
120	0.0020	0.5950	1.32080	1.13	1.79	2.12	1.04	0.48	0.11	1.46	0.52	0.55	0.04	0.20	1.23	0.00
120	0.0016	0.7500	1.41000	0.87	2.18	2.34	2.07	0.29	0.25	0.68	0.26	0.43	0.06	0.20	0.00	0.41
150	0.0060	0.2450	1.03600	0.88	2.06	2.24	1.45	1.18	0.00	1.46	1.19	0.85	0.00	0.00	0.01	0.00
150	0.0045	0.3250	1.13050	1.15	1.49	1.88	1.12	0.71	0.00	0.98	0.70	0.69	0.00	0.00	0.02	0.00
150	0.0039	0.3750	1.16360	1.14	1.61	1.97	1.19	0.81	0.01	1.09	0.86	0.63	0.01	0.19	0.06	0.00
150	0.0035	0.4250	1.18840	1.22	1.38	1.85	1.05	0.56	0.05	0.90	0.56	0.66	0.02	0.21	0.16	0.00
150	0.0031	0.4750	1.23560	1.31	1.25	1.81	0.96	0.31	0.06	0.80	0.43	0.59	0.03	0.19	0.27	0.00
150	0.0028	0.5300	1.24100	1.30	1.37	1.89	1.01	0.44	0.07	0.93	0.52	0.55	0.04	0.17	0.51	0.00
150	0.0025	0.5950	1.30200	1.31	1.43	1.94	0.95	0.24	0.09	1.06	0.30	0.43	0.04	0.18	0.91	0.00
150	0.0020	0.7500	1.34750	1.00	2.07	2.30	1.97	0.38	0.22	0.65	0.32	0.41	0.06	0.17	0.00	0.34
200	0.0197	0.1000	0.67403	1.06	4.48	4.60	3.15	3.02	0.00	3.18	3.04	0.96	0.00	0.00	0.00	0.00
200	0.0127	0.1550	0.80913	0.90	3.02	3.15	2.13	1.96	0.00	2.14	1.96	0.84	0.00	0.00	0.00	0.00
200	0.0080	0.2450	0.95091	0.81	1.91	2.08	1.37	1.11	0.00	1.33	1.16	0.66	0.00	0.00	0.00	0.00
200	0.0061	0.3250	1.03490	1.38	1.78	2.25	1.26	0.90	0.00	1.25	1.07	0.64	0.00	0.00	0.03	0.00
200	0.0053	0.3750	1.10500	1.49	1.40	2.04	1.02	0.48	0.01	0.95	0.61	0.70	0.00	0.18	0.04	0.00
200	0.0046	0.4250	1.11570	1.63	1.26	2.06	1.02	0.43	0.04	0.75	0.49	0.51	0.02	0.21	0.08	0.00
200	0.0041	0.4750	1.12750	1.71	1.16	2.06	0.96	0.15	0.05	0.64	0.20	0.58	0.02	0.14	0.15	0.00
200	0.0037	0.5300	1.21940	1.63	1.26	2.06	0.99	0.28	0.07	0.78	0.42	0.53	0.03	0.15	0.35	0.00
200	0.0033	0.5950	1.20030	1.69	1.37	2.17	0.98	0.11	0.08	0.95	0.20	0.51	0.03	0.15	0.76	0.00
200	0.0026	0.7500	1.26930	1.29	2.12	2.48	2.04	0.41	0.21	0.57	0.27	0.39	0.06	0.18	0.00	0.26
250	0.0246	0.1000	0.64178	1.05	4.14	4.27	2.81	2.67	0.00	3.04	2.92	0.85	0.00	0.00	0.00	0.00
250	0.0159	0.1550	0.77017	0.99	2.62	2.80	1.78	1.57	0.00	1.93	1.78	0.75	0.00	0.00	0.00	0.00
250	0.0100	0.2450	0.88988	0.94	1.74	1.98	1.12	0.77	0.00	1.33	1.14	0.69	0.00	0.00	0.01	0.00
250	0.0076	0.3250	0.97381	1.56	1.28	2.02	1.05	0.53	0.00	0.74	0.60	0.43	0.00	0.00	0.01	0.00
250	0.0066	0.3750	1.00200	1.68	1.38	2.17	1.01	0.44	0.01	0.94	0.74	0.56	0.01	0.17	0.03	0.00
250	0.0058	0.4250	1.06880	1.78	1.43	2.28	1.02	0.41	0.05	0.99	0.87	0.44	0.02	0.17	0.06	0.00
250	0.0052	0.4750	1.07200	2.00	1.27	2.37	1.05	0.39	0.06	0.72	0.56	0.39	0.02	0.15	0.17	0.00
250	0.0046	0.5300	1.18700	1.92	1.24	2.29	1.02	0.32	0.07	0.70	0.49	0.39	0.03	0.16	0.26	0.00
250	0.0041	0.5950	1.16180	2.00	1.38	2.43	1.05	0.24	0.09	0.89	0.34	0.39	0.03	0.20	0.70	0.00
250	0.0033	0.7500	1.26450	1.44	2.12	2.57	2.05	0.23	0.24	0.54	0.25	0.34	0.05	0.20	0.00	0.27
300	0.0295	0.1000	0.60738	1.24	3.57	3.78	2.04	1.84	0.00	2.93	2.84	0.71	0.00	0.00	0.00	0.00
300	0.0191	0.1550	0.71461	1.15	2.37	2.63	1.42	1.14	0.00	1.90	1.78	0.65	0.00	0.00	0.00	0.00
300	0.0121	0.2450	0.83785	1.07	1.54	1.87	1.04	0.63	0.00	1.13	0.98	0.58	0.00	0.00	0.00	0.00
300	0.0091	0.3250	0.93278	1.79	1.34	2.24	1.01	0.42	0.00	0.88	0.70	0.53	0.00	0.00	0.01	0.00
300	0.0079	0.3750	0.98727	1.91	1.29	2.31	1.03	0.42	0.01	0.78	0.54	0.54	0.00	0.12	0.01	0.00
300	0.0069	0.4250	1.02780	2.11	1.33	2.49	1.02	0.30	0.04	0.85	0.62	0.55	0.02	0.17	0.08	0.00
300	0.0062	0.4750	1.07090	2.28	1.28	2.62	1.10	0.40	0.06	0.66	0.28	0.55	0.03	0.15	0.19	0.00
300	0.0056	0.5300	1.13540	2.31	1.20	2.60	1.02	0.13	0.07	0.64	0.39	0.43	0.04	0.15	0.23	0.00
300	0.0050	0.5950	1.12690	2.37	1.35	2.73	1.10	0.28	0.07	0.78	0.27	0.42	0.04	0.16	0.58	0.00
300	0.0039	0.7500	1.21390	1.60	2.13	2.66	2.06	0.15	0.23	0.51	0.20	0.31	0.06	0.19	0.00	0.28
400	0.0656	0.0600	0.46102	1.63	3.36	3.74	1.99	1.72	0.00	2.71	2.62	0.68	0.00	0.00	0.00	0.00
400	0.0394	0.1000	0.54773	1.44	3.48	3.77	1.93	1.71	0.00	2.90	2.81	0.72	0.00	0.00	0.00	0.00
400	0.0254	0.1550	0.65419	1.33	2.45	2.79	1.41	1.13	0.00	2.01	1.91	0.60	0.00	0.00	0.00	0.00
400	0.0161	0.2450	0.77076	1.27	1.55	2.00	1.03	0.61	0.00	1.15	1.00	0.57	0.00	0.00	0.01	0.00
400	0.0121	0.3250	0.88378	2.16	1.23	2.49	1.00	0.32	0.00	0.72	0.54	0.48	0.00	0.00	0.02	0.00
400	0.0105	0.3750	0.93259	2.29	1.36	2.66	1.03	0.33	0.01	0.89	0.77	0.42	0.00	0.13	0.04	0.00
400	0.0093	0.4250	0.98121	2.51	1.39	2.87	1.10	0.41	0.04	0.85	0.58	0.58	0.02	0.18	0.04	0.00
400	0.0083	0.4750	1.00530	2.75	1.27	3.03	1.11	0.30	0.05	0.63	0.37	0.47	0.02	0.14	0.10	0.00
400	0.0074	0.5300	1.07090	2.78	1.21	3.03	1.08	0.20	0.06	0.54	0.28	0.40	0.03	0.12	0.19	0.00
400	0.0066	0.5950	1.07040	2.77	1.47	3.13	1.19	0.42	0.08	0.86	0.57	0.31	0.03	0.17	0.54	0.00
400	0.0053	0.7500	1.13120	1.83	2.08	2.77	2.02	0.17	0.26	0.50	0.10	0.35	0.07	0.21	0.00	0.26

Q^2 [GeV ²]	x	y	$\tilde{\sigma}_{\text{NC}}$	δ_{stat} [%]	δ_{syst} [%]	δ_{tot} [%]	δ_{unc} [%]	$\delta_{\text{unc}}^{\text{E}}$ [%]	$\delta_{\text{unc}}^{\text{had}}$ [%]	δ_{cor} [%]	$\delta_{\text{cor}}^{\text{E}}$ [%]	$\delta_{\text{cor}}^{\ominus}$ [%]	$\delta_{\text{cor}}^{\text{had}}$ [%]	$\delta_{\text{cor}}^{\text{Noi}}$ [%]	$\delta_{\text{cor}}^{\text{Bkg}}$ [%]	$\delta_{\text{cor}}^{\text{WrCh}}$ [%]
500	0.0820	0.0600	0.44817	1.90	3.36	3.86	1.93	1.60	0.00	2.75	2.70	0.55	0.00	0.00	0.00	0.00
500	0.0492	0.1000	0.52648	1.68	3.08	3.50	1.73	1.47	0.00	2.54	2.40	0.84	0.00	0.00	0.00	0.00
500	0.0318	0.1550	0.63634	1.55	2.38	2.84	1.44	1.15	0.00	1.90	1.81	0.58	0.00	0.00	0.00	0.00
500	0.0201	0.2450	0.72436	1.54	1.56	2.20	1.04	0.60	0.00	1.17	1.05	0.50	0.00	0.00	0.00	0.00
500	0.0151	0.3250	0.82089	2.65	1.62	3.11	1.22	0.69	0.00	1.06	0.98	0.42	0.00	0.00	0.02	0.00
500	0.0131	0.3750	0.89744	2.87	1.31	3.16	1.07	0.26	0.01	0.75	0.53	0.53	0.00	0.09	0.02	0.00
500	0.0116	0.4250	0.92318	2.98	1.16	3.20	1.09	0.16	0.05	0.41	0.28	0.25	0.01	0.14	0.05	0.00
500	0.0104	0.4750	0.90898	3.33	1.75	3.76	1.29	0.61	0.06	1.18	1.04	0.51	0.03	0.15	0.19	0.00
500	0.0093	0.5300	0.97325	3.17	1.21	3.40	1.11	0.11	0.06	0.48	0.18	0.42	0.03	0.13	0.09	0.00
500	0.0083	0.5950	0.96396	3.15	1.22	3.38	1.11	0.12	0.10	0.51	0.08	0.38	0.03	0.17	0.29	0.00
500	0.0066	0.7500	1.03800	2.04	1.99	2.85	1.94	0.04	0.22	0.44	0.33	0.16	0.08	0.20	0.00	0.13
650	0.1067	0.0600	0.38648	2.38	1.96	3.08	1.33	0.56	0.00	1.44	1.33	0.55	0.00	0.00	0.00	0.00
650	0.0640	0.1000	0.49141	2.12	3.16	3.81	1.77	1.47	0.00	2.62	2.51	0.73	0.00	0.00	0.00	0.00
650	0.0413	0.1550	0.57349	1.93	2.35	3.04	1.47	1.14	0.00	1.84	1.74	0.58	0.00	0.00	0.00	0.00
650	0.0261	0.2450	0.70114	1.82	1.64	2.44	1.13	0.68	0.00	1.18	1.09	0.47	0.00	0.00	0.00	0.00
650	0.0197	0.3250	0.76832	3.08	1.65	3.49	1.27	0.62	0.00	1.06	0.93	0.51	0.00	0.00	0.01	0.00
650	0.0171	0.3750	0.79689	3.30	1.43	3.59	1.26	0.56	0.02	0.67	0.51	0.42	0.01	0.14	0.01	0.00
650	0.0151	0.4250	0.83946	3.49	1.51	3.81	1.30	0.52	0.04	0.78	0.51	0.58	0.02	0.12	0.00	0.00
650	0.0135	0.4750	0.89646	3.64	1.33	3.87	1.24	0.32	0.06	0.48	0.41	0.17	0.03	0.13	0.11	0.00
650	0.0121	0.5300	0.87971	3.60	1.38	3.86	1.27	0.44	0.08	0.55	0.44	0.26	0.03	0.16	0.12	0.00
650	0.0108	0.5950	0.95858	3.52	1.32	3.76	1.20	0.20	0.07	0.55	0.20	0.40	0.04	0.13	0.30	0.00
650	0.0085	0.7500	0.94014	2.38	1.96	3.08	1.92	0.16	0.22	0.39	0.11	0.30	0.06	0.19	0.00	0.09
800	0.1313	0.0600	0.36789	3.16	1.59	3.53	1.43	0.34	0.00	0.69	0.49	0.49	0.00	0.00	0.00	0.00
800	0.0788	0.1000	0.44056	2.59	2.44	3.56	1.53	1.02	0.00	1.90	1.72	0.81	0.00	0.00	0.00	0.00
800	0.0508	0.1550	0.54244	2.32	2.29	3.27	1.62	1.27	0.00	1.62	1.55	0.46	0.00	0.00	0.00	0.00
800	0.0321	0.2450	0.62016	2.23	1.65	2.78	1.28	0.85	0.00	1.04	0.95	0.44	0.00	0.00	0.00	0.00
800	0.0242	0.3250	0.68869	3.60	1.53	3.91	1.31	0.57	0.00	0.78	0.63	0.47	0.00	0.00	0.01	0.00
800	0.0210	0.3750	0.68826	3.90	1.60	4.22	1.40	0.71	0.01	0.77	0.75	0.14	0.01	0.05	0.01	0.00
800	0.0185	0.4250	0.76923	4.02	1.76	4.39	1.49	0.80	0.02	0.94	0.86	0.35	0.01	0.13	0.05	0.00
800	0.0166	0.4750	0.78076	4.33	1.42	4.56	1.31	0.10	0.09	0.54	0.11	0.49	0.04	0.18	0.06	0.00
800	0.0149	0.5300	0.92886	4.24	1.49	4.50	1.39	0.47	0.08	0.54	0.46	0.19	0.02	0.17	0.15	0.00
800	0.0132	0.5950	0.83065	4.30	1.41	4.52	1.31	0.20	0.08	0.53	0.20	0.42	0.05	0.17	0.18	0.00
800	0.0105	0.7500	0.94152	2.67	1.95	3.30	1.92	0.08	0.19	0.34	0.17	0.18	0.08	0.21	0.00	0.08
1000	0.0985	0.1000	0.40900	3.08	2.52	3.98	1.92	1.46	0.00	1.64	1.55	0.54	0.00	0.00	0.00	0.00
1000	0.0635	0.1550	0.47599	2.75	1.98	3.39	1.49	1.10	0.00	1.30	1.18	0.55	0.00	0.00	0.00	0.00
1000	0.0402	0.2450	0.55922	2.53	1.69	3.04	1.28	0.86	0.00	1.10	0.89	0.64	0.00	0.00	0.00	0.00
1000	0.0303	0.3250	0.70879	4.21	1.32	4.41	1.23	0.43	0.00	0.48	0.44	0.18	0.00	0.00	0.00	0.00
1000	0.0263	0.3750	0.68294	4.38	1.89	4.77	1.53	0.97	0.00	1.10	0.97	0.51	0.00	0.03	0.00	0.00
1000	0.0232	0.4250	0.67915	4.85	1.53	5.08	1.35	0.48	0.03	0.71	0.48	0.50	0.01	0.13	0.09	0.00
1000	0.0207	0.4750	0.71834	5.09	1.57	5.33	1.44	0.60	0.06	0.64	0.60	0.12	0.02	0.11	0.12	0.00
1000	0.0186	0.5300	0.83267	4.76	1.51	4.99	1.38	0.46	0.07	0.62	0.46	0.38	0.05	0.13	0.10	0.00
1000	0.0165	0.5950	0.85073	4.80	1.43	5.01	1.35	0.38	0.08	0.49	0.38	0.24	0.03	0.10	0.16	0.00
1000	0.0131	0.7500	0.83244	2.94	2.14	3.64	1.61	0.22	0.25	1.41	0.08	0.26	0.08	0.19	1.36	0.00

Table C.7: The NC e^+p double differential reduced cross section $\tilde{\sigma}_{\text{NC}}$ measured on the $Q^2 - y$ bin grid for unpolarized leptons with the statistical δ_{stat} , systematic δ_{syst} and total δ_{tot} errors. The quantities shown are total uncorrelated systematic δ_{unc} with the contributions from the electron energy scale uncertainty $\delta_{\text{unc}}^{\text{E}}$ and hadronic energy scale uncertainty $\delta_{\text{unc}}^{\text{had}}$. The effect of other uncorrelated systematic uncertainties is included into δ_{unc} . The correlated systematic error δ_{cor} is shown with the contributions from electron energy scale $\delta_{\text{cor}}^{\text{E}}$, polar angle measurement $\delta_{\text{cor}}^{\ominus}$, hadronic energy scale $\delta_{\text{cor}}^{\text{had}}$, noise subtraction $\delta_{\text{cor}}^{\text{Noi}}$, simulated background $\delta_{\text{cor}}^{\text{Bkg}}$, wrong charge data subtraction $\delta_{\text{cor}}^{\text{WrCh}}$. The normalization and polarization errors are not included into the errors.

Q^2 [GeV ²]	x	y	$\bar{\sigma}_{\text{NC}}$	δ_{stat} [%]	δ_{syst} [%]	δ_{tot} [%]	δ_{unc} [%]	δ_{Eunc} [%]	δ_{hadunc} [%]	δ_{cor} [%]	δ_{Ecor} [%]	$\delta_{\text{Cor}}^{\ominus}$ [%]	δ_{hadcor} [%]	$\delta_{\text{Noi cor}}$ [%]	$\delta_{\text{Bkg cor}}$ [%]	$\delta_{\text{WrCh cor}}$ [%]
90	0.0015	0.5950	1.40180	1.11	1.92	2.22	1.04	0.63	0.10	1.62	0.45	0.64	0.04	0.15	1.41	0.00
90	0.0012	0.7500	1.46230	0.71	2.48	2.58	2.35	0.25	0.24	0.79	0.37	0.53	0.05	0.18	0.00	0.43
120	0.0028	0.4250	1.23910	1.42	1.31	1.93	1.01	0.50	0.04	0.84	0.49	0.64	0.01	0.18	0.12	0.00
120	0.0025	0.4750	1.28640	1.18	1.40	1.83	1.02	0.63	0.06	0.95	0.64	0.66	0.02	0.15	0.20	0.00
120	0.0022	0.5300	1.32790	1.02	1.43	1.76	0.95	0.55	0.08	1.07	0.56	0.68	0.04	0.18	0.58	0.00
120	0.0020	0.5950	1.35780	1.02	1.72	2.00	0.89	0.40	0.11	1.47	0.40	0.58	0.03	0.19	1.28	0.00
120	0.0016	0.7500	1.39360	0.79	2.22	2.36	2.10	0.21	0.24	0.73	0.36	0.46	0.06	0.18	0.00	0.39
150	0.0060	0.2450	1.02810	0.80	1.96	2.11	1.37	1.18	0.00	1.40	1.18	0.75	0.00	0.00	0.00	0.00
150	0.0045	0.3250	1.12570	1.04	1.67	1.97	1.19	0.94	0.00	1.17	0.93	0.70	0.00	0.00	0.03	0.00
150	0.0039	0.3750	1.17380	1.02	1.38	1.72	0.96	0.62	0.02	0.98	0.67	0.70	0.01	0.18	0.03	0.00
150	0.0035	0.4250	1.22460	1.10	1.43	1.80	1.06	0.75	0.03	0.96	0.73	0.58	0.01	0.17	0.14	0.00
150	0.0031	0.4750	1.23100	1.19	1.32	1.77	0.93	0.51	0.05	0.93	0.63	0.61	0.02	0.16	0.26	0.00
150	0.0028	0.5300	1.28250	1.17	1.11	1.61	0.84	0.31	0.07	0.72	0.36	0.47	0.03	0.17	0.38	0.00
150	0.0025	0.5950	1.25750	1.21	1.46	1.90	0.83	0.13	0.11	1.21	0.30	0.44	0.05	0.19	1.07	0.00
150	0.0020	0.7500	1.37470	0.89	2.03	2.22	1.93	0.38	0.22	0.62	0.30	0.39	0.05	0.18	0.00	0.32
200	0.0197	0.1000	0.66421	0.95	4.17	4.28	2.92	2.82	0.00	2.99	2.82	0.97	0.00	0.00	0.00	0.00
200	0.0127	0.1550	0.81022	0.80	3.25	3.35	2.28	2.18	0.00	2.31	2.19	0.76	0.00	0.00	0.00	0.00
200	0.0080	0.2450	0.94989	0.73	1.86	2.00	1.26	1.07	0.00	1.36	1.11	0.79	0.00	0.00	0.00	0.00
200	0.0061	0.3250	1.05120	1.22	1.54	1.96	1.03	0.70	0.00	1.14	0.91	0.69	0.00	0.00	0.03	0.00
200	0.0053	0.3750	1.07040	1.35	1.31	1.88	0.94	0.53	0.02	0.91	0.58	0.67	0.01	0.17	0.03	0.00
200	0.0046	0.4250	1.12320	1.44	1.31	1.94	0.88	0.36	0.05	0.97	0.78	0.54	0.02	0.16	0.08	0.00
200	0.0041	0.4750	1.13830	1.55	1.13	1.91	0.85	0.13	0.07	0.74	0.26	0.64	0.03	0.16	0.20	0.00
200	0.0037	0.5300	1.19110	1.50	1.14	1.89	0.85	0.17	0.06	0.76	0.32	0.53	0.03	0.17	0.41	0.00
200	0.0033	0.5950	1.23660	1.55	1.36	2.06	0.90	0.22	0.10	1.01	0.36	0.46	0.04	0.18	0.81	0.00
200	0.0026	0.7500	1.28650	1.16	2.11	2.41	2.02	0.52	0.21	0.59	0.15	0.47	0.05	0.18	0.00	0.27
250	0.0246	0.1000	0.63555	0.96	3.90	4.02	2.63	2.53	0.00	2.88	2.75	0.87	0.00	0.00	0.00	0.00
250	0.0159	0.1550	0.76530	0.90	2.81	2.95	1.85	1.71	0.00	2.11	1.96	0.78	0.00	0.00	0.00	0.00
250	0.0100	0.2450	0.87430	0.85	1.60	1.81	1.05	0.80	0.00	1.20	1.02	0.62	0.00	0.00	0.01	0.00
250	0.0076	0.3250	0.95468	1.43	1.44	2.03	1.03	0.68	0.00	1.01	0.85	0.54	0.00	0.00	0.02	0.00
250	0.0066	0.3750	1.03430	1.49	1.21	1.92	0.87	0.35	0.01	0.84	0.67	0.49	0.01	0.14	0.02	0.00
250	0.0058	0.4250	1.10270	1.60	1.26	2.03	0.92	0.42	0.06	0.85	0.65	0.50	0.02	0.18	0.13	0.00
250	0.0052	0.4750	1.10610	1.75	1.10	2.07	0.92	0.33	0.05	0.60	0.32	0.47	0.03	0.14	0.14	0.00
250	0.0046	0.5300	1.14720	1.74	1.15	2.09	0.88	0.16	0.06	0.74	0.45	0.46	0.02	0.12	0.34	0.00
250	0.0041	0.5950	1.15610	1.83	1.30	2.24	0.94	0.26	0.09	0.90	0.27	0.42	0.04	0.16	0.73	0.00
250	0.0033	0.7500	1.26460	1.30	2.12	2.49	2.05	0.29	0.27	0.54	0.23	0.34	0.08	0.20	0.00	0.27
300	0.0492	0.0600	0.50825	1.29	2.88	3.16	1.65	1.40	0.00	2.37	2.23	0.79	0.00	0.00	0.00	0.00
300	0.0295	0.1000	0.60500	1.14	3.42	3.61	1.96	1.81	0.00	2.81	2.73	0.67	0.00	0.00	0.00	0.00
300	0.0191	0.1550	0.72317	1.03	2.15	2.39	1.24	1.01	0.00	1.76	1.66	0.59	0.00	0.00	0.00	0.00
300	0.0121	0.2450	0.82208	0.98	1.69	1.95	1.00	0.73	0.00	1.36	1.23	0.58	0.00	0.00	0.01	0.00
300	0.0091	0.3250	0.90943	1.65	1.27	2.08	0.90	0.42	0.00	0.89	0.63	0.63	0.00	0.00	0.01	0.00
300	0.0079	0.3750	0.98116	1.74	1.17	2.10	0.86	0.28	0.00	0.79	0.58	0.54	0.00	0.10	0.02	0.00
300	0.0069	0.4250	1.03040	1.92	1.42	2.39	1.01	0.54	0.04	0.99	0.82	0.53	0.01	0.17	0.10	0.00
300	0.0062	0.4750	1.05550	2.07	1.10	2.35	0.90	0.07	0.04	0.64	0.37	0.50	0.01	0.13	0.10	0.00
300	0.0056	0.5300	1.10660	2.12	1.22	2.44	0.95	0.30	0.08	0.77	0.44	0.51	0.04	0.15	0.34	0.00
300	0.0050	0.5950	1.12990	2.14	1.28	2.50	0.96	0.10	0.09	0.85	0.24	0.39	0.03	0.16	0.70	0.00
300	0.0039	0.7500	1.21120	1.42	2.11	2.54	2.04	0.03	0.26	0.53	0.28	0.31	0.07	0.21	0.00	0.23
400	0.0656	0.0600	0.45828	1.49	3.65	3.94	2.00	1.79	0.00	3.06	3.00	0.57	0.00	0.00	0.00	0.00
400	0.0394	0.1000	0.56203	1.28	3.56	3.79	1.90	1.74	0.00	3.01	2.91	0.79	0.00	0.00	0.00	0.00
400	0.0254	0.1550	0.65363	1.21	2.20	2.51	1.25	1.02	0.00	1.81	1.68	0.68	0.00	0.00	0.00	0.00
400	0.0161	0.2450	0.76660	1.15	1.43	1.84	0.91	0.59	0.00	1.11	1.00	0.47	0.00	0.00	0.00	0.00
400	0.0121	0.3250	0.88264	1.91	1.50	2.43	1.07	0.67	0.00	1.06	0.91	0.54	0.00	0.00	0.01	0.00
400	0.0105	0.3750	0.91073	2.08	1.06	2.34	0.88	0.19	0.01	0.59	0.34	0.47	0.01	0.13	0.02	0.00
400	0.0093	0.4250	0.92869	2.33	1.28	2.66	1.04	0.51	0.04	0.75	0.59	0.42	0.02	0.17	0.08	0.00
400	0.0083	0.4750	0.99503	2.50	1.59	2.96	1.14	0.62	0.06	1.11	1.08	0.20	0.02	0.12	0.14	0.00
400	0.0074	0.5300	1.06160	2.46	1.21	2.74	1.00	0.29	0.06	0.68	0.39	0.48	0.02	0.13	0.26	0.00
400	0.0066	0.5950	1.03540	2.55	1.31	2.86	1.02	0.21	0.09	0.82	0.19	0.59	0.03	0.14	0.52	0.00
400	0.0053	0.7500	1.15730	1.55	2.04	2.56	1.99	0.26	0.23	0.43	0.05	0.32	0.07	0.20	0.00	0.20

Q^2 [GeV ²]	x	y	$\bar{\sigma}_{\text{NC}}$	δ_{stat} [%]	δ_{syst} [%]	δ_{tot} [%]	δ_{unc} [%]	$\delta_{\text{unc}}^{\text{E}}$ [%]	$\delta_{\text{unc}}^{\text{had}}$ [%]	δ_{cor} [%]	$\delta_{\text{cor}}^{\text{E}}$ [%]	$\delta_{\text{cor}}^{\ominus}$ [%]	$\delta_{\text{cor}}^{\text{had}}$ [%]	$\delta_{\text{cor}}^{\text{Noi}}$ [%]	$\delta_{\text{cor}}^{\text{Bkg}}$ [%]	$\delta_{\text{cor}}^{\text{WrCh}}$ [%]
500	0.0820	0.0600	0.44305	1.75	3.23	3.67	1.86	1.58	0.00	2.64	2.53	0.75	0.00	0.00	0.00	0.00
500	0.0492	0.1000	0.54313	1.49	3.62	3.91	1.91	1.74	0.00	3.07	2.99	0.71	0.00	0.00	0.00	0.00
500	0.0318	0.1550	0.61644	1.43	2.34	2.74	1.33	1.11	0.00	1.92	1.83	0.57	0.00	0.00	0.00	0.00
500	0.0201	0.2450	0.73627	1.41	1.58	2.12	1.00	0.69	0.00	1.22	1.08	0.58	0.00	0.00	0.00	0.00
500	0.0151	0.3250	0.80579	2.41	1.08	2.64	0.91	0.17	0.00	0.58	0.39	0.43	0.00	0.00	0.01	0.00
500	0.0131	0.3750	0.87942	2.51	1.41	2.88	1.04	0.47	0.01	0.95	0.78	0.54	0.00	0.09	0.02	0.00
500	0.0116	0.4250	0.86923	2.82	1.26	3.09	1.01	0.21	0.03	0.76	0.38	0.63	0.01	0.16	0.06	0.00
500	0.0104	0.4750	0.93014	2.96	1.39	3.27	1.10	0.42	0.07	0.85	0.63	0.55	0.02	0.18	0.07	0.00
500	0.0093	0.5300	0.93947	2.88	1.15	3.10	1.02	0.24	0.05	0.53	0.36	0.34	0.02	0.10	0.15	0.00
500	0.0083	0.5950	0.96399	2.94	1.28	3.21	1.10	0.41	0.09	0.67	0.36	0.17	0.05	0.17	0.51	0.00
500	0.0066	0.7500	1.04330	1.81	1.96	2.67	1.90	0.12	0.20	0.49	0.35	0.24	0.06	0.18	0.00	0.14
650	0.1067	0.0600	0.39212	2.21	2.17	3.10	1.45	0.92	0.00	1.62	1.39	0.82	0.00	0.00	0.00	0.00
650	0.0640	0.1000	0.47270	1.86	3.25	3.75	1.79	1.56	0.00	2.72	2.58	0.85	0.00	0.00	0.00	0.00
650	0.0413	0.1550	0.56539	1.75	2.47	3.03	1.41	1.16	0.00	2.03	1.94	0.62	0.00	0.00	0.00	0.00
650	0.0261	0.2450	0.68951	1.68	1.41	2.19	0.95	0.55	0.00	1.04	0.86	0.59	0.00	0.00	0.00	0.00
650	0.0197	0.3250	0.72631	2.86	1.40	3.19	1.07	0.40	0.00	0.91	0.79	0.44	0.00	0.00	0.01	0.00
650	0.0171	0.3750	0.74093	3.09	1.46	3.41	1.22	0.67	0.01	0.79	0.62	0.49	0.00	0.08	0.05	0.00
650	0.0151	0.4250	0.85234	3.13	1.13	3.32	1.07	0.17	0.05	0.37	0.28	0.15	0.03	0.20	0.02	0.00
650	0.0135	0.4750	0.80878	3.42	1.31	3.67	1.16	0.39	0.04	0.63	0.35	0.51	0.01	0.10	0.06	0.00
650	0.0121	0.5300	0.89768	3.20	1.22	3.43	1.08	0.15	0.05	0.57	0.17	0.52	0.02	0.10	0.13	0.00
650	0.0108	0.5950	0.88847	3.24	1.28	3.49	1.16	0.41	0.06	0.55	0.42	0.21	0.03	0.10	0.27	0.00
650	0.0085	0.7500	0.98317	2.12	1.96	2.88	1.89	0.24	0.20	0.49	0.23	0.36	0.07	0.20	0.00	0.11
800	0.1313	0.0600	0.36055	2.74	1.43	3.09	1.32	0.10	0.00	0.57	0.12	0.55	0.00	0.00	0.00	0.00
800	0.0788	0.1000	0.48011	2.25	2.78	3.57	1.69	1.33	0.00	2.20	2.00	0.93	0.00	0.00	0.00	0.00
800	0.0508	0.1550	0.53309	2.11	2.00	2.91	1.36	1.03	0.00	1.46	1.38	0.50	0.00	0.00	0.00	0.00
800	0.0321	0.2450	0.61055	1.98	1.53	2.51	1.12	0.74	0.00	1.04	0.93	0.47	0.00	0.00	0.00	0.00
800	0.0242	0.3250	0.66275	3.42	1.29	3.66	1.16	0.38	0.00	0.57	0.49	0.30	0.00	0.00	0.01	0.00
800	0.0210	0.3750	0.71702	3.41	1.97	3.94	1.52	1.05	0.00	1.24	1.13	0.50	0.00	0.05	0.03	0.00
800	0.0185	0.4250	0.70535	3.72	1.39	3.97	1.25	0.51	0.02	0.60	0.52	0.27	0.00	0.13	0.05	0.00
800	0.0166	0.4750	0.71740	4.03	1.42	4.28	1.29	0.47	0.05	0.58	0.46	0.30	0.03	0.16	0.11	0.00
800	0.0149	0.5300	0.76255	3.88	1.33	4.11	1.23	0.32	0.06	0.52	0.33	0.35	0.04	0.12	0.15	0.00
800	0.0132	0.5950	0.83029	3.80	1.45	4.07	1.31	0.28	0.11	0.61	0.28	0.43	0.04	0.15	0.28	0.00
800	0.0105	0.7500	0.90372	2.46	1.95	3.14	1.91	0.26	0.23	0.39	0.07	0.25	0.09	0.24	0.00	0.12
1000	0.1641	0.0600	0.31802	3.69	1.99	4.19	1.74	0.98	0.00	0.97	0.92	0.29	0.00	0.00	0.01	0.00
1000	0.0985	0.1000	0.39276	2.91	1.96	3.51	1.56	1.06	0.00	1.18	1.09	0.47	0.00	0.00	0.00	0.00
1000	0.0635	0.1550	0.47136	2.48	2.35	3.41	1.71	1.46	0.00	1.61	1.53	0.51	0.00	0.00	0.00	0.00
1000	0.0402	0.2450	0.57754	2.24	1.62	2.76	1.24	0.93	0.00	1.04	0.94	0.45	0.00	0.00	0.00	0.00
1000	0.0303	0.3250	0.61093	3.78	1.87	4.22	1.50	1.08	0.00	1.12	1.03	0.43	0.00	0.00	0.00	0.00
1000	0.0263	0.3750	0.64339	4.03	1.18	4.20	1.10	0.18	0.01	0.42	0.17	0.38	0.00	0.06	0.02	0.00
1000	0.0232	0.4250	0.72357	4.22	1.30	4.41	1.16	0.21	0.07	0.58	0.24	0.49	0.03	0.19	0.02	0.00
1000	0.0207	0.4750	0.67679	4.70	1.24	4.86	1.20	0.13	0.02	0.31	0.12	0.26	0.01	0.10	0.06	0.00
1000	0.0186	0.5300	0.73661	4.49	1.34	4.68	1.23	0.38	0.06	0.52	0.38	0.31	0.04	0.12	0.11	0.00
1000	0.0165	0.5950	0.79195	4.43	1.45	4.66	1.30	0.45	0.07	0.64	0.45	0.36	0.03	0.12	0.26	0.00
1000	0.0131	0.7500	0.78891	2.72	2.14	3.46	1.54	0.19	0.23	1.50	0.09	0.31	0.08	0.21	1.44	0.00

Table C.8: The NC e^-p double differential reduced cross section $\bar{\sigma}_{\text{NC}}$ for measured on the $Q^2 - y$ bin grid unpolarized leptons with the statistical δ_{stat} , systematic δ_{syst} and total δ_{tot} errors. The quantities shown are total uncorrelated systematic δ_{unc} with the contributions from the electron energy scale uncertainty $\delta_{\text{unc}}^{\text{E}}$ and hadronic energy scale uncertainty $\delta_{\text{unc}}^{\text{had}}$. The effect of other uncorrelated systematic uncertainties is included into δ_{unc} . The correlated systematic error δ_{cor} is shown with the contributions from electron energy scale $\delta_{\text{cor}}^{\text{E}}$, polar angle measurement $\delta_{\text{cor}}^{\ominus}$, hadronic energy scale $\delta_{\text{cor}}^{\text{had}}$, noise subtraction $\delta_{\text{cor}}^{\text{Noi}}$, simulated background $\delta_{\text{cor}}^{\text{Bkg}}$, wrong charge data subtraction $\delta_{\text{cor}}^{\text{WrCh}}$. The normalization and polarization errors are not included into the errors.

Q^2 [GeV ²]	σ_{NC} [pb/GeV ²]	δ_{stat} [%]	δ_{syst} [%]	δ_{tot} [%]	δ_{unc} [%]	$\delta_{\text{unc}}^{\text{E}}$ [%]	$\delta_{\text{unc}}^{\text{had}}$ [%]	δ_{cor} [%]	$\delta_{\text{cor}}^{\text{E}}$ [%]	$\delta_{\text{cor}}^{\Theta}$ [%]	$\delta_{\text{cor}}^{\text{had}}$ [%]	$\delta_{\text{cor}}^{\text{Noi}}$ [%]	$\delta_{\text{cor}}^{\text{Bkg}}$ [%]	$\delta_{\text{cor}}^{\text{WrCh}}$ [%]
200	18.4160	0.42	1.07000	1.15	0.80	-0.29	0.03	0.71	0.41	0.58	0.01	0.05	0.07	0.02
250	10.8300	0.44	1.44000	1.50	1.14	0.83	0.03	0.87	0.68	0.55	0.01	0.04	0.05	0.02
300	7.0380	0.52	1.48000	1.56	1.14	0.81	0.02	0.93	0.77	0.53	0.01	0.04	0.04	0.02
400	3.5022	0.61	1.31000	1.44	0.96	0.50	0.03	0.89	0.79	0.41	0.01	0.04	0.03	0.02
500	2.0698	0.72	1.35000	1.53	0.98	0.50	0.03	0.93	0.84	0.40	0.01	0.04	0.03	0.01
650	1.0936	0.87	1.42000	1.67	1.03	0.55	0.03	0.98	0.90	0.39	0.01	0.05	0.03	0.01
800	0.6463	1.04	1.39000	1.74	1.02	0.47	0.03	0.95	0.88	0.34	0.02	0.06	0.03	0.01
1000	0.3609	1.26	1.29000	1.81	1.02	0.50	0.04	0.80	0.71	0.28	0.01	0.06	0.22	0.00
1200	0.2252	1.49	1.49000	2.11	1.21	0.79	0.03	0.88	0.82	0.26	0.01	0.05	0.17	0.00
1500	0.1253	1.75	1.54000	2.33	1.28	0.81	0.04	0.86	0.81	0.22	0.02	0.06	0.14	0.00
2000	0.0604	2.15	1.73000	2.76	1.43	0.93	0.04	0.98	0.94	0.23	0.02	0.04	0.16	0.00
3000	0.0209	2.06	1.82000	2.75	1.54	0.96	0.04	0.97	0.94	0.13	0.02	0.04	0.17	0.00
5000	0.0051	2.68	1.93000	3.30	1.76	0.84	0.04	0.81	0.77	0.15	0.02	0.04	0.20	0.00
8000	0.0012	4.74	2.61000	5.42	2.37	1.07	0.03	1.09	1.05	0.04	0.01	0.04	0.28	0.00
12000	0.0003	8.23	3.09000	8.79	2.87	1.70	0.04	1.14	1.09	0.13	0.02	0.05	0.31	0.00
20000	0.0000	16.41	4.88000	17.12	4.53	3.72	0.06	1.81	1.78	0.19	0.05	0.07	0.26	0.00
30000	0.0000	41.59	6.44000	42.09	5.99	4.74	0.06	2.37	2.37	0.05	0.04	0.04	0.12	0.00

Table C.9: The NC e^-p single differential cross section $d\sigma_{\text{NC}}/dQ^2$ for positively polarized ($P_e = +32.5\%$) leptons with the statistical δ_{stat} , systematic δ_{syst} and total δ_{tot} errors. The quantities shown are total uncorrelated systematic δ_{unc} with the contributions from the electron energy scale uncertainty $\delta_{\text{unc}}^{\text{E}}$ and hadronic energy scale uncertainty $\delta_{\text{unc}}^{\text{had}}$. The effect of other uncorrelated systematic uncertainties is included into δ_{unc} . The correlated systematic error δ_{cor} is shown with the contributions from electron energy scale $\delta_{\text{cor}}^{\text{E}}$, polar angle measurement $\delta_{\text{cor}}^{\Theta}$, hadronic energy scale $\delta_{\text{cor}}^{\text{had}}$, noise subtraction $\delta_{\text{cor}}^{\text{Noi}}$, simulated background $\delta_{\text{cor}}^{\text{Bkg}}$, wrong charge data subtraction $\delta_{\text{cor}}^{\text{WrCh}}$. The normalization and polarization errors are not included into the errors.

Q^2 [GeV ²]	σ_{NC} [pb/GeV ²]	δ_{stat} [%]	δ_{syst} [%]	δ_{tot} [%]	δ_{unc} [%]	$\delta_{\text{unc}}^{\text{E}}$ [%]	$\delta_{\text{unc}}^{\text{had}}$ [%]	δ_{cor} [%]	$\delta_{\text{cor}}^{\text{E}}$ [%]	$\delta_{\text{cor}}^{\ominus}$ [%]	$\delta_{\text{cor}}^{\text{had}}$ [%]	$\delta_{\text{cor}}^{\text{Noi}}$ [%]	$\delta_{\text{cor}}^{\text{Bkg}}$ [%]	$\delta_{\text{cor}}^{\text{WrCh}}$ [%]
200	17.9850	0.47	1.09000	1.18	0.81	-0.28	0.03	0.73	0.39	0.61	0.01	0.05	0.06	0.02
250	10.5010	0.49	1.41000	1.49	1.13	0.81	0.03	0.84	0.66	0.52	0.01	0.04	0.04	0.02
300	6.8305	0.57	1.50000	1.61	1.15	0.82	0.03	0.97	0.80	0.54	0.01	0.04	0.04	0.02
400	3.3857	0.67	1.32000	1.48	0.98	0.52	0.03	0.89	0.78	0.43	0.01	0.04	0.03	0.02
500	1.9760	0.81	1.34000	1.57	0.98	0.49	0.03	0.91	0.82	0.40	0.01	0.04	0.03	0.01
650	1.0188	0.98	1.42000	1.73	1.02	0.52	0.03	0.99	0.90	0.40	0.01	0.04	0.02	0.01
800	0.5969	1.19	1.47000	1.90	1.06	0.54	0.04	1.03	0.96	0.36	0.01	0.05	0.02	0.01
1000	0.3360	1.41	1.29000	1.91	1.03	0.52	0.04	0.79	0.71	0.27	0.02	0.05	0.19	0.00
1200	0.2107	1.66	1.50000	2.23	1.21	0.79	0.04	0.89	0.82	0.28	0.01	0.05	0.18	0.00
1500	0.1180	2.06	1.73000	2.69	1.39	0.99	0.03	1.03	0.99	0.20	0.01	0.05	0.18	0.00
2000	0.0542	2.45	1.65000	2.96	1.39	0.87	0.04	0.90	0.85	0.23	0.01	0.04	0.17	0.00
3000	0.0182	2.34	1.92000	3.02	1.60	1.04	0.03	1.06	1.03	0.17	0.01	0.05	0.18	0.00
5000	0.0040	3.28	1.92000	3.80	1.75	0.79	0.03	0.80	0.74	0.12	0.02	0.04	0.28	0.00
8000	0.0009	5.47	2.81000	6.15	2.48	1.26	0.04	1.32	1.22	0.11	0.02	0.03	0.49	0.00
12000	0.0002	10.31	3.42000	10.86	3.17	1.82	0.04	1.30	1.20	0.03	0.02	0.05	0.48	0.00
20000	0.0000	21.42	4.67000	21.92	4.29	3.43	0.07	1.84	1.83	0.07	0.03	0.05	0.12	0.00
30000	0.0000	110.04	6.55000	110.23	6.19	4.45	-0.04	2.15	2.10	0.42	0.00	0.04	0.15	0.00

Table C.10: The NC e^+p single differential cross section $d\sigma_{\text{NC}}/dQ^2$ for negatively polarized ($P_e = -37.6\%$) leptons with the statistical δ_{stat} , systematic δ_{syst} and total δ_{tot} errors. The quantities shown are total uncorrelated systematic δ_{unc} with the contributions from the electron energy scale uncertainty $\delta_{\text{unc}}^{\text{E}}$ and hadronic energy scale uncertainty $\delta_{\text{unc}}^{\text{had}}$. The effect of other uncorrelated systematic uncertainties is included into δ_{unc} . The correlated systematic error δ_{cor} is shown with the contributions from electron energy scale $\delta_{\text{cor}}^{\text{E}}$, polar angle measurement $\delta_{\text{cor}}^{\ominus}$, hadronic energy scale $\delta_{\text{cor}}^{\text{had}}$, noise subtraction $\delta_{\text{cor}}^{\text{Noi}}$, simulated background $\delta_{\text{cor}}^{\text{Bkg}}$, wrong charge data subtraction $\delta_{\text{cor}}^{\text{WrCh}}$. The normalization and polarization errors are not included into the errors.

Q^2 [GeV ²]	σ_{NC} [pb/GeV ²]	δ_{stat} [%]	δ_{syst} [%]	δ_{tot} [%]	δ_{unc} [%]	$\delta_{\text{unc}}^{\text{E}}$ [%]	$\delta_{\text{unc}}^{\text{had}}$ [%]	δ_{cor} [%]	$\delta_{\text{cor}}^{\text{E}}$ [%]	$\delta_{\text{cor}}^{\Theta}$ [%]	$\delta_{\text{cor}}^{\text{had}}$ [%]	$\delta_{\text{cor}}^{\text{Noi}}$ [%]	$\delta_{\text{cor}}^{\text{Bkg}}$ [%]	$\delta_{\text{cor}}^{\text{WrCh}}$ [%]
200	18.3100	0.62	1.12000	1.28	0.91	-0.23	0.02	0.65	0.33	0.56	0.01	0.05	0.06	0.02
250	10.6240	0.65	1.47000	1.61	1.22	0.82	0.02	0.83	0.64	0.52	0.01	0.04	0.05	0.02
300	6.9841	0.76	1.63000	1.80	1.27	0.87	0.03	1.03	0.85	0.56	0.01	0.04	0.03	0.02
400	3.4424	0.91	1.35000	1.63	1.05	0.47	0.03	0.85	0.74	0.42	0.01	0.04	0.03	0.02
500	1.9857	1.07	1.47000	1.82	1.09	0.53	0.03	0.98	0.89	0.42	0.01	0.04	0.02	0.01
650	1.0599	1.29	1.46000	1.95	1.11	0.51	0.03	0.96	0.89	0.34	0.01	0.04	0.02	0.01
800	0.6262	1.59	1.38000	2.11	1.09	0.41	0.03	0.86	0.80	0.30	0.01	0.05	0.02	0.01
1000	0.3583	1.88	1.46000	2.38	1.16	0.61	0.04	0.88	0.80	0.31	0.01	0.04	0.18	0.00
1200	0.2229	2.17	1.56000	2.68	1.29	0.80	0.03	0.88	0.82	0.23	0.01	0.04	0.20	0.00
1500	0.1240	2.72	1.59000	3.15	1.35	0.81	0.04	0.85	0.81	0.22	0.02	0.05	0.10	0.00
2000	0.0587	3.21	1.71000	3.63	1.45	0.86	0.04	0.90	0.86	0.18	0.02	0.05	0.18	0.00
3000	0.0208	2.98	1.83000	3.50	1.58	0.90	0.04	0.93	0.90	0.17	0.02	0.05	0.18	0.00
5000	0.0053	4.10	1.84000	4.50	1.72	0.65	0.04	0.65	0.62	0.11	0.02	0.05	0.16	0.00
8000	0.0015	5.83	2.56000	6.37	2.34	0.99	0.05	1.05	1.01	0.09	0.02	0.06	0.27	0.00
12000	0.0005	9.30	3.14000	9.81	2.90	1.81	0.05	1.20	1.18	0.03	0.02	0.05	0.21	0.00
20000	0.0001	17.85	4.06000	18.31	3.81	2.90	0.05	1.39	1.39	0.11	0.02	0.05	0.04	0.00
30000	0.0000	34.70	6.88000	35.37	6.15	4.64	0.08	3.08	2.51	0.07	0.03	0.04	1.78	0.00

Table C.11: The NC e^-p single differential cross section $d\sigma_{\text{NC}}/dQ^2$ for positively polarized ($P_e = +36.9\%$) leptons with the statistical δ_{stat} , systematic δ_{syst} and total δ_{tot} errors. The quantities shown are total uncorrelated systematic δ_{unc} with the contributions from the electron energy scale uncertainty $\delta_{\text{unc}}^{\text{E}}$ and hadronic energy scale uncertainty $\delta_{\text{unc}}^{\text{had}}$. The effect of other uncorrelated systematic uncertainties is included into δ_{unc} . The correlated systematic error δ_{cor} is shown with the contributions from electron energy scale $\delta_{\text{cor}}^{\text{E}}$, polar angle measurement $\delta_{\text{cor}}^{\Theta}$, hadronic energy scale $\delta_{\text{cor}}^{\text{had}}$, noise subtraction $\delta_{\text{cor}}^{\text{Noi}}$, simulated background $\delta_{\text{cor}}^{\text{Bkg}}$, wrong charge data subtraction $\delta_{\text{cor}}^{\text{WrCh}}$. The normalization and polarization errors are not included into the errors.

Q^2 [GeV ²]	σ_{NC} [pb/GeV ²]	δ_{stat} [%]	δ_{syst} [%]	δ_{tot} [%]	δ_{unc} [%]	$\delta_{\text{unc}}^{\text{E}}$ [%]	$\delta_{\text{unc}}^{\text{had}}$ [%]	δ_{cor} [%]	$\delta_{\text{cor}}^{\text{E}}$ [%]	$\delta_{\text{cor}}^{\Theta}$ [%]	$\delta_{\text{cor}}^{\text{had}}$ [%]	$\delta_{\text{cor}}^{\text{Noi}}$ [%]	$\delta_{\text{cor}}^{\text{Bkg}}$ [%]	$\delta_{\text{cor}}^{\text{WrCh}}$ [%]
200	18.2340	0.42	1.15000	1.22	0.92	-0.27	0.03	0.68	0.36	0.57	0.01	0.05	0.06	0.02
250	10.7940	0.43	1.48000	1.54	1.21	0.81	0.03	0.84	0.64	0.54	0.01	0.04	0.04	0.02
300	6.9212	0.51	1.58000	1.66	1.24	0.82	0.03	0.99	0.82	0.55	0.01	0.04	0.04	0.02
400	3.4965	0.60	1.36000	1.49	1.06	0.49	0.03	0.86	0.76	0.41	0.01	0.05	0.03	0.02
500	2.0738	0.71	1.41000	1.58	1.08	0.51	0.03	0.91	0.83	0.37	0.01	0.04	0.02	0.01
650	1.0821	0.86	1.45000	1.69	1.10	0.50	0.03	0.95	0.88	0.35	0.01	0.05	0.02	0.01
800	0.6416	1.05	1.39000	1.74	1.09	0.42	0.03	0.86	0.80	0.31	0.01	0.05	0.02	0.01
1000	0.3710	1.21	1.41000	1.86	1.14	0.56	0.04	0.84	0.75	0.31	0.02	0.05	0.20	0.00
1200	0.2330	1.45	1.54000	2.12	1.28	0.78	0.04	0.86	0.81	0.24	0.01	0.05	0.15	0.00
1500	0.1351	1.72	1.62000	2.36	1.36	0.83	0.04	0.88	0.83	0.21	0.02	0.05	0.19	0.00
2000	0.0621	2.09	1.74000	2.72	1.46	0.88	0.04	0.95	0.89	0.24	0.02	0.06	0.19	0.00
3000	0.0224	1.96	1.72000	2.60	1.51	0.79	0.03	0.82	0.79	0.16	0.02	0.04	0.14	0.00
5000	0.0060	2.46	1.88000	3.09	1.74	0.70	0.04	0.72	0.69	0.15	0.02	0.04	0.15	0.00
8000	0.0016	3.81	2.54000	4.58	2.33	1.00	0.03	1.00	0.97	0.06	0.01	0.03	0.24	0.00
12000	0.0006	5.73	2.90000	6.42	2.69	1.39	0.05	1.06	1.03	0.01	0.03	0.06	0.26	0.00
20000	0.0001	9.71	4.25000	10.60	3.91	2.96	0.06	1.67	1.53	0.11	0.03	0.04	0.67	0.00
30000	0.0000	25.25	7.17000	26.25	6.54	5.15	0.12	2.94	2.67	0.31	0.04	0.09	1.20	0.00
50000	0.0000	57.78	10.00000	58.64	9.51	6.57	-0.00	3.07	3.02	0.51	0.00	0.00	0.00	0.00

Table C.12: The NC e^-p single differential cross section $d\sigma_{\text{NC}}/dQ^2$ for negatively polarized ($P_e = -26.0\%$) leptons with the statistical δ_{stat} , systematic δ_{syst} and total δ_{tot} errors. The quantities shown are total uncorrelated systematic δ_{unc} with the contributions from the electron energy scale uncertainty $\delta_{\text{unc}}^{\text{E}}$ and hadronic energy scale uncertainty $\delta_{\text{unc}}^{\text{had}}$. The effect of other uncorrelated systematic uncertainties is included into δ_{unc} . The correlated systematic error δ_{cor} is shown with the contributions from electron energy scale $\delta_{\text{cor}}^{\text{E}}$, polar angle measurement $\delta_{\text{cor}}^{\Theta}$, hadronic energy scale $\delta_{\text{cor}}^{\text{had}}$, noise subtraction $\delta_{\text{cor}}^{\text{Noi}}$, simulated background $\delta_{\text{cor}}^{\text{Bkg}}$, wrong charge data subtraction $\delta_{\text{cor}}^{\text{WrCh}}$. The normalization and polarization errors are not included into the errors.

Q^2 [GeV ²]	σ_{NC} [pb/GeV ²]	δ_{stat} [%]	δ_{syst} [%]	δ_{tot} [%]	δ_{unc} [%]	$\delta_{\text{unc}}^{\text{E}}$ [%]	$\delta_{\text{unc}}^{\text{had}}$ [%]	δ_{cor} [%]	$\delta_{\text{cor}}^{\text{E}}$ [%]	$\delta_{\text{cor}}^{\theta}$ [%]	$\delta_{\text{cor}}^{\text{had}}$ [%]	$\delta_{\text{cor}}^{\text{Noi}}$ [%]	$\delta_{\text{cor}}^{\text{Bkg}}$ [%]	$\delta_{\text{cor}}^{\text{WrCh}}$ [%]
200	18.2190	0.31	1.07000	1.12	0.80	-0.29	0.03	0.72	0.40	0.59	0.01	0.05	0.07	0.02
250	10.6800	0.33	1.42000	1.45	1.13	0.82	0.03	0.86	0.67	0.54	0.01	0.04	0.05	0.02
300	6.9429	0.38	1.48000	1.53	1.14	0.82	0.03	0.95	0.78	0.53	0.01	0.04	0.04	0.02
400	3.4487	0.45	1.31000	1.38	0.96	0.51	0.03	0.89	0.78	0.42	0.01	0.04	0.03	0.02
500	2.0268	0.54	1.34000	1.44	0.97	0.50	0.03	0.93	0.83	0.40	0.01	0.04	0.03	0.01
650	1.0593	0.65	1.41000	1.55	1.01	0.54	0.03	0.98	0.90	0.39	0.01	0.04	0.02	0.01
800	0.6237	0.79	1.41000	1.62	1.01	0.50	0.04	0.98	0.92	0.35	0.01	0.05	0.03	0.01
1000	0.3494	0.94	1.27000	1.58	1.00	0.51	0.04	0.79	0.71	0.27	0.01	0.05	0.21	0.00
1200	0.2185	1.11	1.48000	1.85	1.19	0.79	0.03	0.88	0.82	0.27	0.01	0.05	0.18	0.00
1500	0.1219	1.34	1.61000	2.09	1.31	0.89	0.04	0.93	0.89	0.21	0.02	0.05	0.16	0.00
2000	0.0575	1.62	1.68000	2.33	1.38	0.90	0.04	0.95	0.90	0.23	0.02	0.04	0.17	0.00
3000	0.0196	1.55	1.84000	2.41	1.54	0.99	0.04	1.01	0.98	0.15	0.02	0.05	0.17	0.00
5000	0.0046	2.07	1.90000	2.81	1.72	0.82	0.03	0.80	0.76	0.14	0.02	0.04	0.23	0.00
8000	0.0011	3.59	2.63000	4.45	2.35	1.15	0.03	1.18	1.12	0.07	0.02	0.03	0.36	0.00
12000	0.0003	6.43	3.13000	7.16	2.89	1.75	0.04	1.20	1.14	0.09	0.02	0.05	0.38	0.00
20000	0.0000	13.02	4.74000	13.86	4.38	3.61	0.06	1.82	1.80	0.14	0.04	0.06	0.20	0.00
30000	0.0000	38.92	6.11000	39.40	5.67	4.63	0.05	2.28	2.26	0.20	0.02	0.04	0.13	0.00

Table C.13: The NC e^+p unpolarized single differential cross section $d\sigma_{\text{NC}}/dQ^2$ with the statistical δ_{stat} , systematic δ_{syst} and total δ_{tot} errors. The quantities shown are total uncorrelated systematic δ_{unc} with the contributions from the electron energy scale uncertainty $\delta_{\text{unc}}^{\text{E}}$ and hadronic energy scale uncertainty $\delta_{\text{unc}}^{\text{had}}$. The effect of other uncorrelated systematic uncertainties is included into δ_{unc} . The correlated systematic error δ_{cor} is shown with the contributions from electron energy scale $\delta_{\text{cor}}^{\text{E}}$, polar angle measurement $\delta_{\text{cor}}^{\theta}$, hadronic energy scale $\delta_{\text{cor}}^{\text{had}}$, noise subtraction $\delta_{\text{cor}}^{\text{Noi}}$, simulated background $\delta_{\text{cor}}^{\text{Bkg}}$, wrong charge data subtraction $\delta_{\text{cor}}^{\text{WrCh}}$. The normalization and polarization errors are not included into the errors.

Q^2 [GeV ²]	σ_{NC} [pb/GeV ²]	δ_{stat} [%]	δ_{syst} [%]	δ_{tot} [%]	δ_{unc} [%]	$\delta_{\text{unc}}^{\text{E}}$ [%]	$\delta_{\text{unc}}^{\text{had}}$ [%]	δ_{cor} [%]	$\delta_{\text{cor}}^{\text{E}}$ [%]	$\delta_{\text{cor}}^{\Theta}$ [%]	$\delta_{\text{cor}}^{\text{had}}$ [%]	$\delta_{\text{cor}}^{\text{Noi}}$ [%]	$\delta_{\text{cor}}^{\text{Bkg}}$ [%]	$\delta_{\text{cor}}^{\text{WrCh}}$ [%]
200	18.2410	0.35	1.13000	1.18	0.91	-0.26	0.03	0.67	0.35	0.57	0.01	0.05	0.06	0.02
250	10.7280	0.36	1.47000	1.51	1.21	0.82	0.03	0.84	0.64	0.53	0.01	0.04	0.04	0.02
300	6.9307	0.42	1.59000	1.65	1.24	0.84	0.03	1.00	0.83	0.55	0.01	0.04	0.04	0.02
400	3.4733	0.50	1.35000	1.44	1.05	0.49	0.03	0.86	0.75	0.41	0.01	0.04	0.03	0.02
500	2.0419	0.59	1.42000	1.54	1.08	0.52	0.03	0.93	0.85	0.39	0.01	0.04	0.02	0.01
650	1.0721	0.72	1.44000	1.61	1.09	0.50	0.03	0.95	0.88	0.35	0.01	0.05	0.02	0.01
800	0.6346	0.87	1.37000	1.63	1.07	0.41	0.03	0.86	0.80	0.31	0.01	0.05	0.02	0.01
1000	0.3655	1.02	1.41000	1.74	1.13	0.58	0.04	0.85	0.77	0.31	0.02	0.05	0.20	0.00
1200	0.2288	1.21	1.54000	1.95	1.27	0.78	0.04	0.87	0.81	0.24	0.01	0.04	0.16	0.00
1500	0.1309	1.45	1.60000	2.16	1.34	0.83	0.04	0.87	0.83	0.21	0.02	0.05	0.16	0.00
2000	0.0606	1.75	1.71000	2.45	1.43	0.88	0.04	0.93	0.88	0.22	0.02	0.05	0.19	0.00
3000	0.0217	1.64	1.74000	2.39	1.51	0.82	0.03	0.86	0.82	0.16	0.02	0.04	0.15	0.00
5000	0.0057	2.11	1.85000	2.81	1.71	0.69	0.04	0.70	0.67	0.14	0.02	0.04	0.15	0.00
8000	0.0016	3.19	2.51000	4.06	2.30	1.00	0.03	1.01	0.98	0.07	0.01	0.04	0.25	0.00
12000	0.0005	4.88	2.93000	5.69	2.72	1.50	0.05	1.10	1.07	0.00	0.03	0.06	0.24	0.00
20000	0.0001	8.53	4.16000	9.49	3.85	2.94	0.06	1.58	1.49	0.11	0.03	0.04	0.50	0.00
30000	0.0000	20.42	6.80000	21.52	6.12	5.01	0.11	2.96	2.62	0.24	0.04	0.08	1.36	0.00
50000	0.0000	57.80	10.43000	58.73	9.63	7.78	-0.00	4.01	3.97	0.58	0.00	0.00	0.00	0.00

Table C.14: The NC e^-p unpolarized single differential cross section $d\sigma_{\text{NC}}/dQ^2$ with the statistical δ_{stat} , systematic δ_{syst} and total δ_{tot} errors. The quantities shown are total uncorrelated systematic δ_{unc} with the contributions from the electron energy scale uncertainty $\delta_{\text{unc}}^{\text{E}}$ and hadronic energy scale uncertainty $\delta_{\text{unc}}^{\text{had}}$. The effect of other uncorrelated systematic uncertainties is included into δ_{unc} . The correlated systematic error δ_{cor} is shown with the contributions from electron energy scale $\delta_{\text{cor}}^{\text{E}}$, polar angle measurement $\delta_{\text{cor}}^{\Theta}$, hadronic energy scale $\delta_{\text{cor}}^{\text{had}}$, noise subtraction $\delta_{\text{cor}}^{\text{Noi}}$, simulated background $\delta_{\text{cor}}^{\text{Bkg}}$, wrong charge data subtraction $\delta_{\text{cor}}^{\text{WrCh}}$. The normalization and polarization errors are not included into the errors.

x	$x F_3^{\gamma Z}$	δ_{stat}	δ_{tot}
0.020	0.572	0.196	0.224
0.032	0.390	0.077	0.087
0.050	0.279	0.085	0.095
0.080	0.287	0.058	0.065
0.130	0.494	0.053	0.057
0.180	0.381	0.053	0.056
0.250	0.330	0.047	0.049
0.400	0.221	0.041	0.043
0.650	0.026	0.018	0.020

Table C.15: The $x F_3^{\gamma Z}$ structure function transformed to $Q^2 = 1500 \text{ GeV}^2$ with the statistical δ_{stat} and total δ_{tot} errors.

List of Figures

2.1	Deep inelastic scattering kinematics	12
2.2	The QPM picture of the electron-proton scattering.	15
2.3	Observation of scaling: independence of the structure function $\nu W_2 = F_2$ of Q^2 at Bjorken variable $x = 0.25$	16
2.4	Loop corrections to the gluon coupling constant. The α_s^0 denotes a bare coupling constant, and α_s is the measured coupling.	18
2.5	The basic idea of the QCD improved parton model for γ^*p interactions. (a) . The QPM approach. (b) . The QCD improved version.	19
2.6	Diagrams for gluon radiation from a quark line.	20
2.7	Diagrams for quark pair production from gluon in DIS.	21
2.8	Measurement of the reduced cross section $\tilde{\sigma}(x, Q^2)$ as a function of Q^2 at fixed x by H1 and fixed target experiments. The results are compared with the Standard Model expectation determined from H1 PDF 2009 fit.	22
2.9	The Q^2 dependence of the unpolarized $e^\pm p$ NC and CC cross sections $d\sigma/dQ^2$ compared with the SM expectation from the HERAPDF1.0 fit [26].	26
2.10	The dependence of the $e^\pm p$ CC cross section on the lepton beam polarization P_e in comparison with the SM prediction based on the HERAPDF1.0 parametrization [26].	27
2.11	Feynman diagrams for radiation of additional photon in case of (a) NC ISR or Compton process, (b) NC FSR or Compton process and (c) emission from the gauge boson in CC.	28
2.12	The effect of the higher order radiative corrections (HO) to the neutral current cross sections in $e\Sigma'$ variables obtained with the HECTOR 1.0 program [29]. Red delimiters refer to the ranges where HERA-II preliminary measurement has been done.	29
3.1	Schematic view of the HERA collider ring.	32
3.2	The integrated luminosity in the H1 experiment as a function of time for HERA I and HERA II periods.	33
3.3	The average polarization achieved in the years 2003-2004 in positron runs.	34
3.4	The luminosity weighed polarization profiles for (a) e^+p and (b) e^-p data periods.	35
4.1	General view of the H1 experimental setup.	38

4.2	The (top) side and (bottom) frontal views of the Liquid Argon calorimeter.	40
4.3	The side view of the H1 tracking system.	42
4.4	The central tracking detectors.	44
4.5	The H1 trigger system.	45
4.6	The projective Big Towers in LAr calorimeter. Each tower points toward the nominal interaction point.	46
4.7	The thresholds for the LAr_electron_1 and LAr_electron_2 trigger elements as a function of Θ	47
4.8	The Time-of-Flight system. Veto Wall is outside of the visible range to the right side.	48
4.9	The luminosity monitor of the H1 experiment.	49
5.1	The resolution of the reconstructed variable x for different Q^2 bins for different reconstruction methods. x_{rec} (x_{gen}) refers to the reconstructed (generated) values of x . Black (red) symbols refer to the ranges where HERA-I (HERA-II preliminary) measurement has been done.	57
5.2	The resolution of the reconstructed variable Q^2 as a function of x for different Q^2 bins for different reconstruction methods. Q^2_{rec} (Q^2_{gen}) refers to the reconstructed (generated) values of Q^2 . Black (red) symbols refer to the ranges where HERA-I (HERA-II preliminary) measurement has been done.	58
5.3	The statistical correlation between measurements with electron and $e\Sigma'$ methods as a function of x for different Q^2 bins. N_{tot} denotes the number of events registered in a given bin and used for the cross section calculation. N_{corr} denotes the number of events in a given bin which are used in the cross section measurement with both methods. The ratio of $N_{\text{corr}}/N_{\text{tot}}$ is the fraction of events in given bin which are also used for the cross section measurement in some other bins. Black (red) symbols refer to the ranges where HERA-I (HERA-II preliminary) measurement has been done.	59
6.1	Examples of leading order (a) direct and (b) resolved hard photoproduction process diagrams.	63
6.2	Example of the leading order diagram for lepton pair production. . .	63
6.3	Example of leading order W production diagram.	64
6.4	Leading order Compton scattering process diagrams.	64
7.1	The data and background (mostly from the photoproduction) for the NC Nominal analysis selection.	66
7.2	Schematic view of isolation cones used for the electron identification.	67
7.3	Efficiency of the electron finding as a function of E_e , Z_{imp} and ϕ for the whole HERA II statistics. For the $\varepsilon(Z_{\text{imp}})$ efficiency all the events with $Z_{\text{imp}} > 150$ cm are accumulated in the last bin.	69

7.4	The mean of E_e/E^{DA} ratio extracted in Z_{imp} bins (a) before and (b) after the electromagnetic calibration for the Per0607RH period. (c) The double ratio $(E_e/E^{\text{DA}})_{\text{data}}/(E_e/E^{\text{DA}})_{\text{MC}}$ of the data to simulation is shown for entire HERA II data set as a function of the calorimetric stack number.	72
7.5	The mean of E_e/E^{DA} ratio determined in the ϕ bins after the wheel-octant-wise and z -wise calibrations (a) before and (b) after the ϕ -wise calibration.	73
7.6	The resolution of the electron energy measurement as a function of z -position of the impact point (a) before and (b) after the Gaussian smearing of the energy in a simulation.	74
7.7	The $E_t^{\text{clus}}/P_t^{\text{track}}$ ratio for the sample of Compton events for (left) $E_e \in [6, 11]$ GeV and (right) $E_e \in [11, 20]$ GeV.	75
7.8	The $E^{\text{DA}}/E^{\text{gen}}$ ratio as a function of the Z_{bin} for the e^+p data set. . .	76
7.9	Particle trajectory in sz plane.	77
7.10	(a, b) : Difference between the scattered electron polar angle taken from the reconstructed track and from the straight line between the primary vertex and the electron cluster as a function of ϕ_e in different parts of the detector (a) before and (b) after the alignment of the LAr calorimeter. (c, d) : Distribution of the difference of azimuthal angles taken from the reconstructed track and a straight line between the primary vertex and the electron cluster (c) before and (d) after the alignment.	79
7.11	Comparison of the slope parameter $\tan \lambda$ obtained in the track reconstruction with the CJC hits only and in the reconstruction with the CJC and CST hits. The effect of 1 mrad shift of the track's Θ is shown by the blue line. The e^+p data sample is used, obtained in the year 2007 [95].	81
7.12	Difference between the polar angle measurement of the scattered electron from the track reconstruction and from the cluster and vertex positions in bins of Θ_{Trk} . The mean values are determined using Gaussian fits and shown in the plots on left for data and on right for simulation with the statistical uncertainties from the fits. The comparison is presented for the Per0607 period.	82
7.13	Example of the DTNV event. The scattered electron gives an isolated cluster of high energy in the calorimeter and a DTNV track. The HFS interacts with the beam pipe downstream to the proton beam direction providing multiple tracks and a fake primary vertex.	83
7.14	Schematic view of the (a) DTRA and (b) DTNV tracks, vertex and cluster with the essential parameters definition.	84
7.15	Distributions of the vertex z position of the (a) CJC vertices, (b) DTNV vertices and (c) difference between them for events without DTRA track pointing to the electron cluster.	84
7.16	Distributions of the CJC and DTNV vertices for the different regions of the $\Delta Z_{\text{CJC-DTNV}}$ variable.	85

7.17	For the case $\Delta Z_{\text{CJC-DTNV}} < -10$ cm and $Z_{\text{DTNV}} > 20$ cm: event display with a typical event (left plot) and distribution of the CJC vertices for the whole HERA II sample (right plot).	86
7.18	Distributions of the (a) γ_h , (b) $\log_{10}(x_{e\Sigma'})$, (c) $E - P_z$, (d) P_t^{had}/P_t^e , (e) E_e/E^{DA} variables for the DTRA, DTNV, CJC and NoVertex samples for the whole HERA II statistics.	87
7.19	Fractions of the DTRA, DTNV, CJC components and the whole OptimalNC vertex sample in the monitor sample as a function of the γ_h variable.	89
7.20	Efficiency OptimalNC vertex as a function of E_e , Z_{imp} , Q_e^2 and Θ variables.	89
7.21	Efficiency of the DTRA vertex sample as a function of E_e , Z_{imp} , Q_e^2 and Θ variables.	90
7.22	Efficiency of the DTRA vertex as a function of the scattered electron candidate energy E_e measured with the ISR and Compton events. . .	91
7.23	Generated and reconstructed electromagnetic fractions of jet in FB region for the (a) standard algorithm and (b) neural network algorithm [100].	92
7.24	The $P_t^{\text{DA}}/P_t^{\text{gen}}$ ratio as a function of the P_t^{DA} in different regions of γ_h for the PerPos period.	94
7.25	The mean P_t^{bal} values in different P_t^{had} and γ_h bins for data (closed circles) and MC (open circles) for the Per0607 period. Two upper plots (a, b) refer to the uncalibrated case, two bottom plots (c, d) are done after the hadronic calibration was applied.	96
7.26	The $(E - P_z)$ distribution in different y bins for data (circles) and MC (error crosses) (a) before and (b) after the SpaCal calibration. Wrong charge subtraction procedure is applied to eliminate photoproduction background.	98
7.27	The influence of the DTNV calibration on the DTNV sample: the events distribution in P_t^{bal} variable (a) before and (b) after calibration.	99
7.28	The relative difference in P_t^{had} and $(E - P_z)$ variables between the standard (VT) and new (DP) reconstructions for the events migrated from the DTNV (in VT) sample to DTRA (in DP) samples.	99
7.29	Influence of the re-calculation of the HFS for the DTNV sample on the number of the data events passed the NC selection in $x - Q^2$ bins (see explanations in the text). The inner error bars show the statistical uncertainty.	100
7.30	Relative contributions from the calorimeters, tracker and suppressed noise to the y measurement from data (point-like markers) and MC (solid lines) for all e^+p periods.	101
7.31	The effect of the noise addition to the HFS: P_t^{bal} distribution at $x = 0.25$ bins with (a) standard HFS and (b) HFS with a 20% fraction of noise.	101
7.32	The trigger efficiency of the LAr_electron_1 TE for Nominal analysis for the Per0607LH period.	104
7.33	The threshold behavior of the unified effective “electron” TE efficiency in different Z_{imp} regions for the Per0607 period.	105

7.34	Inefficiency of the (a) CIP_T0, (b) (LAr_T0 && !CIP_T0_nextbc) and (c) <i>Veto</i> conditions as a function of scattered electron candidate energy E_e for the Per0607 period.	105
7.35	Inefficiency of the <i>Veto</i> condition determined with the Bethe-Heitler sample as a function of run number.	106
7.36	Inefficiency of the <i>Track</i> condition as a function of number of central tracks N_{cTrk} , Z_{imp} and ϕ_e for the Per0405 period.	107
7.37	Efficiency of the “electron” part of the LAr_electron_1 trigger element in the $Z_{imp} - \phi$ plane with the fiducial volume boundaries (black rectangles) for the Per06em period.	108
7.38	Fraction of wrong charge candidates in data and signal MC as a function of the scattered electron energy for the e^+p and e^-p data sets.	110
7.39	Charge asymmetry of the background measured using the e^+p and e^-p data sets with two methods (see in the text). The lines show the asymmetry values averaged over the bins.	111
7.40	(a) The tagged data are combined with signal and background MCs after normalization of the Django contribution as a function of $E - P_z$. (b) Tagged photoproduction events in the HighY analysis domain. Both plots are for the e^+p period.	113
7.41	The tagged photoproduction events in the Nominal analysis domain for the (a) e^+p and (b) e^-p data sets.	114
7.42	Fractions of events which passed the NC selection in simulation as a functions of E_e , Θ_e , $\log_{10}(Q^2 [\text{GeV}^2])$ and x . The samples are: (deep blue line) Compton events passed the NC selection before the anti-Compton cut, (filled area) Compton events after all the NC cuts including the anti-Compton cut, in particular (light blue) inelastic Compton events from Django generator and (green) elastic and quasi-elastic Compton events from WABGEN generator, (red line) true NC events rejected by the anti-Compton cut.	115
7.43	Fractions of the data (black) and true NC events in MC (hardly visible line in red) were rejected by the non- ep cuts.	116
7.44	The distribution of interaction vertex Z_{vtx} for data (black) and MC (red) (a) before and (b) after the vertex reweighing in simulation.	118
7.45	The ratio of the NC cross sections calculated with the DJANGO14 and HECTOR programs.	119
8.1	The binning scheme in (x, Q^2) plane.	122
8.2	The NC cross section measured using the electron (open circles) and $e\Sigma'$ (filled squares) methods for the e^+p data period.	124
8.3	Ratio of the total uncertainties of the measurement obtained with the electron and $e\Sigma'$ methods. Vertical line marks $y = 0.19$ transition boundary (where it is applicable).	125
8.4	The acceptance, purity and stability for the (a) e^+p and (b) e^-p data periods.	127
8.5	The effect of the higher orders radiative corrections estimated with the HECTOR program. For the setup definitions abbreviated as “Full” and “Std” see in the text.	131

8.6	Distribution for an energy of a scattered electron E_e and a scattering angle Θ_e , $(E - P_z)$, balance of a transversal momentum measured with the HFS and the scattered electron P_t^{had}/P_t^e , an impact position Z_{imp} and distributions for kinematical variables x and Q^2 for the e^+p scattering.	133
8.7	Distribution for an energy of a scattered electron E_e and a scattering angle Θ_e , $(E - P_z)$, balance of a transversal momentum measured with the HFS and the scattered electron P_t^{had}/P_t^e , an impact position Z_{imp} and distributions for kinematical variables x and Q^2 for the e^-p scattering.	134
9.1	The comparison of the total uncertainty δ_{tot} [%] obtained in this analysis (filled squares) and in the measurement using the HERA I data (open circles) for the e^+p NC scattering.	138
9.2	Ratio of the systematic uncertainty obtained in this measurement to the systematic uncertainty of the HERA II preliminary result for the e^-p NC scattering.	139
9.3	The e^+p NC reduced cross section $\tilde{\sigma}_{\text{NC}}(x, Q^2)$ for (full squares) positive and (open points) negative longitudinal polarization of the lepton beam. The inner and outer error bars represent the statistical and total uncertainty respectively. The normalization uncertainty is not included in the error bars. The data are compared to the Standard Model prediction based on HERAPDF1.0.	141
9.4	The e^-p NC reduced cross section $\tilde{\sigma}_{\text{NC}}(x, Q^2)$ for (full squares) positive and (open points) negative longitudinal polarization of the lepton beam. The inner and outer error bars represent the statistical and total uncertainty respectively. The normalization uncertainty is not included in the error bars. The data are compared to the Standard Model prediction based on HERAPDF1.0.	142
9.5	The NC reduced cross section $\tilde{\sigma}_{\text{NC}}(x, Q^2)$ in unpolarized $e^\pm p$ scattering. The inner and outer error bars represent the statistical and total uncertainty respectively. The normalization uncertainty is not included in the error bars. The data are compared to the Standard Model prediction based on HERAPDF1.0.	143
9.6	The unpolarized e^+p NC reduced cross sections $\tilde{\sigma}_{\text{NC}}(x, Q^2)$ measured in this analysis and the HERA I measurement. The inner and outer error bars represent the statistical and total uncertainty respectively. The data are compared to the Standard Model prediction based on HERAPDF1.0.	144
9.7	The Q^2 dependence of the NC cross section $d\sigma/dQ^2$ for unpolarized (solid squares) e^+p and (open circles) e^-p scattering. The data are compared to the Standard Model prediction from the HERAPDF1.0 fits.	146
9.8	The Q^2 dependence of the NC cross section $d\sigma/dQ^2$ for e^+p scattering with the right handed (solid squares) and left handed (open circles) data sets. The data are compared to the Standard Model prediction from the HERAPDF1.0 fits.	147

- 9.9 The Q^2 dependence of the NC cross section $d\sigma/dQ^2$ for e^-p scattering with the right handed (solid squares) and left handed (open circles) data sets. The data are compared to the Standard Model prediction from the HERAPDF1.0 fits. 148
- 9.10 The reduced cross section $\tilde{\sigma}_{NC}$ in unpolarized $e^\pm p$ scattering using the HERA II data set for Q^2 above 1000 GeV². The data are compared to the Standard Model prediction using HERAPDF1.0. The inner error bars represent the statistical uncertainty and the outer error bars represent the total errors. The normalization uncertainty is not included in the error bars. 149
- 9.11 The structure functions **(a)** $x\tilde{F}_3$ and **(b)** $xF_3^{\gamma Z}$ evaluated using HERA II data set (solid points) is shown compared to Standard Model expectation from HERAPDF1.0 (solid curve). The inner error bars represent the statistical uncertainty and the outer error bars represent the total errors which includes the normalization uncertainty. 150
- 9.12 The structure function $xF_3^{\gamma Z}$ extracted from the HERA II data set (solid points) and transformed to $Q^2 = 1500$ GeV² is shown together with the Standard Model expectation using HERAPDF1.0 (solid curve). The inner error bars represent the statistical uncertainty and the outer error bars represent the total errors which includes the normalization uncertainty of the measurement. 151
- 9.13 The Q^2 dependence of the polarization asymmetry A , for e^+p (red circles) and e^-p (blue squares). The data are compared to the Standard Model prediction (full lines). The inner error bars represent the statistical uncertainties and the outer error bars represent the total errors. 152

List of Tables

3.1	Main parameters of the HERA storage rings during the HERA I (1992-1998) and HERA II (2003-2007) operation periods [31].	32
3.2	The run periods for the HERA II used for the analysis.	35
3.3	The naming convention for the data sets used in the analysis.	36
3.4	The luminosity and mean polarizations for the data sets used in the analysis.	36
4.1	The overview of the tracking detectors parameters composing the H1 tracking system.	43
4.2	Detectors of the ToF system.	49
4.3	The correction factors from the Compton luminosity analysis.	50
7.1	The uncorrelated part of the electron energy scale uncertainty.	75
7.2	Trigger requirements for the subtriggers in use. Conditions from different rows supposed to be joint with the AND logical operator.	102
7.3	Background finding algorithms [108] used in the analysis.	116
8.1	The Q^2 and x bin's edges and central values. Indices “ l ” and “ h ” denote the binning scheme below and above $\log_{10}(Q^2 [\text{GeV}^2]) = 2.65$	123
A.1	The trigger efficiencies and uncertainties for the CIP_T0, <i>Veto</i> and L2_LAr_electron conditions.	155
B.1	The QED Compton correction for the luminosity.	157
C.1	The NC e^+p double differential reduced cross section $\tilde{\sigma}_{\text{NC}}$ for positively polarized ($P_e = +32.5\%$) leptons with the statistical δ_{stat} , systematic δ_{syst} and total δ_{tot} errors. The quantities shown are total uncorrelated systematic δ_{unc} with the contributions from the electron energy scale uncertainty $\delta_{\text{unc}}^{\text{E}}$ and hadronic energy scale uncertainty $\delta_{\text{unc}}^{\text{had}}$. The effect of other uncorrelated systematic uncertainties is included into δ_{unc} . The correlated systematic error δ_{cor} is shown with the contributions from electron energy scale $\delta_{\text{cor}}^{\text{E}}$, polar angle measurement $\delta_{\text{cor}}^{\Theta}$, hadronic energy scale $\delta_{\text{cor}}^{\text{had}}$, noise subtraction $\delta_{\text{cor}}^{\text{Noi}}$, simulated background $\delta_{\text{cor}}^{\text{Bkg}}$, wrong charge data subtraction $\delta_{\text{cor}}^{\text{WrCh}}$. The normalization and polarization errors are not included into the errors.	162

- C.2 The NC e^+p double differential reduced cross section $\tilde{\sigma}_{\text{NC}}$ for negatively polarized ($P_e = -37.6\%$) leptons with the statistical δ_{stat} , systematic δ_{syst} and total δ_{tot} errors. The quantities shown are total uncorrelated systematic δ_{unc} with the contributions from the electron energy scale uncertainty $\delta_{\text{unc}}^{\text{E}}$ and hadronic energy scale uncertainty $\delta_{\text{unc}}^{\text{had}}$. The effect of other uncorrelated systematic uncertainties is included into δ_{unc} . The correlated systematic error δ_{cor} is shown with the contributions from electron energy scale $\delta_{\text{cor}}^{\text{E}}$, polar angle measurement $\delta_{\text{cor}}^{\Theta}$, hadronic energy scale $\delta_{\text{cor}}^{\text{had}}$, noise subtraction $\delta_{\text{cor}}^{\text{Noi}}$, simulated background $\delta_{\text{cor}}^{\text{Bkg}}$, wrong charge data subtraction $\delta_{\text{cor}}^{\text{WrCh}}$. The normalization and polarization errors are not included into the errors. 165
- C.3 The NC e^-p double differential reduced cross section $\tilde{\sigma}_{\text{NC}}$ for positively polarized ($P_e = +36.9\%$) leptons with the statistical δ_{stat} , systematic δ_{syst} and total δ_{tot} errors. The quantities shown are total uncorrelated systematic δ_{unc} with the contributions from the electron energy scale uncertainty $\delta_{\text{unc}}^{\text{E}}$ and hadronic energy scale uncertainty $\delta_{\text{unc}}^{\text{had}}$. The effect of other uncorrelated systematic uncertainties is included into δ_{unc} . The correlated systematic error δ_{cor} is shown with the contributions from electron energy scale $\delta_{\text{cor}}^{\text{E}}$, polar angle measurement $\delta_{\text{cor}}^{\Theta}$, hadronic energy scale $\delta_{\text{cor}}^{\text{had}}$, noise subtraction $\delta_{\text{cor}}^{\text{Noi}}$, simulated background $\delta_{\text{cor}}^{\text{Bkg}}$, wrong charge data subtraction $\delta_{\text{cor}}^{\text{WrCh}}$. The normalization and polarization errors are not included into the errors. 168
- C.4 The NC e^-p double differential reduced cross section $\tilde{\sigma}_{\text{NC}}$ for negatively polarized ($P_e = -26.0\%$) leptons with the statistical δ_{stat} , systematic δ_{syst} and total δ_{tot} errors. The quantities shown are total uncorrelated systematic δ_{unc} with the contributions from the electron energy scale uncertainty $\delta_{\text{unc}}^{\text{E}}$ and hadronic energy scale uncertainty $\delta_{\text{unc}}^{\text{had}}$. The effect of other uncorrelated systematic uncertainties is included into δ_{unc} . The correlated systematic error δ_{cor} is shown with the contributions from electron energy scale $\delta_{\text{cor}}^{\text{E}}$, polar angle measurement $\delta_{\text{cor}}^{\Theta}$, hadronic energy scale $\delta_{\text{cor}}^{\text{had}}$, noise subtraction $\delta_{\text{cor}}^{\text{Noi}}$, simulated background $\delta_{\text{cor}}^{\text{Bkg}}$, wrong charge data subtraction $\delta_{\text{cor}}^{\text{WrCh}}$. The normalization and polarization errors are not included into the errors. 171
- C.5 The NC e^+p unpolarized double differential reduced cross section $\tilde{\sigma}_{\text{NC}}$ with the statistical δ_{stat} , systematic δ_{syst} and total δ_{tot} errors. The quantities shown are total uncorrelated systematic δ_{unc} with the contributions from the electron energy scale uncertainty $\delta_{\text{unc}}^{\text{E}}$ and hadronic energy scale uncertainty $\delta_{\text{unc}}^{\text{had}}$. The effect of other uncorrelated systematic uncertainties is included into δ_{unc} . The correlated systematic error δ_{cor} is shown with the contributions from electron energy scale $\delta_{\text{cor}}^{\text{E}}$, polar angle measurement $\delta_{\text{cor}}^{\Theta}$, hadronic energy scale $\delta_{\text{cor}}^{\text{had}}$, noise subtraction $\delta_{\text{cor}}^{\text{Noi}}$, simulated background $\delta_{\text{cor}}^{\text{Bkg}}$, wrong charge data subtraction $\delta_{\text{cor}}^{\text{WrCh}}$. The normalization and polarization errors are not included into the errors. 174

- C.6 The NC e^-p unpolarized double differential reduced cross section $\tilde{\sigma}_{\text{NC}}$ with the statistical δ_{stat} , systematic δ_{syst} and total δ_{tot} errors. The quantities shown are total uncorrelated systematic δ_{unc} with the contributions from the electron energy scale uncertainty $\delta_{\text{unc}}^{\text{E}}$ and hadronic energy scale uncertainty $\delta_{\text{unc}}^{\text{had}}$. The effect of other uncorrelated systematic uncertainties is included into δ_{unc} . The correlated systematic error δ_{cor} is shown with the contributions from electron energy scale $\delta_{\text{cor}}^{\text{E}}$, polar angle measurement $\delta_{\text{cor}}^{\Theta}$, hadronic energy scale $\delta_{\text{cor}}^{\text{had}}$, noise subtraction $\delta_{\text{cor}}^{\text{Noi}}$, simulated background $\delta_{\text{cor}}^{\text{Bkg}}$, wrong charge data subtraction $\delta_{\text{cor}}^{\text{WrCh}}$. The normalization and polarization errors are not included into the errors. 177
- C.7 The NC e^+p double differential reduced cross section $\tilde{\sigma}_{\text{NC}}$ measured on the $Q^2 - y$ bin grid for unpolarized leptons with the statistical δ_{stat} , systematic δ_{syst} and total δ_{tot} errors. The quantities shown are total uncorrelated systematic δ_{unc} with the contributions from the electron energy scale uncertainty $\delta_{\text{unc}}^{\text{E}}$ and hadronic energy scale uncertainty $\delta_{\text{unc}}^{\text{had}}$. The effect of other uncorrelated systematic uncertainties is included into δ_{unc} . The correlated systematic error δ_{cor} is shown with the contributions from electron energy scale $\delta_{\text{cor}}^{\text{E}}$, polar angle measurement $\delta_{\text{cor}}^{\Theta}$, hadronic energy scale $\delta_{\text{cor}}^{\text{had}}$, noise subtraction $\delta_{\text{cor}}^{\text{Noi}}$, simulated background $\delta_{\text{cor}}^{\text{Bkg}}$, wrong charge data subtraction $\delta_{\text{cor}}^{\text{WrCh}}$. The normalization and polarization errors are not included into the errors. . . . 179
- C.8 The NC e^-p double differential reduced cross section $\tilde{\sigma}_{\text{NC}}$ for measured on the $Q^2 - y$ bin grid unpolarized leptons with the statistical δ_{stat} , systematic δ_{syst} and total δ_{tot} errors. The quantities shown are total uncorrelated systematic δ_{unc} with the contributions from the electron energy scale uncertainty $\delta_{\text{unc}}^{\text{E}}$ and hadronic energy scale uncertainty $\delta_{\text{unc}}^{\text{had}}$. The effect of other uncorrelated systematic uncertainties is included into δ_{unc} . The correlated systematic error δ_{cor} is shown with the contributions from electron energy scale $\delta_{\text{cor}}^{\text{E}}$, polar angle measurement $\delta_{\text{cor}}^{\Theta}$, hadronic energy scale $\delta_{\text{cor}}^{\text{had}}$, noise subtraction $\delta_{\text{cor}}^{\text{Noi}}$, simulated background $\delta_{\text{cor}}^{\text{Bkg}}$, wrong charge data subtraction $\delta_{\text{cor}}^{\text{WrCh}}$. The normalization and polarization errors are not included into the errors. 181
- C.9 The NC e^-p single differential cross section $d\sigma_{\text{NC}}/dQ^2$ for positively polarized ($P_e = +32.5\%$) leptons with the statistical δ_{stat} , systematic δ_{syst} and total δ_{tot} errors. The quantities shown are total uncorrelated systematic δ_{unc} with the contributions from the electron energy scale uncertainty $\delta_{\text{unc}}^{\text{E}}$ and hadronic energy scale uncertainty $\delta_{\text{unc}}^{\text{had}}$. The effect of other uncorrelated systematic uncertainties is included into δ_{unc} . The correlated systematic error δ_{cor} is shown with the contributions from electron energy scale $\delta_{\text{cor}}^{\text{E}}$, polar angle measurement $\delta_{\text{cor}}^{\Theta}$, hadronic energy scale $\delta_{\text{cor}}^{\text{had}}$, noise subtraction $\delta_{\text{cor}}^{\text{Noi}}$, simulated background $\delta_{\text{cor}}^{\text{Bkg}}$, wrong charge data subtraction $\delta_{\text{cor}}^{\text{WrCh}}$. The normalization and polarization errors are not included into the errors. 182

- C.10 The NC e^+p single differential cross section $d\sigma_{\text{NC}}/dQ^2$ for negatively polarized ($P_e = -37.6\%$) leptons with the statistical δ_{stat} , systematic δ_{syst} and total δ_{tot} errors. The quantities shown are total uncorrelated systematic δ_{unc} with the contributions from the electron energy scale uncertainty $\delta_{\text{unc}}^{\text{E}}$ and hadronic energy scale uncertainty $\delta_{\text{unc}}^{\text{had}}$. The effect of other uncorrelated systematic uncertainties is included into δ_{unc} . The correlated systematic error δ_{cor} is shown with the contributions from electron energy scale $\delta_{\text{cor}}^{\text{E}}$, polar angle measurement $\delta_{\text{cor}}^{\Theta}$, hadronic energy scale $\delta_{\text{cor}}^{\text{had}}$, noise subtraction $\delta_{\text{cor}}^{\text{Noi}}$, simulated background $\delta_{\text{cor}}^{\text{Bkg}}$, wrong charge data subtraction $\delta_{\text{cor}}^{\text{WrCh}}$. The normalization and polarization errors are not included into the errors. 183
- C.11 The NC e^-p single differential cross section $d\sigma_{\text{NC}}/dQ^2$ for positively polarized ($P_e = +36.9\%$) leptons with the statistical δ_{stat} , systematic δ_{syst} and total δ_{tot} errors. The quantities shown are total uncorrelated systematic δ_{unc} with the contributions from the electron energy scale uncertainty $\delta_{\text{unc}}^{\text{E}}$ and hadronic energy scale uncertainty $\delta_{\text{unc}}^{\text{had}}$. The effect of other uncorrelated systematic uncertainties is included into δ_{unc} . The correlated systematic error δ_{cor} is shown with the contributions from electron energy scale $\delta_{\text{cor}}^{\text{E}}$, polar angle measurement $\delta_{\text{cor}}^{\Theta}$, hadronic energy scale $\delta_{\text{cor}}^{\text{had}}$, noise subtraction $\delta_{\text{cor}}^{\text{Noi}}$, simulated background $\delta_{\text{cor}}^{\text{Bkg}}$, wrong charge data subtraction $\delta_{\text{cor}}^{\text{WrCh}}$. The normalization and polarization errors are not included into the errors. 184
- C.12 The NC e^-p single differential cross section $d\sigma_{\text{NC}}/dQ^2$ for negatively polarized ($P_e = -26.0\%$) leptons with the statistical δ_{stat} , systematic δ_{syst} and total δ_{tot} errors. The quantities shown are total uncorrelated systematic δ_{unc} with the contributions from the electron energy scale uncertainty $\delta_{\text{unc}}^{\text{E}}$ and hadronic energy scale uncertainty $\delta_{\text{unc}}^{\text{had}}$. The effect of other uncorrelated systematic uncertainties is included into δ_{unc} . The correlated systematic error δ_{cor} is shown with the contributions from electron energy scale $\delta_{\text{cor}}^{\text{E}}$, polar angle measurement $\delta_{\text{cor}}^{\Theta}$, hadronic energy scale $\delta_{\text{cor}}^{\text{had}}$, noise subtraction $\delta_{\text{cor}}^{\text{Noi}}$, simulated background $\delta_{\text{cor}}^{\text{Bkg}}$, wrong charge data subtraction $\delta_{\text{cor}}^{\text{WrCh}}$. The normalization and polarization errors are not included into the errors. 185
- C.13 The NC e^+p unpolarized single differential cross section $d\sigma_{\text{NC}}/dQ^2$ with the statistical δ_{stat} , systematic δ_{syst} and total δ_{tot} errors. The quantities shown are total uncorrelated systematic δ_{unc} with the contributions from the electron energy scale uncertainty $\delta_{\text{unc}}^{\text{E}}$ and hadronic energy scale uncertainty $\delta_{\text{unc}}^{\text{had}}$. The effect of other uncorrelated systematic uncertainties is included into δ_{unc} . The correlated systematic error δ_{cor} is shown with the contributions from electron energy scale $\delta_{\text{cor}}^{\text{E}}$, polar angle measurement $\delta_{\text{cor}}^{\Theta}$, hadronic energy scale $\delta_{\text{cor}}^{\text{had}}$, noise subtraction $\delta_{\text{cor}}^{\text{Noi}}$, simulated background $\delta_{\text{cor}}^{\text{Bkg}}$, wrong charge data subtraction $\delta_{\text{cor}}^{\text{WrCh}}$. The normalization and polarization errors are not included into the errors. 186

- C.14 The NC e^-p unpolarized single differential cross section $d\sigma_{\text{NC}}/dQ^2$ with the statistical δ_{stat} , systematic δ_{syst} and total δ_{tot} errors. The quantities shown are total uncorrelated systematic δ_{unc} with the contributions from the electron energy scale uncertainty $\delta_{\text{unc}}^{\text{E}}$ and hadronic energy scale uncertainty $\delta_{\text{unc}}^{\text{had}}$. The effect of other uncorrelated systematic uncertainties is included into δ_{unc} . The correlated systematic error δ_{cor} is shown with the contributions from electron energy scale $\delta_{\text{cor}}^{\text{E}}$, polar angle measurement $\delta_{\text{cor}}^{\Theta}$, hadronic energy scale $\delta_{\text{cor}}^{\text{had}}$, noise subtraction $\delta_{\text{cor}}^{\text{Noi}}$, simulated background $\delta_{\text{cor}}^{\text{Bkg}}$, wrong charge data subtraction $\delta_{\text{cor}}^{\text{WrCh}}$. The normalization and polarization errors are not included into the errors. 187
- C.15 The $x F_3^{\gamma Z}$ structure function transformed to $Q^2 = 1500 \text{ GeV}^2$ with the statistical δ_{stat} and total δ_{tot} errors. 188

Bibliography

- [1] E. Rutherford, The Scattering of α and β Particles by Matter and the Structure of the Atom, *Phil. Mag.* 21:669, 1911
- [2] R. Hofstadter and R.W. McAllister, *Phys. Rev.* 98: 217-218, 1955
- [3] E.D. Bloom *et al.*, *Phys. Rev. Lett.* 23: 930-934, 1969
M. Breidenbach *et al.*, *Phys. Rev. Lett.* 23: 935-939, 1969
- [4] J.D. Bjorken, *Phys. Rev.*, 148: 1467-1478, 1966.
- [5] M. Gell-Mann, *Il Nuovo Cimento* 4 (S2): 848, 1956
T. Nakano and N. Nishijima, *Progr. Theor. Phys.* 10 (5): 581, 1955
- [6] G. Dissertori *et al.*, “Quantum Chromodynamics”, Oxford UK: Univ. Pr. (2003) 554 p.
- [7] D. H. Perkins “Introduction to High Energy Physics”, Oxford UK: Univ. Pr. (2001) 440 p.
- [8] Combined Measurement of Neutral and Charged Current Cross Sections at HERA, H1prelim-10-141 and ZEUS-prel-10-017, 2010
- [9] A. Djouadi, S. Ferrag, *Phys. Lett.* **B586** (2004)
F. Demartin, S. Forte, E. Mariani, J. Rojo, A. Vicini, *Phys. Rev.* **D82** (2010)
- [10] J. Baglio, A. Djouadi, S. Ferrag, R. M. Godbole, *Phys. Lett.* **B699** (2011)
- [11] Combined Electroweak and QCD Fit of Inclusive Neutral and Charged Current Data with Polarized Lepton Beams at HERA, H1prelim-10-042, 2010
- [12] Search for Contact Interactions in $e^\pm p$ Collisions at HERA, DESY-11-114, 2011
- [13] R. Brock *et al.* [CTEQ Collaboration], “Handbook of perturbative QCD: Version 1.0”, *Rev. Mod. Phys.* **67** (1995) 157-248.
- [14] C.G. Callan and D. Gross, *Phys. Rev. Lett.* 22, 156, 1969.
- [15] A. Bodek *et al.*, *Phys. Rev.* D20, 1471, 1979
- [16] D. J. Gross and F. Wilczek, *Phys. Rev.* **D8** , 1973.
- [17] C. Collins, E. Soper and G. Sterman, Factorization of Hard Processes in QCD, A.H. Müller, ed., “Pertubative QCD”, *Adv. Ser. Direct. High Energy Phys.* **5**, 1 (1988), arXiv:hep-ph/0409313v1.

- [18] R. Devenish, A. Cooper-Sarkar, "Deep inelastic scattering", Oxford, UK: Univ. Pr. (2004) 403 p.
- [19] V.N. Gribov and L.N. Lipatov, *Yad. Fiz.* **15**, 781 (*Sov. J. Nucl. Phys.* **15**, 438), 1972.
- [20] G. Altarelli and G. Parisi, *Nucl. Phys.* **B126**, 298, 1977,
Yu.L. Dokshitzer, *Sov. Phys. JETP* 46, 641, 1977,
L.N. Lipatov, *Sov. J. Nucl. Phys.* 20, 94, 1975,
- [21] G. Altarelli and G. Martinelli, Transverse Momentum of Jets in Electroproduction from Quantum Chromodynamics, *Phys. Lett.* **B76**, 89, 1978.
- [22] A.M. Cooper-Sarkar *et. al.*, Measurement of the Longitudinal Structure Function and the Small x Gluon Density of the Proton, *Z. Phys.* **C39**, 281, 1988.
- [23] E. Derman, *Phys. Rev. D* 7, (1973) 2755
- [24] G. Ingelman and R. Rückl, *Phys. Lett. B* 201, (1988) 369
- [25] Electroweak Neutral Currents at HERA, H1prelim-06-142, 2006
- [26] High Q² Charged Current in polarised ep collisions at HERA II, H1prelim-09-043, 2009
- [27] F. Bloch and A. Nordsieck, *Phys. Rev.* **52**, 54, 1937.
- [28] D. Yennie, S. Frautschi, H. Suura, *Ann. Phys.* **13**, 379, 1961
- [29] A. Arbuzov, D. Bardin, J. Blümlein, L. Kalinovskaya, T. Riemann, HECTOR 1.00 A program for the calculation of QED, QCD and electroweak corrections to ep and $l^\pm N$ deep inelastic neutral and charged current scattering, DESY 95-185, 1995
- [30] HERA, A Proposal for a Large Electron-Proton Colliding Beam Facility at DESY, edited by B. H. Wiik, DESY HERA 81/10, 1981
W. Bialowons, Status of HERA, DESY-M-96-13F, 1996
- [31] B. J. Holzer, HERA : Lessons learned from the HERA upgrade, In: Final CARE-HHH Workshop on Scenarios for the LHC Upgrade and FAIR, Chavannes-de-Bogis, Switzerland, 24 - 25 Nov 2008, pp.30-35
U. Schneekloth, (ed.), The HERA luminosity upgrade, DESY-HERA-98-05, 1998
- [32] Particle Data Group, Review of Particle Physics, *Phys. Lett. B* **592**,1 (2004)
- [33] I. Abt *et. al.* (H1), The Tracking, calorimeter and muon detectors of the H1 experiment at HERA, *Nucl. Instr. and Meth. A* **386**, 348-396 (1997)
- [34] The ZEUS Detector, Status Report, DESY, 1993
- [35] HERMES Collab., HERMES Technical Design Report, DESY-PRC-93-06, 1993

- [36] E. Hartouni *et. al.* An Experiment to Study CP Violation in the B System Using an Internal Target at the HERA Proton Ring, Design Report, DESY-PRC-95-01, 1995
- [37] A. A. Sokolov, I. M. Ternov and V. V. Mikhailin, Synchrotron Radiation and Its Application, *Izv. Vuz. Fiz.* **4**, 7 (1976)
- [38] G.Z.M. Berglund, Spin-Orbit Maps and Electron Spin Dynamics for the Luminosity Upgrade Project at HERA, Ph.D. Thesis, Alfvén Laboratory, Stockholm, 2001
- [39] J. Böhme, Precision Measurement with the Transverse Polarimeter at HERA II, *Eur. Phys. J. C* **33**, 2004
- [40] M. Beckman *et. al.* The Longitudinal Polarimeter at HERA, *Nucl. Instr. Meth. A* **479**, 2002
Z. Zhang, Electron Polarization Measurement Using a Fabry-Pérot Cavity at HERA, Proceedings the 2001 HEP, 2001
- [41] L. Favart *et. al.* Proposal for Installation of a Very Forward Proton Spectrometer in H1 after 2000, H1-internal note H1-05/00-582, 2000
- [42] P. Van Eshch *et. al.* The H1 Forward Proton Spectrometer at HERA, *Nucl. Instr. Meth. A* **446**, 2000
- [43] B. List Diffraktive J/psi-Produktion in Elektron-Proton-Stoessen am Speicherring HERA, H1-internal note H1-10/93-319, 1993
- [44] W. Brückner *et. al.* Upgrade of the H1 Forward Neutron Calorimeter, H1-internal note H1-11/99-578, 1999
- [45] R. D. Evans, “The Atomic Nucleus”, McGraw-Hill, New York, 1955
- [46] H1 Calorimeter Group, B. Andrieu *et. al.*, Beam tests and calibration of the H1 liquid argon calorimeter with electrons, *Nucl. Instrum. Meth. A* **350** pp. 57-72, 1994
- [47] B. Andrieu *et. al.* Results from Pion Calibration Runs for the H1 Liquid Argon Calorimeter and Comparisons with Simulations, *Nucl. Instr. Meth. A* **336**, 1993
- [48] R. D. Appuhn *et al.* [H1 SPACAL Group], *Nucl. Instrum. Meth. A* **386** (1997) 397
- [49] D. Pitzl, Tracking group report: DST7, Talk at H1 software plenary, June 2009
- [50] M. Ch. Urban, The new CIP2k z-Vertex Trigger for the H1 Experiment at HERA, Dissertation, Univ. Zürich, DESY-THESIS-2004/044, 2004
- [51] B. List, The H1 Silicon Tracker, *Nucl. Instr. and Meth. A* **549**, 33-36 (2005)
- [52] V. Blobel Software alignment for tracking detectors, *Nucl. Instr. Meth. A* **566**, 5-13, 2006
C. Kleinwort, H1 Alignment Experiences, CERN rep. 2007-004, 2007

- [53] G. Grindhammer *et. al.*, The First Level LAr Trigger Physics Requirement, H1-Note H1-TR-301, DESY, 1987
- [54] C. Kiesling *et. al.*, The H1 Neural Network Trigger, Preprints submitted to Elsevier Preprint, AIHENP 99, Crete, Greece
- [55] C. Beigbeder *et. al.*, Level 2 Topological Trigger (L2TT) Hardware, H1-internal note H1-07/98-547, 1998
- [56] T. Nicholls *et. al.*, IEEE Trans. Nucl. Sci. 45 (1998) 810
- [57] R. Prosi, The 1993 L4 Filter Farm Selection Algorithm, H1-internal note H1-95-432, 1995
- [58] Ch. Wissing *et. al.*, The H1 ToF System in 1996 and 1997, H1-internal note H1-01/98-533, 1998.
- [59] H. Bethe and W. Heitler, On the stopping of Fast Particles and on the creation of Positive Electrons, Proc. Roy. Soc. Lond. A **146**, pp. 83-112, 1934
- [60] I. Abt *et. al.* (H1), The H1 detector at HERA, Nucl. Instr. and Meth. A **386**, 310-347, 1997
- [61] S. Schmitt, QEDC Analysis Status, talk at H1 plenary meeting, February 2011.
- [62] T. Benisch *et. al.*, New Data Storage Model for H1
- [63] V. Blobel, The BOS System, 2003
- [64] R. Brun *et. al.*, GEANT User's Guide, CERN-DD/EE-84-1, 1987
- [65] J. Meyer, Guide for the H1 Simulation Program H1SIM, Internal Software Note 03-11/89, DESY, 1989
- [66] M. Peters, Die parametrisierte Simulation elektromagnetischer Schauer, Dissertation, MPI München, MPI-PhE/92-13, 1992
M. Rudowicz, Hadronische Schauersimulation fuer den H1-Detektor, Dissertation, MPI München, MPI-PhE/92-14, 1992
- [67] Description is available at
<https://www-h1.desy.de/icas/imanuals/h1rec/h1rec9/h1rec.html>
- [68] The H1 OO Group, <https://www-h1.desy.de/icas/oo/>
The H1 OO Group, The H1 OO Physics Analysis Project, 2005
- [69] P. Brun and F. Rademakers, Nucl. Instrum. Meth. A **389**, 81 (1997)
- [70] Description is available at
<https://www-h1.desy.de/icas/imanuals/h1red/>
- [71] A. Blondel and F. Jacquet, Proc. of the *Study of an ep Facility for Europe*, U. Amaldi, DESY 79/48, 391 p, 1971

- [72] U. Bassler and G. Gernardi, On the Kinematic Reconstruction of Deep Inelastic Scattering at HERA, Nucl. Instrum. Meth., **A 361**, pp 197-208, 1995
- [73] U. Bassler and G. Gernardi, Structure Function Measurements and Kinematic Reconstruction at HERA, Nucl. Instrum. Meth., **A 426**, pp 583-598, 1999
- [74] S. Bentvelsen, J. Engelen, P. Kooijman, Reconstruction of (x, Q^2) and extraction of structure functions in neutral current scattering at HERA. In W. Buchmüller and G. Ingelman, Proceedings of the Workshop: Physics at HERA, Vol. 1, pp 23-41, DESY, 1991
- [75] S. Spiesberger HERACLES and DJANGO: Event Generation of ep Interactions at HERA Including Radiative Processes, MZ-TH/05-15, 2005
- [76] L. Lönnblad Comp. Phys. Comm. **71** 15, 1992
- [77] T. Sjöstrand PYTHIA 5.7 and JETSET 7.4, LU TP 95-20, 1995
- [78] A. Mücke *et. al.* SOPHIA: Monte-Carlo Simulations of Photohadronic Processes in Astrophysics, BA-99-33, 1999
- [79] H. Spiesberger, A. Kwiatkowski and H.J. Mohring HERACLES: An Event Generator for ep Interactions at HERA Energies Including Radiative Process: Version 1.0, Comp. Phys. Comm. **69**, pp. 155-172, 1992
- [80] Description is available at
<http://hep.pa.msu.edu/cteq/public/6.0-6.5/cteq6pdf.html>
- [81] High Q² Neutral Current in polarised ep collisions at HERA II , H1prelim-09-042, 2009
- [82] J.F. Owens. Phys. Rev. D **21** (1980), p. 54
M. Drees and F. Halzen. Phys. Rev. Lett. **61** (1988), p. 275
M. Drees and R.M. Godbole. Phys. Rev. D **39** (1989), p. 169
- [83] T. Abe *et. al.* GRAPE – Dilepton: A Generator for Dilepton Production in ep Collisions
- [84] T. Ishikawa *et. al.* GRACE manual, KEK Report 92-19, 1993
- [85] U. Baur, J. A. M. Vermaseren and D. Zeppenfeld, Nucl. Phys. **B375**, 3 (1992)
- [86] Ch. Berger and P. Kandel, A new Generator for Wide Angle Bremsstrahlung. In: A.T. Doyle, G. Grindhammer, G. Ingelman and H. Jung, Editors, Proceedings of the Workshop Monte Carlo Generators for HERA Physics, DESY (1998), p. 596 DESY-PROC-1999-02.
- [87] A. Dubak, Measurement of the $e^\pm p$ Neutral Current DIS Cross Section and the F_2 , F_L , xF_3 Structure Functions in the H1 Experiment at HERA, München, 2003

- [88] A. Nikiforov, Measurement of the Neutral Current $e^\pm p$ Cross Sections Using Longitudinally Polarized Lepton Beams at HERA II, PhD thesis, München, 2007
- [89] P. Bruel, Recherche d'interactions au-delà du Modèle Standard à HERA, PhD thesis, Orsay, 1998.
- [90] B. Heinemann, Measurement of Charged Current and Neutral Current Cross Sections in Positron Proton Collisions at $\sqrt{s} \approx 300 \text{ GeV}^2$, PhD thesis, Hamburg, 1999.
- [91] A. Mehta, New Track Based Electron Finder, Talk at the high Q^2 Analysis meeting, Hamburg, October 2003.
- [92] L. West How to use Heavy Flavour Working Group Track, Muon and Electron Selection Code H1PHAN Version $\geq 3.00/01$, available at https://www-h1.desy.de/icas/imanuals/h1phan/track_manual30106.ps, 2000
- [93] V. Blobel, A new fast track-fit algorithm based on broken lines, Nucl. Instr. and Meth. A 556, 14-17, 2006
- [94] V. Blobel, A new fast track-fit algorithm based on broken lines, Talk at Workshop on Tracking In high Multiplicity Environments, Zürich, October 3-7, 2005
- [95] V. Blobel, Central Track Reconstruction, Talk at H1 tracking group meeting, March 11, 2004
- [96] T. H. Tran, Mesures de précision de la section efficace des processus courant chargé et courant neutre à grand Q^2 à HERA avec le faisceau d'électrons polarisés, Dissertation, Université Paris XI, Orsay, LAL10-28, 2010
- [97] L. Görlich and H.P. Wellisch, Documentation of the LAr Clustering, H1 Internal report, H1-12/91-204 (1991)
- [98] H1 Calorimeter Group, Results from Pion Calibration Runs for the H1 Liquid Argon Calorimeter and Comparisons with Simulations, NIM **A265** (1988) 419, NIM **A275** (1989) 246, DESY 89-22 (1989)
- [99] M. Peez, B. Portheault, E. Sauvan, H1 Internal Note H1-01/05-616
- [100] R. Kogler, Measurement of Jet Production in Deep-Inelastic ep Scattering at HERA, PhD thesis, Hamburg, 2010
- [101] V. Shekelyan, Simulation and Reconstruction in H1 Liquid Argon Calorimetry, H1 Internal Note H1-IN-288(04/1993)
- [102] S. Shushkevich, Talk at H1 ELAN Meeting, May 2010
- [103] M. Peez, B. Portheault *et. al.*, An energy flow algorithm for Hadronic Reconstruction in OO: Hadroo2, H1-IN-616 (2005)
- [104] S. Shushkevich, Talk at H1 ELAN Meeting, September 2008

- [105] Private communication from A. Glazov.
- [106] H1 Collaboration, H1 Fast Trigger Specification of the L1 System, 2000
- [107] Private communication from V. Andreev
- [108] C. Veelken, H1NonepBgFinder - Rejection of Cosmic Muon and Beam-Halo Events in the H1OO Framework, H1 Internal Note H1-09/02-603, 2002
- [109] T.Lastovicka, Eur. Phys. J. C **24** 529, 2002
- [110] J. Blumlein, Z. Phys. **C47** (1990) 89-94
- [111] Private communication from S. Schmitt S. Schmitt, Status of QEDC Lumi analysis, talk at H1 plenary meeting, June 2011.
- [112] B. Sobloher [for the POL2000 Collab.], Polarization and Polarimetry at HERA, PST2009, 2009
- [113] High Q^2 Neutral Current in polarised ep collisions at HERA II, H1prelim-09-042, 2009
- [114] PDF fits including HERA-II high Q^2 data (HERAPDF1.5), H1prelim-10-142, 2010
- [115] Measurement of the longitudinal structure function F_L at high Q^2 at HERA, H1prelim-08-042, 2008

Acknowledgements

The analysis presented in this thesis is a result of collaborative efforts of many people I would like to thank. Especially, I am thankful to the following people:

My supervisor Prof. Dr. Christian Kiesling for the discussions on various (physics and non-physics) topics, usually in a form of tea-and-physics, for the enthusiastic atmosphere he maintains in the MPI group and for his advises in (physical and non-physical) questions.

Dr. Vladimir Chekelian, my day to day supervisor, who, with his professional experience, governed the H1 group at MPI over last years. His contribution to my education of an experimentalist is invaluable, I have learned a lot from daily collaboration with him.

The members of ELAN group: Eram Rizvi, Alexandre Glazov, Zhiqing Zhang, Max Klein, Emmanuel Sauvan, Ana Dubak, Bob Olivier, Andrey Nikiforov, Ringaile Plačakyte, Shiraz Habib, Tran Trong Hieu, — for the inspiring discussions within our group. I have never got any negative response to a material I presented for the discussions, but only positive, constructive and helpful discussions.

My officemates at MPI and at DESY: Kolja Protmann, Roman Kogler, Anreas Moll, Aziz Dossanov, Martin Ritter, Elena Nedelkovska, Daniel Britzger, Susanna Koblitz for discussions, jokes and other things we shared apart from the office.

Special thanks to MPI football team for the outdoor activities I was involved over these years.

I am indebted to my family Nicolai, Marina and Elena Shushkevich for continuous support and patience (they show through my whole life).

This work would take much more time without a help of Elena Polovinkina, who converted most of non-histogram illustrations from jpeg, GIF, strange-ps, very-strange-eps, frames of PDF and plenty of other formats into the eps files which could be included into the LaTeX compilation.

I could never be sure I have recollected all the persons influenced me and my analysis over last three years. So, dear reader, if by accident I have forgotten to include you into the list, accredit this to an absent-mindedness of the author, and do not hesitate to do it yourself.